UNIVERSITÀ DI TRENTO | Department of Physics

ASML

University of Trento

Department of Physics

Ph.D. Thesis

Time-resolved spectroscopic investigation of N_2/H_2 nanosecond pulsed discharges and EUV-induced low-temperature plasmas

---

Supervisors:

prof. Luca Matteo Martini

prof. Richard Engeln

Candidate:

Luca Maestri

Academic Year 2024/2025

Finanziato dall'Unione europea NextGenerationEU | Ministero dell'Università e della Ricerca | Italiadomani PIANO NAZIONALE DI RIPRESA E RESILIENZA | UNIVERSITÀ DI TRENTO

Contents

Preface

Extreme ultraviolet (EUV) lithography is now central to advanced semiconductor manufacturing. At the same time, the low-density plasmas triggered by EUV photons inside scanner-relevant environments remain only partially characterised. Their transient, photon-driven nature complicates invasive diagnostics and makes equilibrium assumptions unreliable. This thesis addresses that gap using optical emission spectroscopy (OES), by studying EUV-induced plasmas in H_2, N_2, and H_2/N_2 mixtures and comparing them with two complementary reference platforms: nanosecond pulsed discharges (NPD) and a mono-energetic electron-beam radiation (EBR) source. The guiding idea is to separate driver-specific fingerprints from shared low-pressure kinetics, and to identify spectroscopic diagnostics that are robust, quantitative, and deployable under tool-relevant constraints.

The work was carried out in close collaboration with ASML and partner laboratories, and is motivated by practical questions that arise directly in EUV scanner operation: How dense and how energetic are EUV-induced plasmas in hydrogen- and nitrogen-containing environments? How do their properties influence charging, surface chemistry, and contamination control? And, crucially for industrial relevance, which diagnostics can be implemented without perturbing the plasma or compromising tool operation? These constraints naturally lead to OES as the primary diagnostic: it is line-of-sight, radiation-based, and compatible with the optical and vacuum restrictions of EUV beamlines.

At the core of the thesis is a calibrated OES framework for non-thermal plasmas in H_2, N_2, and H_2/N_2 mixtures across three different drivers: NPD, EUV irradiation, and EBR. Molecular band systems—the N_2 Second Positive (SPS) and First Negative (FNS) systems and the H_2 Fulcher-α system—are used as sensitive probes of excitation pathways and as rotational and vibrational thermometers where those concepts remain meaningful. The hydrogen Balmer series (Hα–Hϵ) is exploited wherever possible to access timing information and relative changes in excitation. In principle, Stark broadening of Balmer lines can provide time-resolved electron densities in low-temperature plasmas, and this has been demonstrated for nanosecond discharges under conditions comparable to those of this work in the literature. In the present thesis, however, Stark-based n_e retrieval is *not* implemented: under the EUV-

and EBR-driven conditions the expected Stark widths are well below the instrumental and Doppler contributions, and on the NPD platform the focus is placed on rovibrational and kinetic diagnostics, with Stark analysis left as a natural extension for follow-up work. Electron-density trends are therefore inferred only indirectly, from kinetics, modelling considerations, and external reference data. A substantial part of the effort is devoted to calibration and forward modelling: the instrumental function is measured using a diode laser and Fabry–Pérot etalon, and synthetic spectra generated with PGOPHER are consistently convolved with the measured response and fitted line-by-line. This common framework enables quantitative comparisons across sources, pressures, and gas compositions.

Each plasma platform plays a distinct role. NPD provides a reproducible, electrically driven reference with strong non-equilibrium excitation and pronounced afterglows, in which metastables such as $N_2(A^3\Sigma_u^+)$ can feed late-time emission. EUV beamlines deliver the photon-driven plasmas that are directly relevant to lithography, characterised by low densities, short lifetimes, and strong coupling to surfaces and out-of-band radiation. The EBR setup, finally, supplies a clean mono-energetic electron source that generates plasmas without high-voltage pulsing or EUV photons, providing a benchmark for electron-impact kinetics and an independent check of the spectral analysis workflow. Taken together, these platforms allow the thesis to disentangle which spectroscopic signatures are generic to low-pressure H_2/N_2 plasmas and which are specific to the driving mechanism.

Beyond the platform-specific results, the thesis is intended as a methodological contribution. It demonstrates how carefully calibrated OES can be used to extract rotational and vibrational descriptors, follow temporal evolution from nanoseconds to microseconds, and identify qualitative changes in excitation and relaxation pathways under conditions where more direct probes are impractical. At the same time, it makes clear where simplified interpretations break down: Balmer-line populations in low-pressure EUV and EBR plasmas are generally non-Boltzmann, and corona-style electron-temperature estimates based on SPS/FNS ratios can be misleading in pulsed, non-stationary discharges. These findings motivate collisional–radiative and kinetic modelling, and provide concrete experimental benchmarks and boundary conditions for such models.

The project evolved iteratively. Early NPD measurements shaped the calibration and fitting workflow; subsequent EUV campaigns exposed the limits of common diagnostic shortcuts; and later EBR experiments helped isolate electron-impact processes from photon-driven and surface-driven effects. This progression is reflected in the structure of the manuscript and in the way experimental design, data analysis, and physical interpretation inform one another. Although the immediate motivation is industrial, the diagnostic strategies and several physical conclusions are intended to be transferable to other low-temperature plasmas involving nitrogen and hydrogen.

The manuscript is organised as follows. Chapter 1 introduces the physical

and technological context and the role of EUV-induced plasmas in scanner environments. Chapter 2 summarises the relevant spectroscopy of nitrogen and hydrogen and reviews OES methodology and its limitations at low pressure. Chapter 3 details the experimental setups and the data-processing workflow, including instrumental-function calibration and spectral fitting. Chapters 4–6 present platform-specific results for NPD, EUV beamlines, and EBR, respectively, with emphasis on time-resolved behaviour, mixture effects, and diagnostic cross-checks. Chapter 7 synthesises the cross-platform comparison, translates the findings to EUV lithography implications, and outlines a path toward model-guided, on-tool plasma monitoring.

Chapter 1

Introduction

1.1 Nitrogen-containing plasma applications

Plasmas, often referred to as the "fourth state of matter," are partially ionized gases characterized by collective electromagnetic behavior. They occur naturally (e.g., in lightning, auroras, and the solar corona) and are widely exploited in technological applications ranging from materials processing to lighting, medicine, and nuclear fusion.

Among these, **nitrogen-containing plasmas** hold a central position. Nitrogen is the dominant constituent of the Earth's atmosphere, and its plasma chemistry is relevant in diverse applications such as *surface modification*, *thin-film deposition*, *plasma-assisted combustion*, and *sterilization techniques* [1]. Nitrogen is also a widely used benchmark gas in plasma physics, owing to its rich spectroscopic structure. The *Second Positive System* ($C^3\Pi_u \rightarrow B^3\Pi_g$) and the *First Negative System* ($B^2\Sigma_u^+ \rightarrow X^2\Sigma_g^+$) are particularly valuable for diagnostics because their excitation cross sections and radiative properties are well documented [2].

In this thesis, nitrogen plasmas are investigated alongside pure hydrogen and mixed H_2/N_2 systems. Hydrogen plasmas are of great interest in *semiconductor technology* (for cleaning and surface chemistry) and in *fusion research*, while mixed plasmas allow the study of coupled collisional-radiative kinetics and energy transfer [3, 4]. The primary diagnostic applied throughout this work is **optical emission spectroscopy** (OES), which provides direct access to excited states and transient plasma dynamics.

1.2 Non-thermal plasmas

1.2.1 General concepts

Plasmas can be broadly divided into **thermal plasmas**, where electrons, ions, and neutrals share (to a good approximation) a common temperature, and **non-thermal plasmas (NTPs)**, where electrons are much hotter than the heavy particles. In NTPs, electron energies typically range from 1–10 eV,

while ion and neutral temperatures remain close to room temperature [1, 5]. From a thermodynamic point of view, this situation arises when the rate at which energy is supplied to the plasma exceeds the rate at which it can be redistributed among all degrees of freedom, so that a single equilibrium temperature for the whole system cannot be defined.

In low-temperature plasmas sustained by electric fields, the injected energy is first transferred to the electrons because of their small mass compared to the ions and neutrals. Elastic electron–neutral collisions are inefficient at heating the gas, whereas inelastic collisions efficiently populate internal molecular states (electronic, vibrational, rotational) and produce ionization and dissociation once the corresponding thresholds are reached. As a result, different subsystems of the plasma (electrons, heavy-particle translational motion, internal molecular modes) acquire different characteristic energies, and the plasma develops a marked *non-equilibrium* character.

In the physics of non-thermal plasmas it is customary, although somewhat abusive from a strict thermodynamic standpoint, to describe these different mean energies in terms of separate "temperatures": an electron temperature T_e, a gas (or heavy-particle) temperature T_g, and internal temperatures such as the rotational and vibrational temperatures T_rot and T_vib for molecular species [1, 6]. A typical hierarchy in low-pressure discharges is

$$T_\mathrm{e} \gg T_\mathrm{vib} > T_\mathrm{rot} \simeq T_\mathrm{g}. \tag{1.1}$$

Strictly speaking, a temperature is rigorously defined only for degrees of freedom that are close to local thermodynamic equilibrium and whose distributions are approximately Maxwell–Boltzmann. This is usually the case for the translational and rotational motion of heavy particles, and often a good approximation for low-lying vibrational levels, but not for the electrons, whose energy distribution is in general non-Maxwellian. In that case, T_e and T_vib should be understood as *effective* temperatures that parameterize the average energy of the corresponding distributions, while the underlying kinetics is more accurately described by the electron energy distribution function (EEDF) and by state-resolved populations obtained from the Boltzmann and rate equations.

The presence of hot electrons and internally excited molecules has direct consequences for plasma chemistry. Electron-impact excitation to **electronic** and **vibrational** excited states opens pathways for dissociation and ionization at energies that are much lower than would be required to heat the bulk gas to the same effect. For example, in molecular plasmas (N_2, H_2, CO_2, etc.) stepwise vibrational excitation ("vibrational ladder climbing") can bring molecules close to their dissociation limit, so that subsequent collisions or photon absorption lead to bond breaking with relatively small additional energy input [6]. Electronic excitation can proceed through predissociative states or through states that efficiently transfer energy to reactive channels, again without significantly increasing T_g.

At the same time, NTPs generate large densities of **radicals** (e.g. H, N, O, OH) and **ions**, which are key intermediates in plasma-assisted chemistry. Radicals, with their open-shell electronic structure, participate in barrier-less or low-barrier reactions that drive oxidation, reduction, and surface functionalization. Ions enable ion–molecule reactions in the gas phase and ion-surface interactions (sputtering, etching, implantation) at boundaries. The combined action of energetic electrons, vibrationally and electronically excited molecules, radicals, and ions underlies the efficiency of non-thermal plasmas in applications such as *ozone generation, pollution control, plasma medicine, and microelectronics processing*, where substantial chemical conversion is achieved with only modest gas heating [1, 6].

Because equilibrium assumptions break down, NTPs require **state-resolved kinetic descriptions** of electrons, atoms, ions, and molecules, including their internal degrees of freedom and the full network of excitation, de-excitation, dissociation, recombination, and transport processes. Optical emission spectroscopy is particularly powerful in this regard, as it provides in situ access to populations of selected electronic and vibrational states, and thereby indirect information on the underlying EEDF and reaction pathways. State-to-state kinetic frameworks of this type have been extensively developed for molecular plasmas, in particular for low-pressure N_2 discharges and N_2/O_2 mixtures [3, 7], and will be repeatedly invoked throughout this thesis for the interpretation of nitrogen, hydrogen, and H_2/N_2 plasmas.

1.2.2 Discharge plasmas

Electrical discharges are one of the most common methods of generating NTPs. Depending on the driving voltage, geometry, and pressure, they can manifest as DC or RF glow discharges, microwave plasmas, or nanosecond pulsed discharges (NPDs).

Nanosecond pulsed discharges are especially relevant for this thesis. The short rise time (< 100 ns) of the applied pulse produces intense electron heating while limiting gas heating, creating strongly non-equilibrium conditions [8,9]. This makes them ideal for studying excitation kinetics in nitrogen and hydrogen.

In nitrogen, NPDs strongly populate the $C^3\Pi_u$ state, giving rise to the Second Positive System, while in hydrogen they produce prominent Balmer series emission and Fulcher band radiation. Mixed H_2/N_2 plasmas further enrich the picture, as quenching, vibrational energy transfer, and ion–molecule reactions redistribute the deposited energy.

1.2.3 Nanosecond pulsed discharge plasmas: kinetics and dynamics

Within the broad class of electrical discharges introduced above, **nanosecond pulsed discharges (NPDs)** have attracted strong interest

because they provide high reduced electric fields (E/N), strong transient non-equilibrium, and reproducible plasma conditions on short timescales [8–12].

Breakdown and electron energy. When a fast-rising voltage pulse $V(t)$ (rise time $\lesssim$ 10–20 ns) is applied between electrodes separated by distance d, the instantaneous reduced field is

$$\frac{E}{N}(t) = \frac{V(t)}{d\,N}, \tag{1.2}$$

where N is the neutral number density. At pressures of 1–100 mbar, this typically yields $E/N \sim$ 100–500 Td (1 Td = 10^{-21} Vm^2). Such high fields accelerate electrons to mean energies of several eV within nanoseconds, while the gas temperature remains near ambient. In an electrical discharge, the energy of the applied electric field is transferred predominantly to the electrons because of their much smaller mass compared to ions and neutrals ($m_e \ll m_{\mathrm{ion}}, m_{\mathrm{n}}$). Elastic electron–neutral collisions are inefficient at heating the gas: only a small fraction of the electron kinetic energy is converted into translational energy of the heavy particles at each collision. As a result, electrons can be accelerated up to the thresholds for inelastic processes while the heavy species remain close to room temperature.

Once these thresholds are reached, inelastic collisions efficiently populate internal degrees of freedom of the molecules (vibrational and electronic excitation) and produce ionization and dissociation. In molecular plasmas (such as N_2 and H_2), the relative importance of the different channels is governed by the electron energy distribution function (EEDF) and by the corresponding cross sections for excitation, ionization, and dissociation. Typical cross sections exhibit pronounced thresholds and peaks at characteristic energies (see, e.g., representative electron–N_2 collision cross sections in Fig. 1.1), so that, for a given reduced field E/N, electrons preferentially excite particular vibrational or electronic levels rather than uniformly heating the gas. Gas heating itself mainly occurs on longer timescales via vibration–translation (V–T) and other de-excitation processes, reinforcing the strong non-equilibrium between T_{e} and T_{g} discussed in Section 1.2.1.

The electron energy distribution function (EEDF) quickly deviates from a Maxwellian because the timescale for electron acceleration in the electric field and for inelastic energy losses is shorter than the timescale for elastic thermalization with the heavy particles. The shape of the EEDF is therefore determined by the balance between field-driven acceleration, elastic cooling, and discrete inelastic loss channels, rather than by mutual electron–electron collisions. This leads to characteristic non-Maxwellian features, such as enhanced high-energy tails or plateaus near inelastic thresholds, which sustain efficient excitation and ionization of molecular states even when the bulk gas remains cold [8]. This makes NPDs excellent testbeds for studying state-selective electron-impact processes. Quantitative evaluation of the EEDF

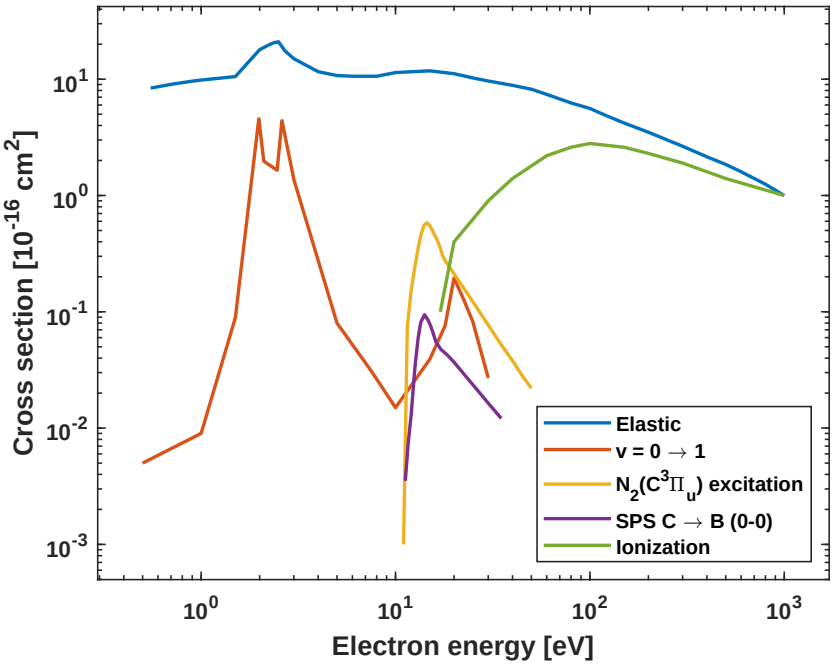

Figure 1.1: Electron–N_2 collision cross sections as a function of electron energy: elastic scattering, vibrational excitation ($v = 0 \to 1$), excitation of the $C^3\Pi_u$ state, emission cross section for the Second Positive System (SPS) C→B (0–0), and total ionization. The pronounced thresholds and peaks of the inelastic channels illustrate how, in nanosecond discharges, electrons preferentially populate internal degrees of freedom and ionize the gas once the corresponding energies are reached, rather than uniformly heating the bulk. Data after Itikawa [2].

in such regimes typically relies on numerical Boltzmann solvers such as the LisbOn KInetics code LoKI-B [13].

Primary ionization and electron balance. The fast breakdown can be described in terms of an electron continuity equation,

$$\frac{\partial n_e}{\partial t} = k_{\text{ion}}(E/N)\, n_e\, n_g - \alpha_{\text{att}}(E/N)\, n_e\, n_g - \alpha_{\text{loss}}\, n_e, \tag{1.3}$$

where k_{ion} is the field-dependent ionization coefficient, α_{att} accounts for electron attachment (notably in electronegative admixtures), and α_{loss} lumps transport/diffusion terms. The steep growth of $k_{\text{ion}}(E/N)$ with field ensures that a sufficiently strong pulse rapidly drives avalanche ionization, reaching peak densities $n_e \sim 10^{14}$–10^{16} cm^{-3} within tens of nanoseconds [11].

Excitation kinetics and emission systems. Energetic electrons populate excited states of N_2 and H_2, giving rise to a rich set of molecular and atomic emission systems. In nitrogen, the most widely used systems in the UV–visible range include the *Second Positive System* (SPS, $C^3\Pi_u \to B^3\Pi_g$) of neutral N_2, the *First Negative System* (FNS, $B^2\Sigma_u^+ \to X^2\Sigma_g^+$) of N_2^+,

and, at shorter wavelengths, the Lyman–Birge–Hopfield and Vegard–Kaplan bands. In hydrogen, the principal features are the atomic *Balmer series* (Hα, Hβ, ...) and the molecular *Fulcher band* ($\mathrm{d}^3\Pi_u \rightarrow \mathrm{a}^3\Sigma_g^+$), complemented at higher energies by the Lyman and Werner band in the VUV region. Together, these systems provide access to rotational and vibrational temperatures, electron-impact excitation rates, and, via Stark broadening of hydrogen lines, electron densities and electric-field-related parameters.

The dominant excitation and emission pathways relevant to this work can be schematically written as

$$\begin{aligned} \mathrm{N_2}(X^1\Sigma_g^+) + e^- &\rightarrow \mathrm{N_2}(C^3\Pi_u) + e^- \quad \text{(e-impact excitation)} \\ \mathrm{N_2}(C^3\Pi_u) &\rightarrow \mathrm{N_2}(B^3\Pi_g) + h\nu \quad \text{(SPS)}, \end{aligned} \tag{1.4}$$

$$\begin{aligned} \mathrm{N_2^+}(X^2\Sigma_g^+) + e^- &\rightarrow \mathrm{N_2^+}(B^2\Sigma_u^+) + e^- \quad \text{(e-impact excitation)} \\ \mathrm{N_2^+}(B^2\Sigma_u^+) &\rightarrow \mathrm{N_2^+}(X^2\Sigma_g^+) + h\nu \quad \text{(FNS)}, \end{aligned} \tag{1.5}$$

$$\begin{aligned} \mathrm{H_2}(X^1\Sigma_g^+) + e^- &\rightarrow \mathrm{H}(n \geq 3) + \mathrm{H} + e^- \quad \text{(dissociative excitation)} \\ \mathrm{H}(n \geq 3) &\rightarrow \mathrm{H}(n = 2) + h\nu \quad \text{(Balmer)}, \end{aligned} \tag{1.6}$$

$$\begin{aligned} \mathrm{H_2}(X^1\Sigma_g^+) + e^- &\rightarrow \mathrm{H_2}(d^3\Pi_u) + e^- \quad \text{(e-impact excitation)} \\ \mathrm{H_2}(d^3\Pi_u) &\rightarrow \mathrm{H_2}(a^3\Sigma_g^+) + h\nu \quad \text{(Fulcher)}. \end{aligned} \tag{1.7}$$

In practice, optical emission spectroscopy (OES) diagnostics exploit these systems in different ways: the rotational structure of the SPS and Fulcher bands is commonly used to infer gas and rotational temperatures; SPS and FNS vibrational populations provide information on vibrational excitation and, indirectly, on the EEDF and reduced electric field; Stark broadening of Balmer lines yields electron density estimates.

In this thesis we will primarily use the $\mathrm{N_2}$ SPS and FNS, together with the H Balmer series and $\mathrm{H_2}$ Fulcher bands, as the main emission systems for time-resolved OES of nanosecond discharges and EUV-induced plasmas. In $\mathrm{H_2/N_2}$ mixtures, vibrational–vibrational (V–V) and vibrational–translational (V–T) processes couple the two gases strongly, redistributing energy between nitrogen and hydrogen and modifying the relative intensities and shapes of these emission systems [10].

Transient plasma decay. After the end of the pulse, the discharge rapidly relaxes. The electron density follows

$$\frac{\mathrm{d}n_e}{\mathrm{d}t} \approx -\alpha_{\mathrm{rec}}\, n_e^2 - \frac{n_e}{\tau_{\mathrm{diff}}}, \tag{1.8}$$

with α_{rec} the effective recombination coefficient and τ_{diff} the ambipolar diffusion time. For low-pressure nanosecond plasmas, typical decay times are microseconds, several orders of magnitude longer than the excitation pulse.

1.2.4 EUV-induced plasmas: mechanisms, scalings, and rate equations

A second class of plasmas investigated in this work is those created by **extreme ultraviolet (EUV) radiation**. In the context of EUV lithography, radiation is concentrated around a narrow band at $\lambda \approx 13.5$ nm. This wavelength was not chosen arbitrarily: multilayer Mo/Si mirrors exhibit a maximum Bragg reflectivity in this region, while laser-produced tin plasmas provide strong line emission near 13.5 nm, so that an efficient combination of source and optics can be realized [14]. For this reason, 13.5 nm was adopted as the industry-standard EUV wavelength. EUV photons at 13.5 nm carry energies around 92 eV, sufficient to photoionize both nitrogen (15.6 eV threshold) and hydrogen (15.4 eV threshold). This direct ionization results in fast plasma formation followed by secondary processes [15].

EUV-induced plasmas differ fundamentally from discharge plasmas:

- They are **photon-driven**, not sustained by external electric fields.
- Plasma densities are relatively low (10^{13}–10^{15} m^{-3}), which, for typical background pressures of a few pascal in EUV scanners (neutral densities $n_g \sim 10^{20}$–10^{21} m^{-3}), corresponds to ionization degrees of only 10^{-8}–10^{-6}.
- Their lifetimes are governed by recombination and diffusion.
- Properties scale with EUV photon flux and pulse structure.

These properties make EUV-induced plasmas especially relevant in environments where high photon fluxes interact with low background pressures, such as in EUV lithography systems.

When an extreme-ultraviolet (EUV) pulse at $\lambda \approx 13.5$ nm ($h\nu \approx 92$ eV) traverses a low-pressure background gas (H_2, N_2, or mixtures), it photoionizes neutrals and creates a transient, weakly ionized plasma, with ionization degrees typically in the range 10^{-8}–10^{-6} under the few-pascal conditions relevant for EUV scanners. . Unlike field-driven discharges, EUV plasmas are *photon-driven* and exist only for the duration of (and shortly after) the EUV pulse, with their evolution governed by photon transport, photoionization, secondary electron processes, electron-impact kinetics, recombination, and diffusion to the walls [14, 15].

Photon transport and primary photoionization. Let $I_\lambda(x,t)$ be the spectral radiance along the beam axis x. For a single species with number density n_g and photoabsorption cross section σ_λ, the Beer–Lambert law gives

$$I_\lambda(x,t) = I_{\lambda,0}(t)\, \exp[-\sigma_\lambda n_g x]\,, \tag{1.9}$$

and the spectral photon flux $\Phi_\lambda(x,t) = I_\lambda(x,t)/(h\nu)$. The volumetric photoionization source term for the electron density is

$$S_{\mathrm{ph}}(x,t) = n_g \int \sigma_\lambda \, \Phi_\lambda(x,t) \, \mathrm{d}\lambda = \frac{n_g}{h} \int \sigma_\lambda \, \frac{I_\lambda(x,t)}{\nu} \, \mathrm{d}\lambda, \tag{1.10}$$

with obvious extension to mixtures, $n_g\sigma_\lambda \to \sum_s n_s\sigma_{\lambda,s}$ for $s \in \{\mathrm{H_2}, \mathrm{N_2}\}$. For a quasi-monochromatic EUV band centered at λ_0 and a top-hat pulse of duration τ_{EUV} and energy E_{p} over illuminated area A, an on-axis estimate of the peak photon flux is

$$\Phi_0 \simeq \frac{E_{\mathrm{p}}}{A\,\tau_{\mathrm{EUV}}\,h\nu_0}, \qquad \nu_0 = \frac{c}{\lambda_0}. \tag{1.11}$$

This sets the order of magnitude of the local photoionization source term near the entrance plane ($x = 0$) of the illuminated plasma volume (cf. Fig. C.1), $S_{\mathrm{ph}} \sim n_g\sigma_{\lambda_0}\Phi_0$.

Photoelectron energies and primary channels. Primary photoelectrons are born with kinetic energy

$$\mathcal{E}_{e,0} = h\nu - I_p - \varepsilon_b, \tag{1.12}$$

where I_p is the ionization potential (15.4 eV for $\mathrm{H_2}$, 15.6 eV for $\mathrm{N_2}$) and ε_b is the binding/ro-vibrational energy of the neutral. For hydrogen, the main channels are

$$\mathrm{H_2} + h\nu \to \mathrm{H_2^+} + e^-, \tag{1.13}$$

$$\mathrm{H_2} + h\nu \to \mathrm{H^+} + \mathrm{H} + e^-, \tag{1.14}$$

followed by rapid ion–molecule reaction

$$\mathrm{H_2^+} + \mathrm{H_2} \to \mathrm{H_3^+} + \mathrm{H}, \tag{1.15}$$

so that $\mathrm{H_3^+}$ often dominates the positive ion population on sub-microsecond scales. For nitrogen, the dominant channel is

$$\mathrm{N_2} + h\nu \to \mathrm{N_2^+} + e^-, \tag{1.16}$$

with possible dissociative pathways depending on the spectral content (including out-of-band photons) and gas conditions.

Secondary (electron-impact) ionization and excitation. The energetic photoelectrons ($\mathcal{E}_{e,0} \lesssim 70$–$80$ eV after subtracting I_p) trigger cascades of electron-impact processes, modifying the electron energy distribution function (EEDF) during and shortly after the pulse. The volumetric electron-impact ionization source reads

$$S_{\mathrm{sec}} = \sum_s k_{\mathrm{ion},s}(T_e, \mathrm{EEDF})\, n_e\, n_s, \tag{1.17}$$

with $k_{\mathrm{ion},s}$ the (effective) ionization rate coefficients for species s (state-averaged over the transient EEDF). Concomitant excitation populates excited states responsible for the emission systems (e.g. N_2 Second Positive and First Negative systems; H Balmer and H_2 Fulcher band) used throughout this thesis.

Global particle balance. Neglecting multi-charged ions and assuming quasineutrality $n_e \approx n_i$, a zero-dimensional electron balance that captures the essential physics is

$$\frac{\mathrm{d}n_e}{\mathrm{d}t} = S_{\mathrm{ph}}(t) + S_{\mathrm{sec}}(t) - \alpha_{\mathrm{rec}}(T_e)\, n_e^2 - \frac{n_e}{\tau_{\mathrm{diff}}}, \tag{1.18}$$

where α_{rec} lumps radiative, dissociative, and three-body recombination appropriate to the dominant ion (e.g. H_3^+ for hydrogen, N_2^+ for nitrogen), and $\tau_{\mathrm{diff}} \sim L^2/D_a$ is an ambipolar diffusion time with L a characteristic chamber dimension. During the pulse ($t \lesssim \tau_{\mathrm{EUV}}$), S_{ph} dominates; afterwards, $S_{\mathrm{ph}} \to 0$ and the evolution reflects the competition of S_{sec}, recombination, and wall/diffusion losses.

Space charge, sheaths, and wall processes. Because EUV photons and hot electrons hit chamber surfaces, *secondary electron emission* (SEE) and *photoelectron emission* from walls and optics contribute additional electrons to the plasma and alter the sheath potentials. These processes lower the mean T_e after the pulse and can significantly modify the transient EEDF and ion energy distributions (IEDFs) impinging on surfaces, relevant for contamination/cleaning and charging [16–19]. In hydrogen environments, the plasma chemistry near surfaces couples to carbon removal and hydrogenation reactions; in nitrogen, charging and local chemistry impact particle transport and defectivity.

Spectral effects and out-of-band radiation. The effective photoionization rate depends not only on the in-band 13.5 nm intensity but also on *out-of-band* (OoB) photons ($\lambda \gtrsim 20$ nm), which can contribute disproportionately due to larger σ_λ at longer wavelengths. Experiments and modeling indicate that OoB components can dominate ionization under certain source/filter conditions, shifting both the magnitude and spatial profile of S_{ph} [20].

Scalings and practical estimates. Combining Eqs. (1.10) and (1.11), the peak electron source density near the entrance plane scales as

$$S_{\mathrm{ph,peak}} \sim \left(\sum_s n_s \sigma_{\lambda_0,s}\right) \frac{E_{\mathrm{p}}}{A\, \tau_{\mathrm{EUV}}\, h\nu_0}. \tag{1.19}$$

For short pulses and low optical depth ($\sigma_{\lambda_0} n_g L \ll 1$), the electron density shortly after the pulse obeys

$$n_e(t \gtrsim \tau_{\mathrm{EUV}}) \approx \int_0^{\tau_{\mathrm{EUV}}} [S_{\mathrm{ph}}(t) + S_{\mathrm{sec}}(t)]\, \mathrm{d}t, \tag{1.20}$$

where S_{sec} depends on the evolving EEDF and gas composition. Subsequent decay follows Eq. (1.18), typically exhibiting sub-μs to μs lifetimes set by diffusion and recombination. Ion composition evolves on similar timescales; for H_2, Eq. (1.15) drives H_3^+ dominance within $\mathcal{O}(0.1\text{–}1\ \mu\mathrm{s})$ at Pa-level pressures, whereas N_2 tends to remain N_2^+-dominated in the same regime.

Implications for diagnostics and for the ASML context. The pulsed, photon-driven origin leads to (i) non-Maxwellian EEDFs during/after the pulse, (ii) strong sensitivity to EUV spectral content and pulse energy, and (iii) low densities that challenge invasive probes. Non-intrusive techniques (time-resolved OES; microwave cavity resonance spectroscopy) and validated kinetic/PIC models are therefore preferred. In EUV scanners, the resulting IEDFs, transient charging, and wall electron yields couple directly to contamination mitigation (e.g. hydrogen-assisted carbon removal) and defectivity control, motivating the comparative approach with nanosecond discharges developed in this thesis [14, 15, 19].

Comparison with nanosecond pulsed discharges. Having introduced both nanosecond pulsed discharges and EUV-induced plasmas, it is useful to briefly compare their main characteristics. NPDs are *field-driven*: the applied voltage pulse controls the reduced electric field E/N, leading to high electron densities and strong non-equilibrium excitation within each pulse. EUV-induced plasmas, in contrast, are *photon-driven* and typically remain at lower densities, with their properties scaling with photon flux and spectral content rather than with E/N. The direct control of electrical parameters in NPDs makes them versatile reference systems for disentangling excitation kinetics in N_2, H_2, and mixtures, and they therefore provide a crucial benchmark for interpreting the spectroscopy of EUV-induced plasmas presented in this thesis [12].

1.2.5 Hydrogen and hydrogen–nitrogen plasmas: spectroscopic perspective

Hydrogen plasmas provide a complementary platform for plasma diagnostics. The **atomic Balmer series** (Hα, Hβ, Hγ, ...) is widely used for electron density measurements via Stark broadening and for electron temperature estimates [21]. Molecular hydrogen contributes additional diagnostics via the **Fulcher band** ($\mathrm{d}^3\Pi_u \rightarrow \mathrm{a}^3\Sigma_g^+$), sensitive to vibrational and rotational excitation [22].

In mixed H_2/N_2 plasmas, complex collisional-radiative coupling emerges:

- Vibrational energy transfer from N_2(X, v) to H_2 enhances dissociation [23].
- Quenching of N_2(C) by H_2 alters the balance of optical emission [6].
- New reactive species (e.g. NH, N_2H^+) appear, relevant for plasma chemistry and surface interactions [4, 24].

Spectroscopically, these systems provide a wide set of emission features (Balmer lines, Fulcher bands, N_2 SPS/FNS) that can be exploited for diagnostics, but also present challenges in spectral overlap and interpretation. In the context of EUV lithography, mixed H_2/N_2 plasmas represent realistic conditions inside the scanner environment. Plasma-activated N_2/H_2 chemistry, including NH and NH_3 formation, has been studied in detail in related low-pressure systems [4,24], underlining the importance of coupled gas-phase and surface processes.

1.3 ASML and the context of EUV lithography

The semiconductor industry has been driven for decades by the continuous miniaturization of devices, with optical lithography as the enabling technology. While deep ultraviolet (DUV) lithography at 193 nm has dominated for over two decades, its physical limits prompted the transition to **extreme ultraviolet (EUV) lithography** at 13.5 nm [14].

EUV light is produced in ASML systems by focusing a high-power CO_2 laser onto a tin droplet, creating a hot plasma that emits at 13.5 nm. The EUV radiation is collected and transported through a series of multilayer Mo/Si mirrors inside a high-vacuum environment.

Operating EUV scanners presents unique challenges:

- **Mirror contamination and cleaning:** Hydrocarbon deposition reduces reflectivity. Hydrogen plasmas help mitigate this by etching carbon but can also cause mirror blistering [25].
- **Charging effects:** EUV-induced plasmas and secondary electron emission can lead to charging of optical components and resists [15].
- **Resist outgassing:** EUV photoresists release volatile species (H_2, N_2, hydrocarbons), which interact with plasmas and mirrors [26].

Hydrogen is intentionally introduced into ASML EUV systems to reduce contamination, while nitrogen is present from outgassing or controlled purges. The interaction of EUV photons with these gases leads to low-density plasmas whose properties are not yet fully understood, but which can strongly impact system performance and lifetime.

This thesis, conducted in collaboration with ASML, addresses this knowledge gap by providing a spectroscopic study of EUV-induced plasmas in H_2,

N_2, and their mixtures, and comparing them to controlled nanosecond pulsed discharges.

1.4 Scope and structure of this thesis

The objective of this work is to provide a comprehensive spectroscopic characterization of non-thermal plasmas in H_2, N_2, and mixed H_2/N_2 environments, focusing on three representative driving mechanisms: nanosecond pulsed discharges (NPD), EUV-induced plasmas in beamline and scanner-like geometries, and electron-beam radiation (EBR) plasmas. A central theme throughout the manuscript is the development and application of a calibrated optical emission spectroscopy (OES) framework that can be transported across these platforms and used to extract rotational and vibrational temperatures, follow temporal dynamics from nanoseconds to microseconds, and constrain excitation pathways under scanner-relevant conditions.

The manuscript is organized as follows:

- **Chapter 1** (this chapter) sets the physical and technological context. It introduces non-thermal plasmas in H_2/N_2 environments, discusses the role of nanosecond pulsed discharges and EUV-induced plasmas, and outlines the relevance of hydrogen and nitrogen plasmas for ASML EUV lithography.

- **Chapter 2** summarises the relevant spectroscopy of nitrogen and hydrogen and introduces the OES methodology used in this work. It reviews the main band systems (N_2 SPS/FNS and H_2 Fulcher), the Balmer series, and the procedures for extracting rotational and vibrational temperatures, excitation temperatures, and (where possible) electron densities from Stark broadening, highlighting the limitations of simplified excitation-plot approaches at low pressure.

- **Chapter 3** details the experimental setups and the data-processing workflow common to all platforms. It describes the optical arrangements, the calibration of the instrumental function, the radiometric response corrections, and the line-by-line fitting strategies used for SPS, Fulcher bands, and Balmer lines, as well as the construction of Boltzmann plots and Franck–Condon–corrected vibrational populations.

- **Chapter 4** presents the nanosecond pulsed discharge (NPD) experiments in nitrogen, hydrogen, and selected mixtures. Time-resolved SPS, Fulcher, and Balmer measurements are used to characterise non-equilibrium excitation, gas heating, and afterglow behaviour, establishing a well-controlled, electrically driven reference case for later comparison.

- **Chapter 5** explores EUV-induced plasmas. It reports measurements on the EBL2 beamline and on a scanner-derived exposure tool, analysing molecular and atomic emission in H_2, N_2, and H_2/N_2 mixtures. Particular emphasis is placed on the low-density, photon-driven nature of these plasmas, on the role of out-of-band radiation, and on the constraints that OES can place on EUV pulse timing and plasma kinetics under tool-relevant conditions.

- **Chapter 6** presents plasmas generated by electron beam radiation (EBR) at low pressure. The EBR platform provides a clean, mono-energetic electron source without high-voltage pulses or EUV photons, serving as a benchmark for electron-impact kinetics and as a testbed for validating the spectral analysis routines developed in earlier chapters.

- **Chapter 7** provides a comparative analysis of NPD, EUV-induced, and EBR plasmas. It compares spectral signatures, temporal dynamics, and inferred temperatures across platforms, draws out the implications for the ASML plasma environment (charging, contamination, mixture effects), and discusses which diagnostics appear robust and deployable in industrial EUV tools. An outlook on future work closes the chapter.

A final **Conclusions** chapter summarises the main findings of the thesis, highlights the methodological contributions of the OES framework, and outlines prospects for combining time-resolved spectroscopy with collisional–radiative and kinetic modelling to further improve plasma diagnostics in EUV lithography and related low-temperature plasma systems.

Chapter 2

Optical Emission Spectroscopy

2.1 Introduction

Optical emission spectroscopy (OES) is one of the most widely used diagnostics for non-thermal plasmas, since it is non-intrusive, applicable over a broad range of pressures and plasma conditions, and provides valuable information on internal energy distributions. In nanosecond pulsed discharges (NPDs) and EUV-induced plasmas, OES is particularly attractive because probe methods are difficult to apply due to short plasma lifetimes and low electron densities. Time-resolved OES, therefore, represents a crucial diagnostic throughout this thesis [27,28]. Complementary absorption-based techniques, such as mid-infrared frequency-comb and dual-comb spectroscopy, have recently been demonstrated for non-thermal molecular plasmas and for tracking ammonia formation in N_2/H_2 mixtures [29, 30], but are experimentally more demanding and were not available in this work.

2.2 Principles of OES and Experimental Arrangement

OES records spontaneous radiation from electronically (and rovibrationally) excited species in the plasma. For a transition $u \to l$ the detected line intensity is, under optically thin conditions, proportional to the population in the upper state and to the Einstein spontaneous emission coefficient, with instrumental throughput and spectral response folded in:

$$I_{ul} \propto N_u \, A_{ul} \, h\nu. \tag{2.1}$$

In the Corona limit, electron-impact excitation from the ground state is followed by radiative decay, so intensities reflect ground-state densities and excitation rates. In many low-temperature plasmas, however, cascading, stepwise excitation, dissociation/recombination, and electron de-excitation contribute; quantitative interpretation then benefits from a collisional–radiative (CR) framework and absolute calibration [3, 7, 31]. In a collisional–radiative

model, the populations of the relevant atomic and molecular states are obtained from rate equations that balance electron-impact excitation and de-excitation, ionization and recombination, radiative decay, and, when necessary, transport losses, providing a self-consistent link between measured emission intensities and plasma parameters.

Spectrometer, grating, and resolution. A typical arrangement uses a Czerny–Turner spectrograph with a ruled diffraction grating. For grating period d and incidence/reflection angles α, β to the grating normal, constructive interference occurs when

$$d(\sin\alpha \pm \sin\beta) = m\lambda, \tag{2.2}$$

with diffraction order m. The resolving power is $R = \lambda/\Delta\lambda = mN$, where N is the number of illuminated grooves. The blaze angle determines the wavelength region of highest efficiency; practical operation balances efficiency, resolution, and free spectral range to capture the targeted band systems with adequate SNR. The entrance slit width and the spectrograph numerical aperture set the trade-off between spectral resolution and photon throughput. Instrumental line shape (ILS) is measured (e.g., with narrow atomic lines) and used to convolve forward models when fitting rotational structure or line broadening.

Collection optics and detector. Light is collected through an optical system (which may include lenses, mirrors, and/or optical fibers), imaged onto the spectrograph entrance slit, and dispersed onto a detector (ICCD or sCMOS). For time-resolved studies of NPDs, ns gating isolates specific discharge phases. Wavelength calibration (e.g., with a pen lamp) and, when quantitative intensities are required, radiometric calibration (with a calibrated broadband source) are performed in the identical optical configuration as used on plasma measurements [31].

Mixtures and overlap. In N_2–H_2 mixtures, the N_2 Second Positive System (SPS) and the H_2 Fulcher-α system overlap in places; sufficient resolving power and accurate wavelength calibration are therefore required. Forward modelling (PGOPHER/SpecAir) including the measured ILS is used to separate contributions and to extract temperatures.

2.3 Spectral Line Intensity and Population Distributions

The link between measured I_{ul} and N_u is straightforward, but the upper-state populations in non-LTE plasmas are often not Boltzmann-distributed. Useful limiting pictures are: (i) *Corona balance*, where excitation from

the ground and radiative decay dominate; (ii) *Saha–Boltzmann* for a subset of high-lying levels that may thermalize with the continuum; and (iii) full *collisional–radiative* kinetics when cascading, stepwise excitation, recombination, and electron de-excitation are appreciable [3, 7, 31]. In this collisional–radiative regime, both collisional processes (primarily electron-impact) and radiative transitions are treated explicitly in the population balance. Unless otherwise stated, we assume optically thin emission and correct spectra for the instrument response when quantitative analysis is attempted.

2.4 Rotational Temperature

The rotational temperature T_{rot} is obtained from the distribution of rotational populations within a given vibrational band:

$$N_J \propto g_J \exp\left(-\frac{E_J}{k_B T_{\mathrm{rot}}}\right), \tag{2.3}$$

with g_J the degeneracy and E_J the rotational energy. Fitting measured spectra with line-by-line simulations convolved with the ILS yields T_{rot}. For nitrogen plasmas, the SPS ($\mathrm{C}^3\Pi_u \rightarrow \mathrm{B}^3\Pi_g$) around 337 nm is widely used. In hydrogen plasmas, the Fulcher-α system ($\mathrm{d}^3\Pi_u \rightarrow \mathrm{a}^3\Sigma_g^+$) provides access to T_{rot}; in this work, analysis focuses on the Q-branch (no use is made of P/R branches). Because rotational relaxation is typically fast (tens of ns at 1–100 mbar), T_{rot} is commonly close to the gas temperature T_{gas}; deviations can occur if strong gradients or non-equilibrium excitation pathways are present [27, 31].

2.5 Vibrational Temperature

Vibrational temperatures in OES are inferred from relative band intensities within the same electronic system, after correcting for transition probabilities, photon energies, and the spectral response of the detection chain. For a transition between vibrational levels ν' and ν'' in an electronic system $E' \rightarrow E''$, the band intensity under optically thin conditions can be written as

$$I_{\nu',\nu''} \;\propto\; C(\lambda_{\nu',\nu''})\, f_{\nu'}^{(E')}\, A_{\nu',\nu''}\, h\nu_{\nu',\nu''}, \tag{2.4}$$

where $C(\lambda)$ is the wavelength-dependent response of the detection system, $f_{\nu'}^{(E')}$ is the population of the upper vibrational level ν' in the emitting electronic state E', $A_{\nu',\nu''}$ the Einstein coefficient, and $\nu_{\nu',\nu''}$ the band frequency. After response correction and division by $A_{\nu',\nu''}\,\nu_{\nu',\nu''}$, the remaining variation of $I_{\nu',\nu''}$ across ν' reflects the vibrational populations $f_{\nu'}^{(E')}$.

If the vibrational manifold of the emitting state is Boltzmann-distributed at a single temperature $T_{\mathrm{vib}}^{(E')}$,

$$\frac{f_{\nu'}^{(E')}}{f_0^{(E')}} = \frac{1}{k}\,\exp\!\left(-\frac{E_{\nu'}-E_0}{k_B T_{\mathrm{vib}}^{(E')}}\right), \tag{2.5}$$

with k a proportionality constant, then a plot of $\ln(f_{\nu'}^{(E')}/f_0^{(E')})$ versus $E_{\nu'}$ yields a straight line whose slope is $-1/(k_B T_{\mathrm{vib}}^{(E')})$. In that ideal case, a *single* vibrational temperature characterizes the entire manifold of the emitting state E'.

In practice, especially in non-equilibrium molecular plasmas, the vibrational-state distributions are often non-Boltzmann: higher-ν' levels are overpopulated relative to a single-temperature fit. This is the case both for ground-state N_2 in many CARS measurements and for the emitting $N_2(C^3\Pi_u)$ state in the SPS [7]. A global linear fit over several ν' then depends sensitively on which points are included and may obscure physically relevant structure.

To obtain a robust measure of the *low-lying* part of the vibrational distribution, it is common to define a "first-level" vibrational temperature T_{01} from the populations of the first two vibrational levels only. This approach is well established for the ground state of N_2 in coherent anti-Stokes Raman scattering (CARS) measurements [32], and we adopt the same idea here for the emitting C state. For the SPS, we define the first-level C-state vibrational temperature

$$T_{01}^{(\mathrm{C})} = \frac{E_1^{(\mathrm{C})}-E_0^{(\mathrm{C})}}{k_B\,\ln\!\left(f_0^{(\mathrm{C})}/f_1^{(\mathrm{C})}\right)}, \tag{2.6}$$

where $f_{\nu'}^{(\mathrm{C})}$ are the relative vibrational populations in $N_2(C^3\Pi_u)$ obtained from the SPS band intensities. In the Boltzmann limit, $T_{01}^{(\mathrm{C})} = T_{\mathrm{vib}}^{(\mathrm{C})}$; when higher-$\nu'$ levels are overpopulated, $T_{01}^{(\mathrm{C})}$ still provides a well-defined and relatively robust measure of the population ratio between the first two levels, without being biased by the non-linear tail.

Throughout this thesis:

- Vibrational temperatures are always understood as *state-specific*. For example, $T_{\mathrm{vib}}^{(\mathrm{C})}$ and $T_{01}^{(\mathrm{C})}$ refer explicitly to the emitting $N_2(C^3\Pi_u)$ state, not to the N_2 ground state.

- For N_2 SPS analysis, we primarily use $T_{01}^{(\mathrm{C})}$ as a compact descriptor of the low-lying C-state vibrational distribution; the full non-Boltzmann behaviour at higher ν' is discussed where relevant.

- For H_2, the Fulcher-α Q-branch analysis is used to derive *ground-state* vibrational populations $f_X(v)$ for $v = 0\ldots3$ via Franck–Condon-corrected back-projection. Given the limited number of resolved levels and the presence of non-Boltzmann features, we report these populations directly rather than compressing them into a single $T_{\mathrm{vib}}^{(X)}$.

In mixtures (e.g. H_2/N_2), strong V–V and V–T coupling can lead to significant differences between rotational and vibrational temperatures and between the vibrational temperatures of different electronic or molecular states. Measured T_{vib} or T_{01} values must therefore be interpreted in the context of mixture composition, discharge phase, and collisional–radiative kinetics rather than as universal "vibrational temperatures" of the gas.

2.6 Excitation Temperature and Electron Temperature

Excitation temperature from atomic lines. A Boltzmann plot of

$$\ln\left(\frac{I_{ul}\lambda}{g_u A_{ul}}\right) = -\frac{E_u}{k_B T_{\mathrm{exc}}} + \mathrm{const} \tag{2.7}$$

provides an effective excitation temperature T_{exc} for a set of lines whose upper levels share similar formation pathways and whose populations follow (or approximately follow) a Boltzmann distribution with a common temperature. In hydrogen plasmas, this is often attempted with Balmer lines; *however, in our measurements the Balmer manifold is non-Boltzmann.* Consequently, a single T_{exc} is not representative; we therefore treat Balmer-based T_{exc} as qualitative and rely on molecular systems (Fulcher Q-branch; N_2 SPS), combined with qualitative collisional–radiative considerations (e.g. on excitation, quenching, and cascading pathways), for kinetic insight. This will be discussed in detail in the following chapters.

On estimating T_e. OES does not directly yield the electron temperature T_e without additional modelling or assumptions. Under specific conditions, upper manifolds may approach partial Saha–Boltzmann equilibrium, allowing an *effective* temperature fit that sometimes correlates with T_e. Alternatively, fitting nitrogen band spectra with forward models that parameterize electron-impact rate coefficients by an assumed T_e can provide a proxy "electron temperature" for the emitting system, with standard caveats regarding non-LTE [31]. Throughout this thesis, we emphasize trends and consistency checks (e.g., discharge phase, pressure, mixture) rather than single-point absolute T_e values from OES alone.

2.7 Electron density from Stark broadening

Electron density n_e can, in principle, be obtained from Stark broadening of hydrogen Balmer lines (Hα, Hβ) or suitable nitrogen lines. The Lorentzian Stark width scales approximately linearly with n_e:

$$\Delta\lambda_{1/2} \approx 2w\left(\frac{n_e}{10^{16}\,\mathrm{cm}^{-3}}\right), \tag{2.8}$$

where w is the tabulated Stark parameter for the line. In practice, accurate extraction requires (i) sufficient spectral resolution so that the Stark (Lorentzian) contribution is not swamped by instrumental/Doppler (Gaussian) broadening, (ii) a well-characterised instrumental line shape (ILS) for deconvolution, (iii) optically thin conditions, and (iv) careful baseline treatment [31].

For nanosecond discharges, these conditions can be met and time-resolved $n_e(t)$ retrieval from Stark broadening has been demonstrated in the literature under operating conditions comparable to those of this work [11, 27], as well as in related measurements by collaborators. In other words, Stark-based electron-density diagnostics are a realistic option for NPD-type plasmas when the spectrometer resolution and signal level are optimised for this purpose.

By contrast, under the EUV-induced plasma conditions studied in this thesis the expected Stark widths are well below the effective instrumental resolution, and the line shapes are dominated by Doppler and instrumental broadening. In this regime, the Stark component cannot be disentangled with sufficient confidence, and reliable n_e retrieval from line broadening is not feasible. Consequently, no quantitative Stark-based electron densities are reported in this thesis; for the EUV case in particular, n_e must instead be inferred indirectly from kinetic and collisional–radiative modelling constrained by the time-resolved OES observables.

2.8 Line Identification in H_2, N_2, and Mixtures

We identify and fit H Balmer lines (Hα–Hϵ), H_2 Fulcher-α *Q-branch* bands, and the N_2 Second Positive System. The molecular systems are especially valuable in H_2/N_2 mixtures for extracting T_{rot} and T_{vib} even when the Balmer series is non-Boltzmann. Assignments are verified by overlays with line-by-line simulations and by tracking pressure and mixing-ratio trends.

2.9 Advantages and Limitations

OES is passive, non-intrusive, and compatible with sub-μs time resolution when combined with gated detectors. It yields T_{rot} (often a proxy for T_{gas}), T_{vib}, qualitative T_{exc} information, and—when resolution allows—n_e from Stark broadening. Limitations include: (i) the need for absolute calibration and CR modelling for quantitative densities; (ii) spectral overlap in mixtures, requiring adequate resolution and forward modelling; (iii) the floor set by the instrument function, which can mask Stark widths or blend rotational features; and (iv) the possibility of non-Boltzmann excited-state populations (e.g., Balmer series), which limits the interpretability of simple Boltzmann plots [31]. In that sense, OES provides stringent but indirect constraints on kinetic models rather than standalone "black-box" plasma parameters, and is best used in combination with collisional–radiative (CR)

and state-to-state kinetic modelling frameworks [3, 7].

2.10 Summary

In this chapter, the methodology of OES is introduced, focusing on rotational and vibrational temperature determination, excitation analysis, and electron density measurements. These diagnostics will be applied systematically to nanosecond pulsed discharges and EUV-induced plasmas in nitrogen, hydrogen, and their mixtures in later chapters. Importantly for this work, (i) Balmer populations are non-Boltzmann; (ii) Stark-based n_e is available for the NPD case but not for the EUV-induced plasma; and (iii) absolute calibration for quantitative densities was not possible during the EUV campaign, so interpretation relies on relative trends and molecular-band analysis.

Chapter 3

Methodology: Data Acquisition, Processing, and Modelling

3.1 Introduction

This chapter describes the experimental and data-analysis workflow used throughout the thesis to extract physical quantities from the recorded optical emission spectra. While Chapters 4–6 focus on specific plasma sources (nanosecond pulsed discharges, EUV-induced plasmas, and electron-beam plasmas), the underlying procedures for spectral calibration, line and band fitting, and population analysis are common. The aim here is to collect these methodological aspects in a single place, so that later chapters can refer back to them without repeating technical details.

We first describe the calibration of the instrumental function and of the wavelength-dependent spectral response of the detection chain, since these underpin all subsequent line-shape, intensity, and temperature analyses. We then present the analysis of the N_2 Second Positive System (SPS), including rotational and vibrational temperature extraction from band-resolved fits and the construction of vibrational population distributions. The second part of the chapter is devoted to molecular hydrogen: we introduce the Fulcher-α ro-vibrational analysis used to obtain rotational (and proxy gas) temperatures and ground-state vibrational populations. Finally, we outline the procedure used for deriving effective excitation temperatures from the hydrogen Balmer series, including spectral pre-processing, uncertainty propagation, and the limitations of Boltzmann-plot interpretations under non-equilibrium conditions.

3.2 Calibration procedure for the instrumental function

The setup instrumental function, modelled here as a Gaussian, is used to convolve the theoretical spectra generated with PGOPHER. Its width

is obtained by a two-step calibration. First, the linewidth of a diode laser (assumed Lorentzian) is measured using a fixed-gap Fabry–Pérot etalon. The etalon produces an interference pattern (figure 3.1); by selecting a region of interest spanning two adjacent fringes, integrating the intensity, and fitting two Gaussians to the peaks (figure 3.2), the peak separation (in pixels) and individual widths are determined.

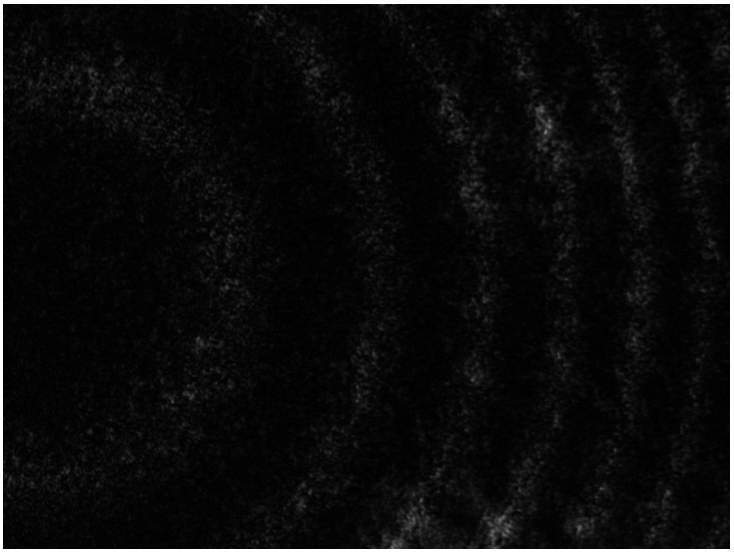

Figure 3.1: Interference pattern of the diode laser transmitted through the etalon.

The Gaussian model used for fitting is

$$f_{\text{Gauss}}(x) \propto \exp\left[-\frac{(x-x_0)^2}{\sigma^2}\right], \tag{3.1}$$

with full width at half maximum

$$\text{FWHM} = 2\sqrt{2\ln 2}\,\sigma. \tag{3.2}$$

The pixel-based FWHM is converted to frequency units using the known free spectral range (FSR = 10 GHz) and the measured fringe spacing. Knowing the laser central wavelength, the linewidth is then converted to nanometres and used as the fixed Lorentzian width in the next step.
Second, the measured laser spectrum is fitted with a Voigt profile (Lorentzian laser emission convolved with the Gaussian instrumental function):

$$f_{\text{Lorentz}}(x) \propto \frac{\gamma}{(x-x_0)^2+\gamma^2}, \tag{3.3}$$

where γ is half the laser linewidth. An example is shown in figure 3.3.

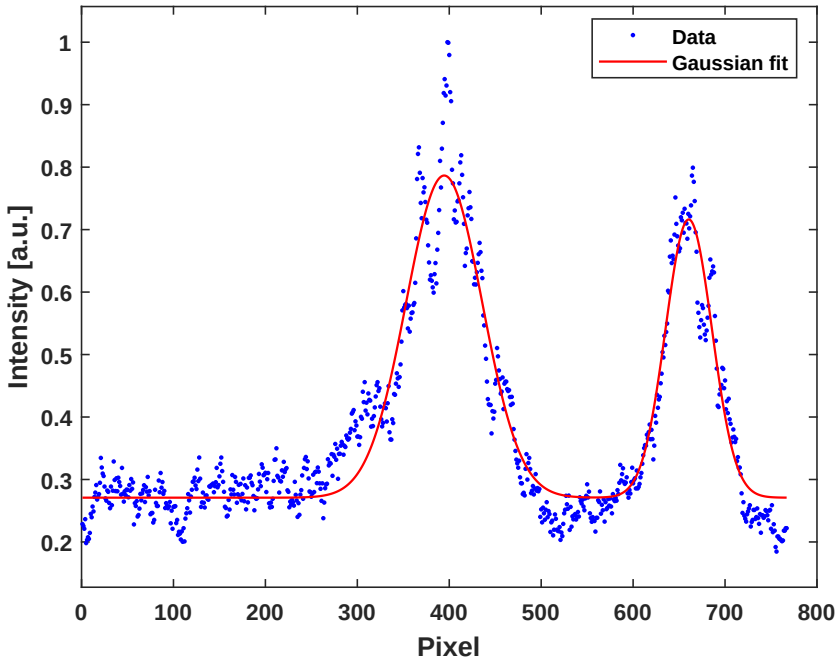

Figure 3.2: Integrated intensity across two neighbouring fringes (points) and Gaussian fits (lines).

Relative spectral-response (irradiance) calibration. In addition to the instrumental width, quantitative use of line and band intensities requires the wavelength-dependent spectral response of the detection chain (optics, spectrometer, grating, and camera). This response, denoted $C(\lambda)$ in Eq. (3.6), is obtained from measurements of a calibrated broadband lamp with known spectral irradiance $E_{\mathrm{ref}}(\lambda)$ (traceable manufacturer calibration). For each grating/center-wavelength setting used in the experiments, a lamp spectrum $S_{\mathrm{lamp}}(\lambda)$ is recorded with the same optical configuration as for the plasma (identical lenses, fibre, slit, and exposure settings), and a dark spectrum $S_{\mathrm{dark}}(\lambda)$ is subtracted:

$$S_{\mathrm{corr}}(\lambda) = S_{\mathrm{lamp}}(\lambda) - S_{\mathrm{dark}}(\lambda). \tag{3.4}$$

The relative spectral response is then defined as

$$C(\lambda) \propto \frac{E_{\mathrm{ref}}(\lambda)}{S_{\mathrm{corr}}(\lambda)}, \tag{3.5}$$

normalised to unity at a reference wavelength within the window (so that only *relative* irradiance is used in the analysis). In practice, $C(\lambda)$ is stored as calibration files and applied to all plasma spectra recorded with the corresponding spectrometer setting by multiplying the background-subtracted signal by $C(\lambda)$. Within a given spectral window, the uncertainty of $C(\lambda)$ is dominated by the lamp calibration (few percent) and its slow wavelength variation; for the line-by-line fits presented here, the statistical fit uncertainty typically exceeds the relative response error across the $\sim$10–20 nm windows of interest.

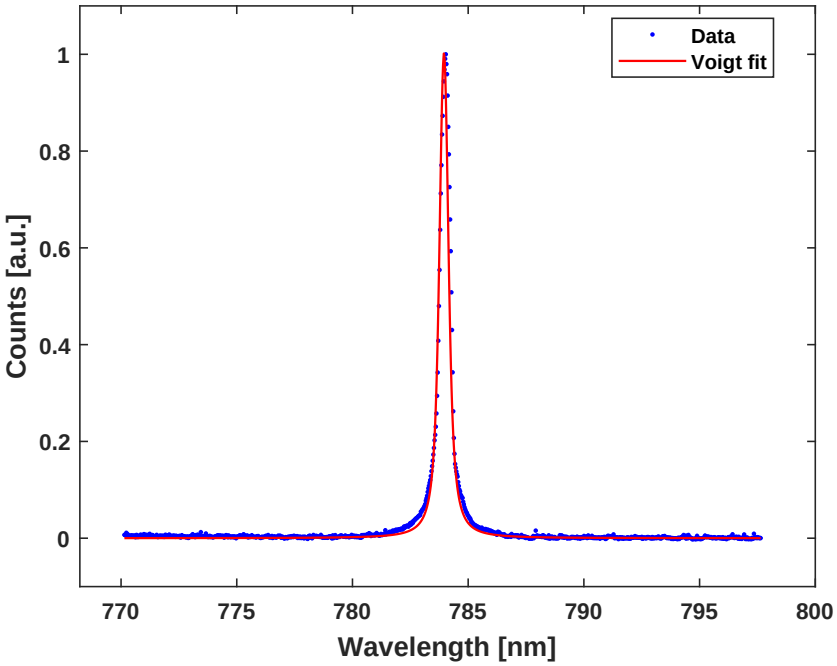

Figure 3.3: Diode-laser spectrum (points) and Voigt fit (line) used to extract the instrumental Gaussian width.

3.3 N_2 Second Positive System data analysis

The analysis presented here targets the Second Positive System (SPS) of N_2 for vibrational branches with $\Delta\nu = \nu' - \nu'' = -2$, focusing on the first three bands (0–2, 1–3, 2–4).

Population mechanisms and diagnostic content. In low-pressure nanosecond discharges in pure nitrogen, the C $^3\Pi_u$ state is populated primarily by electron-impact excitation out of the ground state X $^1\Sigma_g^+$ (both from $v = 0$ and from vibrationally excited X levels), with additional contributions from stepwise channels via the metastable A $^3\Sigma_u^+$ and, at higher pressures and in the afterglow, from pooling reactions such as

$$N_2(A) + N_2(A) \rightarrow N_2(C) + N_2,$$

and related N_2(A/B)-assisted pathways [3,32–35]. Because the radiative lifetime of N_2(C) is short (tens of ns at low pressure), rotational re-distribution in C is inefficient and the rotational envelope of the SPS mirrors, to first order, the X-state rotational (gas) temperature. In contrast, the C-state vibrational distribution reflects a mixture of direct excitation from X and metastable-/pooling-driven channels, and is not in simple equilibrium with the ground-state vibrational manifold. In this thesis, we therefore interpret T_{rot} from the SPS as a proxy for T_{gas}, while the first-level C-state vibrational temperature $T_{01}^{(\mathrm{C})}$ is used as a compact measure of the relative population of the lowest C-state vibrational levels, rather than as a direct ground-state T_{vib}.

Experimental spectra are fitted with a model that accounts for an absolute wavelength shift, the theoretical band spectrum, and the instrumental function of the setup. The theoretical spectra are generated with PGOPHER [36] using the electronic, rotational, and vibrational constants from Ventura and Fellows [37].

Similar band-by-band SPS fitting strategies have been adopted in recent work on low-pressure nitrogen plasmas and synthetic spectra modelling [38–40]. Figure 3.4 shows an example of the simulated emission for the $\nu' = 0 \rightarrow \nu'' = 2$ band.

The simulated spectrum is convolved with the instrumental transfer function (see Section 3.2) and the result is used as the model for band fitting. The main band ($\nu' = 0 \rightarrow \nu'' = 2$) is fitted first, and the resulting rotational temperature T_{rot} is then held fixed when fitting the remaining bands. This assumes that the rotational distribution—and hence the gas temperature—is the same for all v' of the C state; for lines within a given vibrational level this is automatic, while extending the same T_{rot} across different v' reflects the usual low-pressure SPS assumption of a single T_{gas}.

Applying the same procedure to the other two bands ($\nu' = 1 \rightarrow \nu'' = 3$ and $\nu' = 2 \rightarrow \nu'' = 4$), the full spectrum is reproduced and the relevant parameters are extracted. An example fit is shown in Figure 3.5.

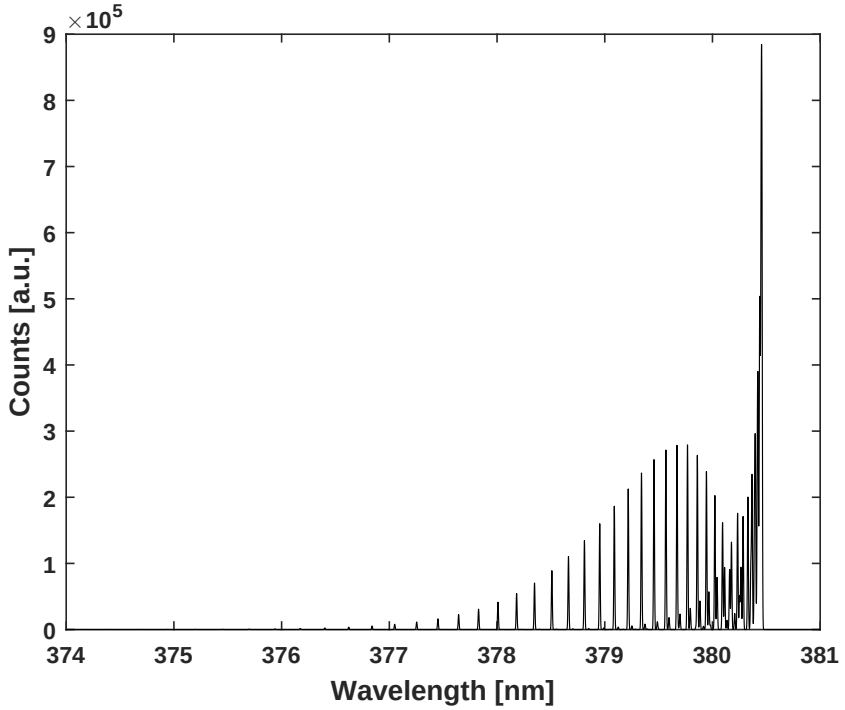

Figure 3.4: Simulated SPS spectrum of nitrogen ($\Delta\nu = -2$, 0–2 band) generated with PGOPHER at 320 K.

From the fitted bands, relative intensities are obtained and used to determine the vibrational-state populations in the emitting $N_2(C^3\Pi_u)$ state. The band intensity for a transition between vibrational levels ν' and ν'' is

$$I_{\nu',\nu''} = \frac{C(\lambda_{\nu',\nu''})\, f_{\nu'}\, A_{\nu',\nu''}}{\lambda_{\nu',\nu''}}, \tag{3.6}$$

where $I_{\nu',\nu''}$ is the measured intensity, $C(\lambda_{\nu',\nu''})$ the spectral response of the detection chain, $\lambda_{\nu',\nu''}$ the band wavelength, $f_{\nu'}$ the population of the emitting upper vibrational level in the C state, and $A_{\nu',\nu''}$ an effective (band-averaged) Einstein coefficient for the $\nu' \to \nu''$ band (i.e. the line-strength–weighted average over all rovibronic transitions contributing to that band).

Assuming a normalised Boltzmann distribution for the C-state vibrational manifold,

$$\begin{aligned} \frac{f_{\nu'}}{f_0} &= \frac{1}{f_0 k}\, \exp\left(-\frac{E_{\nu'}}{k_B T_{\mathrm{vib}}^{(\mathrm{C})}}\right), \\ \ln\left(\frac{f_{\nu'}}{f_0}\right) &= -\frac{E_{\nu'}}{k_B T_{\mathrm{vib}}^{(\mathrm{C})}} - \mathrm{const}, \end{aligned} \tag{3.7}$$

where f_0 is the $\nu' = 0$ population, k a proportionality constant, $E_{\nu'}$ the vibrational energy of the upper level, k_B the Boltzmann constant, and $T_{\mathrm{vib}}^{(\mathrm{C})}$ the apparent vibrational temperature of the emitting $N_2(C^3\Pi_u)$ state. The

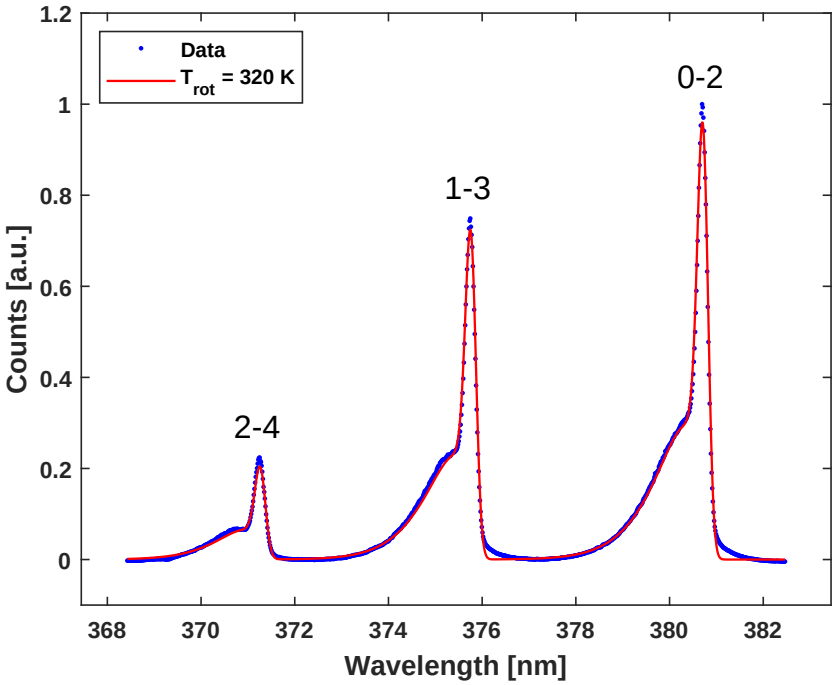

Figure 3.5: Experimental SPS spectrum of nitrogen ($\Delta\nu = -2$; blue points) and model fit (red line).

vibrational energies are described (to second order) as

$$E_{\nu'} = \omega_e\left(\nu' + \frac{1}{2}\right) - \omega_e x_e\left(\nu' + \frac{1}{2}\right)^2 + \cdots , \tag{3.8}$$

with ω_e and $\omega_e x_e$ taken from the NIST database [41].

Equation (3.7) implies a linear dependence of $\ln(f_{\nu'}/f_0)$ on $E_{\nu'}$. In principle, a linear regression over several ν' would yield a single $T_{\mathrm{vib}}^{(\mathrm{C})}$. In practice, however, the higher-ν' levels of $N_2(C)$ are often overpopulated and the full distribution deviates from a straight line. To characterise the low-lying part of the C-state vibrational distribution in a way that is robust to such non-Boltzmann tails, we follow the approach used for ground-state N_2 in CARS measurements (e.g. Burnette *et al.* [32]) and define a two-level, or "first-level", vibrational temperature:

$$T_{01}^{(\mathrm{C})} = \frac{E_1 - E_0}{k_B \ln\!\left(f_0/f_1\right)}. \tag{3.9}$$

In the limit of a Boltzmann distribution, $T_{01}^{(\mathrm{C})}$ coincides with $T_{\mathrm{vib}}^{(\mathrm{C})}$; when the high-$\nu'$ tail is non-Boltzmann, it still provides a well-defined measure of the relative population of the first two C-state vibrational levels.

Figure 3.6 shows a representative plot of $\ln(f_{\nu'}/f_0)$ versus $E_{\nu'}$. The straight line connecting the first two points corresponds to $T_{01}^{(\mathrm{C})} \approx 4490$ K in this example.

An example of $T_{01}^{(\mathrm{C})}$ versus time (1 ns steps) is reported in Figure 3.7, where the delay is referenced to the discharge onset.

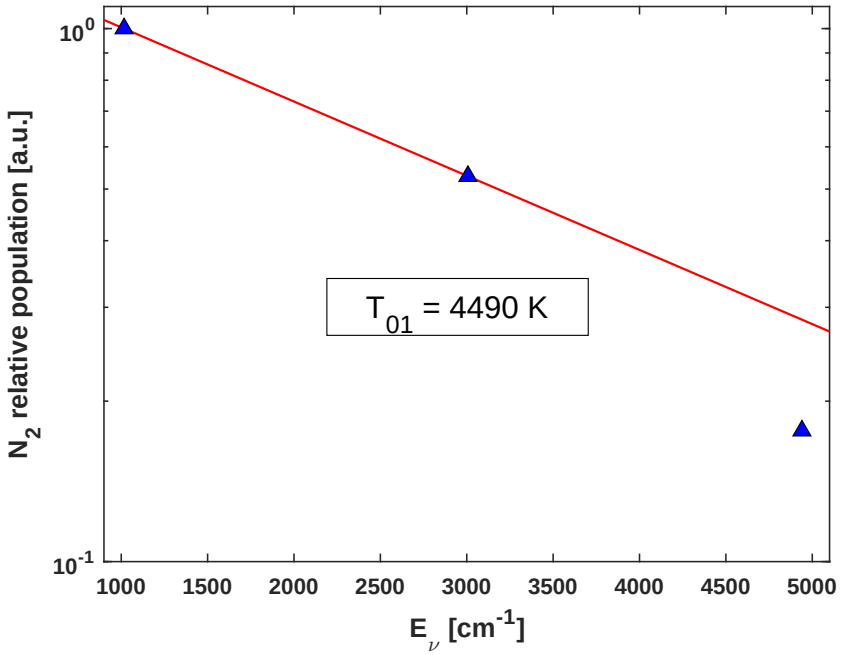

Figure 3.6: Normalised C-state vibrational-state distribution for the SPS of nitrogen ($\Delta\nu = -2$) relative to the 0–2 band (blue points). The straight line through the first two points defines the first-level C-state vibrational temperature $T_{01}^{(\mathrm{C})}$.

Uncertainty estimation for SPS fits. For each spectrum, the SPS model (PGOPHER band synthesis convolved with the instrumental function and multiplied by $C(\lambda)$) is fitted to the data by non-linear least squares. The fit parameters include an absolute intensity scale, a wavelength shift, the rotational temperature T_{rot} (assumed common to all $\Delta\nu = -2$ bands in a given fit window), and the relative amplitudes of the individual bands $I_{\nu',\nu''}$. The fitting routine returns a covariance matrix for these parameters; the statistical uncertainty on each band intensity $I_{\nu',\nu''}$ is obtained from the corresponding diagonal element (and, where relevant, including the covariance with the global intensity scale). The upper-state vibrational populations $f_{\nu'}$ are then computed from Eq. (3.6),

$$f_{\nu'} \;\propto\; \frac{I_{\nu',\nu''}\,\lambda_{\nu',\nu''}}{C(\lambda_{\nu',\nu''})\,A_{\nu',\nu''}}, \tag{3.10}$$

so that, to first order, the relative uncertainty on $f_{\nu'}$ is

$$\frac{\delta f_{\nu'}}{f_{\nu'}} \approx \sqrt{\left(\frac{\delta I_{\nu',\nu''}}{I_{\nu',\nu''}}\right)^2 + \left(\frac{\delta C(\lambda_{\nu',\nu''})}{C(\lambda_{\nu',\nu''})}\right)^2}, \tag{3.11}$$

where $\delta C/C$ is the (few-percent) uncertainty of the spectral-response calibration within the ∼10–20 nm window. Uncertainties in $A_{\nu',\nu''}$ are much smaller than the fitting error and are treated as systematic.

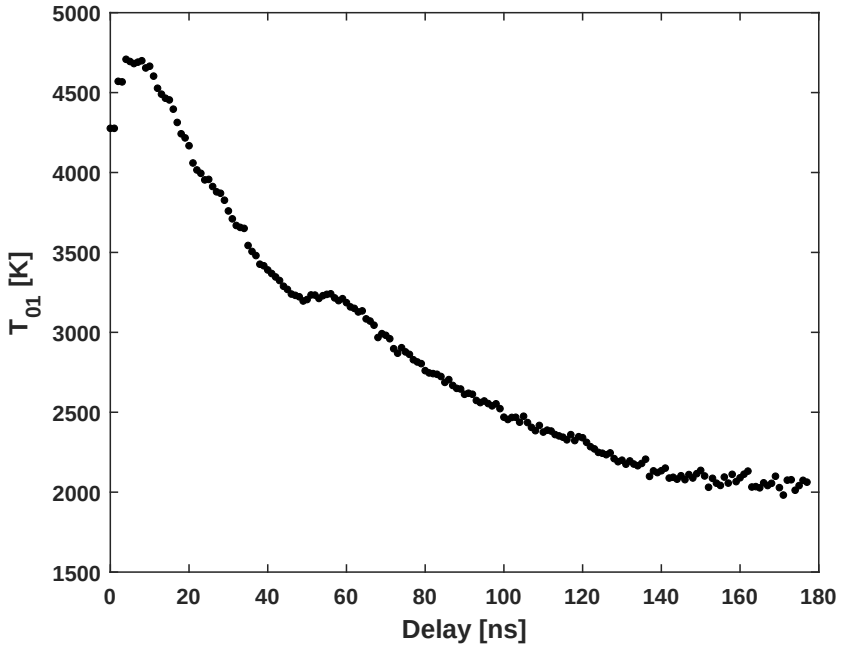

Figure 3.7: Time evolution of the first-level C-state vibrational temperature $T_{01}^{(\mathrm{C})}$ over a kinetic series. The delay is referenced to the discharge start. The trend shows an initial increase in $T_{01}^{(\mathrm{C})}$ followed by a decay as the discharge evolves.

For the first-level C-state vibrational temperature $T_{01}^{(\mathrm{C})}$, only the ratio of the first two populations enters:

$$T_{01}^{(\mathrm{C})} = \frac{E_1 - E_0}{k_B \, \ln\!\big(f_0/f_1\big)}. \tag{3.12}$$

Writing $R = f_1/f_0$, the relative uncertainty on R follows from the errors on f_0 and f_1 (assumed uncorrelated),

$$\frac{\delta R}{R} = \sqrt{\left(\frac{\delta f_1}{f_1}\right)^2 + \left(\frac{\delta f_0}{f_0}\right)^2}, \tag{3.13}$$

and standard error propagation gives

$$\delta T_{01}^{(\mathrm{C})} = \frac{E_1 - E_0}{k_B} \, \frac{\delta R}{R \left[\ln(f_0/f_1)\right]^2}. \tag{3.14}$$

In practice, the quoted error bars on $T_{01}^{(\mathrm{C})}$ are dominated by the statistical uncertainty on the fitted band intensities (through $\delta I_{\nu',\nu''}$). Systematic contributions from the response calibration $C(\lambda)$ and from the band-averaged $A_{\nu',\nu''}$ are smaller over the limited wavelength range considered and are discussed qualitatively when comparing absolute values across data sets.

3.4 Fulcher-α band emission (H_2): ro-vibrational analysis

The Fulcher-α system corresponds to the triplet transition $d\,^3\Pi_u \rightarrow a\,^3\Sigma_g^+$ and is one of the most intense H_2 molecular features in low-pressure plasmas (590–650 nm for the most prominent part). In low-temperature, low-density conditions the $d\,^3\Pi_u$ state is populated predominantly by electron-impact excitation out of $X\,^1\Sigma_g^+$ with the selection rule $\Delta N = 0$, and its short radiative lifetime ($\sim$ 40 ns) prevents rotational re-distribution in the excited state; contributions from cascades are typically minor for these conditions. Therefore, the Q-branch emission of the $d\,^3\Pi_u^-$ component provides (to first order) a direct image of the *ground-state* rotational distribution projected into the excited state [42,43]. Predissociation reduces the intensity for $v' \geq 4$; we thus restrict the analysis to the diagonal bands $v' = v'' = 0, 1, 2, 3$ [42,43].

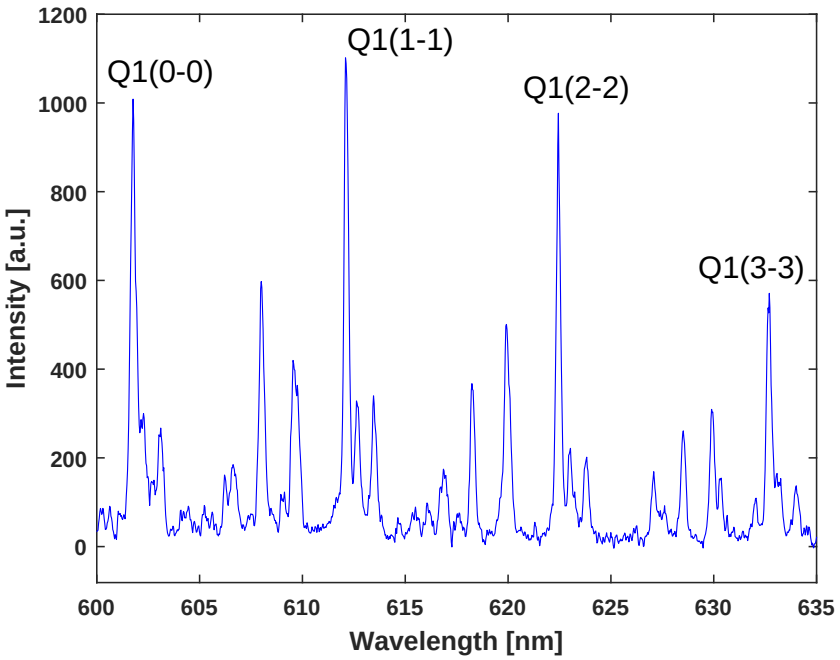

Figure 3.8: Representative Fulcher-α spectrum for nanosecond-pulsed H_2 discharges (NPD), covering 600–635 nm. A flat baseline across the window enables reliable response-corrected band sums and ro-vibrational analysis.

Spectral model and line fitting. Unlike the SPS analysis (Section 3.3) where full PGOPHER simulations are convolved with the instrumental function, here we resolve and fit individual *Q-branch* rotational lines (Q_1, Q_2, Q_3) for each $v' = 0 \ldots 3$ with Gaussian profiles. The fit model for a single line at pixel (or wavelength) coordinate x is

$$I(x) = B + A \exp\left[-\frac{(x - x_0)^2}{2\sigma^2}\right], \tag{3.15}$$

where B is a local baseline, A the amplitude, x_0 the centroid and σ the (Gaussian) width, previously constrained by the instrumental function calibration (see Section 3.2). Line areas $\mathcal{A}_{v',N'} = A\,\sigma\sqrt{2\pi}$ are then converted to absolute or relative *emissivities* $\varepsilon^{v',N'}$ after correcting for the spectral response $C(\lambda)$ of the detection chain (as in Eq. (3.6)).

We focus on the Q branch from $d\,^3\Pi_u^-$ only, to avoid known perturbations that affect P/R branches via $d\,^3\Pi_u^+$ [42, 43]. Self-absorption in the considered lines is negligible under our conditions (optically thin regime) [44].

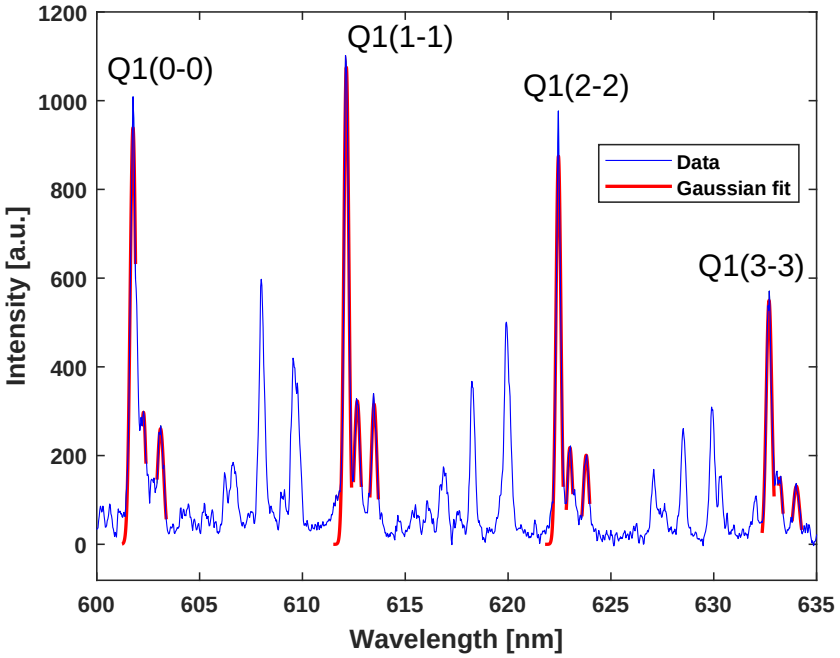

Figure 3.9: Example Gaussian fits to the $Q_1(N' = 1, 2, 3)$ lines for $v' = 0 \ldots 3$ (NPD). Line widths are bound by the instrumental function; residuals remain small, indicating consistent wavelength calibration and spectral-response correction.

Rotational temperature per vibrational level. For the Q branch of a $^3\Pi \rightarrow {}^3\Sigma$ transition, the emissivity of a rovibrational line originating from (v', N') scales as

$$\varepsilon^{v',N'} \;\propto\; S^{N'}\,(2N'+1)\,n^{v',N'}, \tag{3.16}$$

with $S^{N'}$ the Hönl–London factor and $n^{v',N'}$ the upper-level population. For a Boltzmann distribution within a given v',

$$\frac{n^{v',N'}}{n^{v',N'=1}} \;=\; \frac{g}{1}\,\frac{2N'+1}{3}\,\exp\!\left[-\frac{\Delta E_{\mathrm{rot}}(N')}{k_B T_{\mathrm{rot}}(d,v')}\right], \tag{3.17}$$

where g accounts for the nuclear-spin statistical weight (ortho/para alternation) and $\Delta E_{\mathrm{rot}}(N')$ is the rotational energy relative to $N' = 1$ (Hund's case (b)) [42, 43]. Eliminating $n^{v',N'}$ yields the canonical Boltzmann-plot

relation

$$\ln\left[\frac{\varepsilon^{v',N'}}{g\,S^{N'}}\right] \;=\; -\frac{\Delta E_{\mathrm{rot}}(N')}{k_B\,T_{\mathrm{rot}}(d,v')} \;+\; \text{const.} \tag{3.18}$$

Practically, we build the plot using $N' = 1, 2, 3$ only (the best S/N lines) and obtain $T_{\mathrm{rot}}(d, v')$ from a weighted linear fit to the three points. We avoid a two-temperature ("hockey-stick") fit on purpose: with only the first three N' the high-N' non-thermal tail cannot be constrained reliably [42, 43].

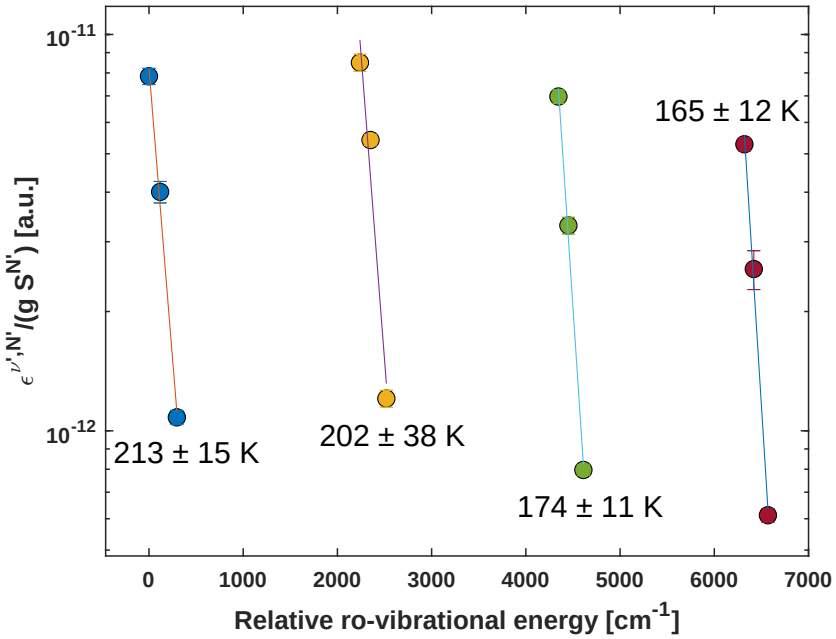

Figure 3.10: Rotational Boltzmann plots for $d\,^3\Pi_u^-$ (NPD), formed from the response-corrected $Q_1(N' = 1, 2, 3)$ emissivities for $v' = 0 \ldots 3$. The fitted slopes yield $T_{\mathrm{rot}}(d, v')$; values are typically below room temperature and show a mild decrease with increasing v', consistent with low-pressure conditions and a short d-state lifetime.

Projection to the gas temperature. To infer the ground-state rotational/gas temperature, the standard back-projection via rotational constants is applied:

$$T_{\mathrm{gas}} = T_{\mathrm{rot}}\big(X\,^1\Sigma_g^+,\, \nu = 0\big) = \frac{B_\nu\big(X\,^1\Sigma_g^+,\, \nu = 0\big)}{B_\nu(d\,^3\Pi_u^-,\, \nu')}\, T_{\mathrm{rot}}\big(d\,^3\Pi_u^-,\, \nu'\big)\,, \tag{3.19}$$

using literature values of B_ν for X and d [42,43]. To make this more explicit, we use the standard first-order expression for the vibrational dependence of the rotational constant,

$$B_v = B_e - \alpha_e\left(v + \tfrac{1}{2}\right), \tag{3.20}$$

with B_e and α_e taken from the NIST Webbook for H_2 [45]. For the ground state $X\,^1\Sigma_g^+$ one has $B_e(X) = 60.853$ cm^{-1} and $\alpha_e(X) = 3.062$ cm^{-1}, giving

$$B_0\big(X\,^1\Sigma_g^+\big) = B_e(X) - \alpha_e(X)\left(\tfrac{1}{2}\right) = 60.853 - 3.062 \times 0.5 \approx 59.32 \text{ cm}^{-1}. \tag{3.21}$$

For the excited state $d\,^3\Pi_u$ one has $B_e(d) = 30.364$ cm^{-1} and $\alpha_e(d) = 1.545$ cm^{-1}, so that

$$B_0\big(d\,^3\Pi_u\big) = B_e(d) - \alpha_e(d)\left(\tfrac{1}{2}\right) = 30.364 - 1.545 \times 0.5 \approx 29.59 \text{ cm}^{-1}. \quad (3.22)$$

and thus

$$\frac{B_0(X,0)}{B_0(d,0)} \approx \frac{59.32}{29.59} \approx 2.00. \quad (3.23)$$

Evaluating $B_v(d)$ for $v' = 1$–3 yields ratios $B_0(X,0)/B_{v'}(d)$ in the range ~ 2.1–2.4. Inserting these values into Eq. (3.19) implies

$$T_{\text{gas}} \;\approx\; (2.0\text{–}2.3)\, T_{\text{rot}}(d, v') \quad (3.24)$$

under our conditions; sub-room-temperature values of $T_{\text{rot}}(d)$ are therefore physically consistent with room-temperature (or higher) gas temperatures [44]. We report T_{rot} separately for each v' and quote T_{gas} from Eq. (3.19); for H_2 the back-projection from $v' = 2$ often agrees best with independent T_{gas} diagnostics [43].

Vibrational populations from band-summed, FC-corrected intensities. From the fitted lines we form the band-integrated (within a given v') quantity

$$I_{v'} \;\equiv\; \sum_{N'=1}^{3} \frac{\varepsilon^{v',N'}}{g\, S^{N'}} \;\times\; \underbrace{\sum_{N'=4}^{N'_{\max}} \left[\frac{\varepsilon^{v',N'}}{g\, S^{N'}}\right]_{\text{extrap}}}_{\substack{\text{optional, if S/N allows} \\ \text{extrapolation using} \\ T_{\text{rot}}(d,v')}}, \quad (3.25)$$

i.e. we sum the response-corrected line emissivities over the resolved low-N' lines; optionally, if the S/N permits, we extrapolate the tail using the *same* $T_{\text{rot}}(d, v')$ (noting the limitation discussed above). The vibrational population in the *excited* state is then

$$n_d(v') \;\propto\; \frac{I_{v'}}{A^{(\text{eff})}_{v'v''}}, \quad (3.26)$$

where $A^{(\text{eff})}_{v'v''}$ is the corresponding band-averaged Einstein coefficient for emission to $a\,^3\Sigma_g^+$ (diagonal $v'' = v'$ here), defined in the same sense as $A_{\nu',\nu''}$ for the N_2 SPS in Section 3.3. To express the inferred d-state vibrational populations in terms of a *ground-state* vibrational distribution, we apply a simplified Franck–Condon (FC) back-projection. Specifically, we assume that excitation into d originates predominantly from X, $v = 0$ and we correct for vibrational overlap in both the excitation ($X \to d$) and emission ($d \to a$) steps:

$$f_X(v) \;\propto\; \frac{n_d(v')}{q^{X\to d}_{v\to v'}\; q^{d\to a}_{v'\to v''}}\,, \qquad (v = v'' = v'), \quad (3.27)$$

where $q_{v\to v'}^{i\to j}$ are Franck–Condon (FC) factors, i.e. squared overlaps of the *vibrational nuclear wavefunctions* $\chi_v^{(i)}(R)$ and $\chi_{v'}^{(j)}(R)$ associated with electronic states i and j,

$$q_{v\to v'}^{i\to j} \;=\; \left| \int \chi_v^{(i)}(R)\, \chi_{v'}^{(j)}(R)\, \mathrm{d}R \right|^2 , \tag{3.28}$$

with R the internuclear separation. The overlap is symmetric, so $q_{v\to v'}^{X\to d} = q_{v'\to v}^{d\to X}$. In practice, we take FC factors from the tabulations of Fantz and Wünderlich [46]; an earlier FC-based formulation of the same type of back-projection for hydrogen isotopologues is given by Fantz and Heger [47]. For reference, the diagonal values used here ($v = v' = v'' = 0\ldots3$) are listed in Table 3.1.

Table 3.1: Diagonal Franck–Condon factors used in the FC-only back-projection (H_2, $v = 0\ldots3$), from Fantz and Wünderlich [46].

v	$q_{v\to v}^{X\to d}$	$q_{v\to v}^{d\to a}$
0	0.10008	0.93016
1	0.16280	0.79701
2	0.08412	0.67139
3	0.00031	0.55514

We then normalise the inferred ground-state vibrational distribution by enforcing $\sum_{v=0}^{3} f_X(v) = 1$. This "FC-only" back-projection is a standard, pragmatic approach when cross sections are not available and when only the first few N' are measured; its limitations vs. comprehensive rovibrational modelling are well documented [43]. In our case, we report the *normalised* $f_X(v)$ and emphasise $v = 0\ldots3$. The observed trend—a peak at $v = 2$ followed by a decrease—corresponds to low-n_e conditions with fixed T_e in collisional–radiative modelling, where direct excitation and radiative decay dominate the level kinetics [48].

Uncertainty estimation and error propagation. For each fitted line, the Gaussian least-squares routine returns a covariance matrix for the parameters (A, x_0, σ). The statistical uncertainty on the line area, $\mathcal{A}_{v',N'} = A\,\sigma\sqrt{2\pi}$, is obtained by standard error propagation using this covariance matrix (including the A–σ covariance term). These area uncertainties are then combined with the spectral-response uncertainty of $C(\lambda)$ to give an error on the emissivity $\varepsilon^{v',N'}$; for the plots shown, the statistical contribution from the fit dominates over the (slowly varying) response-calibration error within a given spectral window.

In the rotational Boltzmann plots, the ordinate is $y_{N'} = \ln[\varepsilon^{v',N'}/(g\,S^{N'})]$ and the corresponding standard deviation is $\delta y_{N'} = \delta\varepsilon^{v',N'}/\varepsilon^{v',N'}$, since g and $S^{N'}$ are assumed exact. These $\delta y_{N'}$ define the weights $w_{N'} = 1/\delta y_{N'}^2$ used in the weighted linear regression of Eq. (3.18). The regression yields a slope

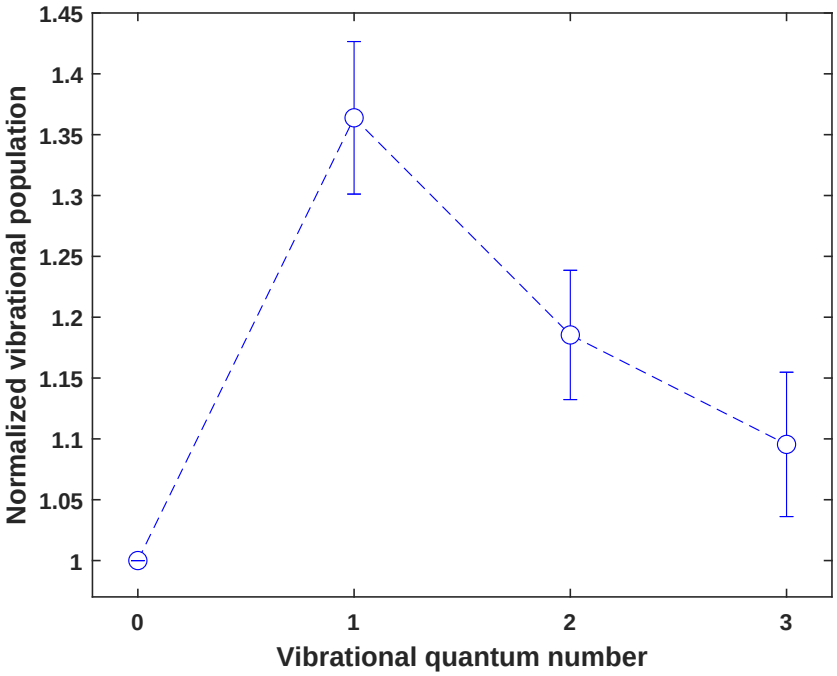

Figure 3.11: Franck–Condon–corrected ground-state vibrational populations $f_X(v)$ ($v = 0 \ldots 3$) inferred from the diagonal Fulcher-α bands (NPD). The envelope peaks near $v = 2$ and then decreases, consistent with low-density conditions where direct excitation and radiative decay dominate. A quantitative T_v is not assigned here.

m and intercept with an associated standard error δm from the covariance matrix of the fit. Because $m = -1/(k_B T_{\mathrm{rot}})$, the uncertainty on the rotational temperature for a given v' follows directly as

$$T_{\mathrm{rot}}(d, v') = -\frac{1}{k_B m}, \qquad \delta T_{\mathrm{rot}}(d, v') = \frac{1}{k_B m^2}\,\delta m. \tag{3.29}$$

The back-projected gas temperature and its error are then

$$T_{\mathrm{gas}} = \frac{B_\nu(X,0)}{B_\nu(d,v')}\,T_{\mathrm{rot}}(d,v'), \qquad \delta T_{\mathrm{gas}} \approx \frac{B_\nu(X,0)}{B_\nu(d,v')}\,\delta T_{\mathrm{rot}}(d,v'). \tag{3.30}$$

because the literature B_ν values carry much smaller relative uncertainties than the fitted quantities; their errors are therefore neglected in the propagation and the B_ν are treated as fixed input parameters.

For the vibrational analysis, the band-integrated quantity $I_{v'}$ is formed by summing the emissivities over $N' = 1 \ldots 3$ (and, where used, the extrapolated tail). Assuming uncorrelated line errors, the variance on $I_{v'}$ is the sum of the individual variances, so that $\delta I_{v'}^2 = \sum_{N'} \delta\varepsilon_{v',N'}^2$ (with an additional, smaller term when the high-N' tail is extrapolated from T_{rot}). The uncertainties on $n_d(v')$ and on the FC-corrected ground-state populations $f_X(v)$ follow by linear propagation of Eq. (3.27) and subsequent normalisation. In practice, the quoted error bars on $f_X(v)$ are dominated by the weakest band ($v = 3$) and by systematic contributions from the Franck–Condon factors

and band-averaged A values; these systematics are not folded into the formal error bars and should be kept in mind when comparing absolute $f_X(v)$ across platforms. The displayed uncertainties therefore represent mainly the statistical confidence from the line fits and band sums, while systematic effects are discussed qualitatively in the notes below.

Workflow summary used in this thesis.

1. For each diagonal band $v' = 0 \dots 3$, identify Q_1, Q_2, Q_3; fit Gaussians with fixed (or bounded) σ from the instrumental calibration; subtract a local baseline; correct areas by $C(\lambda)$ to obtain $\varepsilon^{v',N'}$.

2. Build the Boltzmann plot of Eq. (3.18) using $N' = 1, 2, 3$ and extract $T_{\mathrm{rot}}(d, v')$; project to T_{gas} with Eq. (3.19).

3. Compute FC-corrected vibrational populations with Eq. (3.27); normalise $f_X(v)$ across $v = 0 \dots 3$.

Notes on assumptions and uncertainties. (i) Restricting to $N' = 1 \dots 3$ avoids bias from a possible non-thermal high-N' tail ("two-slope" behaviour) seen in many hydrogen plasmas; using only low N' is the recommended practice when S/N or resolution precludes a reliable two-temperature fit [42, 43]. (ii) The back-projection $T_{\mathrm{rot}}(d, v') \to T_{\mathrm{gas}}$ assumes $\Delta N = 0$ excitation and negligible redistribution in d (valid at low pressure) and uses B_ν ratios; consequently $T_{\mathrm{rot}}(d)$ may be below room temperature while T_{gas} is not, consistent with the factor ~ 2 in Eq. (3.19) [44] (iii) The FC-only vibrational back-projection neglects v-resolved electron-impact cross sections and branching via predissociation; a comprehensive treatment is possible but requires additional data and a global fit to the full rovibrational manifold [43, 48].

Note. Fulcher-α (H_2) ro-vibrational fitting and population analysis are presented with the EUV-induced plasma results in Chapter 5, where the working relations are summarised for reference.

3.5 Balmer series (H): excitation temperature analysis

In addition to the molecular diagnostics based on the N_2 SPS and H_2 Fulcher-α system, the hydrogen Balmer series is analysed to extract an *effective* electronic excitation temperature T_{exc} for a subset of atomic levels. The basic idea follows the standard Boltzmann-plot approach outlined in Section 2.6: after correcting the line-integrated intensities for instrumental

response and transition probabilities, the upper-level populations N_u are inferred from

$$N_u \propto \frac{I_{ul}\,\lambda_{ul}}{A_{ul}\,g_u}, \tag{3.31}$$

with I_{ul} the line-integrated intensity, λ_{ul} the wavelength, A_{ul} the Einstein coefficient, and g_u the statistical weight of the upper level. If the set of levels under consideration is close to Boltzmann among themselves, $\ln(N_u)$ scales linearly with E_u, and the slope yields T_{exc}. As discussed in Chapter 2, this is not guaranteed in general; in fact, for the EUV-induced plasma (EBL2) the Balmer manifold is clearly non-Boltzmann and no meaningful single T_{exc} can be defined. In contrast, the nanosecond pulsed discharge (NPD) data exhibit a nearly linear Balmer distribution over the accessible levels, enabling a quantitative fit.

Spectral pre-processing and line integration

For the NPD measurements, individual Balmer lines Hα–Hδ are recorded in separate spectral windows using a calibrated spectrometer–camera system. Raw spectra are first corrected for background and instrumental response:

1. A background spectrum (same integration time and optical configuration, but with the discharge off) is subtracted from each plasma spectrum.

2. The resulting signal is multiplied by the wavelength-dependent calibration curve $C(\lambda)$ obtained from a radiometric standard lamp, using the same optical path as for the plasma measurements. For the Hα window, a long-pass interference filter is mounted in front of the spectrometer to suppress shorter-wavelength stray light (continuum and other plasma lines); its transmission curve is measured and folded into $C(\lambda)$, so that the calibrated spectra already represent the true spectral response of the detection chain in that configuration.

3. A slowly varying baseline is removed using MATLAB's `msbackadj` routine, consistent with the molecular-band analysis.

A Gaussian model is then fitted to each Balmer line within a narrow wavelength window,

$$I(\lambda) = a\,\exp\left[-\left(\frac{\lambda - b}{c}\right)^2\right], \tag{3.32}$$

yielding amplitude a, centroid b, and width parameter c. The line-integrated intensity is

$$\mathcal{I} = a\,|c|\,\sqrt{\pi}, \tag{3.33}$$

and parameter uncertainties are obtained from the $(1-\alpha) = 99.5\%$ confidence interval of the fit (MATLAB `confint`), converted to 1σ standard errors via

the Student-t factor. Propagating these errors to the integrated intensity gives

$$\delta\mathcal{I} = \sqrt{(\delta a\,|c|)^2 + (\delta c\,a)^2}\,\sqrt{\pi}, \tag{3.34}$$

which is used as the uncertainty on each Balmer line area.

Relative upper-level populations and error propagation

For a given Balmer transition $n \to 2$ (Hα: $n = 3$, Hβ: $n = 4$, etc.), the quantity proportional to the upper-level population is

$$S_n \;\equiv\; \frac{\mathcal{I}_n\,\lambda_n}{A_n\,g_n}, \tag{3.35}$$

where $\mathcal{I}_n$ is the integrated line intensity from Eq. (3.32), λ_n the central wavelength, A_n the Einstein coefficient, and $g_n = 2n^2$ the hydrogen degeneracy. To remove the unknown proportionality constant (which contains collection geometry, absolute sensitivity, and integration volume) and to facilitate comparison across discharges, the quantities S_n are normalised to Hα:

$$N_n = \frac{S_n}{S_3} = \frac{\mathcal{I}_n\,\lambda_n/(A_n g_n)}{\mathcal{I}_3\,\lambda_3/(A_3 g_3)}. \tag{3.36}$$

Assuming uncorrelated errors on the line areas, the relative uncertainty on N_n is

$$\frac{\delta N_n}{N_n} = \sqrt{\left(\frac{\delta\mathcal{I}_n}{\mathcal{I}_n}\right)^2 + \left(\frac{\delta\mathcal{I}_3}{\mathcal{I}_3}\right)^2}, \tag{3.37}$$

with $\delta\mathcal{I}_n$ from Eq. (3.34). In the NPD case, Hα–Hδ are available with sufficient signal-to-noise; Hϵ has too low intensity and is therefore omitted.

Boltzmann plot and fitted T_{exc}

Using the absolute upper-level term energies E_n (referenced to the ground state) and subtracting the $n = 3$ energy to form $\Delta E_n = E_n - E_3$, the usual Boltzmann relationship can be written for the normalised populations:

$$\ln N_n = -\frac{\Delta E_n}{k_B T_{\mathrm{exc}}} + \text{const.} \tag{3.38}$$

Equation (3.38) is fitted with a weighted linear regression, using

$$y_n = \ln N_n, \qquad \sigma_{y_n} = \frac{\delta N_n}{N_n}, \qquad w_n = \frac{1}{\sigma_{y_n}^2}, \tag{3.39}$$

so that points with smaller relative uncertainty carry higher weight. The fit has the form

$$y = m\,\Delta E + b, \tag{3.40}$$

with $m = -1/(k_B T_{\mathrm{exc}})$. The excitation temperature and its uncertainty follow as

$$T_{\mathrm{exc}} = -\frac{1}{k_B m}, \qquad \delta T_{\mathrm{exc}} = \frac{1}{k_B m^2}\,\delta m, \tag{3.41}$$

where δm is obtained from the standard error of the slope (computed from the confidence interval of the weighted fit).

Figure 3.12 shows a representative Boltzmann plot for the NPD Balmer data (Hα–Hδ). The error bars correspond to δN_n, while the solid line denotes the weighted linear fit used to extract T_{exc}.

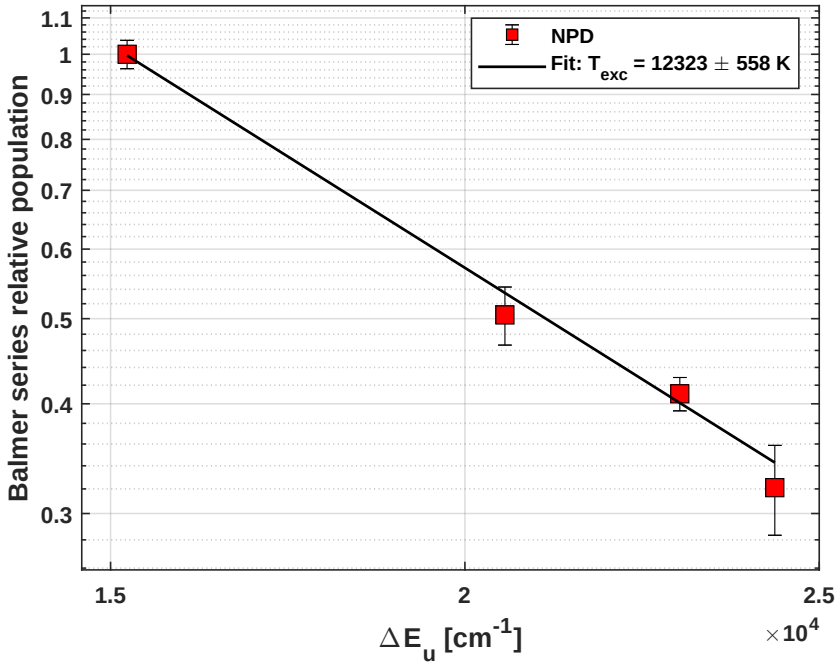

Figure 3.12: Balmer-series Boltzmann plot for the nanosecond pulsed discharge (NPD). Symbols show the relative upper-level populations N_n (normalised to Hα) with propagated uncertainties; the solid line is a weighted linear fit to Eq. (3.38). The slope yields the effective excitation temperature T_{exc} for the Balmer manifold under NPD conditions.

Application to different sources and limitations

The same analysis pipeline (Gaussian line fits, response correction, population normalisation, and error propagation) is applied to all three sources: the nanosecond pulsed discharge (NPD), the EUV-induced plasma in the EBL2 chamber, and the DC glow in the EBR reactor. However, only for the NPD does the Balmer manifold exhibit an approximately linear behaviour on the Boltzmann plot over Hα–Hδ, so that a single T_{exc} is meaningful. For the EUV-induced plasma (EBL2), the populations deviate strongly from a straight line, confirming the non-Boltzmann character of the Balmer series already discussed in Chapter 2. In those cases, T_{exc} is not quoted, and the

Balmer data are used qualitatively (e.g., relative changes in line ratios) rather than as a quantitative electron-temperature proxy.

Even for the NPD, the extracted T_{exc} should be interpreted as an *effective* excitation temperature for the subset of Balmer levels considered, not as a direct measurement of the electron temperature T_e. Cascades, stepwise excitation, and non-Maxwellian electron energy distributions can all affect the level populations. In the following chapters, T_{exc} from the NPD Balmer analysis is therefore used together with the molecular diagnostics (Fulcher-α and N_2 SPS) and with collisional–radiative reasoning, rather than as a stand-alone indicator of plasma conditions.

Chapter 4

Nanosecond pulsed discharge plasma

4.1 Introduction

This chapter presents the nanosecond pulsed discharge (NPD) experiments in nitrogen and hydrogen and the associated optical emission spectroscopy (OES) analysis. The goal is to establish a well-characterised, electrically driven reference case against which the EUV-induced and electron-beam plasmas in later chapters can be compared.

We first describe the OES setup used for NPDs and the timing scheme that enables nanosecond-resolved measurements. The subsequent sections summarise the N_2 Second Positive System (SPS) and First Negative System (FNS) results over 1–500 mbar and at a fixed low pressure of 0.05 mbar, including the retrieved rotational temperatures and the first-level C-state vibrational temperature $T_{01}^{(C)}$ and their pressure and time dependence. A dedicated "long measurement" section shows how stitched kinetic series extend the accessible time window into the microsecond range, revealing the role of $N_2(A)$ metastables and pooling in the afterglow.

The second part of the chapter focuses on hydrogen plasmas. Fulcher-α diagnostics are used to infer ground-state rotational (gas) temperatures and vibrational populations in NPD H_2 discharges, and the Balmer series is analysed to extract an effective excitation temperature for a subset of atomic levels. Throughout, the methodology follows the procedures developed in Chapter 3, and the NPD results are explicitly framed as a baseline for the EUV- and EBR-driven plasmas discussed in the following chapters.

4.2 Optical emission spectroscopy setup for NPDs

In an optical emission spectroscopy (OES) experiment, the light emitted by the plasma is analysed by an ICCD camera coupled to a spectrograph.

The plasma is generated in a vacuum chamber by a nanosecond high-voltage (HV) discharge in a flowing gas mixture (flow set by a mass flow controller; pressure regulated by a pumping system). In our setup, the discharge can be operated either in a pin-to-plate or in a plate-to-plate electrode configuration. The nanosecond nitrogen measurements at 1–500 mbar use a pin-to-plate geometry (tungsten pin, steel plate), whereas the low-pressure nitrogen measurements in the 10^{-2} mbar range and the H_2 Fulcher-α measurements use a plate-to-plate geometry.
Precise synchronisation between the HV pulse and the waveform generator, as well as between the ns-pulse and the ICCD acquisition gate, is essential for successful measurements; a trigger delay generator is therefore included in the timing chain.
Light is transported to the spectrograph using an optical fiber and a round-to-linear fiber bundle. A two-lens relay focuses the plasma image onto the fiber core while matching the fiber numerical aperture; the bundle output is then coupled to the spectrograph through an F#-matcher.
A schematic of the experimental configuration is shown in Figure 4.1. Further details of each subsystem (with laboratory photographs) are reported in a dedicated appendix describing the OES setup for NPDs.

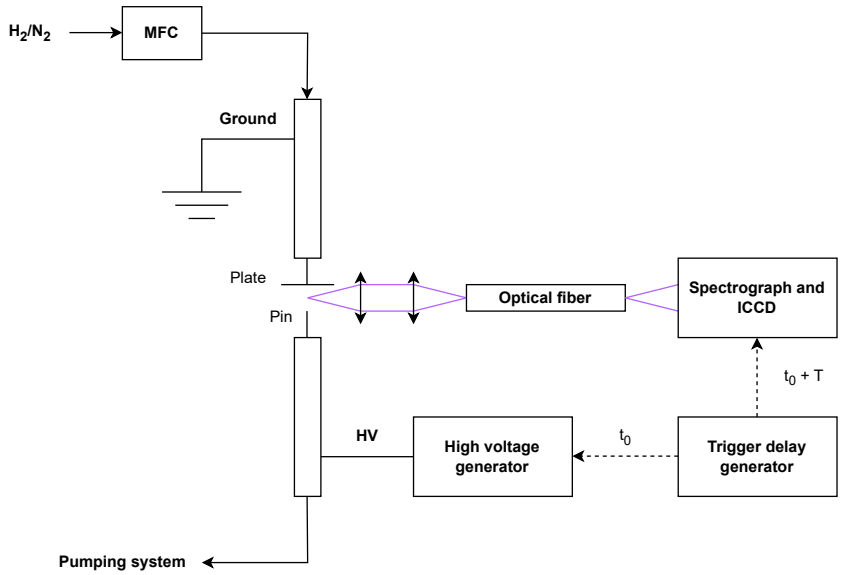

Figure 4.1: Scheme of the optical emission spectroscopy setup.

The initial OES campaign in pure nitrogen focused on the Second Positive System (SPS) of N_2 ($C^3\Pi_u \rightarrow B^3\Pi_g$). Emission spectra were recorded with the ICCD in kinetic-series mode to resolve the fast discharge dynamics. For each setting, a sequence of 300 spectra was acquired over a total window of $\sim$300 ns with 1 ns time steps. The series start time was set approximately 20 ns before the high-voltage trigger in order to capture the onset of plasma formation and the subsequent early-time evolution.

4.3 N_2 Second Positive System (1–500 mbar)

Here we summarise the SPS ($C\,^3\Pi_u \rightarrow B\,^3\Pi_g$, $\Delta\nu = -2$) results in the 1–500 mbar range and explicitly *recall* the example figures already presented in Chapter 3. The modelling workflow—PGOPHER band synthesis with literature constants, convolution with the calibrated instrumental function, and response correction—is identical throughout.

As illustrated by the example full-spectrum fit in Chapter 3, Fig. 3.5, the three-band window (0–2, 1–3, 2–4) is well reproduced across 1–500 mbar. The normalised vibrational-state plot used to extract the first-level C-state vibrational temperature $T_{01}^{(C)}$ (Chapter 3, Fig. 3.6) shows that, at these pressures, $T_{01}^{(C)}$ responds to the discharge dynamics and to post-pulse chemistry. In kinetic series (Chapter 3, Fig. 3.7), $T_{01}^{(C)}$ first rises during the current peak and then decays, while at higher pressures additional late-time features appear due to pooling via $N_2(A)$.

The main pressure-dependent trends observed here are:

- **Rotational envelope and T_{rot}:** T_{rot} increases moderately with pressure and with proximity to the current peak. Fits remain robust over the three bands when T_{rot} determined on 0–2 is propagated to 1–3 and 2–4, as in Chapter 3.

- **Vibrational excitation ($T_{01}^{(C)}$):** at 1–11 mbar, $T_{01}^{(C)}$ closely follows the discharge current evolution and relaxes back towards its pre-pulse value within a few tens of nanoseconds after each pulse, i.e. no pronounced late-time increase or plateau is observed between pulses. At 110–500 mbar, the late-time $T_{01}^{(C)}$ rise/plateau (documented extensively in Section 4.6) indicates A-state build-up and pooling-driven population of $C\,^3\Pi_u$ on $\gtrsim$100 ns timescales, consistent with state-to-state kinetic modelling of low-pressure N_2 discharges and repetitively pulsed plasmas [3, 35].

- **SPS/FNS ratio:** the relative contribution of FNS decreases with pressure, consistent with enhanced ion quenching and altered electron-impact pathways.

These 1–500 mbar results provide the high-pressure baseline against which we compare the *low-pressure* NPD data at 0.05 mbar (Sections 4.4–4.8) and the EUV-induced nitrogen spectra in the following chapter.

4.4 N_2 Second Positive System (0.05 mbar)

At a scanner-relevant low pressure of 0.05 mbar, the SPS of N_2 ($C\,^3\Pi_u \rightarrow B\,^3\Pi_g$, $\Delta\nu = -2$ series: 0–2, 1–3, 2–4) was analysed with the same modelling workflow detailed in Chapter 3 (PGOPHER band synthesis, convolution with

the calibrated instrumental function, global response correction). Both *integrated* and *time-resolved* datasets yield stable, well-posed fits across the three bands, without the long-time distortions seen at higher pressures.

In the time-resolved series, the retrieved rotational temperature T_{rot} and the first-level C-state vibrational temperature $T_{01}^{(\mathrm{C})}$ remain essentially *constant over the pulse* within uncertainties. This behaviour is expected at such low pressure: pooling and related A-state–mediated channels are strongly suppressed, so there is no late-time build-up of $C\,^3\Pi_u$ via $N_2(A)$ and no post-pulse drift of the rotational/vibrational envelopes, in line with kinetic simulations of low-pressure N_2 discharges where stepwise and metastable-assisted pathways become negligible in the low-collision-rate limit [3, 35]. As a result, integrated fits coincide with the time-averaged parameters from the gated series.

A representative fit is shown in Fig. 4.2. The band heads and rotational envelope are reproduced by the model, and the T_{rot} extracted from the leading band (0–2) is consistent with the values obtained when fitting 1–3 and 2–4 at fixed T_{rot} (Chapter 3). The inferred temperatures are in the expected range for low-pressure nanosecond discharges and provide a clean baseline for the EUV-induced nitrogen spectra discussed later. As a forward reference, we note that the same SPS workflow applied to EUV-induced N_2 at EBL2 (next chapter) yields unusually low, "under-thermal" T_{rot} and poorer fits; by contrast, the low-pressure NPD results here confirm that the modelling pipeline itself is sound.

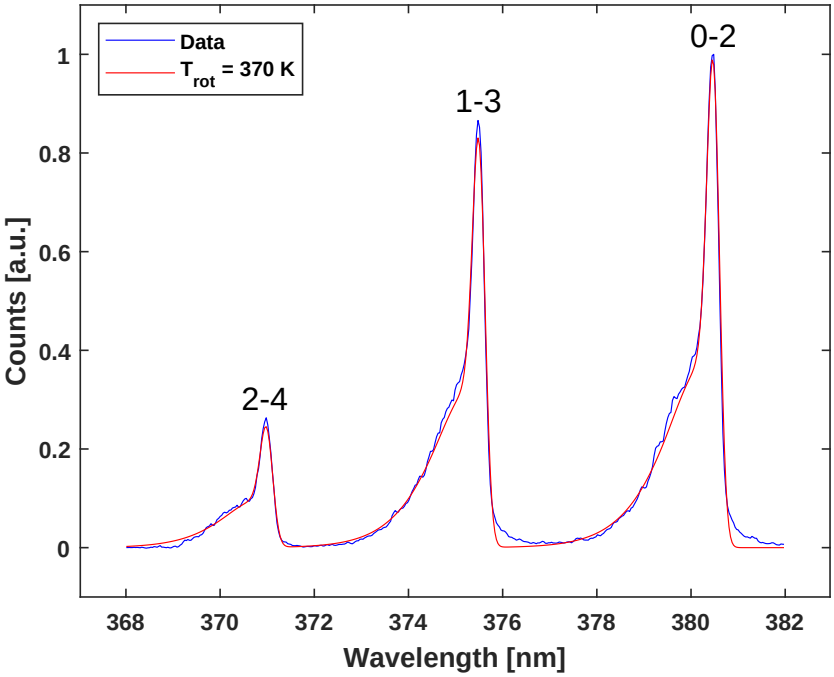

Figure 4.2: Integrated SPS spectrum of N_2 at 0.05 mbar (blue) and best-fit model (red) using the Chapter 3 workflow (PGOPHER synthesis + instrumental-function convolution + response correction). The band heads (0–2, 1–3, 2–4) and the rotational envelope are well captured by the model. The fitted T_{rot} agrees with time-resolved averages and remains stable throughout the pulse at this pressure, while the first-level C-state vibrational temperature $T_{01}^{(\mathrm{C})}$ is likewise time-independent within uncertainties.

4.5 N_2 First Negative System (1–500 mbar)

Measurements in pure nitrogen were extended to include the First Negative System (FNS) of N_2^+ ($B^2\Sigma_u^+ \longrightarrow X^2\Sigma_g^+$). The analysis procedure mirrors that used for the SPS: the first-level C-state vibrational temperature $T_{01}^{(C)}$ is derived from the first two SPS bands with $\Delta\nu = -2$, while global fits include the FNS branches with $\Delta\nu = 0$ (0–0, 1–1) and the SPS bands with $\Delta\nu = -3$. Four pressure regimes were studied, as listed in Table 4.1.

Data set	Pressure [mbar]	Gas flow [sccm]
1	1	100
2	11	100
3	110	500
4	500	500

Table 4.1: Pressure and nitrogen flow for each measurement set.

Figures 4.3, 4.5, 4.7, and 4.9 show representative spectra at the start of the discharge (for 1, 11, 110, and 500 mbar) with best-fit models at the corresponding T_{rot}. The ratio of FNS to SPS emission decreases markedly with increasing pressure.
Figures 4.4, 4.6, 4.8, and 4.10 report examples of the $T_{01}^{(C)}$ evolution for the four pressure sets, together with the discharge current. The $T_{01}^{(C)}$ trend generally follows the discharge dynamics (initial points within the first few nanoseconds are unreliable due to low signal), increasing at current peaks and relaxing afterwards. Because the ICCD MCP gain is kept fixed within a kinetic series, the signal decays rapidly with delay, limiting reliable fitting at late times. To probe longer times, dedicated measurements with adjusted gate/gain were carried out (section 4.6).

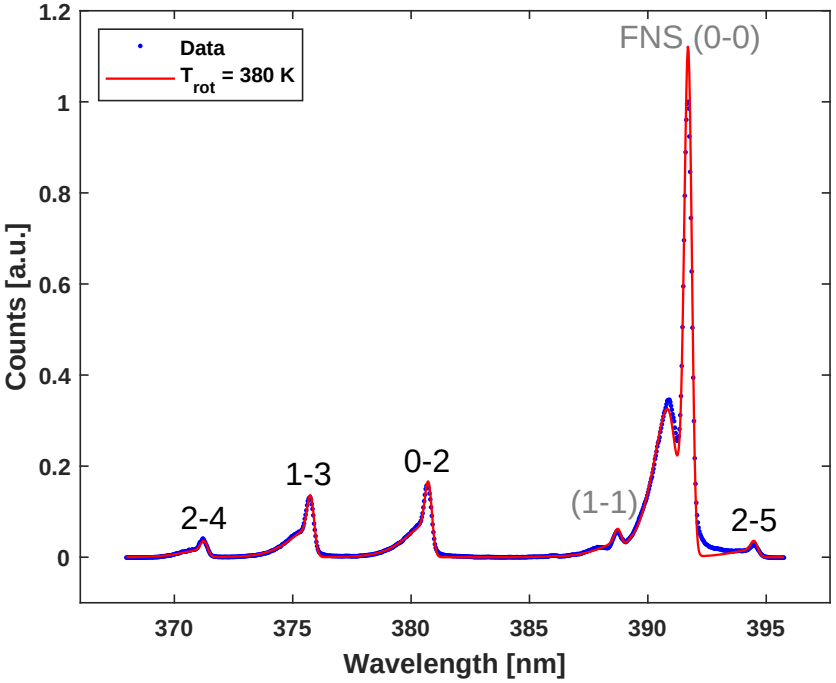

Figure 4.3: Integrated SPS+FNS spectrum at $P = 1$ mbar (blue) with best-fit model (red). The simulation reproduces the SPS $\Delta\nu = -2$ bands and the N_2^+ FNS $\Delta\nu = 0$ structure with good agreement across the window, enabling consistent extraction of T_{rot} and $T_{01}^{(\mathrm{C})}$ (first-level C-state vibrational temperature).

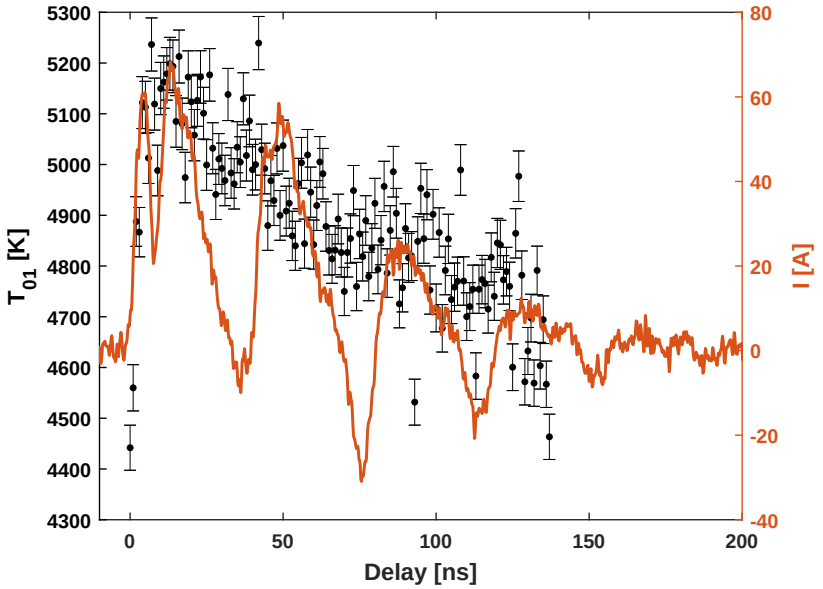

Figure 4.4: Kinetics at $P = 1$ mbar: time evolution of $T_{01}^{(\mathrm{C})}$ (black, from SPS) and discharge current (orange). $T_{01}^{(\mathrm{C})}$ increases during the current peak and relaxes afterward; earliest points can be uncertain due to low signal at the start of the gate sequence.

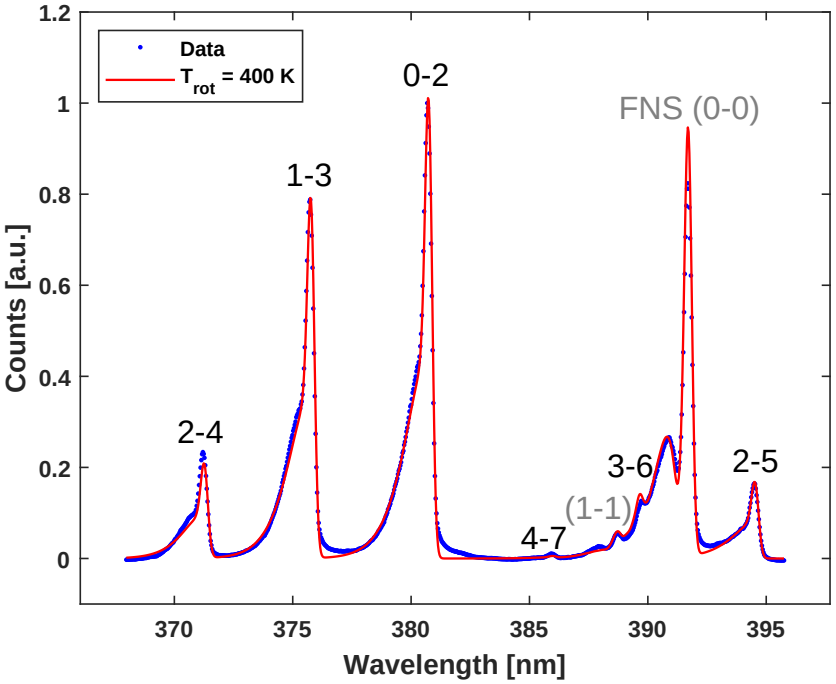

Figure 4.5: Integrated SPS+FNS spectrum at $P = 11$ mbar (blue) and model (red). The relative FNS intensity is reduced compared with 1 mbar; SPS band heads and envelopes remain well matched by the model with a single T_{rot} propagated across the $\Delta\nu = -2$ bands.

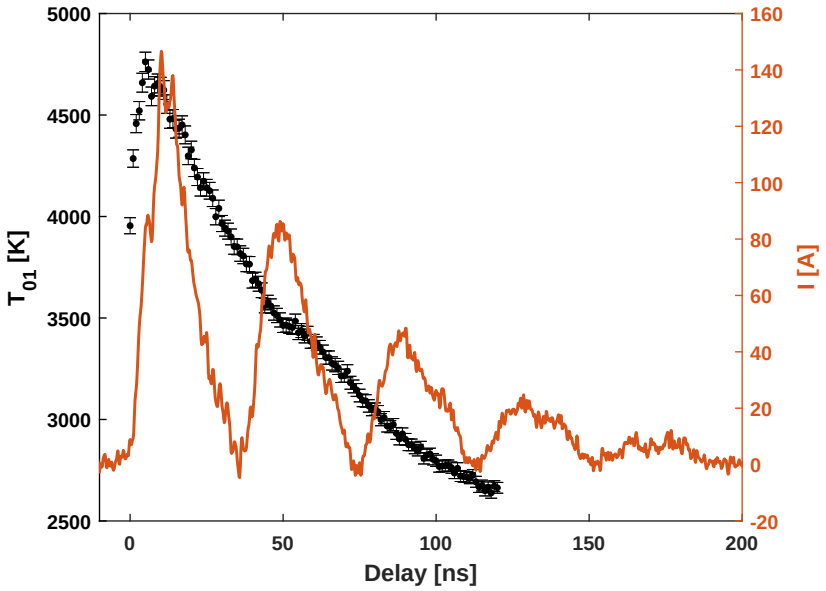

Figure 4.6: Kinetics at $P = 11$ mbar: $T_{01}^{(\mathrm{C})}$ (black) follows the discharge current (orange) with limited afterglow, indicating that A-state pooling is still weak in this pressure regime.

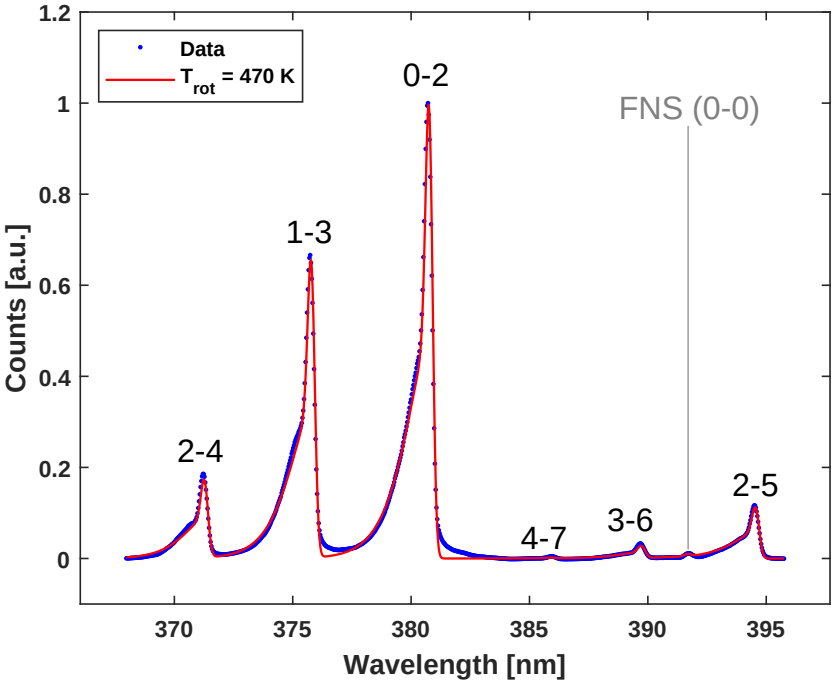

Figure 4.7: Integrated SPS+FNS spectrum at $P = 110$ mbar (blue) and model (red). Fits are robust across the window; careful baseline management is required as continuum and overlapping features grow with pressure.

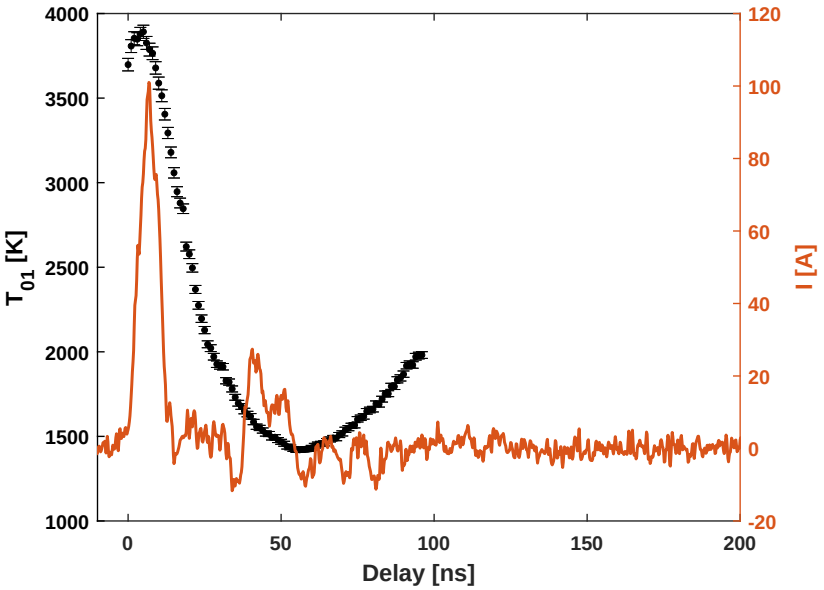

Figure 4.8: Kinetics at $P = 110$ mbar: $T_{01}^{(C)}$ (black) rises with the current (orange) and shows the onset of a late-time increase, signalling the growing role of N_2(A)-mediated pooling into $C\,^3\Pi_u$.

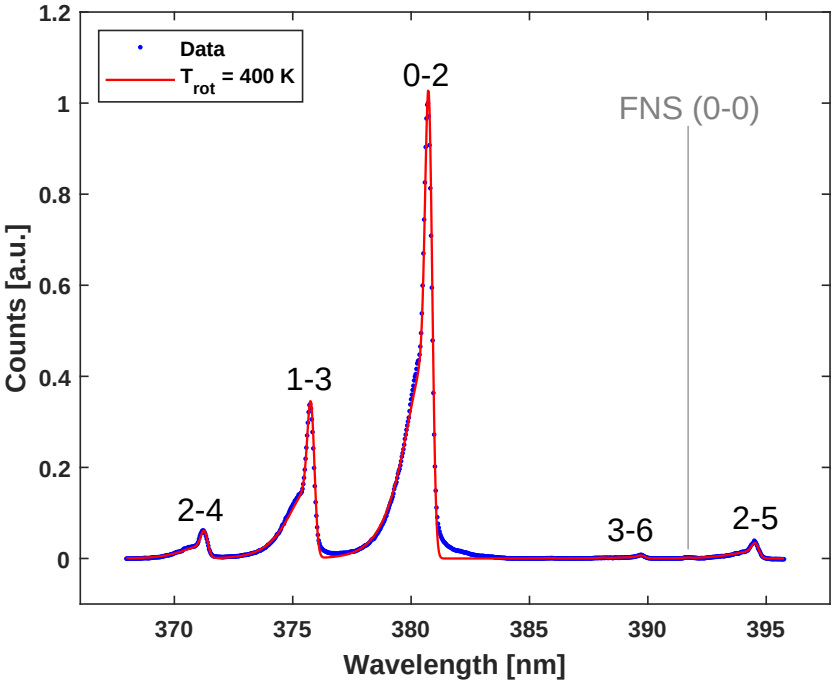

Figure 4.9: Integrated SPS+FNS spectrum at $P = 500$ mbar (blue) and best-fit model (red). The FNS contribution is further suppressed; the SPS envelope remains well captured by a single T_{rot} across the $\Delta\nu = -2$ bands when the baseline is modelled carefully.

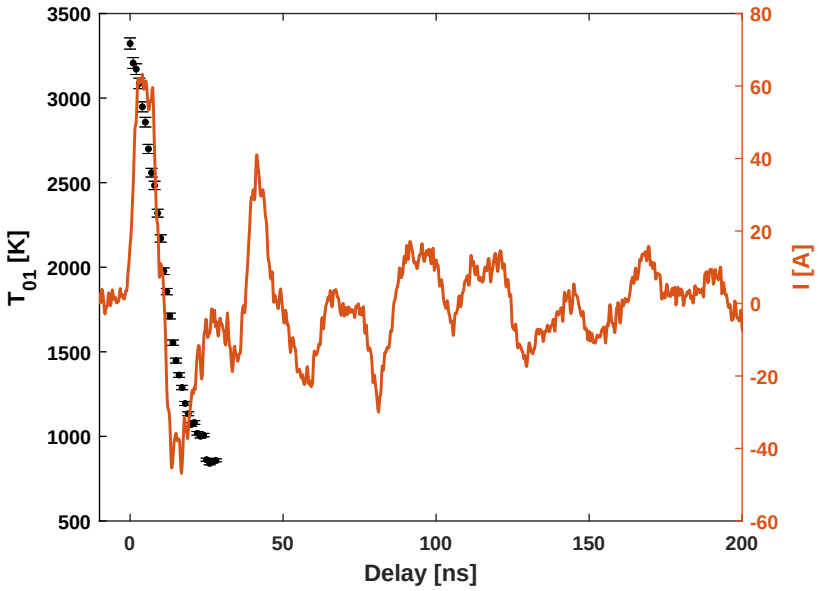

Figure 4.10: Kinetics at $P = 500$ mbar: $T_{01}^{(\mathrm{C})}$ (black) follows the current (orange) and exhibits a pronounced post-pulse rise/plateau driven by pooling via the $N_2(A)$ manifold.

4.6 Long measurement

In a single kinetic series, the signal typically drops below the fitting threshold after ∼100 ns delay, making late-time analysis unreliable. To capture the full discharge evolution over several microseconds while preserving nanosecond-scale information around the current pulses, the measurement is therefore divided into consecutive short kinetic series with progressively increased ICCD gate and MCP gain. In this way, signal can be recorded up to microseconds after the discharge start and the full temporal evolution characterised without saturating the detector at early times.
Figure 4.11 shows the first-level C-state vibrational temperature $T_{01}^{(C)}$ versus time for pure nitrogen at 110 mbar together with the discharge current.

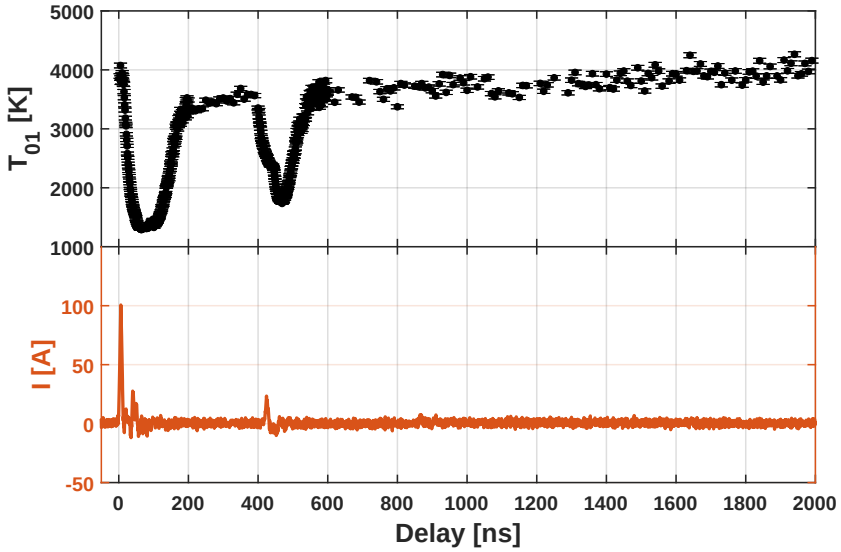

Figure 4.11: Extended $T_{01}^{(C)}$ kinetics (top panel, black) together with discharge current (bottom panel, orange), reconstructed from seven stitched series (Table 4.2). After the prompt rise and decay around each current pulse, a late-time increase and plateau of $T_{01}^{(C)}$ appear in the interpulse intervals, consistent with the build-up of $N_2(A)$ and pooling into $C\,^3\Pi_u$. Spectra with insufficient signal-to-noise ratio at the longest delays are excluded from the analysis and are not shown, so that the plotted trend reflects only reliably fitted points.

The plot comprises seven consecutive series with different delays, MCP gains, and exposure times (Table 4.2); each series is recorded with fixed camera settings and then mapped onto a common time axis using the programmed gate delays.
As in the short-window examples, $T_{01}^{(C)}$ increases at current peaks and decreases immediately after. A pronounced late-time increase and plateau of $T_{01}^{(C)}$ in pulse-free intervals is also evident. Spectra with insufficient signal-to-noise ratio at the longest delays are discarded and not included in the analysis. This behaviour is consistent with the build-up of $N_2(A^3\Sigma_u^+)$ metastables feeding the $C^3\Pi_u$ population via pooling and related channels, as cap-

#	Delay [ns]	Time steps [ns]	Exp. time MCP [ns]	MCP gain [a.u.]
1	0–50	1	10	400
2	50–100	1	10	1200
3	100–200	1	10	2700
4	200–400	10	50	2300
5	400–500	1	50	1800
6	500–600	1	50	3300
7	600–2000	10	50	3600

Table 4.2: Kinetic-series settings used to reconstruct the long-time discharge evolution. Each block is acquired with fixed ICCD parameters and then stitched in delay to form the composite time trace.

tured in detailed state-to-state models of nitrogen afterglows and pulsed discharges [3, 35].
To corroborate this, the normalised integral of the SPS emission (each spectrum divided by its MCP gain and exposure time) is plotted versus delay in Figure 4.12.

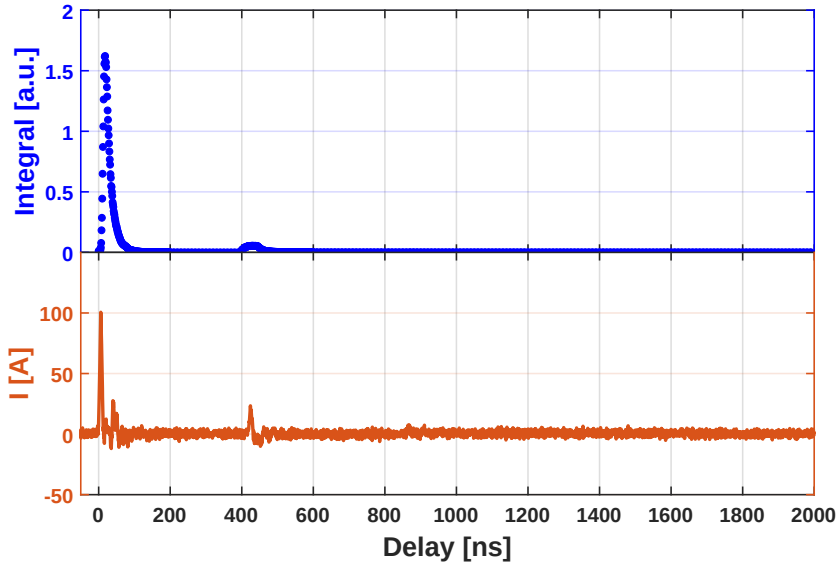

Figure 4.12: Normalised SPS integral and discharge current over the stitched long-window sequence. Top panel: SPS integral on a logarithmic intensity scale, highlighting the decay between pulses over several orders of magnitude and revealing the slowly varying afterglow tail. Bottom panel: discharge current on a linear scale. Both panels share the same time axis; peaks in the SPS integral coincide with current pulses, and the integral decays between pulses.

To directly compare the long-time evolution of $T_{01}^{(\mathrm{C})}$ and the SPS emission, both quantities are plotted together with the discharge current in Figure 4.13.

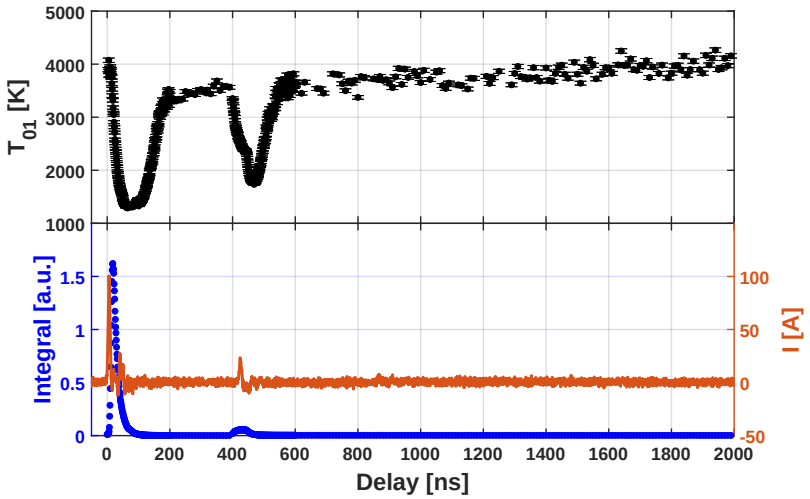

Figure 4.13: Combined long-time kinetics of $T_{01}^{(C)}$ (top panel, black), normalised SPS integral (bottom panel, blue) and discharge current (bottom panel, orange) for pure nitrogen at $P = 110$ mbar, reconstructed from the seven stitched series in Table 4.2. Peaks in both $T_{01}^{(C)}$ and the SPS integral coincide with current pulses, while the late-time rise and plateau of $T_{01}^{(C)}$ between pulses follow the slowly decaying SPS emission, consistent with afterglow excitation via accumulated $N_2(A)$ and pooling into $C^3\Pi_u$. Small inter-segment offsets arise from baseline removal and the different MCP/gate settings used to extend the dynamic range, but do not affect the qualitative trends.

4.7 Comparison with literature

Measured parameters have been compared with literature values.
In [39,49], rotational temperatures are reported for nanosecond discharges in atmospheric-pressure air. Absolute values are not directly comparable to our pure-N_2 results at 1–500 mbar; however, qualitative trends can be contrasted. In [39,49], T_{rot} rises from ∼1500 K to ∼2500 K within ∼25 ns, whereas our data show an initial decrease from ∼470 K to ∼440 K over the first 50 ns, followed by a rise to ∼500 K over the next 50 ns. Between pulses, our T_{rot} oscillates within 450–500 K; comparable inter-pulse data are not available in [39,49].
Our retrieved T_{rot} and first-level C-state vibrational temperatures $T_{01}^{(C)}$ are consistent in magnitude with [38,50] (300–500 K and 3000–5000 K, respectively), noting that those studies address capacitively/inductively coupled plasmas and present temperature versus RF power/frequency rather than nanosecond-resolved kinetics.
Electron temperature/density extraction from a single SPS/FNS intensity ratio, as in [40], relies on restrictive assumptions (direct electron-impact excitation to $C^3\Pi_u$, Maxwellian EEDF, corona balance) that are not valid under our conditions, where multistep and metastable-assisted channels are significant. A more suitable approach for our H_2/N_2 studies is Stark-broadening analysis of N^+ and H_α as suggested in [51].

The late-time rise and plateau of $T_{01}^{(\mathrm{C})}$ can be explained by the build-up of $\mathrm{N}_2(\mathrm{A}^3\Sigma_u^+)$ and subsequent pooling,

$$\mathrm{N}_2\big(\mathrm{A}^3\Sigma_u^+\big) + \mathrm{N}_2\big(\mathrm{A}^3\Sigma_u^+\big) \longrightarrow \mathrm{N}_2\big(\mathrm{C}^3\Pi_u, \nu\big) + \mathrm{N}_2, \tag{4.1}$$

which increases the C-state population on $\gtrsim$100 ns timescales, consistent with [33]. Similar afterglow behaviour in the vibrational temperature has been reported in [32, 34]. Extending measurements to the sub-ms/ms range would allow a more direct comparison with those studies and with metastable-density kinetics such as those reported in [52].

4.8 N_2^+ First Negative System (0.05 mbar)

The N_2^+ FNS ($B\,^2\Sigma_u^+ \rightarrow X\,^2\Sigma_g^+$, $\Delta\nu = 0$) was recorded and fitted under the same low-pressure conditions as the SPS measurements, i.e.0.05 mbar, using the identical band-simulation framework (state-resolved line lists, instrumental convolution, response correction). As for SPS, both integrated and time-resolved spectra are modelled accurately. The extracted T_{rot}(FNS) agrees with T_{rot}(SPS) within uncertainties, and no long-time evolution is observed over the pulse—again consistent with the absence of pooling-driven late excitation at low pressure.

Figure 4.14 shows a representative integrated fit around the prominent 0–0 and 1–1 bands. The band heads and rotational structure are reproduced with low residuals across the full window, confirming internal consistency between the ion and neutral nitrogen diagnostics at low pressure. This contrasts with the EUV-induced N_2 case at EBL2 (next chapter), where SPS/FNS fits exhibit "under-thermal" envelopes and degraded match; the NPD results here therefore serve as a reference demonstrating that the fitting procedure and calibrations are robust.

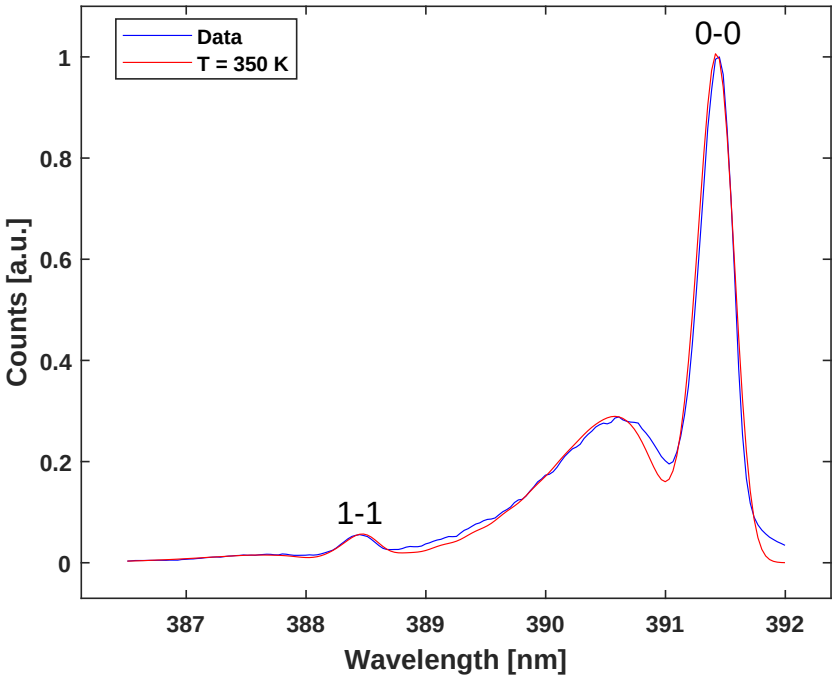

Figure 4.14: Integrated N_2^+ FNS spectrum at 0.05 mbar (blue) and best-fit model (red). The simulation reproduces the 0–0 and 1–1 band heads and the associated rotational envelope over the full window. The inferred T_{rot}(FNS) is consistent with the SPS-based T_{rot}, and both remain steady during the pulse at this pressure, reflecting the suppression of late-time metastable pathways.

4.9 Hydrogen plasma

4.9.1 Fulcher band emission

For nanosecond-pulsed H_2 discharges (NPD), the Fulcher-α system ($d\,^3\Pi_u \rightarrow a\,^3\Sigma_g^+$) serves as a proxy for the ground-state rotational and vibrational distributions via the Q-branch of the $d\,^3\Pi_u^-$ component. The analysis strictly follows the methodology established in Section 3.4: we fit the $Q_1(N' = 1, 2, 3)$ lines for the diagonal bands $v' = 0 \ldots 3$ with Gaussian profiles (instrumental width constrained), construct rotational Boltzmann plots per v', project to the gas temperature using rotational-constant ratios, and form Franck–Condon–corrected vibrational populations $f_X(v)$.

The resulting rotational temperatures $T_{\mathrm{rot}}(d, v')$ are low — often below room temperature — and exhibit a mild decrease with increasing v', consistent with the short lifetime of the d state and low-pressure excitation conditions. Using Eq. (3.19), the corresponding ground-state rotational (gas) temperature is approximately a factor of ~ 2 larger and thus remains above room temperature. The inferred vibrational populations display the characteristic envelope with a maximum near $v = 2$ and a decrease towards higher v, in line with low-density kinetics dominated by direct excitation and radiative decay.

For completeness and to keep all relevant panels together in this chapter, Fig. 4.15 re-displays the four example plots introduced in Chapter 3 (Section 3.4) as a single 2×2 composite: (a) spectrum, (b) single-line fits, (c) rotational Boltzmann plots, and (d) Franck–Condon–corrected vibrational populations.

Summary. NPD Fulcher diagnostics provide internally consistent rotational temperatures and vibrational population trends that serve as a baseline for comparison with EUV-induced plasmas (EBL2, OLT-TS, EBR) presented in subsequent chapters. The low $T_{\mathrm{rot}}(d)$ values and the $v = 2$ population maximum are recurring features across platforms; quantitative interpretation of $f_X(v)$ in terms of a vibrational temperature is deferred pending a dedicated collisional–radiative model.

4.9.2 Balmer-series excitation temperature

In addition to the molecular diagnostics based on the Fulcher-α system (Section 4.9.1), the hydrogen Balmer series was analysed for the nanosecond-pulsed H_2 discharges (NPD) to obtain an *effective* electronic excitation temperature T_{exc} for a subset of atomic levels. The detailed methodology—Gaussian line fitting, response correction, population normalisation, and weighted Boltzmann plotting—is presented in Chapter 3, Section 3.5. Here we summarise the key steps and results for the NPD case.

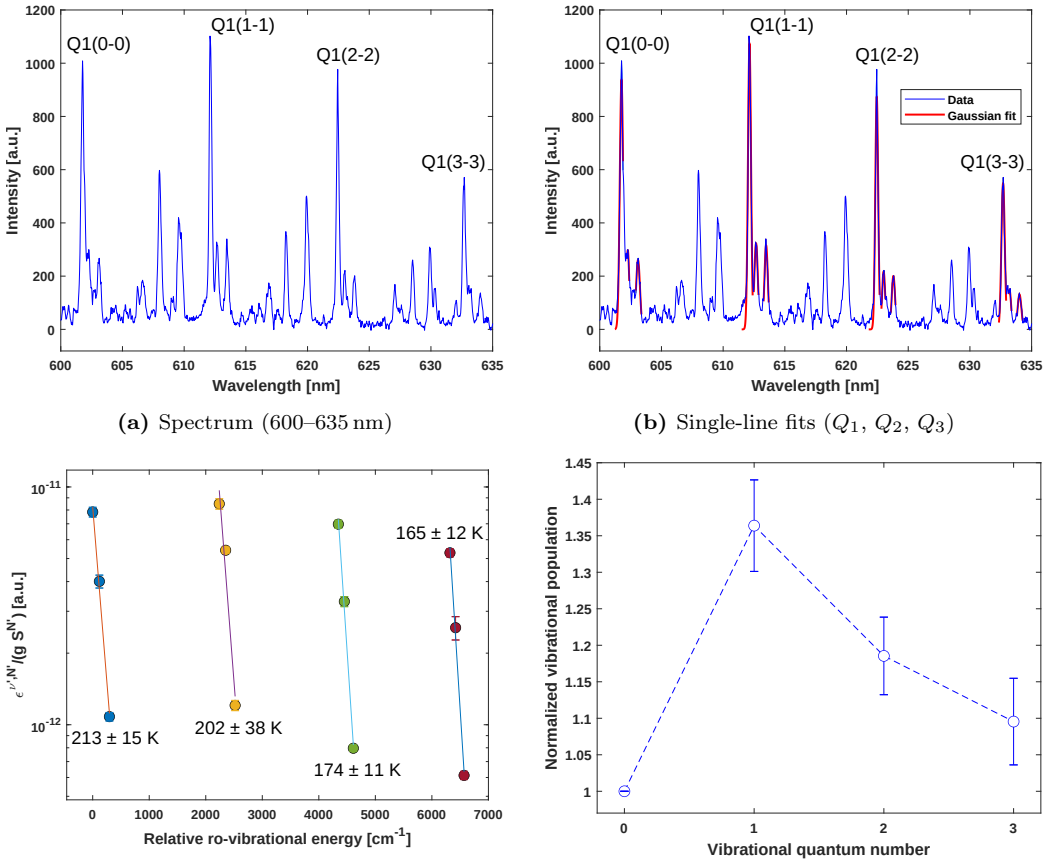

(a) Spectrum (600–635 nm)

(b) Single-line fits (Q_1, Q_2, Q_3)

(c) Rotational Boltzmann plots

(d) Vibrational populations $f_X(v)$

Figure 4.15: Fulcher-α analysis for nanosecond-pulsed H_2 discharges (NPD), arranged as a 2×2 composite for compact reference. (a) Representative spectrum with fit windows in the 600–635 nm range. (b) Gaussian fits to $Q_{N'}(N' = 1, 2, 3)$ lines for $v' = 0 \ldots 3$ (instrumental width constrained). (c) Rotational Boltzmann plots yielding $T_{\mathrm{rot}}(d, v')$, typically below room temperature and decreasing mildly with v'. (d) Franck–Condon–corrected ground-state vibrational populations $f_X(v)$, peaking near $v = 2$ and then decreasing. The workflow and assumptions are detailed in Section 3.4.

Procedure (recap). Individual Balmer lines Hα–Hδ are recorded in separate, calibrated spectral windows. For each line:

1. A background spectrum (discharge off) is subtracted from the plasma spectrum.

2. The signal is corrected for the wavelength-dependent spectral response using a previously measured calibration curve. For Hα, a long-pass interference filter (cut-on around 590 nm) is inserted in front of the spectrometer to suppress shorter-wavelength molecular emission and second-order grating contributions near 656 nm; its transmission curve is therefore divided out so that the corrected spectrum reflects the true Hα line intensity.

3. A smooth baseline is removed using MSBACKADJ, as in the molecular-band analysis.

4. The line profile is fitted with a Gaussian model,

$$I(\lambda) = a \exp\left[-\left(\frac{\lambda - b}{c}\right)^2\right], \tag{4.2}$$

from which the integrated intensity

$$\mathcal{I} = a\,|c|\,\sqrt{\pi} \tag{4.3}$$

and its uncertainty $\delta\mathcal{I}$ are obtained. The latter is computed by propagating the parameter errors from the $(1-\alpha) = 99.5\%$ confidence interval of the fit.

Using the line-integrated intensities, the upper-level populations are formed as

$$S_n \;\equiv\; \frac{\mathcal{I}_n\,\lambda_n}{A_n\,g_n}, \tag{4.4}$$

with λ_n the wavelength, A_n the Einstein coefficient, and $g_n = 2n^2$ the statistical weight of the upper level. To remove the unknown proportionality factor and to facilitate comparison across data sets, the populations are normalised to Hα ($n = 3$):

$$N_n = \frac{S_n}{S_3}, \tag{4.5}$$

with uncertainties δN_n obtained by standard error propagation (assuming uncorrelated errors on $\mathcal{I}_n$ and $\mathcal{I}_3$).

Boltzmann plot and T_{exc}. Using the upper-level term energies E_n (referenced to the ground state), the relative excitation energies are defined as $\Delta E_n = E_n - E_3$. Under the assumption of a quasi-Boltzmann distribution within the Balmer manifold, the normalised populations satisfy

$$\ln N_n = -\frac{\Delta E_n}{k_B T_{\mathrm{exc}}} + \text{const.} \tag{4.6}$$

A weighted linear fit of $\ln N_n$ versus ΔE_n (Hα–Hδ) is performed, using weights $w_n = 1/\sigma_{y_n}^2$ with $\sigma_{y_n} = \delta N_n / N_n$. The fitted slope m and intercept b then give

$$T_{\mathrm{exc}} = -\frac{1}{k_B m}, \qquad \delta T_{\mathrm{exc}} = \frac{1}{k_B m^2}\,\delta m, \tag{4.7}$$

where δm is the standard error of the slope derived from the fit confidence interval.

A representative Balmer Boltzmann plot for NPD, including propagated error bars and the weighted linear fit, is shown in Chapter 3, Fig. 3.12. The

points lie close to a straight line within uncertainties, indicating that, for the NPD conditions and over the restricted set of levels probed (Hα–Hδ), the Balmer manifold behaves approximately Boltzmann-like. The resulting T_{exc} is of order $(1\text{–}2)\times10^4$ K (corresponding to $\sim$1–2 eV), i.e. several times higher than the rotational temperatures (few 10^2 K) and the C-state/ground-state vibrational temperatures (few 10^3 K) obtained from the SPS and Fulcher analyses, as expected for electronic excitation in a low-temperature plasma.

Role of NPD T_{exc} in this thesis. The NPD Balmer analysis serves two purposes:

- It provides a self-consistent, internally error-barred estimate of an *effective* excitation temperature for the Balmer levels, under conditions where the Boltzmann-plot assumption is reasonably satisfied.
- It offers a reference against which to assess the EUV-induced and electron-driven plasmas (EBL2, EBR). In those systems the Balmer populations strongly deviate from a straight line on the Boltzmann plot, so that no single T_{exc} can be meaningfully defined; instead, the Balmer series is used only qualitatively (line ratios, trends).

Even in the NPD case, T_{exc} must be interpreted with care: it reflects a balance of direct electron-impact excitation from the ground state, stepwise excitation via metastable and low-lying excited levels, recombination-driven channels, and radiative cascades from higher n, all within the restricted Balmer manifold that we sample. In nanosecond repetitively pulsed (NRP) discharges the situation is particularly complex: the fast overvoltage during the rise of the HV pulse produces a highly non-Maxwellian electron energy distribution, which then relaxes on a timescale comparable to the pulse duration; during this evolution, excitation, ionization, recombination, and quenching pathways all contribute to the populations of the $n = 3$–6 levels that form the Balmer series [3, 7, 31, 32, 34, 39, 49]. A single-slope Balmer Boltzmann plot therefore yields only an *effective* excitation temperature for that subset of levels, and cannot be identified with the electron temperature T_e in a strict sense.

Throughout this work, the NPD T_{exc} is thus used in a complementary way: it is considered together with the rotational and vibrational information from molecular diagnostics (Fulcher-α, N_2 SPS/FNS) and with qualitative collisional–radiative reasoning on the dominant excitation and quenching mechanisms inferred from the literature cited above, rather than as a standalone, quantitative measure of the plasma "temperature" or of T_e.

Chapter 5

EUV-induced plasma

Introduction

The previous chapter focused on electrically driven plasmas generated by nanosecond high-voltage discharges (NPD, Chapter 4), where electrons are accelerated by an applied electric field and sustain the plasma via impact ionisation and excitation. In contrast, the systems considered in this chapter are *photon-driven*, where extreme-ultraviolet (EUV) photons around 13.5 nm ionise and excite the gas, and the resulting plasmas are sustained by photoelectrons and their secondary collisions rather than by an external discharge field. Later in the thesis, we will return to electrically driven plasmas in the form of DC glow and electron-beam sources (Chapter 6) and compare them directly with the EUV-induced cases discussed here.

EUV-induced plasmas are directly relevant to EUV lithography, where tin-based EUV sources operate in low-pressure H_2/N_2 ambients and where both plasma chemistry and surface modification are critical. Here we use optical emission spectroscopy (OES) to characterise EUV-driven plasmas in such scanner-relevant environments, with particular emphasis on how their rotational, vibrational, and electronic excitation differs from the discharge plasmas studied earlier.

Two complementary platforms are used. The first is the EBL2 EUV beamline facility at TNO (Delft, The Netherlands), which provides a controlled EUV exposure environment based on a Sn-fuelled laser-triggered discharge-produced plasma source with in-situ diagnostics. The second is the OLT-TS 2.5 research exposure tool at ASML, derived from the scanner source concept and operated under production-like H_2 conditions. Across these tools, we analyse molecular nitrogen emission (Second Positive System, First Negative System), hydrogen Fulcher-α bands, and atomic Balmer lines, and we use the time evolution of selected emission lines as an optical proxy for the EUV pulse timing.

The chapter is organised as follows. Section 5.1 introduces EBL2 and presents EUV-induced plasma results in pure N_2, pure H_2, and H_2/N_2 mixtures, including SPS/FNS diagnostics, Fulcher-α analysis, Balmer-

population studies, and pulse reconstruction. Section 5.1.7 highlights the use of N_2^+ FNS as an impurity tracer in H_2. The subsequent OLT-TS section reports Fulcher-α diagnostics and Balmer-based pulse reconstructions under scanner-like source conditions, providing a bridge between the controlled beamline environment of EBL2 and an industrially derived exposure tool.

5.1 EBL2: EUV beamline facility for plasma spectroscopy

The EBL2 (EUV Beam Line 2) facility, operated by TNO at the Van Leeuwenhoek Laboratory in Delft, is a unique exposure platform for extreme ultraviolet (EUV) radiation under semiconductor industry-relevant conditions. Developed in collaboration with industry partners such as Ushio Inc. and ASML, it enables EUV-induced plasma experiments with well-controlled and reproducible radiation conditions, making it highly suitable for investigating fundamental processes such as photoionization, photodissociation, and secondary electron-driven excitation in gases like N_2, H_2, and their mixtures [53,54]. A more detailed description of the EBL2 geometry, source, and diagnostic layout is provided in Appendix B.

Unlike electrical discharges, where electrons are energized directly by an external field, EUV-induced plasmas are driven by photoabsorption. Photons in the 13.5 nm band (92 eV) ionize and excite gas molecules and atoms, triggering cascades of secondary electron collisions. The resulting plasmas are highly transient (few µs lifetime), spatially localized to the beam footprint, and strongly dependent on gas species and pressure [15, 17, 18]. EBL2 allows for precise control over these parameters, providing a well-characterized environment to isolate photon-driven plasma behavior [53].

The source of EUV radiation in EBL2 is a Sn-fuelled laser-triggered discharge-produced plasma (LDP) developed by Ushio. A focused laser pulse pre-ionizes a tin vapour plume between rotating Sn-coated electrodes; a subsequent high-current discharge pulse drives and pinches the plasma, producing in-band EUV radiation at 13.5 nm (2% spectral bandwidth, hereafter abbreviated BW) [55–57]. A dual-mirror grazing-incidence collector then images the source into an intermediate focus and relays the beam to the sample plane, allowing control of spot size and dose via the focus setting and repetition rate [53, 54].

Importantly, EBL2 integrates in-situ diagnostics for beam profiling and exposure monitoring, as well as a connected X-ray Photoelectron Spectroscopy (XPS) system for surface analysis. The ability to expose samples in gas environments with precise pressure control, and to analyze them without breaking vacuum, makes EBL2 uniquely suited to study EUV-induced plasmas in conditions analogous to those encountered in EUV lithography tools [58].

5.1.1 N_2 Second Positive System

The SPS of N_2 ($C\,^3\Pi_u \rightarrow B\,^3\Pi_g$, $\Delta\nu = -2$ window with 0–2, 1–3, 2–4) was analysed at 1, 2, and 5 Pa using the same PGOPHER-based workflow introduced in Chapter 3 (band synthesis, instrumental-function convolution, response correction). Figure 5.1 shows a representative time-resolved spectrum and fit at 5 Pa.

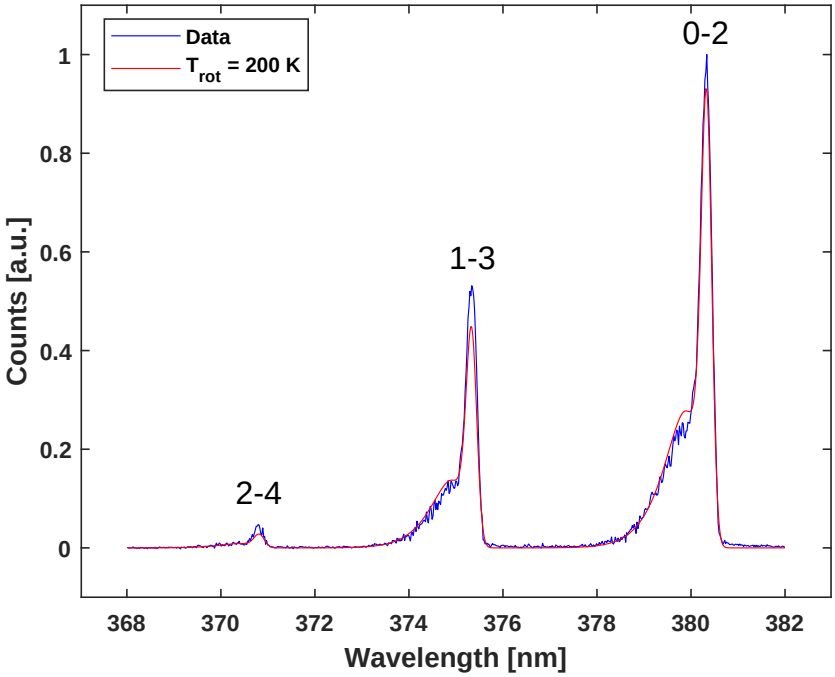

Figure 5.1: Time-resolved SPS spectrum of N_2 at 5 Pa (blue) and best-fit simulation (red) using the Chapter 3 workflow. The retrieved T_{rot} is ∼200 K and the fit underestimates the observed envelope in parts of the band head/wing, evidencing the "under-thermal" rotational structure characteristic of EBL2.

In sharp contrast to NPD (Chapter 4) and EBR (Chapter 6), **the best-fit SPS envelopes at EBL2 are systematically "under-thermal"**: the retrieved rotational temperature is well below room temperature (typically ∼200 K) and the simulated rotational envelope does not fully reproduce the experimental band head/wing balance. This behaviour is observed *both* in time-resolved gated series and in *integrated* spectra, indicating that it is not a gating artefact. For the integrated measurements, spectra were accumulated with an integration time of 5 μs; the corresponding integrated spectrum and fit at 5 Pa are shown in Fig. 5.2.

We emphasise that the fitting pipeline itself is validated on NPD (5 Pa) and EBR, where the same workflow yields stable fits and physically plausible T_{rot}, in line with collisional–radiative modelling of low-pressure nitrogen discharges and afterglows [3, 59]. The EBL2 outcome therefore points to differences in excitation/relaxation pathways specific to EUV-driven N_2 excitation at very low pressure (photoionization, photoelectron cascades, rapid

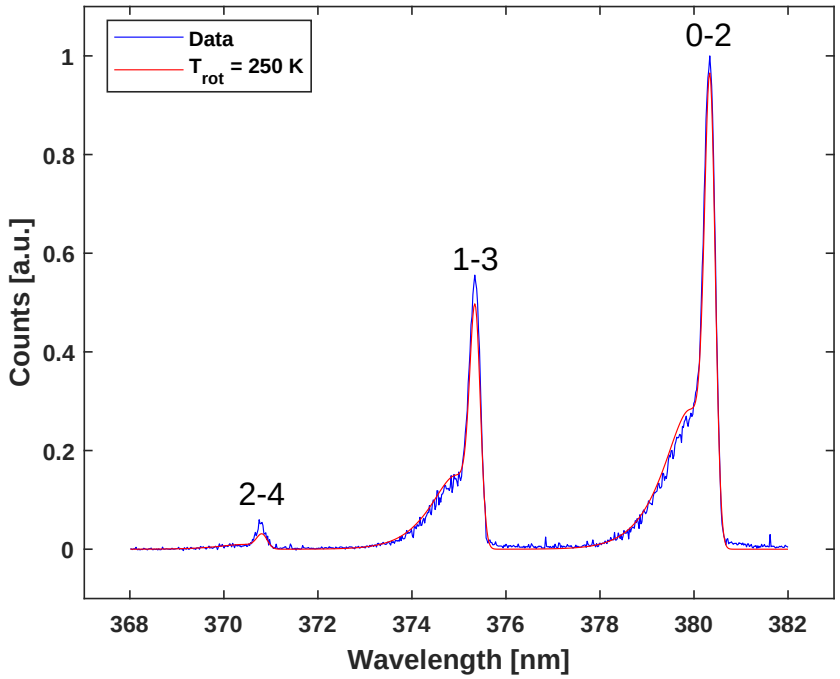

Figure 5.2: Integrated SPS spectrum at 5 Pa (blue) with best-fit model (red), accumulated with an integration time of 5 μs. The same under-thermal behaviour is present in integrated data, ruling out a purely gating-related artefact. By comparison, NPD and EBR fits with the same pipeline (Ch. 4, 6) are well reproduced with plausible T_{rot}.

quenching, and limited rotational randomisation of the SPS upper state). To our knowledge, detailed literature on EUV-induced N_2 rotational envelopes is lacking; this under-thermal SPS is thus a key observation of this thesis and motivates follow-up campaigns and modelling.

Peak-maximum kinetics and EUV pulse proxy. To gain insight into how the photon-driven plasma builds up and decays with respect to the EUV light pulse, we use the time evolution of the SPS peak intensity as a simple optical timing marker. For each gate delay in a kinetic series (fixed gate width and time step), a full spectrum is recorded by the ICCD; from that spectrum we extract the maximum intensity within the SPS window and plot this *peak intensity* versus gate delay. This "peak-maximum" trace condenses the spectrally resolved SPS emission into a single number per gate while preserving the overall temporal evolution of the molecular light.

Figure 5.3 compares the SPS peak traces for 1, 2, and 5 Pa. In all three

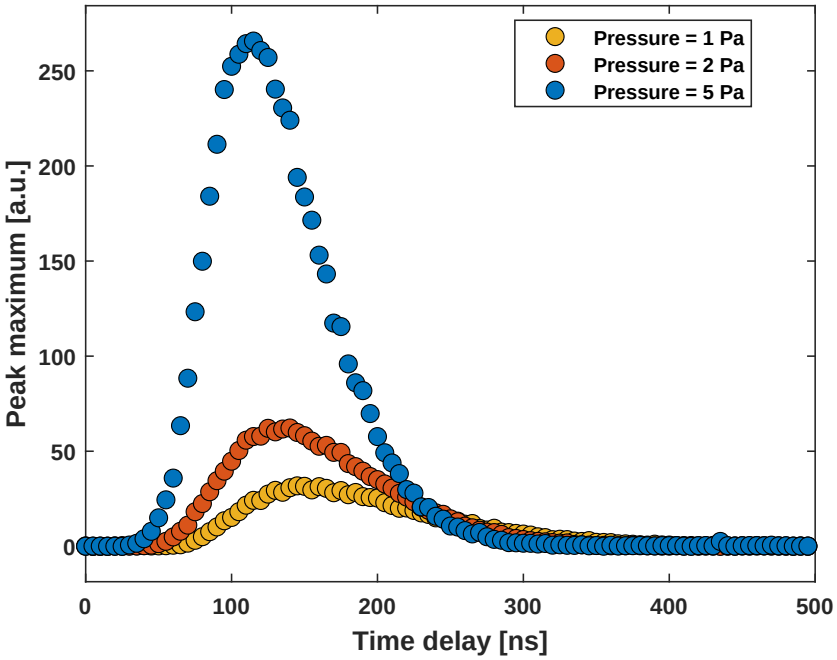

Figure 5.3: SPS peak intensity vs. time for 1, 2, and 5 Pa. Intensity scales down with pressure. A relative delay between pressure sets is visible; because runs were taken separately, a contribution from trigger timing differences cannot be excluded.

cases the SPS light is collected with the same optical chain (same line-of-sight, spectrograph, and ICCD settings) and recorded as a gated time series; only the background gas pressure is changed between runs. The EUV pulse itself is measured independently with a fast photodiode, using the same external trigger as for the ICCD. As expected, the absolute SPS intensity decreases with decreasing pressure. A noticeable *relative shift* of the peak positions is also observed between the pressure sets. At our present level of control we cannot determine whether these shifts are mainly due to a genuine pressure dependence of the SPS build-up/decay, or to small systematic effects in the timing synchronisation (e.g. fixed offsets or run-to-run jitter between the external trigger, the EUV source, and the ICCD gate). We therefore treat this as an unresolved uncertainty rather than as a robust pressure trend.

Figure 5.4 overlays the *normalised* SPS peak traces with the EUV photodiode pulse. The SPS envelope is broader and lags the EUV rise, which

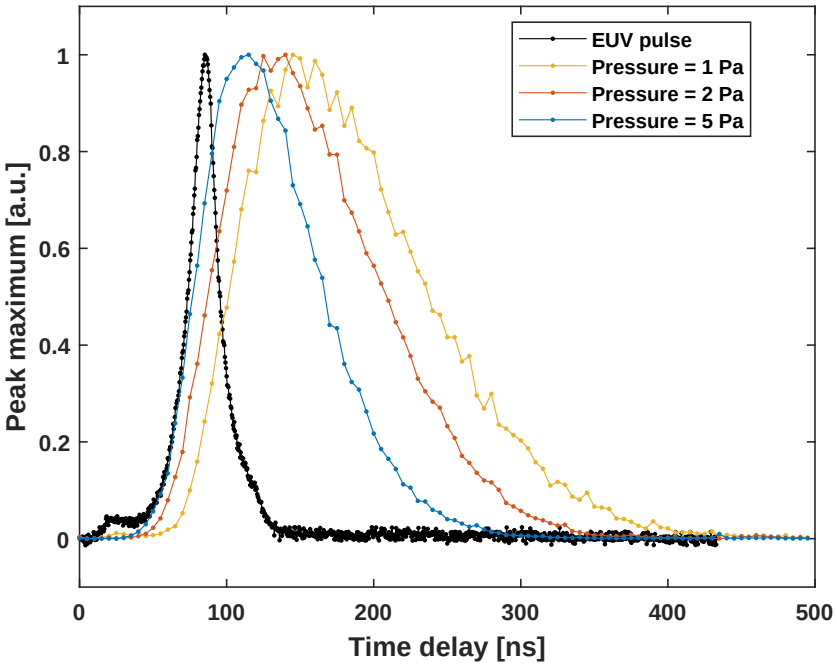

Figure 5.4: Normalised SPS peak traces compared to the EUV detector signal. The time axis is referenced to the common external trigger used for both measurements; no additional per-pressure shifts are applied. The SPS response is broader and delayed relative to the EUV pulse, reflecting the collisional–radiative build-up of the molecular emission driven by photoelectrons. Small horizontal offsets between the different pressures are comparable to the trigger/gating uncertainty and are not interpreted quantitatively.

is consistent with SPS formation via secondary electrons and molecular kinetics rather than being a direct, prompt proxy of the EUV pulse itself. In all traces, the time axis is referenced to the common external trigger that starts both the EUV photodiode acquisition and the ICCD gate sequence; no additional per-pressure time shifts are applied. Small horizontal offsets between the SPS peaks at 1, 2, and 5 Pa are therefore comparable to the combined timing uncertainty set by the gate width, the step size, and the trigger jitter. Within this "few–tens of nanoseconds" uncertainty, we do not regard the ordering of the maxima as a reliable pressure-dependent trend: in principle a higher pressure would be expected to shorten the characteristic excitation time through increased collision rates, but with the present timing resolution this cannot be demonstrated unambiguously. A more detailed block diagram of the timing electronics and detector gating, together with quantitative estimates of the timing uncertainty, is provided in the dedicated EBL2 appendix and underpins this interpretation.

5.1.2 N_2^+ First Negative System

The FNS of N_2^+ ($B\,^2\Sigma_u^+ \rightarrow X\,^2\Sigma_g^+$, $\Delta\nu = 0$) exhibits a similar pattern at EBL2. Figure 5.5 shows a representative time-resolved spectrum and fit at 5 Pa.

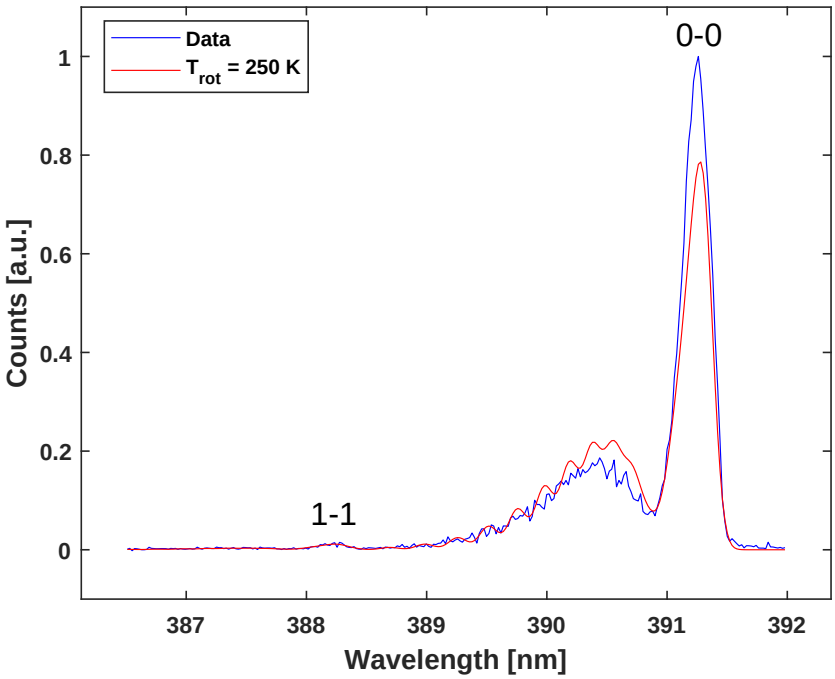

Figure 5.5: Time-resolved N_2^+ FNS spectrum at 5 Pa (blue) and best-fit model (red). The fit suggests an under-thermal T_{rot} and the simulated envelope does not fully reproduce the experimental band head/wing balance, unlike the well-behaved NPD/EBR benchmarks.

As for SPS, the fits converge but the *apparent* rotational structure is again under-thermal (T_{rot} ∼200 K) and the model does not reproduce the envelope with the fidelity observed on NPD and EBR. The effect is weaker than for SPS but remains systematic in both gated and integrated data, indicating that it is not a time-gating artefact. For the integrated measurements, spectra were accumulated with an integration time of 5 μs; the corresponding integrated spectrum and fit at 5 Pa are shown in Fig. 5.6.

We thus interpret the FNS outcome as another manifestation of EUV-specific excitation/relaxation channels at very low pressure (prompt ion formation by photoionization, fast electron-impact excitation, and incomplete rotational thermalisation of the $N_2^+(B)$ upper state before radiative decay), leading to a sub-thermal rotational distribution analogous to what is inferred for $N_2(C)$ from the SPS analysis.

Peak-maximum kinetics and EUV pulse proxy. Peak intensity traces for 1, 2, and 5 Pa are shown in Fig. 5.7; intensity decreases with pressure as expected. Figure 5.8 compares the *normalised* FNS peaks to the EUV

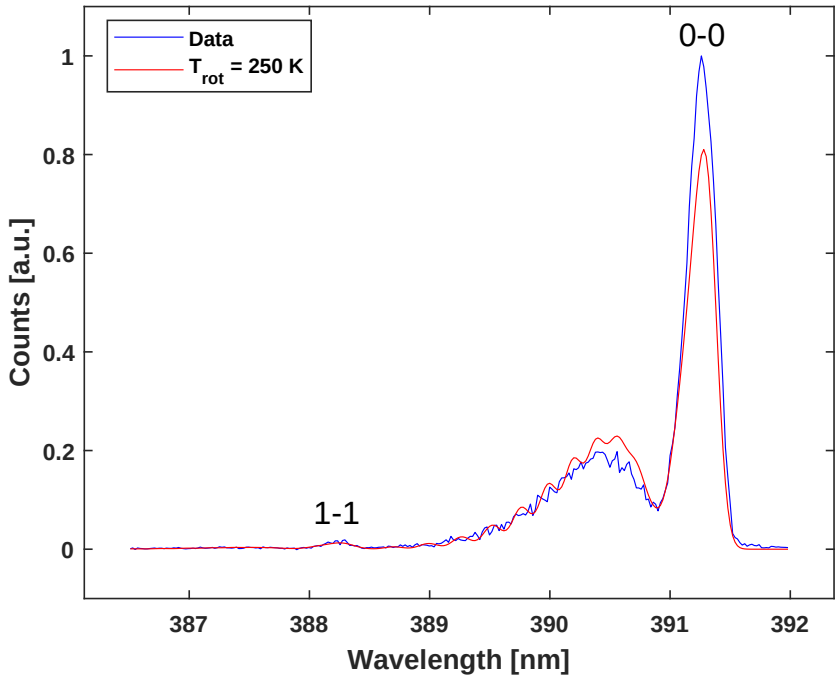

Figure 5.6: Integrated FNS spectrum at 5 Pa (blue) with best-fit model (red), accumulated with an integration time of 5 μs. The under-thermal envelope persists in integrated data, pointing to EUV-driven kinetics rather than to time-gating artefacts.

detector signal. As with SPS, the FNS response is broader than the EUV pulse, consistent with ion-band emission being governed by fast but not instantaneous collisional–radiative processes seeded by the EUV photon burst. In addition to the build-up dynamics, the finite radiative lifetimes of the relevant upper states already imply a response that is intrinsically longer than the EUV pulse: under low-pressure conditions, $\tau_{\mathrm{rad}}\big(\mathrm{N}_2^+(B\,^2\Sigma_u^+)\big) \approx 67$ ns and $\tau_{\mathrm{rad}}\big(\mathrm{N}_2(C\,^3\Pi_u)\big) \approx 41$–$43$ ns, depending on the vibrational level [60]. Collisional quenching further reduces the effective lifetimes according to

$$\tau_{\mathrm{eff}}^{-1} = \tau_{\mathrm{rad}}^{-1} + \sum_q k_q\, n_q,$$

where k_q is the quenching rate coefficient for collider species q and n_q its number density. At higher pressures the quenching term can dominate, shortening the decay relative to the purely radiative values, whereas at the few-pascal conditions of EBL2 the additional term remains relatively small and the effective lifetime is still of the order of several tens of nanoseconds. Any small inter-run delay offsets between the FNS peak and the EUV photodiode signal may also contain a contribution from trigger and gating differences, as discussed above for SPS.

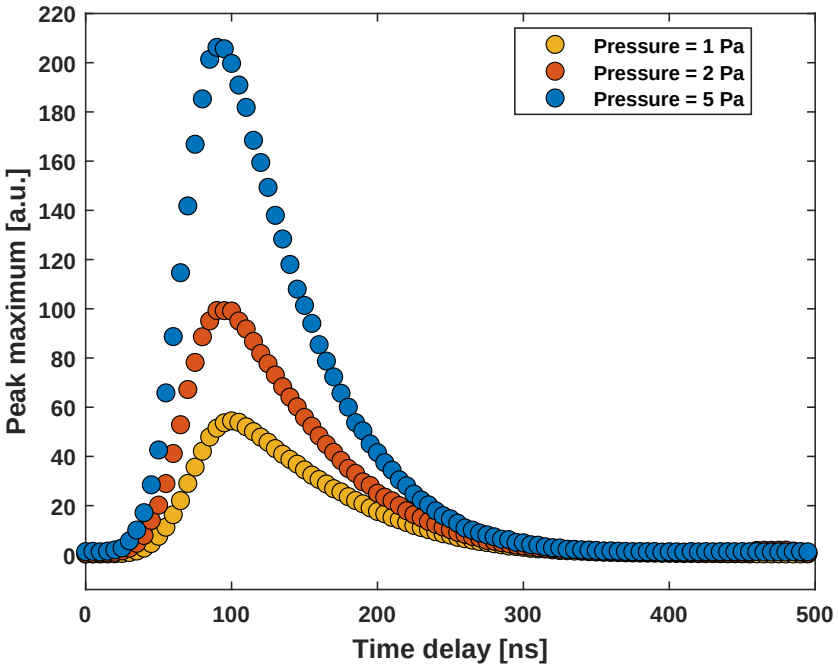

Figure 5.7: FNS peak intensity vs. time at 1, 2, and 5 Pa. The absolute level scales with pressure. Small relative time shifts between traces may contain a contribution from run-to-run trigger offsets.

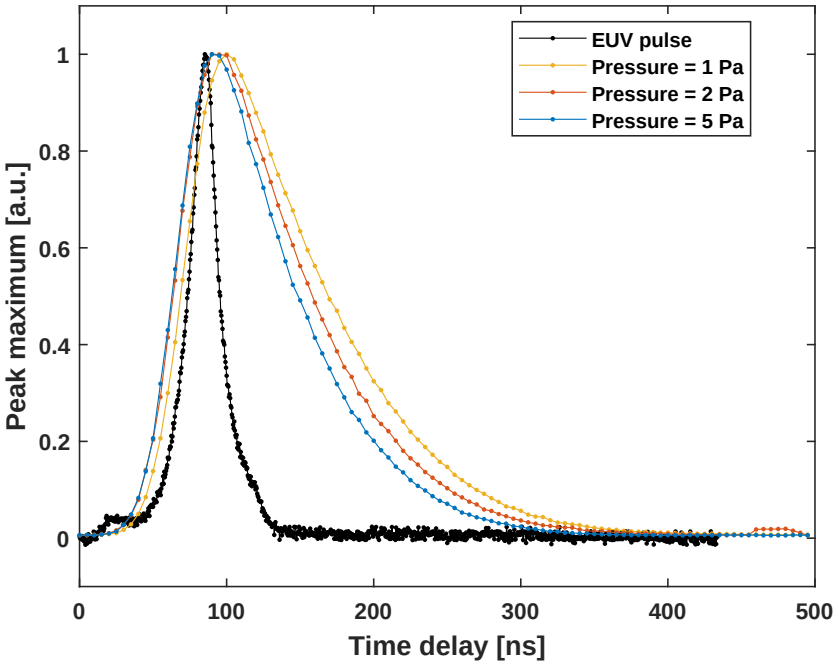

Figure 5.8: Normalised FNS peaks compared to the EUV detector pulse. The ion-band response is broader and slightly delayed relative to EUV, as expected from collisional–radiative formation following photoionization and secondary-electron excitation.

5.1.3 Atomic nitrogen emission

Atomic N emission was monitored in two spectral regions. First, an isolated N I line at 648.27 nm, listed in the NIST Atomic Spectra Database [61], lying close to Hα. This line was recorded both for EUV-induced plasmas at EBL2 and for nanosecond-pulsed discharges (NPD). Because it was not subjected to the same systematic analysis as the Balmer and molecular systems, it is not discussed further in this thesis; we simply note its presence as an additional potential diagnostic for future work.

Second, and central to the discussion here, we analyse the prominent N I triplet in the near-infrared, around 746 nm. This triplet consists of three closely spaced lines at 742.364, 744.229, and 746.831 nm, corresponding to the allowed transitions

$$\mathrm{N}\big(3p\,^4S^\circ_{3/2}\big) \;\rightarrow\; \mathrm{N}\big(3s\,^4P_J\big)\,, \qquad J = \tfrac{1}{2}, \tfrac{3}{2}, \tfrac{5}{2},$$

which are a standard diagnostic feature in nitrogen-containing plasmas. In the analysis we either treat the three components individually or use their summed intensity (after deblending) as a single "atomic-N" proxy.

In the same spectral window we also observe molecular emission from the N_2 First Positive System (FPS), which corresponds to the

$$\mathrm{N_2}\big(\mathrm{B}^3\Pi_g\big) \;\rightarrow\; \mathrm{N_2}\big(\mathrm{A}^3\Sigma^+_u\big)$$

transition. The FPS forms a structured band system in the red/near-infrared, with multiple overlapping vibrational bands. Under our EUV-induced plasma conditions at a few pascal, the recorded FPS emission appears as a relatively broad molecular band with partially resolved structure, on top of which the narrow atomic N I triplet is superimposed. An example spectrum of this region, showing the atomic triplet together with the FPS band emission, is reported in Figure 5.9. In the present work we do not perform a quantitative FPS analysis; it is used mainly as a reference molecular background when discussing the timing of the atomic-N emission.

The upper level $\mathrm{N}(3p\,^4S^\circ_{3/2})$ has a natural radiative lifetime of order 10^2 ns. Time-resolved laser-spectroscopy and time-resolved LIBS measurements report lifetimes in the range $\sim$ 70–200 ns for the $3p\,^4S^\circ_{3/2} \rightarrow 3s\,^4P_J$ multiplet, depending on J and the specific transition [62, 63]. These values are comparable in magnitude to the 41–43 ns and 67 ns lifetimes of $N_2(C^3\Pi_u)$ and $N_2^+(B^2\Sigma_u^+)$ discussed above [60]. At the few-pascal pressures considered here, collisional quenching is weak, so the effective decay time of the atomic-N emission is expected to remain close to this natural lifetime, apart from modest distortions due to transport of the emitting species and line-of-sight averaging in the optical collection. As for the molecular systems, an effective lifetime

$$\tau_{\mathrm{eff}} \;=\; \frac{1}{A + k_q n_q}$$

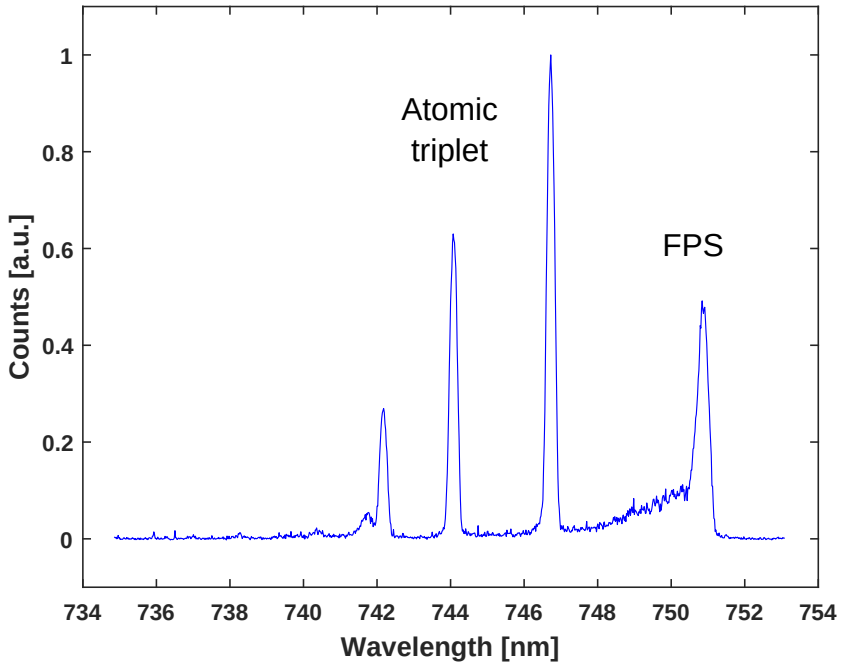

Figure 5.9: Example spectrum in the near-infrared window at EBL2, showing the atomic N I triplet near 746 nm (narrow lines) superimposed on the broader N_2 First Positive System (FPS, $B^3\Pi_g \rightarrow A^3\Sigma_u^+$) band emission.

can be defined, where A is the Einstein coefficient for spontaneous emission, k_q is the net collisional quenching rate coefficient, and n_q is the density of quenching partners (here dominated by N_2 and H_2). Under our low-pressure conditions $k_q n_q \ll A$, so $\tau_{\text{eff}} \approx 1/A$ and radiative decay dominates.

Unlike SPS and FNS, the *timing* of the atomic lines more closely follows the *leading edge* of the EUV pulse: their peak-maximum traces rise rapidly and track the EUV onset better than the molecular features (although the decay still extends longer than the EUV pulse). This behaviour is consistent with the higher excitation thresholds of the atomic lines: the $3p\,^4S^\circ_{3/2} \rightarrow 3s\,^4P_J$ multiplet around 742–747 nm is populated from excited states with threshold energies of $\sim$ 11.8–12 eV [64], which favours direct electron-impact excitation from the ground state and from low-lying levels by the prompt photoelectron population. In contrast, the molecular systems (SPS, FNS, FPS) are fed more strongly by stepwise, metastable-assisted, and recombination pathways, which naturally broaden and delay their temporal response relative to the EUV pulse.

Figure 5.10 shows the pressure series (1, 2, 5 Pa) for the atomic-N triplet. Figure 5.11 overlays the *normalised* atomic peaks with the EUV detector signal, highlighting the relatively sharp rise compared to SPS/FNS. Finally, Fig. 5.12 compares atomic-N and the *simultaneously recorded* FPS molecular emission in the same camera window: the FPS onset is visibly delayed and its decay slightly longer than the atomic line, consistent with its predominantly molecular, lower-threshold excitation pathways.

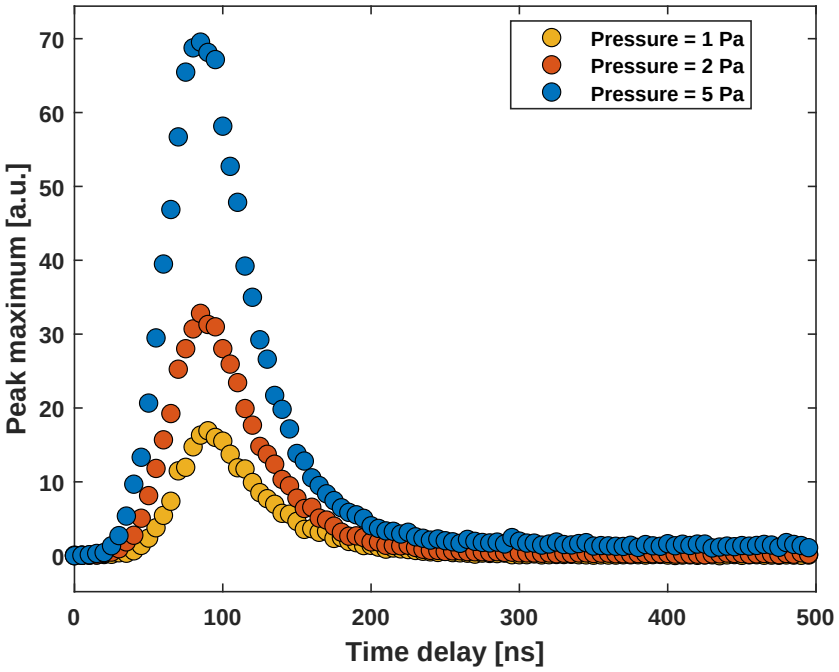

Figure 5.10: Atomic-N peak intensity vs. time for 1, 2, and 5 Pa. Intensity decreases with pressure. The rise is sharper than for SPS/FNS, indicating a closer link to prompt photoelectron-driven excitation.

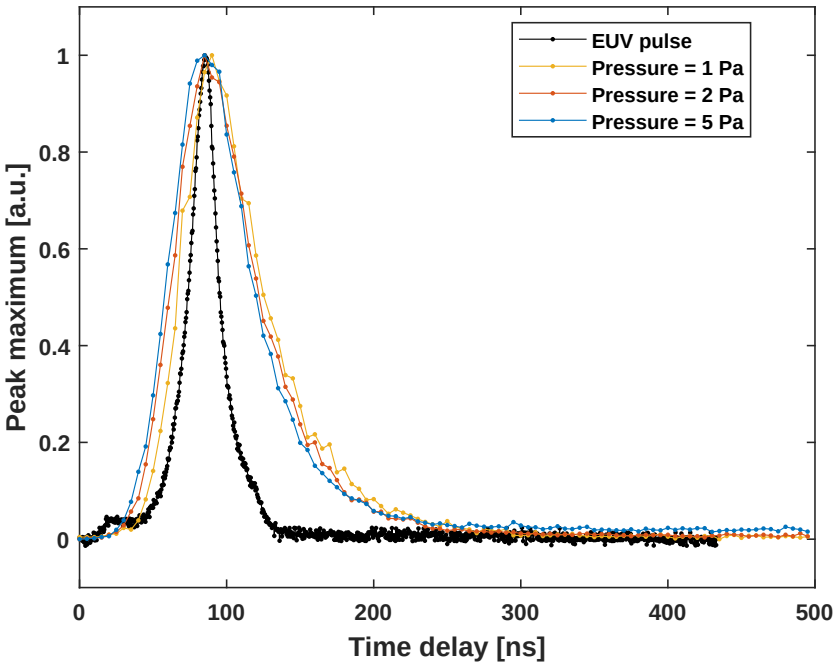

Figure 5.11: Normalised atomic-N peak compared to the EUV detector pulse. The atomic emission follows the leading edge more closely than SPS/FNS, but its decay still exceeds the EUV pulse width due to collisional–radiative relaxation.

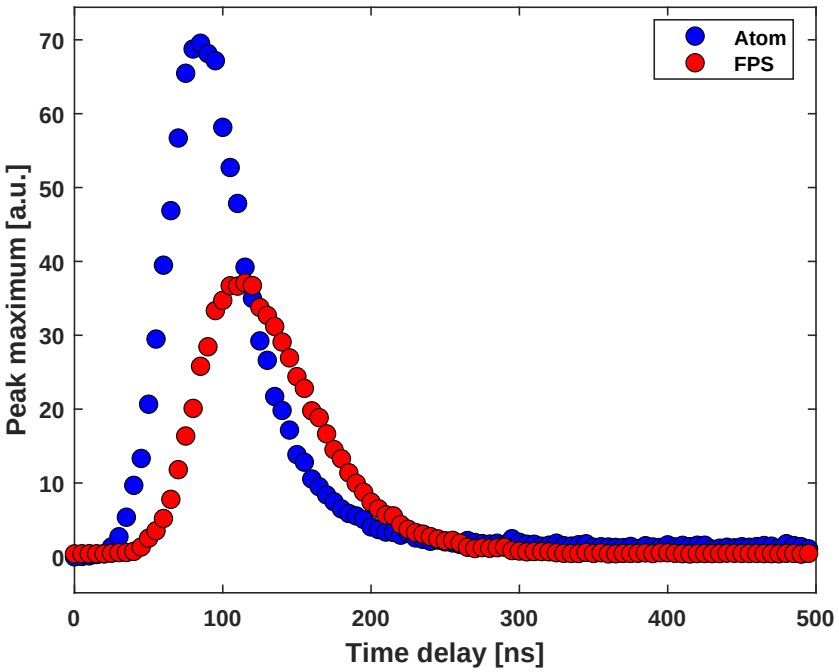

Figure 5.12: Simultaneous atomic-N vs. FPS (molecular) peak traces from the same camera window. The FPS onset is delayed and its decay slightly longer relative to the atomic line, consistent with molecular formation pathways and lower-threshold excitation.

5.1.4 Fulcher band emission

Under EUV excitation in low-pressure H_2, the Fulcher-α system ($d\,^3\Pi_u \rightarrow a\,^3\Sigma_g^+$, 590–650 nm) provides a sensitive probe of the ground-state rotational distribution via the Q-branch of the $d\,^3\Pi_u^-$ component. At EBL2, we recorded the 600–635 nm window in *integration mode* with a 5 μs exposure time per spectrum, and analysed the diagonal bands $v' = v'' = 0 \ldots 3$ by fitting the $Q_1(N' = 1, 2, 3)$ lines with Gaussians of width constrained by the instrumental function (Chapter 3.4). The controlled environment at EBL2 (no additional metrology or diagnostic light sources, such as ellipsometer illumination, coupled into the OES line-of-sight) yielded clean baselines across the entire window, allowing robust band sums and rovibrational fits.

Figure 5.13 shows a representative spectrum with the fit regions. The absence of baseline artifacts at the short-wavelength edge (contrast with OLT-TS in a later chapter) enables consistent response-corrected areas across all diagonal bands.

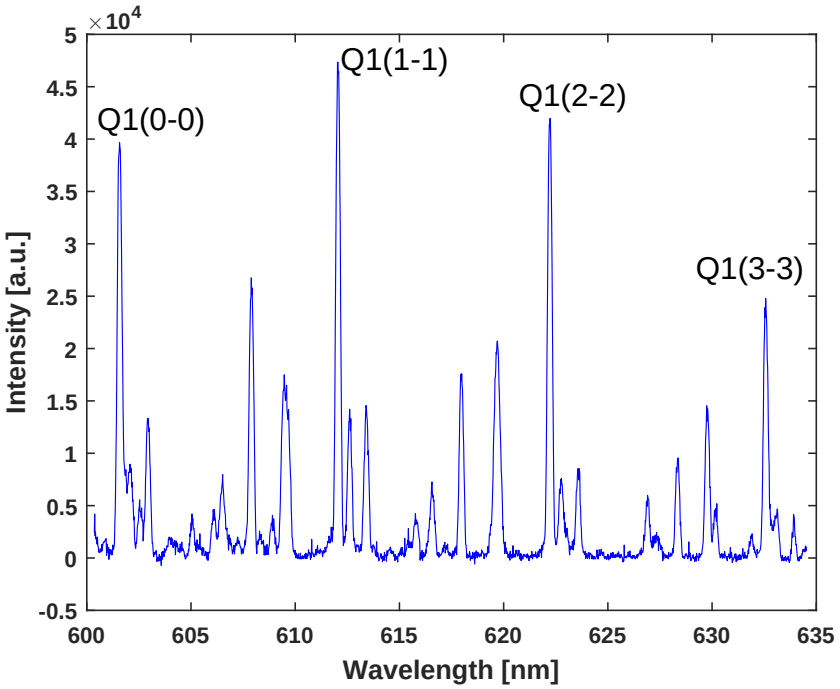

Figure 5.13: Representative Fulcher-α spectrum at EBL2 in H_2 ($\sim$ 5 Pa unless noted), recorded in integration mode. A flat baseline across 600–635 nm facilitates accurate band sums and rovibrational analysis.

Example single-line fits for two sets of bands are displayed in Fig. 5.14. The constrained widths and small residuals confirm that the instrumental calibration transfers reliably to the EBL2 optical chain and that the Q_1 lines are well resolved at our spectral resolution.

From the response-corrected line areas of the $Q_1(N' = 1, 2, 3)$ lines for $v' = 0 \ldots 3$, we construct rotational Boltzmann plots (Fig. 5.15) following the procedure detailed in Section 3.4. The resulting $T_{\mathrm{rot}}(d, v')$ values are low

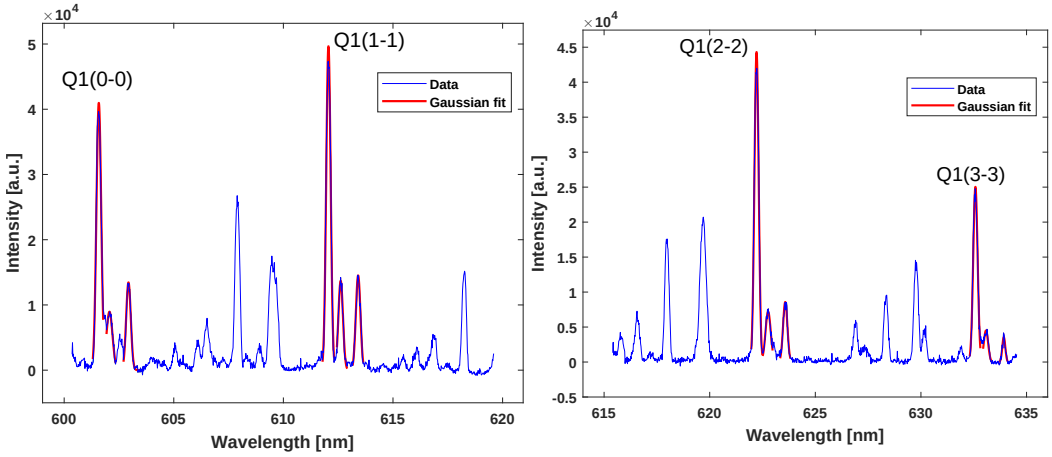

(a) Fits for $v' = 0, 1$

(b) Fits for $v' = 2, 3$

Figure 5.14: Gaussian fits to $Q_1(N' = 1, 2, 3)$ lines of the Fulcher-α Q-branch at EBL2. Line widths are bound by the instrumental function; residuals are low, indicating stable and consistent response correction.

— often below room temperature — and tend to decrease with increasing v'. This is physically plausible for the *excited* $d\,^3\Pi_u$ state, which is populated primarily by electron-impact excitation from the ground state and by radiative cascades from higher triplet levels: under our low-pressure conditions, the d-state lifetime is short and rotational re-thermalisation with the gas is incomplete, so its rotational distribution does not have to coincide with the gas temperature. Using the rotational-constant ratio in Eq. (3.19), the corresponding ground-state rotational (gas) temperature is $\approx 2 \times T_{\mathrm{rot}}(d, v')$ and therefore remains above room temperature under the EBL2 conditions.

Figure 5.16 presents the Franck–Condon–corrected vibrational populations $f_X(v)$ ($v = 0 \ldots 3$) projected to the ground state. In contrast to measurements with baseline artifacts on other platforms, the EBL2 populations follow the same qualitative behaviour as in the NPD Fulcher analysis (Section 4.9.1) and as will be reported later for EBR: a rise towards $v = 2$ followed by a decrease, similar to envelopes obtained in collisional–radiative modelling of low-pressure hydrogen plasmas [65]. We deliberately refrain from assigning a vibrational temperature T_v because a validated collisional–radiative model for EUV-driven H_2 is not yet available. Ongoing collaborations on kinetics modelling are expected to clarify the implications for T_v and to constrain electron density and temperature (n_e, T_e) consistent with the Fulcher and Balmer observables.

Fulcher-α Q-branch data processing. For completeness, we summarise here the relations used to derive $T_{\mathrm{rot}}(d, v')$ and T_{gas} from the Fulcher-α Q-branch line areas (see also Eqs. (3.18) and (3.19) in Chapter 3).

For each diagonal band $v' = v''$, we measure the response- and baseline-corrected line area $\varepsilon^{v',N'}$ of the $Q_1(N')$ line, which is proportional to the emissivity of the transition from the upper level (v', N'). In the optically thin

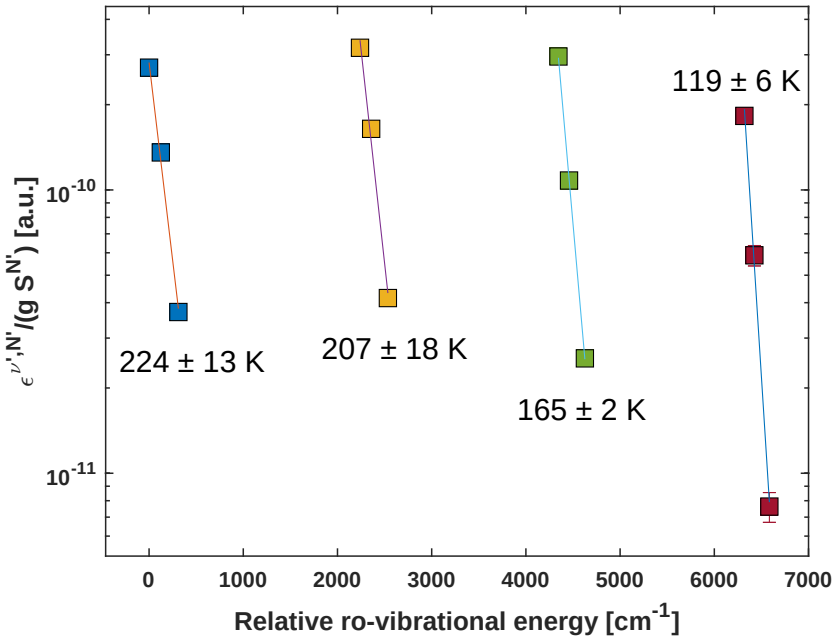

Figure 5.15: Rotational Boltzmann plots for the $d\,^3\Pi_u^-$ state at EBL2, using $Q_1(N' = 1, 2, 3)$ for $v' = 0 \ldots 3$. The slopes yield $T_{\mathrm{rot}}(d, v')$, which are low and show a mild decrease with v'. Using Eq. (3.19), the corresponding ground-state (gas) temperature is $\sim 2 \times T_{\mathrm{rot}}(d)$, remaining above room temperature.

limit, this emissivity is proportional to the population $n^{v',N'}$ of the upper level multiplied by the appropriate spectroscopic factors. Using the Hönl–London factor $S^{N'}$ and the rotational degeneracy $2N' + 1$, we can write

$$\varepsilon^{v',N'} \;\propto\; \frac{S^{N'}}{2N' + 1}\, n^{v',N'}, \tag{5.1}$$

which simply states that, once the known line-strength and degeneracy factors are taken out, the measured line area tracks the upper-state population $n^{v',N'}$.

Within a given vibrational manifold v' of the $d\,^3\Pi_u^-$ state, we assume that the rotational sublevels are Boltzmann-distributed at a temperature $T_{\mathrm{rot}}(d, v')$. Defining the rotational energy offset with respect to the reference level $N' = 1$ as

$$\Delta E_{\mathrm{rot}}(N') \;\equiv\; E_{\mathrm{rot}}(N') - E_{\mathrm{rot}}(1) \;\geq 0, \tag{5.2}$$

the relative population of level N' can then be written as

$$\frac{n^{v',N'}}{n^{v',1}} \;\propto\; g\,(2N' + 1)\, \exp\!\left[-\frac{\Delta E_{\mathrm{rot}}(N')}{k_B\, T_{\mathrm{rot}}(d, v')}\right], \tag{5.3}$$

where g is the (constant) spin-statistical factor for the manifold and $2N' + 1$ again accounts for the rotational degeneracy. Equation (5.3) expresses the

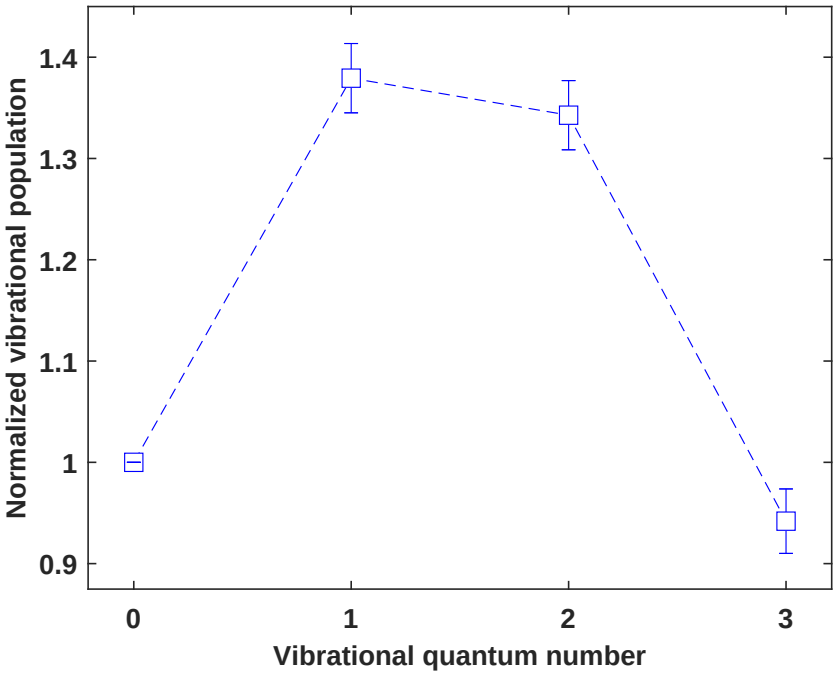

Figure 5.16: Franck–Condon–corrected ground-state vibrational populations $f_X(v)$ ($v = 0 \ldots 3$) inferred from Fulcher-α diagonal bands at EBL2. The trend (peak near $v = 2$) mirrors the behaviour found in the NPD chapter and is consistent with later results at EBR. No vibrational temperature is quoted pending a dedicated EUV–H_2 collisional–radiative model.

usual Boltzmann decrease of the population with increasing rotational energy, relative to the reference level $N' = 1$.

Combining Eqs. (5.1) and (5.3) and eliminating the (unknown) proportionality constants yields the working expression for the rotational Boltzmann plot:

$$\ln\left[\frac{\varepsilon^{v',N'}}{g\,S^{N'}}\right] \;=\; -\frac{\Delta E_{\mathrm{rot}}(N')}{k_B\,T_{\mathrm{rot}}(d,v')} \;+\; \text{const.} \tag{5.4}$$

By plotting $\ln\!\left[\varepsilon^{v',N'}/(g\,S^{N'})\right]$ as a function of $\Delta E_{\mathrm{rot}}(N')$ for $N' = 1, 2, 3$, we obtain a straight line whose slope is $-1/(k_B T_{\mathrm{rot}}(d,v'))$. The intercept absorbs all remaining calibration and normalisation factors and is not needed to determine $T_{\mathrm{rot}}(d,v')$.

To relate the excited-state rotational temperature to the gas temperature, we use the ratio of effective rotational constants for the ground and excited states. Denoting by $B_\nu(X,\nu=0)$ the rotational constant of the ground state $X\,{}^1\Sigma_g^+$ at $\nu = 0$ and by $B_\nu(d,\nu')$ that of the $d\,{}^3\Pi_u^-$ state at the vibrational level v', we write

$$T_{\mathrm{gas}} \;=\; T_{\mathrm{rot}}\!\left(X\,{}^1\Sigma_g^+, \nu=0\right) \;=\; \frac{B_\nu\!\left(X\,{}^1\Sigma_g^+,\,\nu=0\right)}{B_\nu(d\,{}^3\Pi_u^-,\,\nu')}\,T_{\mathrm{rot}}\!\left(d\,{}^3\Pi_u^-,\,\nu'\right). \tag{5.5}$$

This relation assumes that excitation to the d state is approximately sudden and does not strongly reshuffle the rotational distribution, so that the shape

of the rotational manifold in $d\,^3\Pi_u^-$ reflects that of the ground state up to the scaling factor given by the ratio of rotational constants.

In practice, we fit Gaussian profiles to the $Q_1(N' = 1, 2, 3)$ lines for each $v' = 0 \ldots 3$, use Eq. (5.4) to construct the rotational Boltzmann plot and extract $T_{\mathrm{rot}}(d, v')$, and finally project to T_{gas} using the rotational-constant ratio above. Since the spectral resolution and S/N at EBL2 do not robustly constrain higher N' or $v' \geq 4$, we restrict the fits to $N' = 1$–3 and avoid two-slope ("hot tail") or full-manifold extrapolations.

5.1.5 Balmer-series populations: non-Boltzmann behaviour

For the EUV-induced hydrogen plasma at EBL2, the atomic Balmer lines (Hα–Hϵ) were analysed with the same processing chain used for the nanosecond-pulsed discharge (NPD) case: baseline subtraction, spectral-response correction, Gaussian fitting of each line, and construction of relative upper-level populations from the line-integrated intensities. For each transition $u \to l$ we form

$$S_u \equiv \frac{I_{ul}\,\lambda_{ul}}{A_{ul}\,g_u}, \tag{5.6}$$

where I_{ul} is the fitted line area, λ_{ul} the wavelength, A_{ul} the Einstein coefficient and $g_u = 2n^2$ the degeneracy of the upper level. The resulting S_u values are then normalised to Hα ($n = 3$),

$$N_u = \frac{S_u}{S_{n=3}}, \tag{5.7}$$

with uncertainties propagated from the Gaussian-fit errors on the individual line integrals.

If the Balmer manifold were close to Boltzmann among itself, these normalised populations would satisfy

$$\ln N_u = -\frac{\Delta E_u}{k_B T_{\mathrm{exc}}} + \mathrm{const}, \tag{5.8}$$

where $\Delta E_u = E_u - E_{n=3}$ is the excitation energy of the upper level relative to Hα, and a straight-line fit of $\ln N_u$ versus ΔE_u would yield an effective excitation temperature T_{exc}, as done for the NPD case in Chapter 4.

Figure 5.17 shows the corresponding Boltzmann plot for the EBL2 hydrogen plasma. Each point represents a normalised population N_u for $n = 3 \ldots 7$ with propagated error bars.

The last point in Fig. 5.17, corresponding to Hϵ, exhibits a noticeably larger error bar than the lower-n lines. This is not a purely statistical effect but reflects the more complicated spectral environment around Hϵ in the EBL2 configuration. As discussed in the introductory description of the EUV setup (tin source and optics), the Hϵ line lies on top of a broad

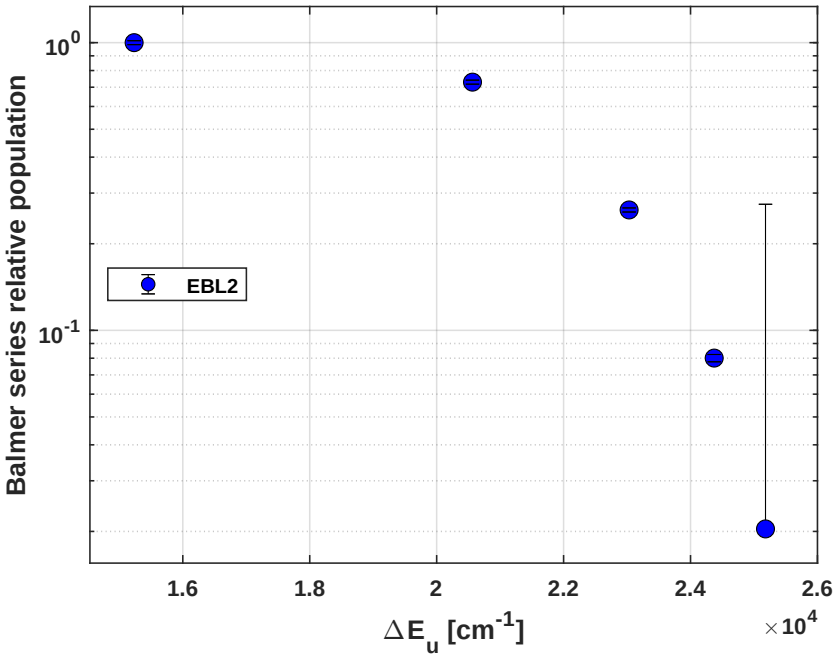

Figure 5.17: Balmer Boltzmann plot for the EUV-induced hydrogen plasma at EBL2. Normalised populations N_u for Hα–Hϵ are plotted versus upper-level excitation energy ΔE_u (referenced to $n = 3$), with error bars from the Gaussian-fit uncertainties. The systematic curvature and level-to-level deviations demonstrate that the Balmer manifold is *not* Boltzmann-distributed in this case.

tin-related background generated by scattered light directly from the EUV source. In practice, the Hϵ feature has to be fitted together with an additional double-Lorentzian component that models this tin-induced baseline. The strong correlation between the Balmer Gaussian and the overlapping Lorentzians inflates the formal uncertainty on the extracted Hϵ area, which propagates into a large error bar on the corresponding population N_u. This point, therefore, carries little statistical weight in any weighted fit and should be interpreted with caution.

Even ignoring Hϵ, however, the remaining Balmer points do *not* align on a straight line: the higher-n levels are over- or under-populated relative to any single-slope trend, and the deviations are much larger than the statistical error bars. Forcing a linear fit would therefore produce an arbitrary "T_{exc}" that strongly depends on which subset of lines is chosen and has no clear physical meaning. In line with the discussion in Chapter 2, we therefore do *not* assign an excitation temperature from the EBL2 Balmer data.

Physically, this non-Boltzmann behaviour is consistent with the EUV-driven formation mechanism: photoionisation and subsequent recombination, stepwise excitation from excited states, and radiative cascades populate the Balmer levels via multiple channels, with insufficient collisional redistribution to enforce Boltzmann equilibrium within the manifold [3,17]. In this regime, the Balmer series primarily provides qualitative information (e.g. relative

line strengths and trends between sources), while quantitative temperature diagnostics rely on the molecular systems (Fulcher-α, N_2 SPS/FNS) and collisional–radiative reasoning.

The same analysis applied to the EBR data (Chapter 6) yields similarly curved, non-linear Boltzmann plots, confirming that a single T_{exc} cannot be meaningfully defined for the Balmer series in the EUV-induced plasmas considered here. For both EBL2 and EBR, Balmer-based excitation temperatures are therefore *not* used; instead, those plots serve as a visual demonstration of the non-equilibrium character of the atomic hydrogen manifold.

5.1.6 EUV pulse reconstruction from time-resolved Balmer emission

To proxy the EUV temporal profile with optical emission, we recorded gated time series of the Balmer lines Hα, Hβ, and Hγ in pure H_2 at the EBL2 working pressure (of order a few pascal, typically $\sim$5 Pa). For each gate delay, the peak line intensity was extracted from the spectrum and plotted as a function of time. This "peak-maximum" trace is not an EUV detector signal; rather, it reflects the collisional–radiative response of the hydrogen plasma seeded by the EUV-driven photoelectrons. As such, it generally *overestimates* the true pulse width: the rise tracks the build-up of excited populations, and the decay includes afterglow kinetics and finite radiative lifetimes.

Figure 5.18 shows representative Hα, Hβ, and Hγ peak traces versus gate delay. The three lines differ in absolute intensity, as expected from their transition probabilities and detector response, but more importantly, they display slightly different decay behaviour. Hβ and Hγ are very similar in shape and nearly overlap over the full time range. Hα reaches a comparable peak but then decays *faster immediately after the maximum*, so that, beyond the peak region, its curve lies below the Hβ/Hγ traces while following a similar overall trend. Within the timing resolution set by the ICCD gate (2 ns) and the overall timing uncertainty from trigger distribution and jitter (of order 5 ns), the onset of emission is the same for all three Balmer lines; the main difference resides in this line-dependent early decay.

To compare directly with the source timing, Fig. 5.19 overlays the *normalised* Hα, Hβ, and Hγ peak traces with the EBL2 EUV photodiode signal. The EUV pulse is substantially narrower (tens of ns) and rises earlier; the Balmer emission trails the EUV onset but follows it relatively closely on the *leading edge*. The decay of all three Balmer lines is markedly longer than the EUV pulse due to afterglow kinetics (recombination, cascading, and continuing excitation by residual secondaries). The modest line-to-line differences seen in Fig. 5.18 (faster early decay of Hα vs. Hβ/Hγ) persist in this overlay but do not alter the overall picture: among the nitrogen and hydrogen features analysed in this chapter, the atomic Balmer lines provide the closest

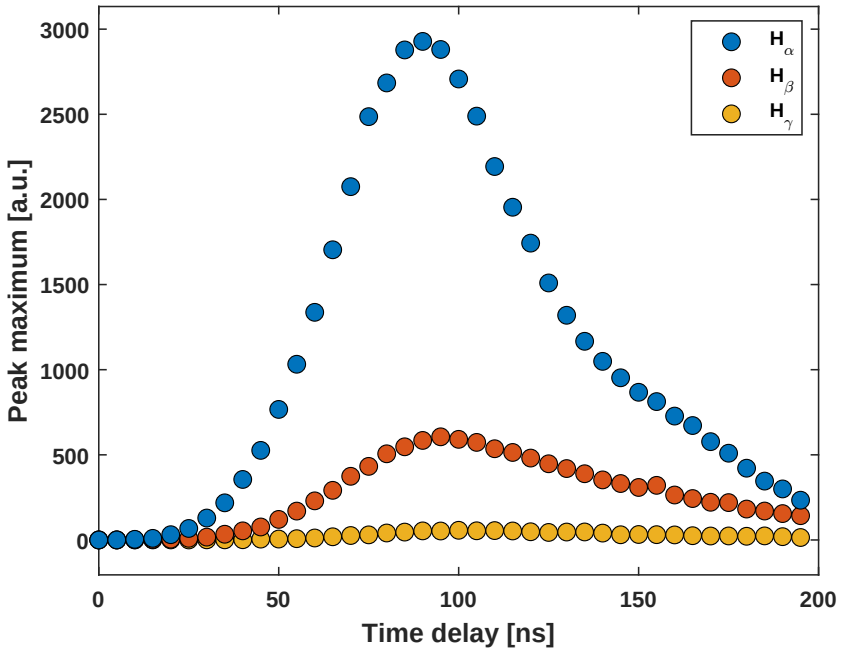

Figure 5.18: Peak-maximum traces of Hα, Hβ, and Hγ versus gate delay for EUV-induced H_2 plasma at the EBL2 working pressure (few pascal). Hβ and Hγ exhibit almost identical temporal evolution, whereas Hα decays faster immediately after its maximum and then remains below the other two while following a similar overall shape.

optical proxy to the EUV timing on the rising edge—consistent with their higher excitation thresholds and strong linkage to prompt electron-impact channels—while still overestimating the true pulse width on the falling edge.

Notes. (i) The finite ICCD gate width temporally convolves the OES response and broadens the apparent pulse; (ii) small timing mismatches between the source trigger and the detector gate can shift the absolute time axis by a few nanoseconds; (iii) absolute EUV timing and pulse width should be taken from the photodiode, while OES excels at highlighting relative changes in rise time, afterglow, and line-to-line behaviour.

5.1.7 Nitrogen/hydrogen gas mixture

To assess the sensitivity of OES as a non-invasive impurity monitor for scanner-relevant ambients, we recorded FNS spectra in H_2 at 5 Pa with trace of N_2. The FNS bands remain detectable down to $\sim 10^{-6}$ mbar partial pressure of N_2 (and likely into the 10^{-7} mbar decade with further optimisation), demonstrating promising diagnostic sensitivity without intrusive probes. Figure 5.20 shows the measured spectra for decreasing N_2 partial pressure. While N_2/H_2 plasma chemistry and ammonia formation have been extensively studied in both catalytic and purely plasma reactor configurations [66–70], here we exploit the FNS purely as a spectroscopic impurity

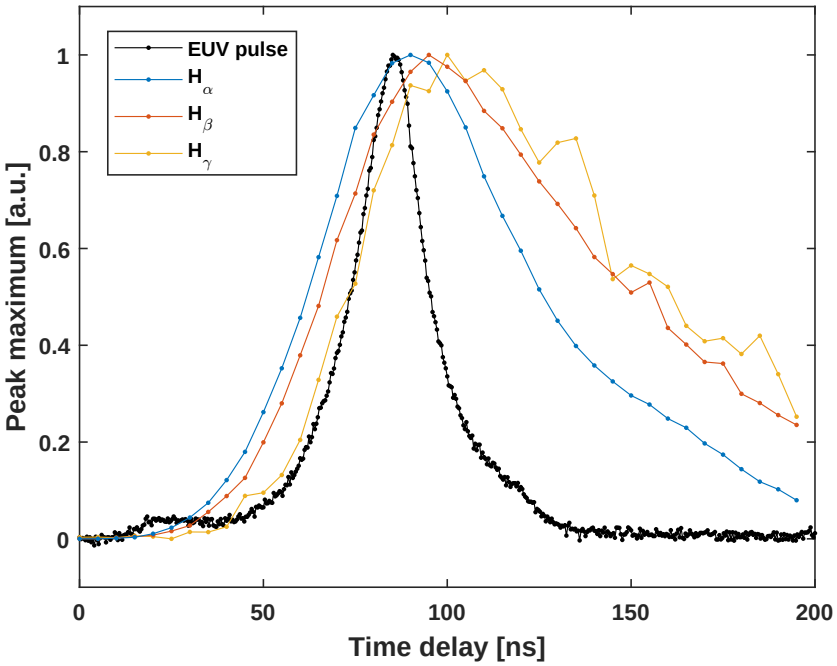

Figure 5.19: Normalised Hα, Hβ, and Hγ peak-maximum traces compared with the EBL2 EUV photodiode pulse. The EUV pulse is shorter and leads the OES response; Balmer emission tracks the leading edge relatively well but decays more slowly due to collisional–radiative afterglow. Small differences between Hα and Hβ/Hγ reflect line-dependent excitation and decay pathways.

tracer in an EUV-driven environment.

Beyond FNS, the *broad* (350–700 nm) spectra taken for context show multiple spectral lines attributable to Sn (source material) as a background. Intriguingly, several narrow features overlapping the FNS long-wavelength tail and others near ∼386 nm are *not* listed in common databases for tin in this region. While a full line-identification campaign is beyond scope here, these features are consistent with Sn emission leaking into the detection path (stray/scattered light or plasma sidebands) and may represent *previously unreported* Sn lines in this spectral range. Follow-up measurements with higher-resolution spectrometers and line-identification tools are warranted.

Summary of nitrogen results at EBL2. Taken together, the nitrogen measurements at EBL2 reveal a consistent picture of EUV-driven N_2 kinetics at very low pressure. First, SPS and FNS fits at 1–5 Pa are systematically under-thermal ($T_{\mathrm{rot}} \sim 200$ K) and not perfectly reproduced by the model, both in gated and in integrated spectra. This behaviour stands in clear contrast to NPD and EBR, where the same analysis workflow performs reliably, and thus points to an intrinsic feature of the excitation and relaxation pathways specific to EUV-driven N_2.

In the time domain, the peak-maximum traces show that all molecular channels (SPS, FNS, FPS) are broader and slightly delayed with respect to

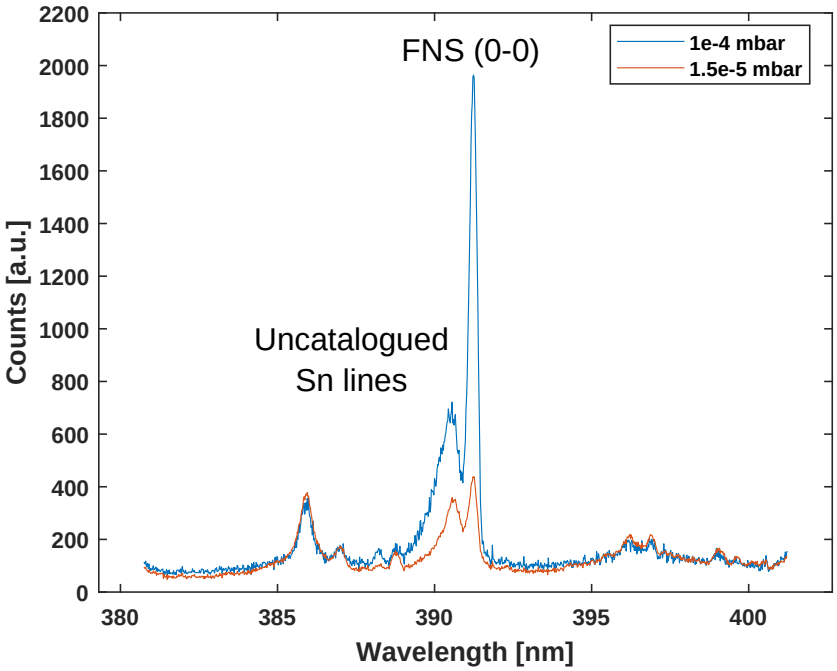

Figure 5.20: FNS spectra in 5 Pa H_2 with trace of N_2. The N_2^+ bands remain detectable down to $\sim 10^{-6}$ mbar N_2 (with prospects for 10^{-7} mbar). Additional narrow features coincident with the FNS tail and near 386 nm are consistent with Sn emission; several are not catalogued in standard databases for this region, suggesting candidates for new Sn lines pending dedicated identification.

the EUV photodiode signal, whereas the atomic-N triplet tracks the EUV rise much more closely, in line with its higher-threshold, more direct excitation by prompt photoelectrons. Finally, in H_2 with trace of N_2, the N_2^+ FNS bands remain detectable down to $\sim 10^{-6}$ mbar N_2, demonstrating the usefulness of FNS as a sensitive, non-invasive impurity monitor. In the same spectra, additional narrow features likely associated with Sn are observed—some not catalogued in this wavelength range—providing candidates for targeted high-resolution spectroscopy and line identification in future work.

5.2 OLT-TS

The OLT-TS 2.5 platform is a research exposure tool derived from the EUV scanner source concept: a tin LPP source images into an intermediate focus (IF) in a low-pressure hydrogen ambient, but without the full projection optics and mirrors of a lithography machine (see the schematic drawing C.1 in Appendix C). In this configuration, the chamber is used primarily for sample exposures and methodological studies. All measurements reported here were conducted in the ASML cleanroom under standard tool operating conditions with ~ 5 Pa H_2 (the reference pressure used throughout the thesis).

Measurement context and constraints. We did not have dedicated beamtime on OLT-TS. Instead, we carried out passive optical emission spectroscopy (OES) opportunistically during customer-oriented or development exposures. As a result, we had no authority to vary pressures, gas mixtures, or timing sequences, and measurement windows were short and often on short notice. Within these constraints, we recorded time-resolved Balmer-line emission (at least Hα and Hβ) and time-integrated molecular emission from the H_2 Fulcher-α system. The analysis workflow (instrument function, response correction, Gaussian line fitting, and rovibrational post-processing) follows the methodology established in section 3.4 and in Appendix C, enabling comparison to the EBL2 and EBR data sets.

A further practical limitation during several OLT sessions was the simultaneous operation of an ellipsometer. Its illumination introduced a broadband offset on the OES baseline. Despite efforts to remove this contribution, a residual baseline distortion remained at the short-wavelength edge of our Fulcher window (600–605 nm), which impacts band-summed quantities and, in particular, the inferred v-population ratios. Where relevant, we qualify these effects below and interpret trends with appropriate caution.

5.2.1 Fulcher band emission

We recorded the prominent portion of the Fulcher-α system ($d\,^3\Pi_u \rightarrow a\,^3\Sigma_g^+$) between 600 and 635 nm in *integration mode* (no ICCD gating) due to the low molecular signal under scanner-like EUV excitation. As in the other facilities, the analysis focuses on the Q-branch of the $d\,^3\Pi_u^-$ component for the diagonal bands $v' = v'' = 0 \ldots 3$: individual $Q_1(N' = 1, 2, 3)$ lines are fitted with Gaussians using the previously calibrated instrumental width, line areas are corrected by the spectral response $C(\lambda)$, and rovibrational parameters are derived from Boltzmann plots restricted to $N' = 1$–3 (Eq. (3.18)). Gas temperature estimates follow the standard back-projection via rotational-constant ratios (Eq. (3.19)). Because the SNR and resolution at OLT do not allow robust constraints at higher N' or $v' \geq 4$, no two-slope ("hot tail") fits or full-manifold modelling were attempted.

Figure 5.21 shows a representative spectrum in the 600–635 nm range.

A raised baseline is evident near 600–605 nm; this is attributed to the ellipsometer illumination present during the exposure and is not intrinsic to the plasma emission.

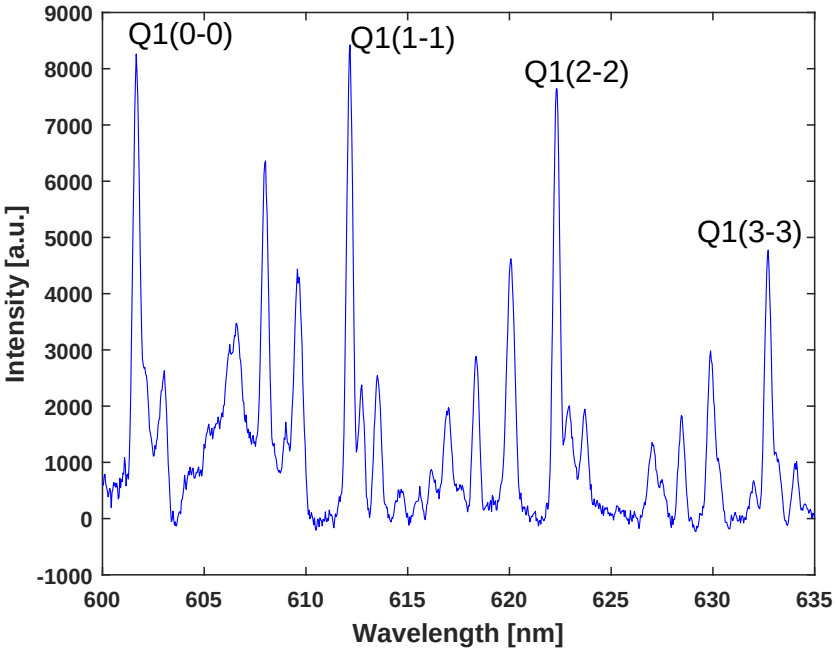

Figure 5.21: Representative OLT-TS Fulcher-α spectrum in H_2 at ~ 5 Pa, recorded in integration mode. A residual baseline uplift is visible near 600–605 nm, attributed to concurrent ellipsometer illumination; this mainly impacts band-summed quantities and v-population ratios.

The single-line fits for two bands are illustrated in Fig. 5.22; the constrained widths indicate that the instrumental function and response correction carried over consistently to the OLT configuration.

From the response-corrected line areas, we construct rotational Boltzmann plots per v' (Fig. 5.23). The retrieved $T_{\mathrm{rot}}(d, v')$ values are low — often below room temperature — and decrease mildly with increasing v', in line with our findings on EBL2 and EBR under similar low-pressure conditions. This outcome is physically consistent for the *excited* d state: using the rotational-constant ratio in Eq. (3.19), the ground-state rotational (gas) temperature is approximately a factor of ~ 2 larger, and therefore remains above room temperature.

Finally, Fig. 5.24 summarises the FC-corrected vibrational populations $f_X(v)$ projected to the ground state. Here the residual baseline uncertainty at the short-wavelength edge affects the balance between the $v' = 0$ and $v' = 1$ band sums, yielding a $v = 0{:}1$ ratio that deviates from NPD/EBL2/EBR trends; we therefore treat those two points as biased and focus on the qualitative envelope across $v = 0 \ldots 3$. Future campaigns without concurrent ellipsometer operation—and with time-resolved gating on the molecular window—should remove this ambiguity and enable a more comprehensive Fulcher analysis.

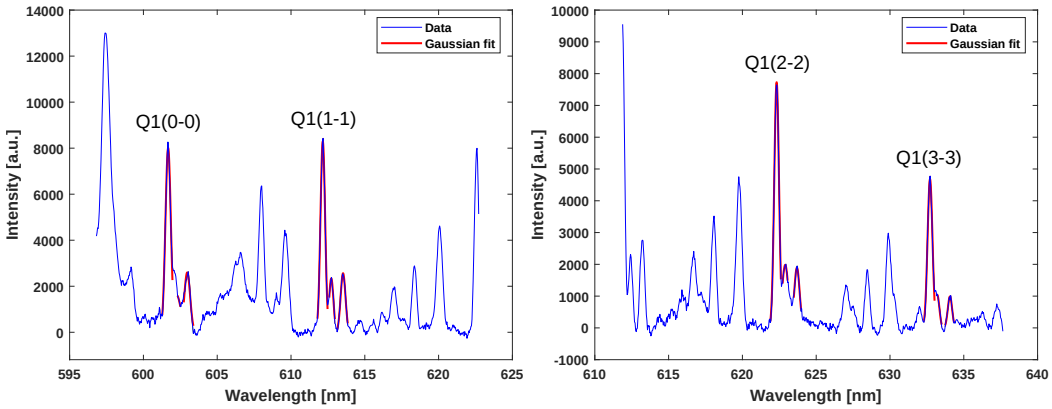

(a) Example fits for $v' = 0, 1$ **(b)** Example fits for $v' = 2, 3$

Figure 5.22: Gaussian fits to individual $Q_1(N' = 1, 2, 3)$ lines of the Fulcher-α Q-branch at OLT-TS. The line widths are constrained by the instrumental function measured off-line; residuals remain small, supporting consistent response correction in the OLT optical chain.

Summary and outlook. Under scanner-relevant H_2 conditions and with opportunistic access, OLT-TS Fulcher diagnostics reproduce the low $T_{\mathrm{rot}}(d)$ trends observed on other sources and support the standard back-projection to $T_{\mathrm{gas}} >$ room temperature. The principal limitation is a baseline artifact linked to concurrent ellipsometry, which perturbs v-population ratios at the short-wavelength edge. Dedicated sessions without auxiliary illumination—and, where feasible, gated measurements in the molecular window—are expected to remove this constraint and enable full-manifold Fulcher analysis.

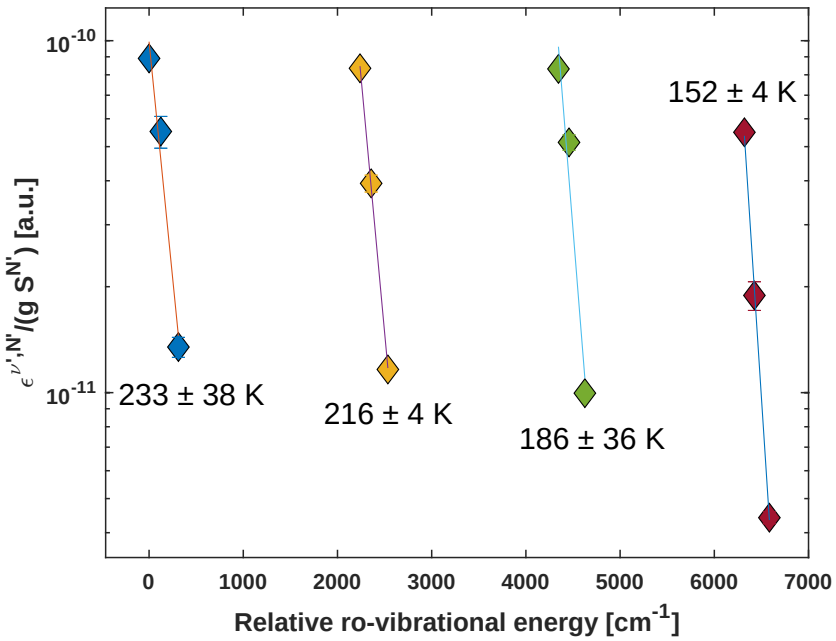

Figure 5.23: Rotational Boltzmann plots for the $d\,^3\Pi_u^-$ state, built from $Q_1(N' = 1, 2, 3)$ of $v' = 0 \ldots 3$. The fitted slopes yield $T_{\mathrm{rot}}(d, v')$, which are low (often below room temperature) and exhibit a weak decrease with v'. Via Eq. (3.19), the corresponding ground-state (gas) temperature is $\sim 2 \times T_{\mathrm{rot}}(d)$, and thus remains above room temperature, consistent with expectations at low pressure.

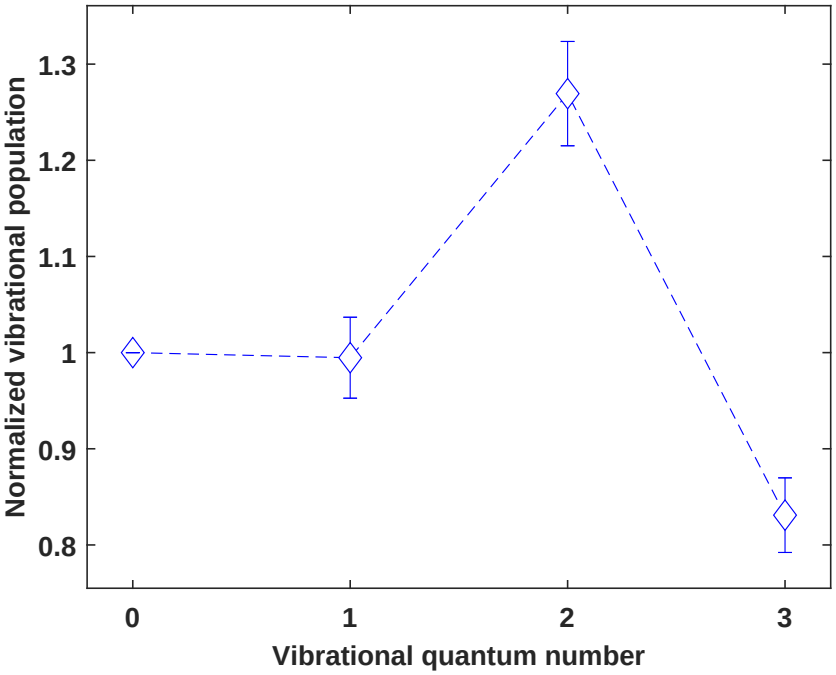

Figure 5.24: Franck–Condon–corrected vibrational populations $f_X(v)$ for $v = 0 \ldots 3$ projected to the ground state from the Fulcher-α bands. The anomalous $v = 0{:}1$ ratio relative to NPD/EBL2/EBR is attributed to a residual baseline offset at 600–605 nm during sessions with the ellipsometer active. Aside from this bias, the envelope across $v = 0 \ldots 3$ is consistent with low-density EUV-induced hydrogen plasmas.

5.2.2 EUV pulse reconstruction from time-resolved emission

To reconstruct the temporal profile of the EUV pulse, we performed time-resolved optical emission spectroscopy (OES) on the Hα line of the Balmer series using an iCCD gate of 10 ns unless otherwise noted. As described earlier in the thesis, we interpret the gate-integrated Hα emissivity as a time tag of the plasma formation and early decay associated with the EUV-generating discharge. The objective here is not to reproduce the exact impulse response of an EUV photodetector, but to obtain a sensitive proxy of the underlying plasma dynamics and source timing.

Figure 5.25 shows the Hα-based reconstruction on a linear scale. A notable feature is the appearance of a *double peak* rather than a single dominant maximum. In later beamtimes, this secondary peak was not observed; however, source settings and/or trigger timing may have changed between campaigns. We therefore attribute the double structure to differences in source conditions, rather than to an intrinsic property of Hα emission or to an artifact of the reconstruction. Importantly, this illustrates that the diagnostic is sufficiently sensitive to small variations in plasma creation and source pulse shape, which was one of the main design goals of the setup.

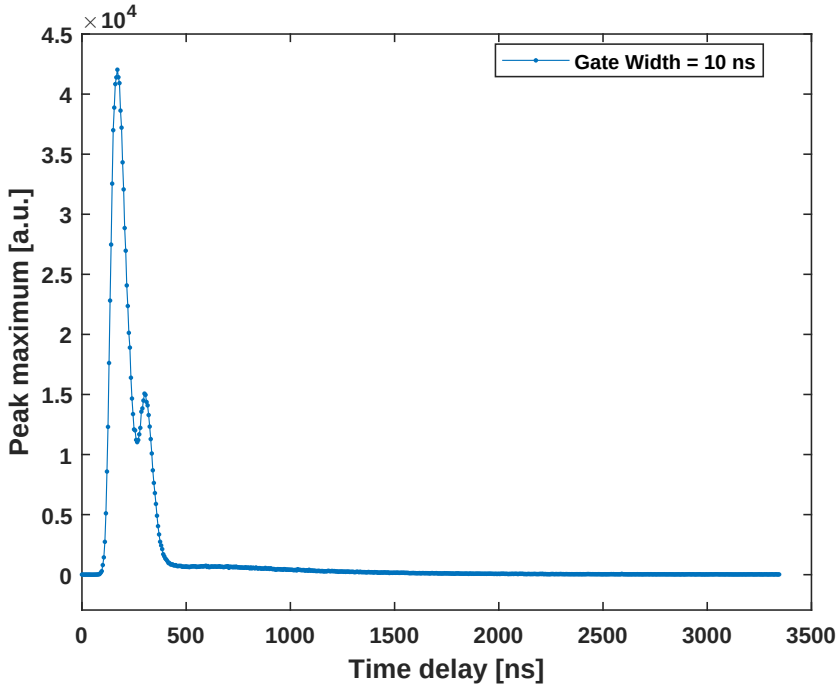

Figure 5.25: Hα-based EUV pulse reconstruction with 10 ns gate (linear scale). A double-peaked structure is observed in this beamtime, attributed to source/trigger conditions rather than an intrinsic effect. The method highlights sensitivity to small changes in plasma formation and source pulse shape.

The same dataset is shown in Fig. 5.26 on a logarithmic scale. The loga-

rithmic view reveals a long, low-level tail: the Hα signal does not immediately return to baseline but persists for hundreds of nanoseconds to microseconds after the main pulse. In extended scans up to the next cycle at 50 kHz (20 μs period), the signal eventually decays to background just before the following pulse; in those records, a weak pre-pulse preceding the main event is discernible, consistent with expectations for this type of source.

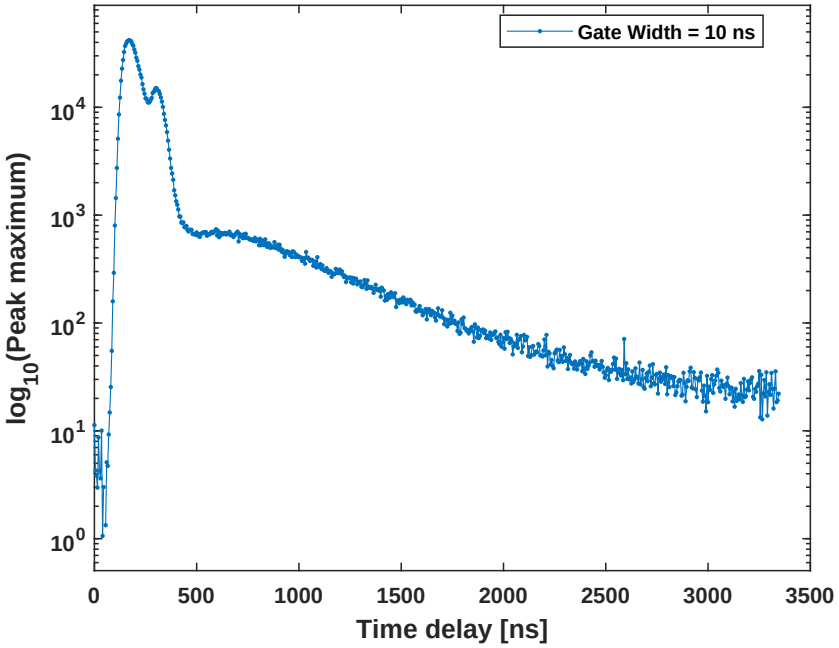

Figure 5.26: Same reconstruction as Fig. 5.25 on a logarithmic scale. The extended tail shows that Balmer emission persists for hundreds of nanoseconds to microseconds after the main pulse. In longer scans at 50 kHz (20 μs period), the signal returns to baseline just before the next pulse and a weak pre-pulse can be observed.

In Fig. 5.27, we overlay the Hα-based reconstruction from OLT-TS (Veldhoven) with a direct EUV detector measurement from an ASML source in San Diego. The Hα curve shown here uses *exactly the same data points* as in Figs. 5.25–5.26, but the time axis is restricted to the first $\sim$ 700 ns to highlight the detailed pulse shape around the main event. The EUV trace is narrow (a few tens of nanoseconds) with a sharp leading edge, whereas the OES-based profile is broader and smoother (and, in this dataset, shows the double peak discussed above). This difference is expected: line emission reflects collisional–radiative population dynamics, transport, and finite radiative lifetimes, and the finite gate width further convolves the true temporal profile. The Hα reconstruction should thus be read as a *plasma-dynamics proxy* rather than a one-to-one surrogate for an EUV photodiode signal.

Finally, Fig. 5.28 compares reconstructions built from Hα and Hβ when using a 50 ns gate (and overlays the earlier 10 ns series for reference). The Hα time-evolution has the same overall behavior at reduced temporal resolution, while Hβ reproduces the double-peak structure, confirming that it was not

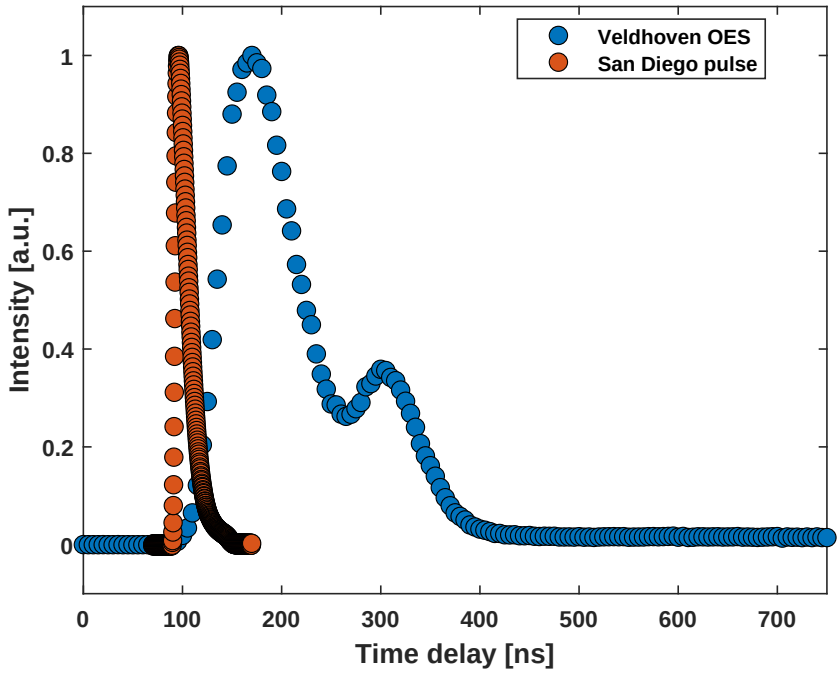

Figure 5.27: Comparison between the Hα-based reconstruction from OLT-TS in Veldhoven (blue; same data points as in Figs. 5.25–5.26, but shown only for the first $\sim$ 700 ns) and an EUV detector trace from the San Diego source (orange). The EUV pulse is only a few tens of nanoseconds long with a sharp rise, while the OES-based profile is broader and smoother (and in this dataset exhibits a double peak). Differences reflect collisional–radiative kinetics and the finite 10 ns gate.

a line-specific artifact of the Hα measurement. Differences in relative peak heights and in the late-time tail are consistent with line-dependent excitation pathways and optical-depth effects, combined with the broader 50 ns gating that smooths sharp features.

Limitations and outlook. The reconstructed profiles should be interpreted with some care. The finite iCCD gate width inevitably convolves the true temporal evolution and broadens sharp features, while small jitter between the source trigger and the detector gate introduces an uncertainty on the absolute time axis. On top of this instrumental contribution, the measured Hα and Hβ signals reflect the full collisional–radiative response of the plasma rather than the instantaneous EUV power: excitation, transport, and radiative decay all contribute to the observed pulse width and afterglow. For absolute EUV timing and amplitude, direct EUV detection therefore remains the reference, whereas OES is particularly well suited to track *relative* changes in pulse timing, shape, and late-time behaviour between different operating conditions or beamtimes.

Taken together, the OLT-TS measurements show that Balmer-line–based reconstructions provide a sensitive, non-intrusive handle on source dynamics under scanner-relevant H_2 conditions. Future campaigns with dedicated

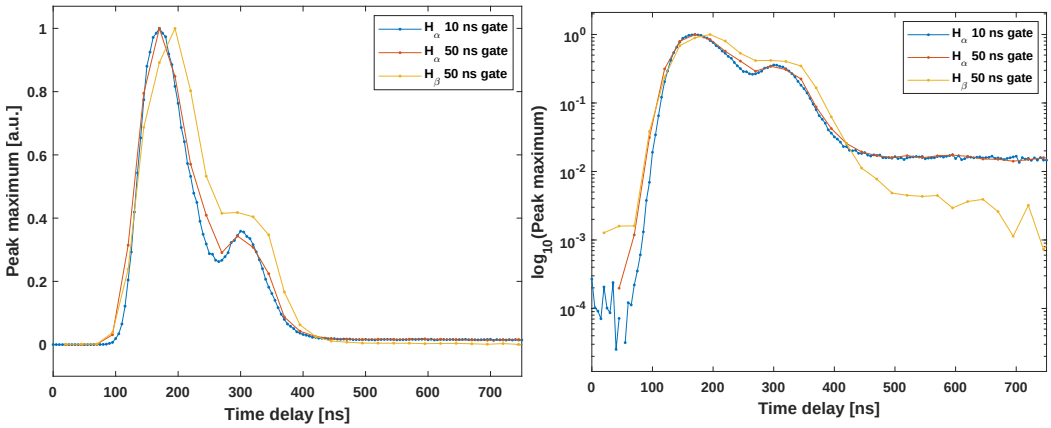

(a) Linear scale **(b)** Log scale

Figure 5.28: Pulse reconstructions from Balmer lines with 50 ns gate (Hα and Hβ), overlaid with the 10 ns series for reference. Hα retains its overall shape with reduced temporal resolution. Hβ shows the same double-peak structure, confirming that the feature was real and not a line-specific artifact; relative peak ratios and late-time decay differ due to line-dependent kinetics and optical depth, and due to the broader 50 ns gate.

access and simultaneous EUV and OES monitoring could further refine the timing analysis and exploit these diagnostics for routine source characterisation and stability studies.

Chapter 6

Electron Beam Radiation plasma

6.1 Introduction

This chapter presents the investigation of plasmas generated using Electron Beam Radiation (EBR), carried out at the TNO facility in the Netherlands. EBR is a non-thermal plasma generation method in which an energetic electron beam ionises a low-pressure gas [71]. The objective is to characterise the resulting optical emission using optical emission spectroscopy (OES) and to compare the EBR plasma with the nanosecond pulsed discharges (NPD) of Chapter 4 and the EUV-induced plasmas of Chapter 5, in a regime that is particularly well suited for collisional–radiative modelling [3].

Measurements were performed in pure nitrogen, pure hydrogen, and H_2/N_2 mixtures to enable direct comparison with the previous chapters. In the overall logic of this thesis, EBR provides a clean electron-impact benchmark: the plasma is driven by a known external, approximately monoenergetic electron source in the 0.5–2 keV range (see Appendix D and [72]), without an applied inter-electrode field or EUV photons, thereby helping to separate electron-impact kinetics from discharge-specific and photon-driven effects.

6.2 Plasma formation and operating conditions

The plasma is created by injecting a focused electron beam into a vacuum chamber filled with gas at controlled low pressures [71]. The electron beam is pulsed, with pulse durations of the order of microseconds and beam energies sufficient to ionise and excite the target gases. Experiments were conducted over pressures between 2 and 20 Pa in pure N_2, pure H_2, and H_2/N_2 mixtures.

A key distinction from discharge plasmas is that no sustaining voltage is applied across the plasma region. Plasma production is initiated directly by electron-impact processes associated with the injected beam; subsequent evolution is governed by collisional excitation, radiative decay, and particle losses to the walls and through diffusion. This makes the EBR platform comparatively stable and repeatable for diagnostic work and provides favourable

conditions for comparison to kinetic and collisional–radiative models [3].

6.3 Optical emission spectroscopy measurements

Emission spectra were recorded with a spectrometer and an ICCD camera. Unless stated otherwise, the ICCD was operated with a gate (integration) width of 5 µs, synchronised to the electron-beam pulse, and spectra were accumulated over many repeated pulses to reach a sufficient signal-to-noise ratio. Throughout this chapter, spectra shown at 5 Pa should be understood as representative examples within the 2–20 Pa range rather than as the only operating point; the conclusions are based on measurements performed across the full explored pressure range.

In nitrogen, the N_2 Second Positive System (SPS; $C\,^3\Pi_u \rightarrow B\,^3\Pi_g$) is the dominant molecular emission in the near-UV/visible range under the present conditions [37]. In addition, the $N_2{}^+$ First Negative System (FNS; $B\,^2\Sigma_u^+ \rightarrow X\,^2\Sigma_g^+$) is observed and provides a complementary probe of ion excitation. In hydrogen, the molecular Fulcher-α band system ($d\,^3\Pi_u \rightarrow a\,^3\Sigma_g^+$) is clearly detected and enables rovibrational analysis [42, 43, 73]. Atomic hydrogen Balmer emission (Hα–Hϵ, when available) is used to examine relative excited-state populations and to support cross-platform comparison.

All analyses of molecular emission in this chapter (SPS, FNS, and Fulcher-α) follow the calibrated workflow established in Chapter 3. Synthetic spectra generated with PGOPHER [36] are convolved with the independently measured instrumental function and corrected with the spectral response of the detection chain. Fits to these systems then yield rotational temperatures and vibrational descriptors that can be compared consistently across the three plasma drivers considered in this thesis.

6.4 Temperature estimates and diagnostic strategy

Rotational temperatures (T_{rot}) are extracted by fitting the rotational envelopes of selected bands in the N_2 SPS/FNS systems and in the H_2 Fulcher-α system, using the same forward-modelling approach as in Chapter 3. Vibrational behaviour is inferred either from state-resolved band intensities (for N_2) or, for H_2 Fulcher-α, from Franck–Condon-corrected projections of diagonal band intensities to the ground-state vibrational distribution [40, 73].

In nitrogen, the EBR data yield rotational temperatures in the few-hundred-kelvin range (typically ∼300–500 K under the present conditions), while the vibrational excitation of the emitting electronic state is significantly higher, reflecting non-equilibrium excitation by electron impact. In hydrogen, the Fulcher-based analysis produces the same qualitative behaviour seen

throughout this thesis: the apparent excited-state rotational temperatures $T_{\mathrm{rot}}(d, v')$ are low, often below room temperature, while back-projection to the ground state indicates gas temperatures above room temperature. The inferred ground-state vibrational populations exhibit a characteristic envelope rather than a simple Boltzmann distribution, consistent with the need for collisional–radiative interpretation at low pressure [73].

The following subsections present the nitrogen SPS/FNS results, the hydrogen Fulcher analysis, and the Balmer-series population behaviour, emphasising their role as benchmarks for the EUV- and discharge-driven plasmas studied in the neighbouring chapters.

6.4.1 N_2 Second Positive System

For N_2, the SPS ($C\,^3\Pi_u \rightarrow B\,^3\Pi_g$) was recorded in ICCD-gated acquisition (5 µs gate) with accumulation over many beam pulses. Across the explored pressure range (2–20 Pa), the spectra exhibit well-defined band heads and rotational envelopes. This makes SPS in EBR a useful benchmark for validating the molecular-nitrogen fitting workflow introduced in Chapter 3 (band modelling, instrumental-function convolution, and spectral-response correction).

We fitted the SPS progression with the same PGOPHER-based procedure used elsewhere in the thesis (fixed line lists, calibrated Gaussian instrumental width, and global baseline), and a representative spectrum with best-fit simulation is shown in Fig. 6.1. The retrieved rotational temperatures $T_{\mathrm{rot}}(\mathrm{SPS})$ fall in the expected range for low-pressure, electron-beam–driven N_2 and are consistent with literature values for comparable nitrogen plasmas [38, 50]. They are higher than the H_2 Fulcher d-state T_{rot} obtained in Section 6.4.3, and well above the under-thermal values observed in EUV-induced N_2 at EBL2 (Chapter 5). Overall, the agreement between measured and simulated SPS shapes supports the role of EBR as a stable reference for the nitrogen analysis pipeline.

Remark on EUV-induced N_2. Time-resolved and integrated N_2 spectra at EBL2 (EUV-induced plasma, Chapter 5) exhibit an "under-thermal" behaviour with apparent T_{rot} well below room temperature and fits that are systematically less faithful to the band-head/wing balance than in NPD and EBR. The canonical behaviour observed for EBR SPS here provides a useful control case: it confirms that the modelling and calibration chain can reproduce standard N_2 rotational envelopes under electron-impact conditions, and it supports the interpretation that the EUV case reflects different excitation/relaxation pathways rather than a methodological artefact.

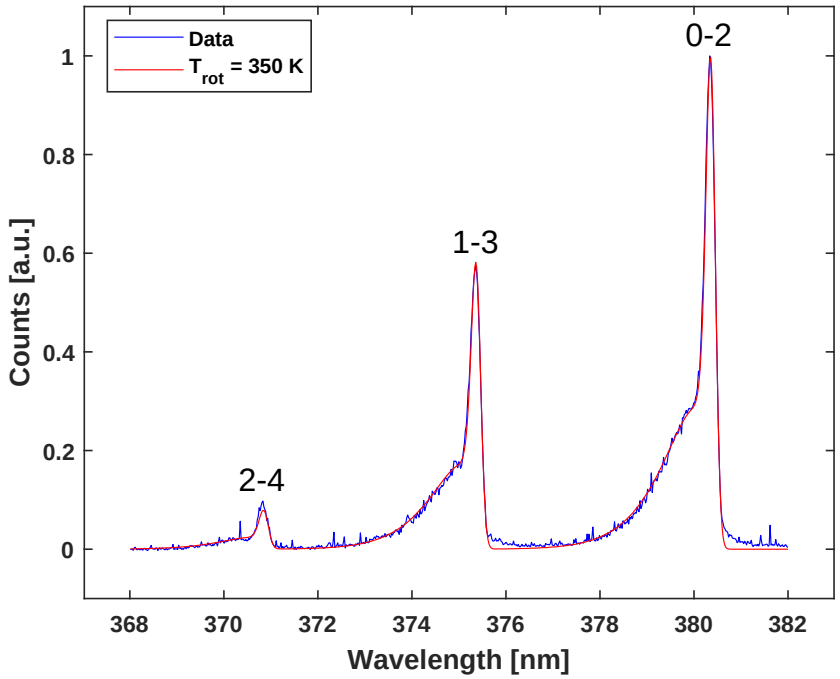

Figure 6.1: Representative N_2 SPS spectrum ($C\,^3\Pi_u \rightarrow B\,^3\Pi_g$) in EBR with best-fit simulation using the workflow of Chapter 3. Data were recorded with a 5 µs ICCD gate and accumulated over many beam pulses. The example shown corresponds to a representative operating point (here 5 Pa) within the explored pressure range (2–20 Pa).

6.4.2 N_2^+ First Negative System

The N_2^+ First Negative System (FNS; $B\,^2\Sigma_u^+ \rightarrow X\,^2\Sigma_g^+$) was likewise recorded using ICCD-gated acquisition (5 µs) with multi-pulse accumulation. In the EBR spectra, the FNS band features are well resolved, enabling reliable extraction of rotational temperatures T_{rot}(FNS) with the same band-simulation framework used for SPS (state-resolved line lists, instrumental convolution, and response correction).

The fitted T_{rot}(FNS) values agree with SPS-inferred temperatures within uncertainties and show the expected sensitivity to operating conditions (notably pressure within 2–20 Pa). A representative FNS spectrum with best-fit simulation is shown in Fig. 6.2. Together, the SPS and FNS results demonstrate that EBR provides clean, reproducible N_2/N_2^+ spectra suitable for benchmarking the nitrogen-modelling procedures used throughout the thesis.

Summary of nitrogen diagnostics in EBR. Across the explored pressure range (2–20 Pa), the SPS and FNS systems in EBR are straightforward to analyse and provide stable temperature estimates. In practice, this shows that the shared spectroscopy pipeline (line lists, instrumental width, response curve, and baseline handling) delivers canonical rotational temperatures of a few hundred kelvin for a clean, electron-impact–driven N_2 plasma.

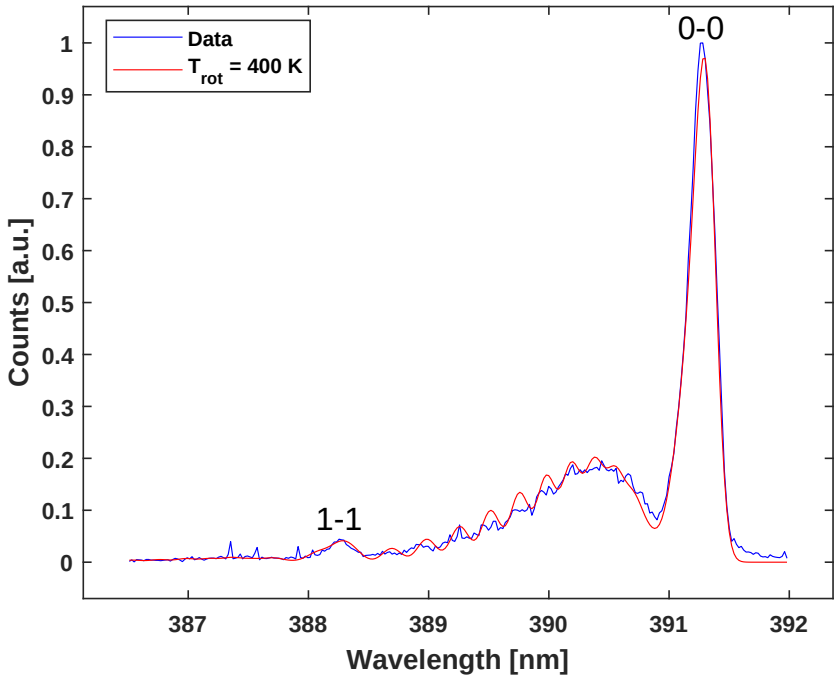

Figure 6.2: Representative $N_2{}^+$ FNS spectrum ($B\,^2\Sigma_u^+ \rightarrow X\,^2\Sigma_g^+$) in EBR with best-fit simulation. Data were recorded with a 5 µs ICCD gate and accumulated over many beam pulses. The example shown corresponds to a representative operating point (here 5 Pa) within the explored pressure range (2–20 Pa).

When the same pipeline is applied to EUV-induced N_2 at EBL2 and yields under-thermal SPS/FNS envelopes ($T_{\mathrm{rot}} \sim 200$ K) with imperfect head/wing balance, the discrepancy can therefore be attributed to EUV-specific excitation and relaxation pathways rather than to a hidden systematic error in the analysis. Likewise, the absence of late-time pooling signatures or strong continuum in EBR clarifies the role of afterglow chemistry and field/surface effects in nanosecond discharges (Chapter 4), where $T_{01}^{(\mathrm{C})}$ exhibits late-time plateaus and the SPS/FNS emission remains strong well after the pulse. EBR thus acts as a clean electron-impact reference against which the more complex behaviours observed in EUV-induced and pulsed-discharge plasmas can be identified and interpreted.

6.4.3 Fulcher band emission

In H_2, the Fulcher-α system ($d\,^3\Pi_u \rightarrow a\,^3\Sigma_g^+$) provides access to rovibrational information via the Q-branch, in particular through the Q_1 lines of the $d\,^3\Pi_u^-$ component. For EBR, we analysed the 600–635 nm window in ICCD-gated acquisition (5 µs gate) with accumulation over many beam pulses, following the same workflow as in Section 3.4. In brief, Gaussian fits were applied to $Q_1(N' = 1, 2, 3)$ for the diagonal bands $v' = v'' = 0 \ldots 3$ with widths constrained by the independently measured instrumental function; integrated line areas were corrected by the spectral response $C(\lambda)$; per-v' rotational Boltzmann plots were constructed; and Franck–Condon-corrected projections were used to infer ground-state vibrational populations.

Figure 6.3 shows a representative spectrum and the fit regions. Under EBR conditions, the baseline across 600–635 nm is sufficiently flat to support robust band integration and line fitting.

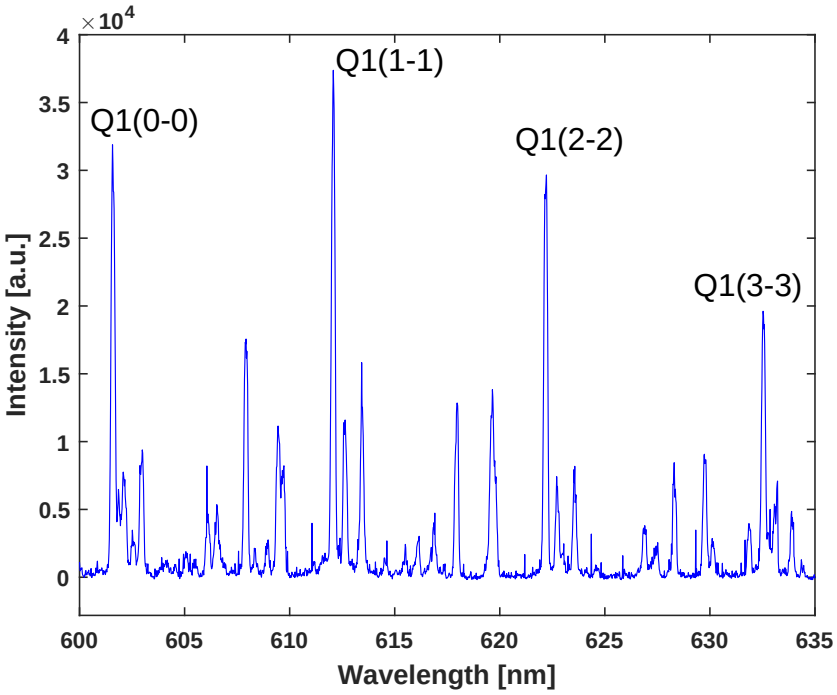

Figure 6.3: Representative Fulcher-α spectrum for H_2 in the EBR setup (2–20 Pa; 5 µs ICCD gate; accumulation over many beam pulses). The flat baseline across 600–635 nm enables response-corrected band sums and rovibrational analysis.

Example single-line fits are given in Fig. 6.4. The fitted line widths remain consistent with the independently measured instrumental function, supporting the internal consistency of the wavelength calibration and spectral-response correction in the EBR optical chain.

From the response-corrected line areas, we construct rotational Boltzmann plots (Fig. 6.5). As for the other platforms studied in this thesis, the retrieved $T_{\mathrm{rot}}(d, v')$ values are low—often below room temperature—and ex-

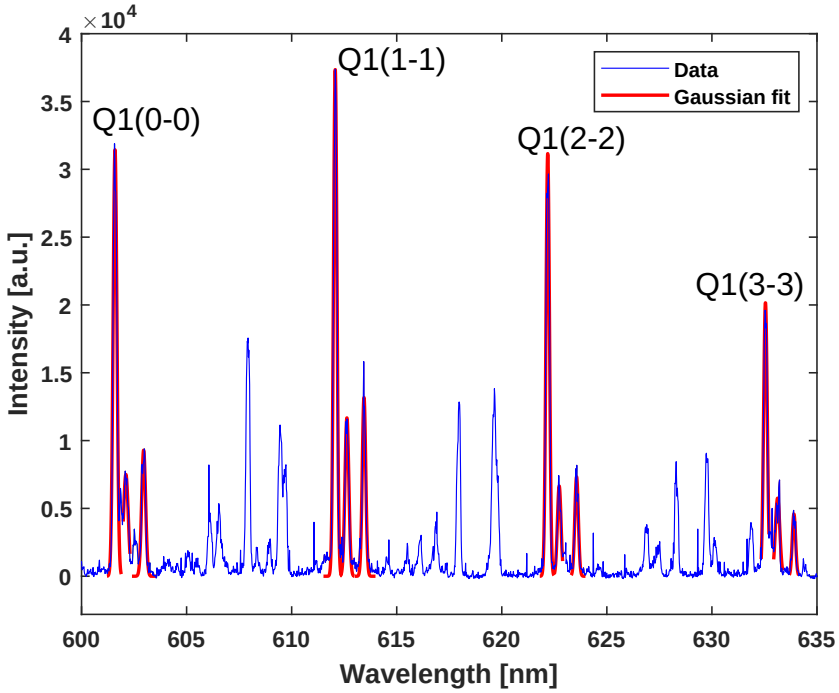

Figure 6.4: Gaussian fits to the $Q_1(N' = 1, 2, 3)$ lines (diagonal bands $v' = 0 \ldots 3$) of the Fulcher-α Q-branch at EBR. Line widths are constrained by the instrumental function.

hibit a mild decrease with increasing v'. Using Eq. (3.19), the corresponding ground-state (gas) temperature remains higher by approximately a factor of ~ 2, and thus above room temperature under our conditions, consistent with established Fulcher-based diagnostics in low-pressure hydrogen plasmas [42, 43, 73].

Finally, Fig. 6.6 presents the Franck–Condon-corrected ground-state vibrational populations $f_X(v)$ ($v = 0 \ldots 3$). The inferred envelope matches the behaviour observed on the other platforms—a maximum near $v = 2$ followed by a decrease—consistent with expectations from collisional–radiative modelling of low-pressure H_2 plasmas [65]. In line with the rest of this thesis, we do not assign a single quantitative vibrational temperature T_v here; instead, the inferred $f_X(v)$ is retained as a model constraint for future collisional–radiative interpretation.

Summary. EBR Fulcher diagnostics, therefore, provide a hydrogen-based temperature and vibrational benchmark that is fully consistent with the NPD and EUV results. The common analysis pipeline and the similar $f_X(v)$ envelope across platforms are exploited in Chapter 7 for cross-comparison.

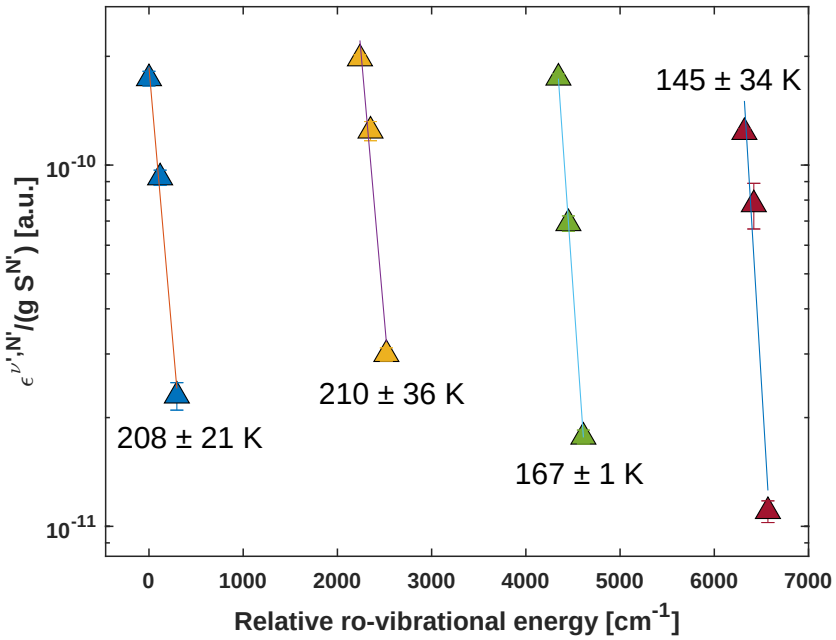

Figure 6.5: Rotational Boltzmann plots for $d\,^3\Pi_u^-$ at EBR, formed from response-corrected $Q_1(N' = 1, 2, 3)$ emissivities for $v' = 0 \ldots 3$. The fitted slopes yield $T_{\mathrm{rot}}(d, v')$, typically below room temperature and decreasing mildly with v'. Via Eq. (3.19), the corresponding ground-state (gas) temperature is $\sim 2 \times T_{\mathrm{rot}}(d)$ and remains above room temperature.

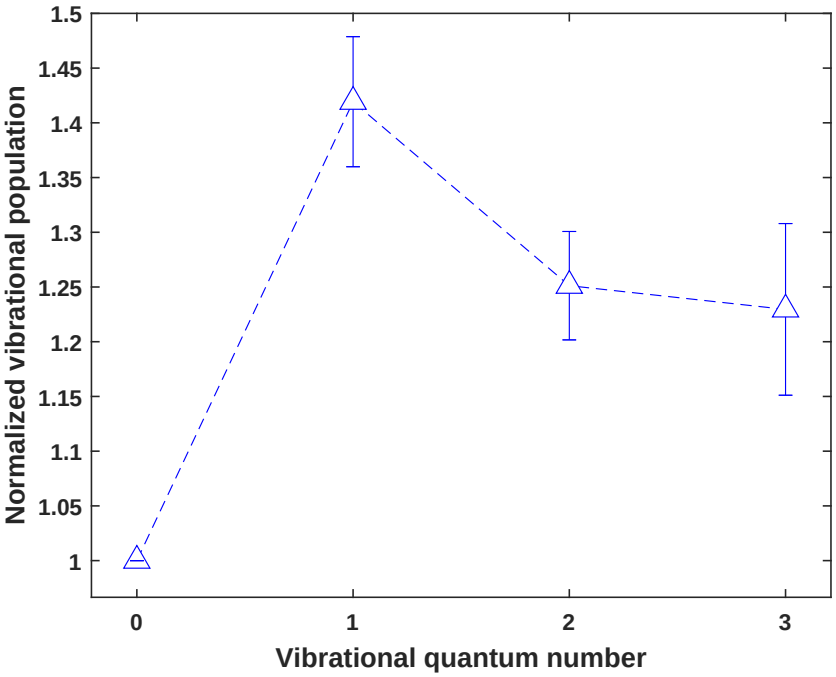

Figure 6.6: Franck–Condon-corrected ground-state vibrational populations $f_X(v)$ $(v = 0 \ldots 3)$ inferred from the diagonal Fulcher-α bands at EBR. The envelope (peak near $v = 2$ then decrease) agrees with NPD and EUV-driven results. A single vibrational temperature T_v is not assigned; interpretation is deferred to collisional–radiative modelling.

6.4.4 Balmer-series populations: non-Boltzmann behaviour

For the hydrogen EBR measurements, we complemented the Fulcher-α analysis with an assessment of the atomic Balmer series (Hα–Hϵ, when available). The procedure follows the approach outlined in Chapters 2 and 4: line-integrated intensities are obtained from Gaussian fits to each Balmer line, corrected for the spectral response of the detection chain, and converted into relative upper-level populations.

For each transition $u \to l$, we form

$$S_u \equiv \frac{I_{ul}\,\lambda_{ul}}{A_{ul}\,g_u}, \tag{6.1}$$

where I_{ul} is the fitted line area, λ_{ul} the transition wavelength, A_{ul} the Einstein coefficient, and $g_u = 2n^2$ the degeneracy of the upper level with principal quantum number n. The quantities S_u are then normalised to Hα ($n = 3$),

$$N_u = \frac{S_u}{S_{n=3}}, \tag{6.2}$$

and the uncertainties on N_u are obtained by propagating the Gaussian-fit errors on the individual line integrals, including the correlation with the reference line.

If the Balmer manifold were close to Boltzmann among itself, the normalised populations would satisfy

$$\ln N_u = -\frac{\Delta E_u}{k_B T_{\mathrm{exc}}} + \mathrm{const}, \tag{6.3}$$

with $\Delta E_u = E_u - E_{n=3}$ the excitation energy relative to Hα. As shown in Chapter 4 for nanosecond pulsed discharges, an approximately linear trend can sometimes be used to define an effective excitation temperature T_{exc}.

Figure 6.7 shows the corresponding Balmer "Boltzmann plot" for the EBR hydrogen plasma. Visual inspection indicates mild curvature and level-to-level scatter beyond the statistical error bars. A straight-line fit restricted to a subset of levels (for example, $n \geq 4$) can be made compatible with the data within uncertainties, but the inferred slope depends sensitively on the chosen line set and does not capture the residual curvature. For this reason, we do not quote a numerical value for the Balmer excitation temperature of EBR. Instead, the Balmer populations are retained as a qualitative diagnostic and as an additional constraint for future collisional–radiative modelling.

The observed non-Boltzmann behaviour is consistent with the excitation mechanism in electron-beam plasmas: direct electron-impact excitation from the ground state, excitation from already excited levels, and radiative cascades all contribute to the Balmer populations, while collisional redistribution between Rydberg levels is not expected to enforce Boltzmann equilibrium at these pressures and beam parameters [3, 17]. In the present framework,

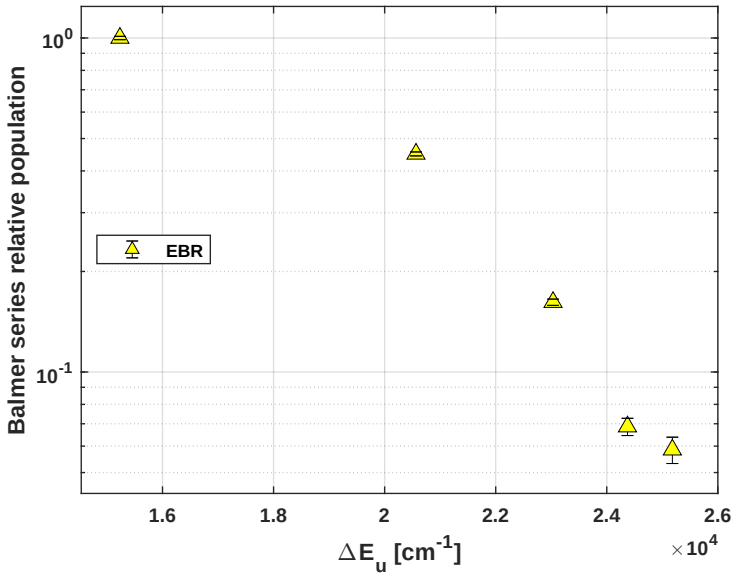

Figure 6.7: Balmer Boltzmann plot for the electron-beam–driven hydrogen plasma (EBR). Normalised populations N_u for Hα–Hϵ are plotted versus the upper-level excitation energy ΔE_u (referenced to $n = 3$), with error bars derived from the Gaussian-fit uncertainties on the line areas.

quantitative temperature diagnostics in EBR therefore rely primarily on the molecular systems (Fulcher-α, SPS/FNS). In contrast, Balmer-series populations provide a qualitative comparison between plasma sources and input for future modelling.

6.5 Comparison with nanosecond discharges

Nanosecond pulsed discharges (Chapter 4) involve strong transient electric fields and can produce high instantaneous electron energies, dense plasmas, and pronounced afterglows [27, 28]. By contrast, the EBR plasma is formed by a mono-energetic electron beam in the absence of a self-sustaining discharge [71]. This separation of the driving electron source from discharge dynamics reduces ambiguity when interpreting emission: in EBR, excitation is more directly connected to electron-impact kinetics, while in NPD, stepwise processes, field evolution, and afterglow chemistry can be comparatively more important.

From a diagnostic perspective, EBR spectra are typically weaker than those from nanosecond discharges for comparable acquisition times, but the band structure can be analysed reproducibly due to stable operating conditions and reduced discharge-related continuum contributions. As a result, EBR is particularly valuable for benchmarking the OES analysis procedures used in this thesis and for providing controlled reference cases against which EUV-driven and discharge-driven plasmas can be contrasted.

6.6 Summary

Electron Beam Radiation provides a reliable method for producing low-pressure plasmas in a controlled environment. Using ICCD-gated OES (typically 5 µs) and multi-pulse accumulation, emission spectra in N_2, H_2, and H_2/N_2 mixtures were recorded over pressures between 2 and 20 Pa. In nitrogen, the SPS and FNS systems yield stable rotational temperatures in the few-hundred-kelvin range and serve as a clean benchmark for the PGOPHER-based fitting and calibration workflow established in Chapter 3. In hydrogen, Fulcher-α analysis reproduces the cross-platform behaviour observed throughout the thesis, including low apparent $T_{\mathrm{rot}}(d, v')$ and a ground-state vibrational envelope peaking near $v = 2$. Balmer-series populations show departures from a single Boltzmann trend and are therefore retained as qualitative constraints rather than used to define a unique excitation temperature. Overall, the EBR platform provides an electron-impact reference that strengthens interpretation of the more complex behaviours observed in EUV-induced plasmas (Chapter 5), and nanosecond pulsed discharges (Chapter 4), and it underpins the comparative discussion of Chapter 7.

Chapter 7

Comparative analysis of EUV-induced, electron-beam-driven and NPD plasmas

7.1 Spectral features: molecular vs atomic emission

7.1.1 Fulcher band

The Fulcher-α system ($d\,^3\Pi_u \rightarrow a\,^3\Sigma_g^+$, 600–635 nm window) provides a common molecular diagnostic across all three platforms. As detailed in Chapter 3 (Section 3.4), we restrict the analysis to the Q-branch of the $d\,^3\Pi_u^-$ component and fit the $Q_1(N' = 1, 2, 3)$ lines for the diagonal bands $v' = v'' = 0 \ldots 3$ with Gaussian profiles whose widths are bounded by the instrumental function. From response-corrected line areas we build rotational Boltzmann plots per v' and infer $T_{\mathrm{rot}}(d, v')$; projecting via rotational-constant ratios (Eq. (3.19)) yields an estimate of T_{gas}. Vibrational populations are obtained from band-summed, Franck–Condon–corrected intensities and projected back to the ground state as $f_X(v)$ (Eq. (3.27)).

Cross-platform spectral quality. Figure 7.1 juxtaposes representative spectra. EBR and NPD show clean baselines with well-resolved Q_1 triplets; EBL2 spectra are likewise clean when acquired without auxiliary illumination in the line of sight (contrast with the OLT sessions in Chapter 5). The common spectral window and identical processing pipeline make the Fulcher system an ideal cross-facility benchmark.

Rotational structure and projection to T_{gas}. Across platforms, the d-state rotational plots (Fig. 7.2) consistently yield *sub-room* $T_{\mathrm{rot}}(d, v')$ that decrease mildly with v'. This is physically expected for short-lived d-state emis-

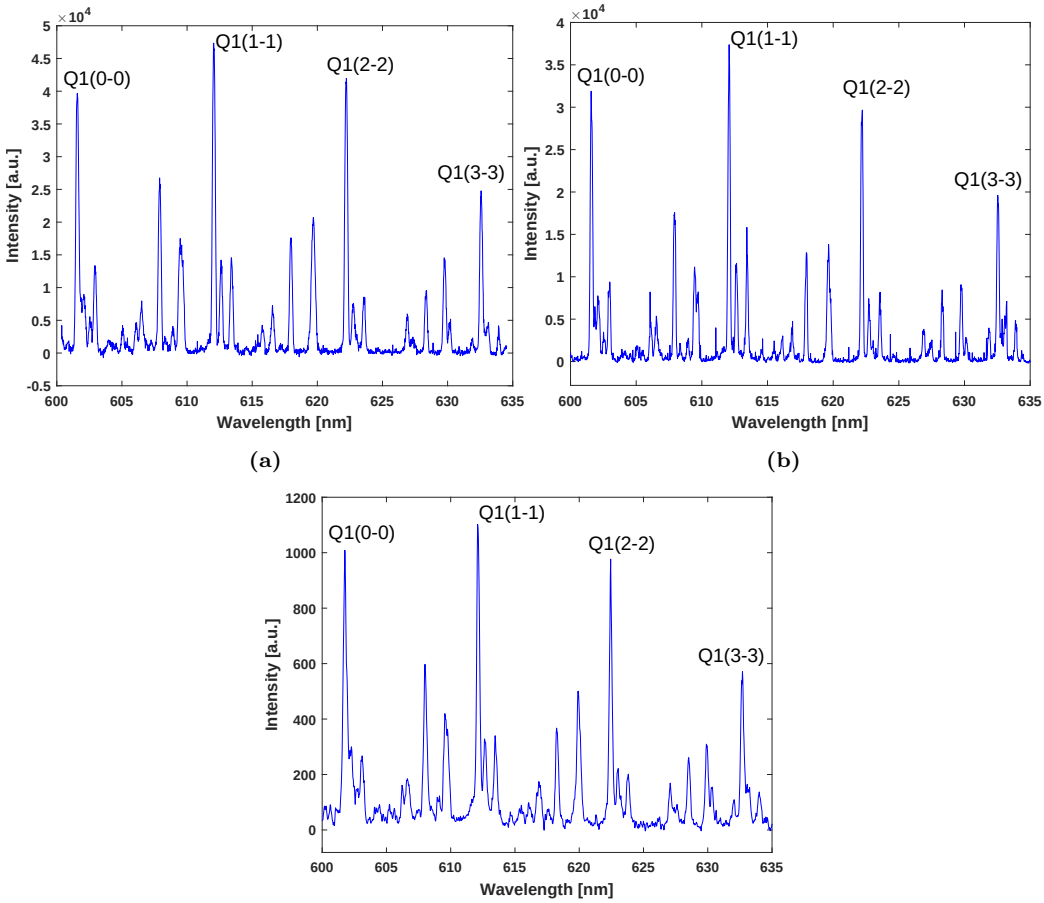

Figure 7.1: Fulcher-α spectra (600–635 nm, Q-branch of $d\,^3\Pi_u^-$) across platforms: (a) EBL2 EUV-induced plasma ($\sim$5 Pa H_2, integration), (b) EBR electron-beam plasma (few–tens of Pa H_2, integration), and (c) NPD nanosecond discharge (low-pressure H_2, time-integrated). All panels show the diagonal bands $v' = v'' = 0 \ldots 3$ used for rovibrational analysis and provide a common baseline for cross-facility comparison.

sion at low pressure: using Eq. (3.19), $T_{\mathrm{gas}} \approx 2\,T_{\mathrm{rot}}(d, v')$, placing the gas temperature above room temperature under our conditions, in line with established Fulcher-based diagnostics in low-pressure hydrogen plasmas [42,43,73]. We deliberately restrict fits to $N' = 1$–3 to avoid bias from possible non-thermal high-N' tails, which cannot be robustly constrained at our resolution/SNR (cf. Chapter 3).

Vibrational populations. The Franck–Condon–corrected $f_X(v)$ (Fig. 7.3) exhibits the same low-density envelope on all platforms: a rise from $v = 0$ to $v = 2$ followed by a decrease. This trend is consistent with direct excitation from $X, v = 0$ into the d state, modest redistribution, and radiative decay [42, 43, 48]; we refrain from assigning a unique T_v without a dedicated CR model for each source (EUV, beam, discharge).

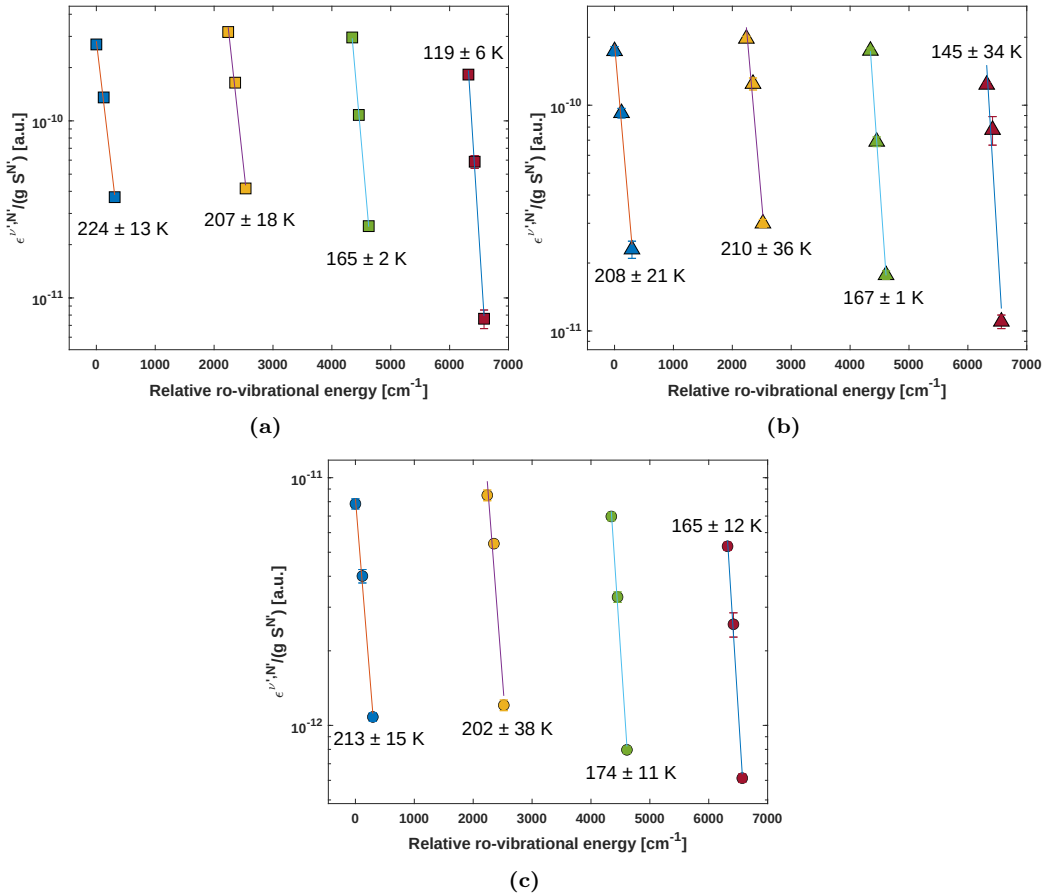

Figure 7.2: Rotational (Boltzmann) plots from $Q_1(N' = 1, 2, 3)$ for $v' = 0 \ldots 3$: (a) EBL2, (b) EBR, (c) NPD. In all cases the excited d-state appears "cold" (sub-room $T_{\mathrm{rot}}(d)$) with a mild decrease vs. v'; via rotational-constant ratios this projects to $T_{\mathrm{gas}} \approx 2\, T_{\mathrm{rot}}(d)$, i.e. above room temperature. Fits use only $N' = 1 \ldots 3$ to avoid high-N' tail bias.

Caveats and good practice. (i) Treat $T_{\mathrm{rot}}(d)$ strictly as an excited-state parameter; only its projection via rotational constants should be interpreted as T_{gas} [42, 43]. The short lifetime of the d state and its specific excitation pathway mean that its rotational distribution is not, by itself, in equilibrium with the bulk gas, so using $T_{\mathrm{rot}}(d)$ directly as a gas thermometer would systematically under-estimate T_{gas}.

(ii) Prefer EBR/NPD (or EUV sessions without auxiliary illumination) to build absolute band sums; otherwise baseline artefacts (e.g. OLT ellipsometer contributions) can perturb v-population ratios at the window edge. Small baseline slopes or local bumps translate into biased integrated areas for individual bands, which in turn distort the inferred $f_X(v)$ and any comparison of vibrational envelopes between platforms or operating conditions.

(iii) Because predissociation reduces $v' \geq 4$, we limit the analysis to $v' = 0 \ldots 3$ where our SNR is robust [42, 43]. At higher v' the combination of weaker emission and increased sensitivity to modelling assumptions (overlapping lines, baseline) would make the derived populations strongly uncertain,

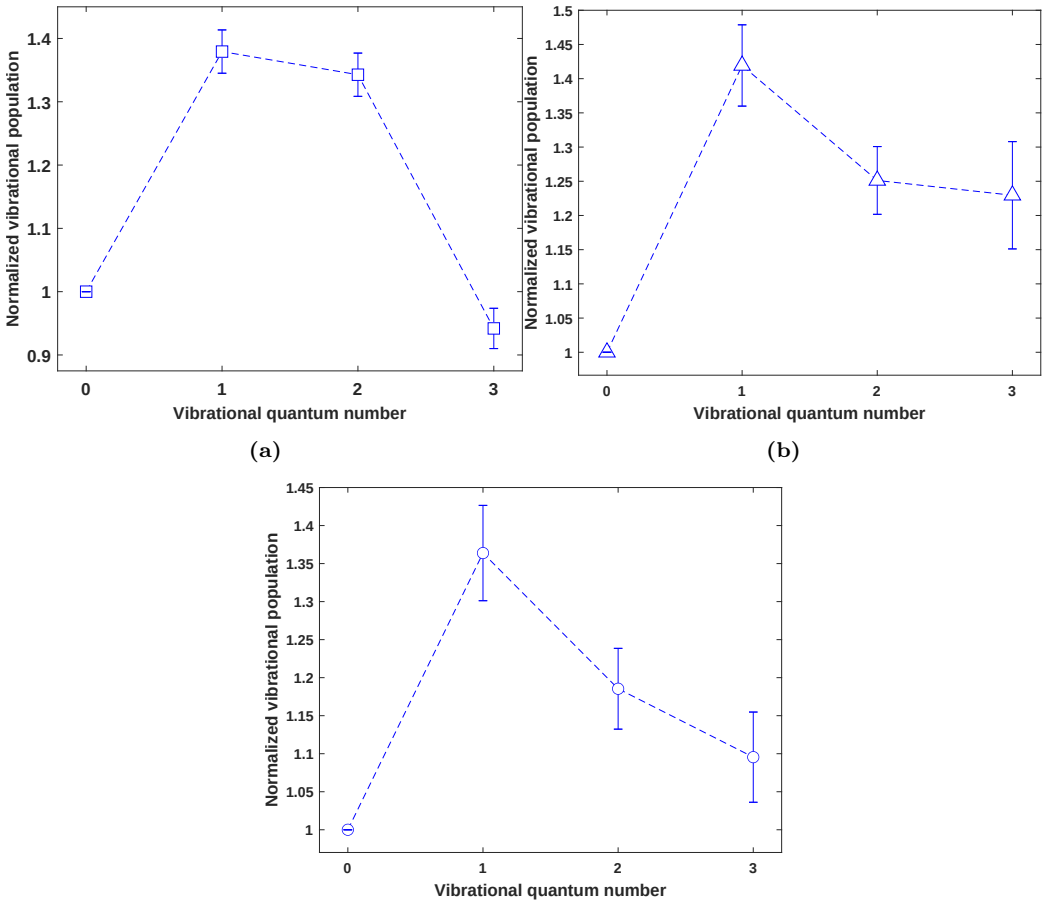

Figure 7.3: Franck–Condon–corrected ground-state vibrational populations $f_X(v)$ for $v = 0 \ldots 3$: (a) EBL2, (b) EBR, (c) NPD. All platforms exhibit the characteristic low-density envelope with a maximum near $v = 2$ followed by a decrease. Consistent with the main chapters, no single T_v is assigned pending a dedicated collisional–radiative model for EUV/beam/discharge H_2.

so truncating the analysis to the well-constrained bands yields more reliable and reproducible trends across all three plasma sources.

7.1.2 Balmer series

For all three platforms (NPD, EBL2, EBR), the atomic hydrogen Balmer lines (Hα–Hϵ, when available) are processed with the same pipeline introduced in Chapter 3 and applied in Chapters 4 and 6. For each line $u \to l$, a Gaussian (or composite) fit provides the line-integrated intensity, which is then corrected for the spectral response and converted into an upper-level population proxy $S_u \propto I_{ul}\,\lambda_{ul}/(A_{ul}g_u)$. These S_u are normalised to Hα ($n = 3$) to form N_u, and the resulting normalised populations are plotted as $\ln N_u$ versus the upper-level excitation energy $\Delta E_u = E_u - E_{n=3}$ to build a "Balmer Boltzmann plot". Under a true Boltzmann distribution of the Balmer manifold, this would yield a straight line with slope $-1/(k_B T_{\mathrm{exc}})$ and thus define an effective excitation temperature T_{exc}.

In practice, all three plasmas deviate from this ideal picture, but in *different* ways. The following comparison is therefore qualitative: the Balmer plots are used as shape diagnostics and as cross-checks on the excitation mechanisms, rather than as primary thermometers [31, 73].

EUV-induced vs beam-driven plasmas (pure H_2).

Figure 7.4 compares the normalised Balmer populations for the EUV-induced plasma at EBL2 and the electron-beam plasma at EBR in nominally pure H_2. In both cases the points *do not* line up on a straight line within the propagated uncertainties, confirming that the Balmer manifold is non-Boltzmann. Higher-n levels are systematically misaligned with respect to any single-slope trend, and the apparent slope depends strongly on which subset of lines is selected.

Although the exact curvature differs slightly between EBL2 and EBR, the qualitative message is the same: direct electron-impact excitation (from the EUV-generated photoelectrons or the injected beam), cascades, and stepwise channels populate the Balmer levels in a way that does not equilibrate to a Boltzmann distribution over the relevant timescales and pressures [31, 73]. For both sources we therefore *do not* quote a Balmer-based T_{exc}.

Effect of H_2O admixture at EBL2.

The second comparison (Fig. 7.5) repeats the EBL2–EBR overlay for the case where a small amount of H_2O is admixed at EBL2, while the EBR reference remains in pure H_2. Within the uncertainties, the overall non-Boltzmann character of the Balmer manifold is preserved: introducing water does not "restore" a straight Boltzmann line.

The modest changes in the envelope probably reflect the fact that adding H_2O introduces extra inelastic and quenching channels in the hydrogen plasma (for instance via OH- and O-containing reaction pathways and a modified electron energy distribution). We do not attempt a quantitative mechanistic interpretation here; the key point is that, even with H_2O present, the Balmer manifold at EBL2 remains clearly non-Boltzmann and therefore cannot be used as an equilibrium thermometer.

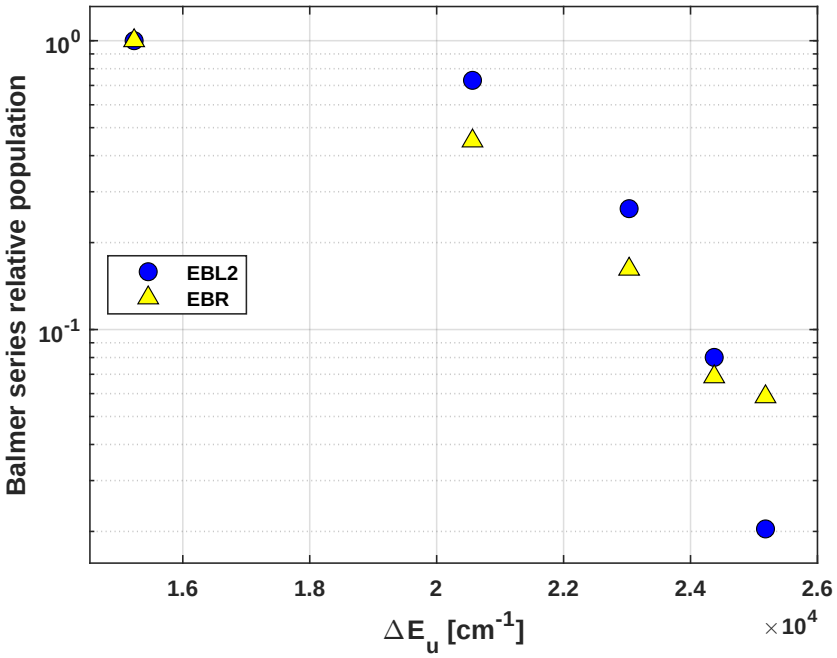

Figure 7.4: Comparison of normalised Balmer populations N_u (Hα–Hδ/Hϵ) between the EUV-induced hydrogen plasma at EBL2 and the electron-beam plasma at EBR (pure H_2). Points are obtained from response-corrected line areas and normalised to Hα; error bars reflect Gaussian-fit uncertainties propagated through the normalisation. In both cases the distributions are clearly non-Boltzmann: a single straight-line fit would depend strongly on the chosen subset of lines and is therefore not assigned a physical T_{exc}.

Including nanosecond-pulsed discharges (NPD).

Figures 7.6 and 7.7 extend the comparison to the nanosecond-pulsed discharge in H_2 (NPD). Here the Balmer populations come *closer* to a straight line over the first few levels, and in Chapter 4 a tentative T_{exc} was extracted from a restricted subset of lines (low n only). Nonetheless, once higher levels and full error propagation are included, curvature and scatter remain visible and caution is still required.

The last point in the EBL2 series (Hϵ) deserves specific comment. As discussed in Chapter 4, the Hϵ region at EBL2 is contaminated by a tin-related scattered-light feature from the EUV source, which is modelled as a superposition of a Lorentzian baseline and neighbouring structures. The Balmer line itself is therefore fitted as part of a composite model (Gaussian Hϵ on top of a double-Lorentzian background). This significantly inflates the uncertainty on the recovered Hϵ area, and the corresponding error bar on N_u is accordingly very large (Fig. 7.6). The point is retained for completeness but carries little weight in any trend discussion.

To show the underlying trends more clearly, Fig. 7.7 repeats the three-way comparison with Hϵ excluded for all sources.

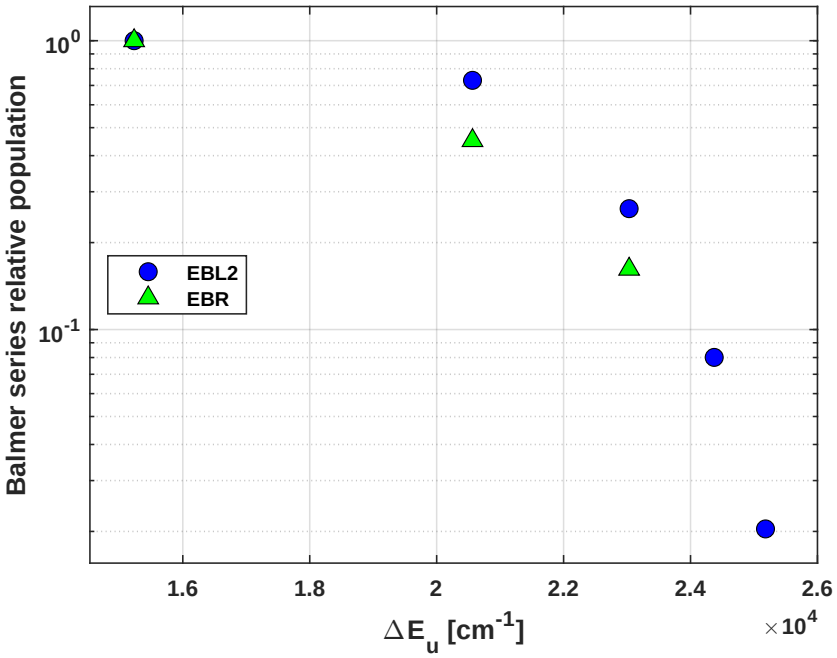

Figure 7.5: Balmer-population comparison between EBL2 (with H_2O admixture in H_2) and EBR (pure H_2). The presence of H_2O modifies the relative level populations at EBL2 (through changed quenching, additional reaction pathways, and altered electron kinetics), but the manifold remains clearly non-Boltzmann: no single T_{exc} can be assigned.

Summary of Balmer comparison. Across all three platforms, the Balmer series provides a useful *qualitative* probe of atomic excitation, but only in the NPD case does it approach a regime where an effective T_{exc} is marginally defensible (and then only over a restricted range of levels). For the EUV-induced plasma at EBL2 and the electron-beam plasma at EBR, the Balmer manifolds are clearly non-Boltzmann; we therefore refrain from assigning T_{exc} and instead use the Balmer plots as shape constraints for future collisional–radiative modelling and as a comparative metric between sources [31,73]. Molecular diagnostics (Fulcher-α, N_2 SPS/FNS) thus remain the primary temperature probes throughout this work.

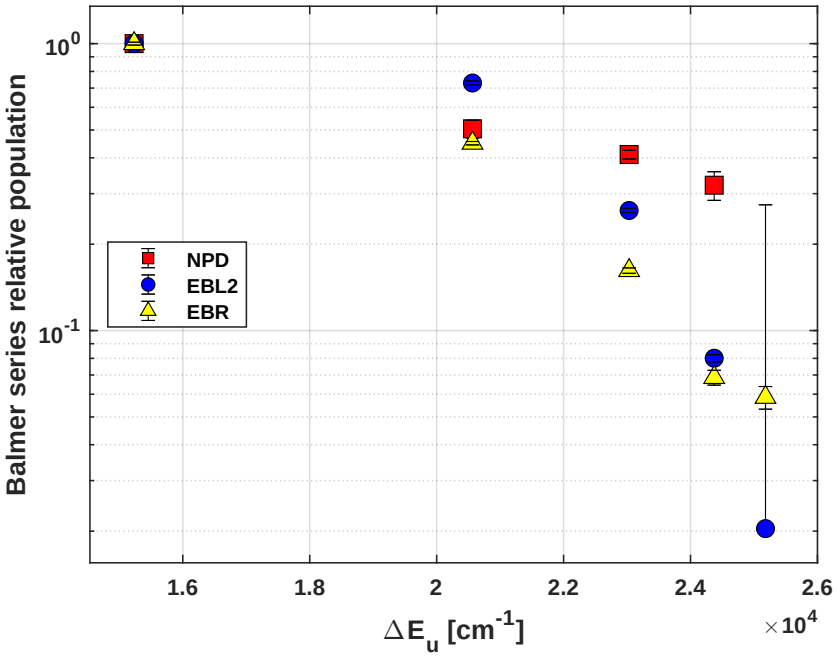

Figure 7.6: Balmer Boltzmann-style plots for all three platforms (NPD, EBL2, EBR), including Hϵ where available. NPD shows the closest approach to a straight line over the first few levels, whereas EBL2 and EBR exhibit stronger curvature. The large error bar on the EBL2 Hϵ point reflects the more complex fit model needed for that line (see text).

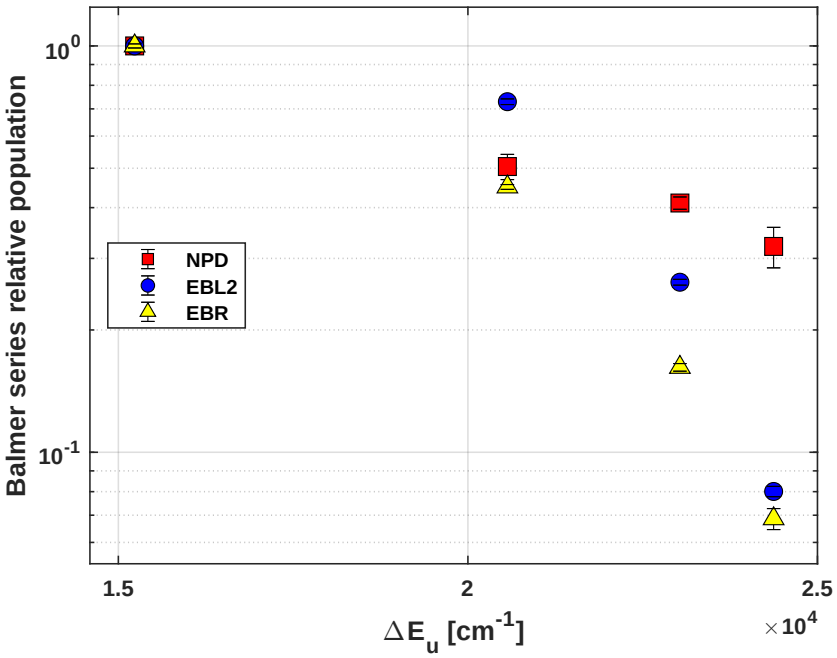

Figure 7.7: Same as Fig. 7.6, but excluding Hϵ from all datasets. With the problematic EBL2 Hϵ point removed, the relative shapes of the NPD, EBL2, and EBR Balmer manifolds are easier to compare: NPD is closest to a single-slope trend over the first few levels, while EBL2 and EBR remain clearly non-Boltzmann.

7.1.3 Nitrogen systems: SPS, FNS, and atomic N

Nitrogen provides a second common thread across the three platforms, this time through the N_2 Second Positive System (SPS), the N_2^+ First Negative System (FNS), and a set of atomic-N lines. Taken together, these emitters let us compare how neutral and ionic nitrogen respond to the different drivers (EUV, nanosecond discharge, electron beam) and how closely their apparent rotational/vibrational structure can be linked to the underlying gas conditions.

SPS/FNS envelopes and rotational structure. A first striking difference is seen directly in the SPS/FNS rotational envelopes. In the EUV-induced plasma at EBL2 (Chapter 5, Figs. 5.1–5.2 and 5.5–5.6), the best-fit SPS and FNS profiles are systematically *under-thermal*: the apparent rotational temperatures are of order $T_{\mathrm{rot}} \sim 200$ K, i.e. well below room temperature, and the fits struggle to reproduce band heads and wings with a single T_{rot}. This behaviour does not appear in the reference sources. In the electron-beam plasma (EBR, Chapter 6, Figs. 6.1, 6.2), the same PGOPHER-based workflow yields physically reasonable rotational temperatures in the few-hundred-kelvin range with low, structureless residuals across both SPS and FNS. Likewise, in the nanosecond pulsed discharge (NPD, Chapter 4, Figs. 4.2, 4.14) the SPS/FNS fits at 5 Pa are well-behaved and remain quantitatively interpretable as pressure is increased to the 1–500 mbar range.

The comparison is important for interpretation. Because SPS/FNS envelopes are perfectly standard in EBR and NPD, the anomalously low T_{rot} and imperfect head/wing balance under EUV cannot be blamed on the fitting pipeline or on calibration artefacts. Instead, they point to genuinely different excitation and relaxation pathways in EUV-induced N_2 at very low pressure, where photoelectron-driven kinetics, long mean free paths, and strong line-of-sight averaging are likely to produce non-equilibrium rotational distributions that no single T_{rot} can faithfully represent.

Vibrational excitation. The SPS-based first-level C-state vibrational temperature T_{01} adds a second layer of comparison. In NPD (Chapter 4), T_{01} follows the discharge current: it rises during the voltage pulse and relaxes afterwards. At 1–11 mbar this evolution is fairly prompt; at higher pressures (110–500 mbar) the N_2(A) metastable manifold builds up between pulses and feeds the C-state via pooling, producing the characteristic late-time rise and plateau documented in Section 4.6 (Fig. 4.11) and consistent with previous afterglow studies [32–34]. In EBR, SPS emission simply tracks the beam pulse: T_{01} responds to the power input without pronounced afterglow structure, as expected for a system driven by a well-defined external electron source in a simple geometry. For the EUV case at EBL2, the behaviour is more diffuse: SPS/FNS emission is broadened and slightly delayed with respect to the EUV pulse, reflecting the time it takes for photoelectrons and

secondaries to populate the molecular channels and for radiative cascades and metastable pathways to contribute. In other words, while T_{01} is tightly locked to the driver in NPD and EBR (current or beam), it responds in a more smeared-out fashion to the EUV burst.

Atomic N timing. Atomic nitrogen provides a complementary, more "prompt" view of the excitation. At EBL2, atomic-N lines rise earlier and more sharply than SPS and FNS (Chapter 5, Figs. 5.10–5.11). This is consistent with their higher excitation thresholds and their closer connection to the hot photoelectron population generated during the EUV pulse: atomic lines respond quickly to the earliest, most energetic electrons, whereas molecular emission builds up more slowly through a mix of direct excitation, stepwise processes, and cascades. A similar hierarchy is present in NPD and EBR, even though we did not perform equally detailed timing scans there: in all cases, atomic channels are the first to follow the driver, with SPS and FNS lagging and broadening relative to the source waveform.

Taken together, the nitrogen systems reinforce the timing hierarchy already seen in hydrogen and highlight the EUV case as qualitatively different. Under EUV irradiation, SPS and FNS look rotationally "colder" and temporally more blurred than in their electron-beam and nanosecond-discharge counterparts, indicating that nitrogen diagnostics must be interpreted with particular care in scanner-relevant EUV conditions.

7.2 Temporal dynamics

We compare the time evolution of key emitters (Balmer, SPS, FNS, atomic N) against the driving source in each platform, using the "peak-maximum vs. delay" proxy compiled in the source chapters.

EUV-induced plasma (EBL2)

Leading edge and width. Normalised Balmer peaks (Hα/Hβ) rise shortly *after* the EUV photodiode signal and are significantly broader (Chapter 5, Fig. 5.19). SPS/FNS peaks show an even longer delay/broadening (Figs. 5.4, 5.8). Atomic N follows the EUV onset more closely than SPS/FNS (Fig. 5.11).

Pressure trends. All channels weaken with decreasing pressure (photoabsorption $\downarrow$), and the lag tends to increase as secondary-electron production drops (Figs. 5.3, 5.7, 5.18). Small inter-series offsets reflect unsynchronised runs and finite gate convolution.

Kinetic picture. During the EUV pulse, S_{ph} dominates (Eq. (1.10)); the Balmer and atomic-N rises reflect prompt electron-impact excitation from

photoelectrons. Molecular emission continues after the photon burst as S_{sec} and radiative cascades decay on $\mathcal{O}$(10–100) ns, with total plasma decay set by recombination and diffusion (Eq. (1.18)) [31].

Nanosecond pulsed discharge (NPD)

Discharge-synchronous response. At 5 Pa the SPS/FNS envelopes and T_{01} are nearly time-invariant over the pulse (Chapter 4, Sections 4.4, 4.8). At 1–500 mbar, T_{01} rises with current and exhibits a late-time plateau driven by N_2(A) pooling (Section 4.6, Fig. 4.11, and Refs. [32–34]). Balmer-based T_{exc} can be fitted over low-n lines only (Section 4.9.2).

Decay. After the pulse the decay reflects recombination and ambipolar diffusion (Eq. (1.8)), with μs-scale tails in integrated emission, in line with previous nanosecond-discharge studies [27, 28]. Stark-based $n_e(t)$ is measurable in NPD (Chapter 2, Section 2.7); this was not feasible at EBL2.

Electron-beam plasma (EBR)

Beam-synchronous, clean baselines. Integrated SPS/FNS/Fulcher signals track the beam pulse without parasitic baselines; rotational fits are stable (Chapter 6). Balmer plots remain non-Boltzmann (Section 6.4.4), akin to EBL2, supporting a common "cascade/stepwise" origin for the curved manifolds [31, 73].

Timing hierarchy across platforms

The time-resolved analyses in the previous chapters point to a common *ordering* in how different emitters respond to the driving source, even though the detailed waveforms differ between EUV, NPD, and EBR. In all three platforms the earliest, sharpest response is carried by atomic lines, while molecular systems appear slightly delayed and temporally broadened.

For the EUV-induced plasma at EBL2 (Chapter 5), this is most clearly seen by comparing the EUV photodiode signal with the Balmer lines and the nitrogen systems: Balmer peaks (Hα/Hβ) rise shortly after the EUV burst, atomic-N lines follow the onset more closely than the molecular bands, and SPS/FNS emission is broader and more delayed than both (see Figs. 5.19, 5.4, 5.8, 5.11). A complementary view is provided by time–wavelength–intensity maps (e.g. Fig. 7.8), where the atomic-N features clearly "light up" earlier and more sharply than the SPS/FNS band heads as the plasma evolves.

In nanosecond pulsed discharges (Chapter 4), the same qualitative ordering is present: the discharge current defines a sharp electrical timescale, Balmer emission reacts promptly to the high-energy electrons generated in the voltage rise, and SPS/FNS intensities, together with T_{01}, respond over a slightly longer window and can exhibit afterglow structure at higher

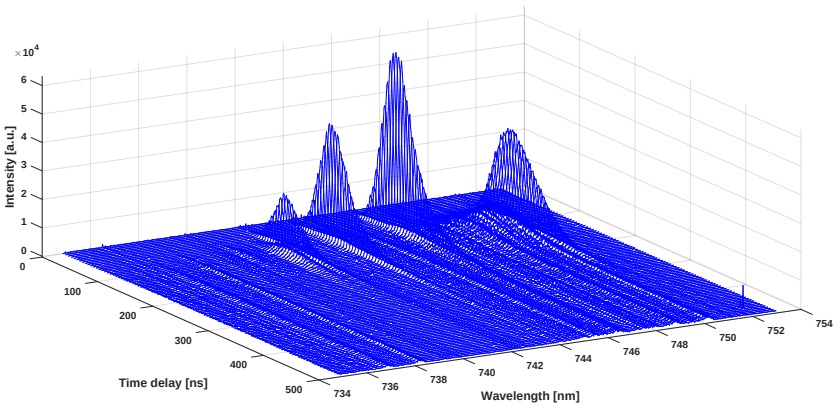

Figure 7.8: Example time–wavelength–intensity map for the EUV-induced nitrogen plasma at EBL2. Atomic-N lines rise promptly after the EUV pulse, while the FPS band heads develop slightly later and over a broader time window, illustrating the timing hierarchy between atomic and molecular emission discussed in the text.

pressures (Sec. 4.6). In the electron-beam plasma (EBR, Chapter 6), the SPS/FNS/Fulcher signals follow the beam pulse in a comparatively simple fashion, while the Balmer series again shows the fastest response among the optical channels, consistent with direct excitation by the mono-energetic beam electrons.

This recurring pattern can be summarised schematically as

$$\text{Source trigger} \;\rightarrow\; \text{atomic (Balmer, N)} \;\rightarrow\; \text{molecular (FNS, SPS, Fulcher)},$$

with increasing temporal breadth and lag from left to right, modulated by pressure, geometry, and driver specifics. In the rest of this chapter, this "timing hierarchy" is used as a shorthand to interpret how different processes (electron-impact excitation, cascades, metastables, afterglow chemistry) shape the observed OES signals across platforms.

7.3 Implications for the ASML plasma environment

In the ASML context, the central question behind this work is how far non-invasive OES can be pushed as a practical diagnostic for scanner-relevant plasmas: what can realistically be monitored from the light alone, and what requires dedicated hardware (photodiodes, ion/neutral probes, etc.)? The cross-platform comparison of EUV-induced, NPD, and EBR plasmas provides the pieces to answer this. In this section we translate the comparative results into a set of concrete guidelines for scanner-relevant diagnostics and operations—i.e. how the findings of this thesis can be used in practice in an ASML-type plasma environment.

1. **EUV pulse proxy from OES.** Balmer leading edges provide the

closest optical proxy to the EUV timing, but they systematically *overestimate* the pulse width due to collisional–radiative tails and the finite ICCD gate width (Chapter 5, Fig. 5.19; OLT: Figs. 5.25–5.28). In practice, this means that photodiodes should remain the reference for absolute EUV timing and for specifying the source pulse shape, whereas OES is better used to track *relative* changes: e.g. the appearance of a second peak, a systematic shift of the emission maximum, or a change in afterglow length. The expected outcome is a two-layer monitoring strategy: fast, hardware-based EUV timing for specification compliance, complemented by slower but more diagnostically rich OES to flag drifts in the underlying excitation and quenching kinetics.

2. **Gas-state and temperature proxies.** Fulcher Q-branch analysis is robust across platforms and yields a stable projection to T_{gas} via rotational constants (Figs. 7.2), consistent with previous Fulcher-based thermometry [42,43,73]. This suggests a practical use-case in scanners: Fulcher analysis can act as a non-invasive "thermometer" for the hydrogen background, particularly in low-n_e regimes where invasive probes are undesirable or impossible. Operationally, one would not interpret $T_{\mathrm{rot}}(d)$ directly, but use the calibrated projection to T_{gas} as a slow-varying health metric of the thermal state of the gas in front of the optics or sample.

3. **Impurity sensitivity ($\mathbf{N_2}$ in $\mathbf{H_2}$).** FNS remains detectable in H_2 down to $\sim 10^{-6}$ mbar N_2 partial pressure at EBL2 (Chapter 5, Fig. 5.20), making it a sensitive, non-invasive impurity monitor. In practice this means that a simple, periodically recorded $N_2{}^+$ FNS window is sufficient to detect small leaks or contamination in a nominally pure H_2 ambient, well below the level that would typically be visible in standard pressure or flow readouts. The intended use is "spectral health checks": small changes in FNS intensity immediately flag changes in gas composition without disturbing tool operation.

4. **Baseline management and source-related stray light.** Out-of-band and scattered light from the source or auxiliary optics can subtly corrupt parts of the spectrum (for example, the Hϵ region in the presence of Sn-related stray light), and composite fits in such regions inflate the uncertainties on line areas (Chapter 5, Section 5.1.5). The general lesson is that spectral "hygiene" matters: diagnostics should, as far as possible, avoid spectral regions strongly affected by stray light, overlapping instrumentation, or strong reflections, or should be accompanied by tailored optical filtering and background characterisation. In a tool environment this translates to scheduling dedicated OES windows with minimal auxiliary illumination in the diagnostic range of interest, and to designing the optical path such that critical lines (e.g. Balmer, FNS) sit in relatively clean spectral regions.

5. **Interpreting nitrogen T_{rot} at EUV.** Under-thermal SPS/FNS envelopes at EBL2 are physical and *not* an analysis artefact: the same fitting pipeline returns canonical few-hundred-kelvin T_{rot} in NPD and EBR. This cautions against using SPS/FNS T_{rot} as a direct proxy for T_{gas} under EUV conditions at very low pressure. Instead, nitrogen emission under EUV should be interpreted primarily as a kinetic probe (sensitive to photoelectron-driven pathways and metastable dynamics), while Fulcher-based T_{gas} in H_2 is used where a temperature estimate is required [31]. The expected benefit is to avoid misinterpreting EUV nitrogen spectra as "cold gas" when they in fact reflect non-equilibrium excitation.

6. **Model-guided monitoring.** Because Balmer manifolds are non-Boltzmann in EUV and EBR, a single Balmer-based T_{exc} is not a reliable scalar health metric. A more robust strategy is to compare the *shape* of the Balmer manifold (curvature, level-to-level ratios) to precomputed model look-up grids or reference datasets once available (see Outlook) [31, 73]. In operational terms, this means that changes in the Balmer shape—not just its overall intensity—can be used to flag shifts in the dominant excitation pathways (e.g. more cascade-dominated vs. more direct-impact dominated), even when standard macroscopic parameters (pressure, flow, pulse energy) are unchanged.

Taken together, these points translate the comparative plasma analysis of this thesis into a concrete "toolbox" for in-tool monitoring: which spectral features to use for timing, temperature, and impurity tracking, and how to interpret them reliably in an ASML-type EUV environment.

7.4 Outlook for future work

The cross-platform picture suggests targeted developments that will materially improve quantitative interpretation and tool monitoring:

(i) Collisional–radiative (CR) modelling tied to measured manifolds. Build and validate a reduced-kinetics CR model for H_2 and N_2 at 1–10 Pa, using as input: (i) Franck–Condon–corrected Fulcher $f_X(v)$ ($v = 0 \ldots 3$) and $T_{\mathrm{rot}}(d, v')$ with projection to T_{gas}; (ii) nitrogen SPS/FNS band ratios and rotational envelopes (including the EBL2 under-thermal case); (iii) Balmer *shapes* (non-linear $\ln N_u$ vs ΔE_u) rather than a single T_{exc}, in line with best practice for non-equilibrium hydrogen diagnostics [31, 73].

(ii) Synchronized timing campaigns. Repeat the EBL2 pressure series with hardware-synchronised triggers (common clock to ICCD and EUV diode) and narrower gates to remove inter-run offsets and gate convolution from the timing comparison.

(iii) Spectral hygiene in tool environments. Plan dedicated OES windows without auxiliary illumination (ellipsometry) in the Fulcher range; where this is not possible, use simple optical filtering in front of the spectrometer (e.g. a short-pass or a narrow notch filter centred on the strongest Sn feature) to reduce Sn stray light in the Balmer-ϵ region.

(iv) Absolute calibration + auxiliary probes. A calibrated white-light path during the EUV beamtimes would lift residual response uncertainties. Where feasible, complement OES with cavity-based n_e (MCRS) or microwave resonance in NPD-like references to cross-validate decay constants in Eq. (1.18) [31].

(v) Line identification of Sn features. High-resolution scans of the 350–700 nm range to catalogue narrow Sn features observed at EBL2 (Chapter 5, Fig. 5.20) will prevent misassignment in mixture runs and may add secondary diagnostics of source state.

Key comparative findings

For ease of reference, the most important cross-platform conclusions of this chapter (and of the thesis as a whole) are summarised here as a concise list:

1. **Fulcher across all platforms** is internally consistent: $T_{\mathrm{rot}}(d, v')$ appears "cold" (sub-RT), but projects via rotational constants to $T_{\mathrm{gas}} >$ RT; $f_X(v)$ peaks near $v = 2$ (Figs. 7.1–7.3) [42, 43, 73].

2. **Balmer manifolds** are *non-Boltzmann* in EUV and EBR; in NPD they are closest to linear over low-n only. A single T_{exc} is not generally meaningful outside NPD (Figs. 7.6, 7.7) [31, 73].

3. **Nitrogen under EUV** shows persistently under-thermal SPS/FNS envelopes (EBL2) despite flawless fits in EBR/NPD, pointing to EUV-specific kinetics at very low pressure.

4. **Timing hierarchy** holds robustly: atomic lines track the driver's leading edge best; molecular systems broaden/lag. OES provides a sensitive *relative* pulse proxy, not an absolute EUV waveform [31].

5. **Practical diagnostics for ASML:** use FNS as a high-sensitivity N_2 impurity monitor in H_2; use Fulcher for T_{gas}; use Balmer shapes (not T_{exc}) to track changes in excitation pathways [31, 42, 43, 73].

Conclusions

Summary of objectives

The overarching goal of this thesis was to develop and apply a consistent, transportable optical emission spectroscopy (OES) framework to *non-thermal* plasmas in N_2, H_2, and H_2/N_2 mixtures, with a specific focus on scanner-relevant, low-pressure environments. Three plasma-driving mechanisms were considered: nanosecond pulsed discharges (NPD), EUV-induced plasmas, and electron-driven plasmas (EBR). Across these platforms, the thesis aimed to (i) extract rotational and vibrational descriptors from molecular band systems, (ii) track fast temporal dynamics from nanoseconds to microseconds, and (iii) identify robust spectral signatures and limitations that matter in the ASML EUV-lithography context.

Main findings

Nanosecond pulsed discharges as a controlled benchmark

Nanosecond pulsed discharges provided a reproducible, electrically driven reference case in which excitation conditions are set primarily by the applied reduced field and by the discharge geometry. The main results for this configuration can be summarised as follows:

- **Nitrogen SPS/FNS at 1–500 mbar:** the N_2 SPS ($C^3\Pi_u \rightarrow B^3\Pi_g$) can be modelled robustly with the PGOPHER-based workflow developed in Chapter 3. The retrieved rotational temperatures remain in the few-hundred-kelvin range and vary moderately with pressure and discharge phase. The first-level C-state vibrational temperature $T_{01}^{(C)}$ lies in the few 10^3 K range and is strongly sensitive to the discharge dynamics.

- **Afterglow physics and metastable pooling:** extending the measurement window by stitching multiple kinetic sequences reveals a pronounced late-time rise/plateau of $T_{01}^{(C)}$ at high pressure (e.g. 110–500 mbar), consistent with the build-up of the N_2(A) manifold and

pooling-assisted feeding of $N_2(C)$ in the interpulse afterglow. This long-window approach exposes kinetics that are invisible in single short series and provides a direct experimental handle on metastable-assisted channels.

- **Low-pressure nitrogen (0.05 mbar):** the SPS and FNS fits remain stable and do not show the long-time distortions seen at higher pressures. Both T_{rot} and $T_{01}^{(\mathrm{C})}$ are essentially time-independent within the pulse, consistent with the suppression of pooling and reduced collisional relaxation at very low density.

- **Hydrogen NPD (Fulcher and Balmer):** Fulcher-α Q-branch analysis yields low $T_{\mathrm{rot}}(d, v')$ values that are nonetheless compatible with gas temperatures above room temperature after standard back-projection. The Franck-Condon-corrected ground-state vibrational populations consistently show an envelope peaking near $v = 2$. In contrast to the EUV-induced case, the NPD Balmer manifold is close to linear on a Boltzmann plot for the accessible lines, enabling extraction of an *effective* excitation temperature (order 1–2 eV). This value should not be interpreted as a direct measurement of T_e, but it provides a useful internal consistency check and a reference for cross-platform comparisons.

Overall, the NPD results establish that the analysis pipeline (instrumental function, response correction, forward modelling, and uncertainty propagation) is internally consistent and can retrieve physically plausible trends under conditions where collisional redistribution is sufficiently effective.

EUV-induced plasmas: EUV-specific kinetics at low pressure

EUV-induced plasmas differ qualitatively from discharges: they are photon-driven, low-density, and governed by photoelectron cascades, recombination, and wall/diffusion losses, rather than sustained by an applied field. The results show that this change in driving mechanism leaves clear, diagnostically relevant signatures in the spectra. The key EUV-specific findings are:

- **Under-thermal rotational envelopes in N_2 at EBL2:** the most striking observation of the thesis is that, at EBL2 (1–5 Pa), both SPS and FNS fits converge to systematically "under-thermal" rotational temperatures (well below room temperature) and do not reproduce the experimental band-head/wing balance with the fidelity observed for NPD (5 Pa) and for EBR. The persistence of this behaviour in both gated and integrated spectra rules out a purely gating-related

artefact and points instead to EUV-specific excitation/relaxation pathways. A plausible picture is that EUV photons generate a highly non-Maxwellian photoelectron population that excites N_2 into the emitting states on timescales comparable to, or shorter than, the rotational relaxation time at 1–5 Pa; if the C/B-state molecules radiatively decay before their rotational distribution can fully equilibrate with the gas, the observed envelopes will appear "colder" than the actual gas temperature. Additional state-selective channels (e.g. excitation from specific ground-state rotational/vibrational levels or ion–neutral reactions) may further bias the populated J manifolds. Clarifying the relative importance of these mechanisms requires dedicated collisional–radiative and kinetic modelling, and is therefore identified as a key target for future work.

- **Temporal response and EUV pulse proxy:** peak-maximum traces show that molecular emission (SPS/FNS/FPS) is broader and delayed relative to the EUV photodiode pulse. In contrast, atomic emission (notably the N triplet near 746 nm) follows the leading edge more closely, consistent with more direct, higher-threshold electron-impact excitation by prompt photoelectrons. In H_2, Balmer-line peak traces provide the closest optical proxy to the EUV timing on the rising edge, but systematically overestimate the pulse width on the falling edge due to collisional–radiative afterglow.

- **Hydrogen Fulcher diagnostics under EUV:** Fulcher-α analysis at EBL2 yields the same qualitative behaviour as in NPD: low $T_{\mathrm{rot}}(d, v')$ with a weak v' dependence, and a ground-state vibrational envelope peaking near $v = 2$. This suggests that, for H_2, the molecular rovibrational observables are comparatively robust across driving mechanisms, even when the electron source is photoelectric rather than field-driven.

- **Balmer non-Boltzmann behaviour under EUV:** unlike the NPD case, the EBL2 Balmer manifold is clearly non-Boltzmann: the level populations show systematic curvature and deviations that cannot be captured by a single excitation temperature. This reinforces the need to treat Balmer-based T_{exc} as a conditional diagnostic and to rely on molecular systems and modelling for quantitative interpretation in EUV-driven regimes.

- **Mixtures and impurity detection:** $N_2{}^+$ FNS emission remains detectable in H_2 down to very low N_2 partial pressures (down to $\sim 10^{-6}$ mbar in the present configuration), demonstrating that OES can serve as a sensitive, non-invasive impurity monitor in scanner-relevant environments.

Taken together, these findings show that EUV-induced plasmas can exhibit spectral behaviour that is not captured by assumptions that work well

for discharges (e.g. rotational thermalisation within emitting states). The "under-thermal" N_2 rotational envelopes emerge as a key open problem and a concrete target for follow-up experiments and modelling.

Industrial relevance: implications for EUV lithography environments

From the ASML perspective, the results support three practical conclusions:

- **OES is well suited for non-intrusive monitoring in low-density, short-lived plasmas:** the diagnostic can track EUV-triggered plasma formation and decay without perturbing the environment, where probes are impractical.
- **Atomic emission is a better fast-timing proxy than molecular emission:** atomic lines (Balmer in H_2, atomic N in N_2) follow the EUV rise more closely, whereas molecular systems inherently broaden/delay due to their formation pathways and finite radiative lifetimes.
- **Mixture sensitivity enables impurity tracking:** the $N_2{}^+$ FNS is a strong candidate for tracing N_2 impurities in predominantly H_2 ambients under EUV exposure.

Together, these conclusions indicate where OES can realistically be embedded into scanner operation (timing, contamination, and general plasma "health"), and where additional or complementary diagnostics would be required.

Methodological contributions

Beyond the plasma-specific findings, this thesis contributes an OES workflow that is designed to be portable across facilities and driving mechanisms. The main methodological elements are:

- A **validated forward-modelling pipeline** for N_2 SPS/FNS (PGOPHER synthesis $\rightarrow$ instrumental convolution $\rightarrow$ response correction $\rightarrow$ non-linear fitting) with consistent use of shared parameters and uncertainty propagation.
- A **robust descriptor for non-Boltzmann vibrational behaviour** in $N_2(C)$: the first-level temperature $T_{01}^{(C)}$ provides a stable metric for early vibrational populations without being dominated by non-linear high-ν' tails.

- A **Fulcher-α Q-branch analysis chain** that separates rotational fitting (restricted low-N' Boltzmann plots) from vibrational population inference (Franck–Condon-corrected back-projection), making explicit which quantities are well constrained and which remain model dependent.

- A **long-window, stitched kinetic approach** that extends the dynamic range of ns-gated OES into the μs regime and reveals afterglow processes (metastable build-up and pooling) that are otherwise missed.

Taken together, these elements form a reusable analysis template that can be ported to other plasma sources and facilities with minimal modification.

Limitations of the present work

Several constraints shaped the scope and interpretation of the results. The most relevant ones are:

- **Absolute calibration constraints:** for parts of the EUV campaign, full absolute calibration was not available, limiting the use of OES for absolute densities and shifting emphasis to relative trends and shape-based diagnostics.

- **Limited applicability of Stark-broadening diagnostics:** in principle, Stark broadening of hydrogen and nitrogen lines can provide time-resolved electron densities in low-temperature plasmas, and this has been demonstrated for nanosecond discharges under conditions comparable to those of this work in the literature [11, 27] and in related measurements by collaborators. Under the EUV conditions studied here, however, the expected Stark widths are well below the instrumental resolution, so this diagnostic could not be applied and n_e had to be inferred only indirectly from kinetics and modelling considerations rather than from direct line-broadening measurements.

- **Baseline artefacts in industrial environments:** on OLT-TS, concurrent illumination (ellipsometry) introduced baseline distortions that bias band-summed vibrational ratios. This underscores the need for dedicated optical conditions if quantitative mixture or vibrational analysis is required in-tool.

- **Model dependence in EUV-driven kinetics:** several key observables (notably the under-thermal N_2 envelopes and the non-Boltzmann Balmer manifold) require collisional–radiative and/or kinetic modelling to connect spectra to plasma parameters unambiguously.

Outlook

The results of this thesis suggest clear next steps, both experimentally and in modelling, to strengthen plasma diagnostics for EUV lithography. The most promising directions are:

- **Resolve the "under-thermal" N_2 problem:** targeted experiments should vary EUV dose, pulse structure, pressure, and wall conditions while recording SPS/FNS with higher spectral resolution and controlled backgrounds. On the modelling side, a dedicated CR/PIC treatment should test whether the observed envelopes can arise from (i) state-selective excitation by non-Maxwellian photoelectrons, (ii) vibrationally selective ion/neutral channels, and/or (iii) incomplete rotational redistribution in the emitting states.
- **Combine OES with complementary diagnostics where feasible:** adding microwave cavity resonance spectroscopy, calibrated EUV timing, or absorption-based vibrational diagnostics would reduce degeneracy in interpreting spectra and constrain n_e and the EEDF more directly.
- **Strengthen mixture-capable monitoring strategies:** systematic calibration of $N_2{}^+$ FNS sensitivity in H_2 (including stray-light control and line-identification of source-related backgrounds) can turn the demonstrated impurity detection into a deployable monitoring concept.
- **Improve in-tool robustness:** future OLT/industrial campaigns should prioritise controlled optical baselines (avoid auxiliary illumination in the OES line-of-sight) and, where possible, introduce gated acquisition for molecular windows to separate prompt and afterglow contributions.

Closing remark. This thesis demonstrates that a carefully calibrated and consistently applied OES framework can bridge fundamentally different plasma-driving mechanisms (NPD, EUV-induced, and electron-driven sources) and can reveal both robust cross-platform trends (e.g. Fulcher-based rovibrational behaviour) and mechanism-specific fingerprints (notably the under-thermal N_2 envelopes under EUV excitation). These outcomes provide a practical foundation for diagnostics in scanner-relevant environments and define concrete modelling and experimental targets for advancing plasma understanding in EUV lithography.

Appendix A: NPD setup

In an optical emission spectroscopy (OES) experiment, the plasma-emitted light is analysed by an ICCD camera coupled to a spectrograph. The plasma is generated in a vacuum chamber through a nanosecond high-voltage (HV) discharge in a flowing gas mixture (flow set by a mass flow controller; pressure regulated by a vacuum pumping system). In our setup, the discharge can be operated either in a pin-to-plate or in a plate-to-plate electrode configuration; unless otherwise stated, the measurements in this thesis refer to the pin-to-plate geometry, while the very-low-pressure nitrogen experiments at 0.05 mbar reported in Chapter 4 were performed with a plate-to-plate configuration.
Precise synchronisation between the HV pulse and the waveform generator, as well as between the ns-pulse and the ICCD acquisition gate, is essential. A trigger delay generator is therefore included in the timing chain.
Light collection to the spectrograph is implemented via an optical fibre and a round-to-linear fibre bundle. A two-lens relay images the plasma onto the fibre core while matching the fibre numerical aperture. The bundle output is then coupled to the spectrograph through an F#-matcher.
A schematic of the experimental configuration is shown in figure A.1. Details of each subsystem are provided in the following sections.

Vacuum chamber

The vacuum vessel is a steel cube ($45\times45\times45$ cm^3) mounted on a rail for convenient access. It houses the electrodes that generate the discharge and allows operation in both pin-to-plate and plate-to-plate configurations. In the pin-to-plate geometry, a tungsten pin mounted on an aluminium post faces a mushroom-shaped steel plate; both are coated with PTFE (Teflon) to suppress parasitic surface discharges (with the trade-off of parasitic current associated with dielectric capacitance). For the plate-to-plate geometry used in the 0.05 mbar nitrogen measurements (Chapter 4), the same chamber layout is employed with two opposing electrodes instead of a sharp pin.

The bottom electrode is fixed at the chamber center, whereas the upper electrode (pin or plate, depending on the configuration) can be positioned along all three orthogonal directions using external micrometric handles. The

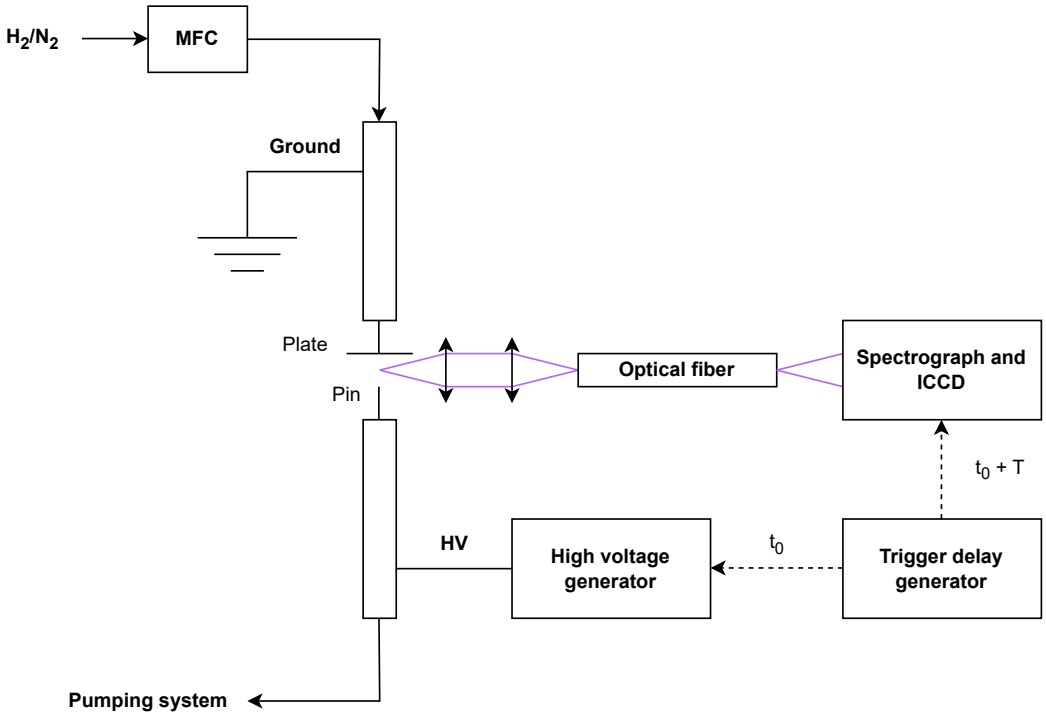

Figure A.1: Scheme of the optical emission spectroscopy setup.

nominal minimum gap for breakdown studies in the pin-to-plate configuration is 5 mm; in both configurations, the gap can be adjusted from outside with the chamber closed to meet the experimental requirements.

Pumping system

The chamber pressure is actively regulated during measurements. The pumping system consists of a stacked mechanical booster backed by a rotary vane pump, which increases throughput and allows operation over a wide pressure range. Pressure is monitored using a combination of a Pirani gauge (Edwards APG-M-NW16 Active Pirani Gauge D02171000), two capacitive gauges (MKS Instruments 627BX.1MDD1B Baratron 0.1 mbar, Vacuum General Pressure Transducer CM-02-10 10 Torr), and a strain gauge (Edwards High Vacuum D35726000 Strain Gauge Diaphragm Transducer ASG 1000 mbar), together covering an absolute pressure range from $\sim 10^{-3}$ to 10^{3} mbar. The primary gauges are mounted on the chamber top flange to measure the local process pressure.
Controllers for all gauges are installed above the setup. The pumps themselves are located in a separate room below the laboratory to minimise acoustic and mechanical noise at the setup. Because this requires a longer vacuum line, an additional Pirani gauge is placed in-line between the chamber base and the pumps to monitor pressure along the line and verify consistency with the chamber readings.

Gas lines

Hydrogen and nitrogen are introduced into the chamber to produce H_2/N_2 pulsed plasmas with the HV discharge. The gases are supplied from external cylinders; two inlet valves feed the chamber and enable arbitrary mixture ratios.
Flows are controlled by a dedicated gas line equipped with a mass flow meter and a mass flow controller (MFC), allowing setpoints up to 5000 sccm. A constant chamber pressure is maintained by balancing gas inflow (MFC setpoint) and pumping speed. With the vacuum valve open, continuous-flow operation enables stable pressures that depend on the MFC settings. The gas line hardware and control electronics (including National Instruments boards and software) are installed adjacent to the chamber.

Pump velocity

An initial characterisation of the effective pumping speed was performed by recording the steady-state chamber pressure as a function of N_2 flow (figure A.2). At the maximum tested flow (5000 sccm), the pressure reached only 1.6 mbar—insufficient for the intended operating range.
To extend the accessible pressure window, the vacuum line at the chamber base was split into two branches. One branch uses a large-bore (tombak) tube to reach low pressures quickly or to evacuate the chamber. The second branch includes a pronounced reduction in conductance and an additional throttle valve to finely control throughput, enabling higher and more stable pressures (up to hundreds of mbar) during discharges. Only one branch is opened at a time (the other remains isolated by a safety valve) to maintain control of the gas flow.

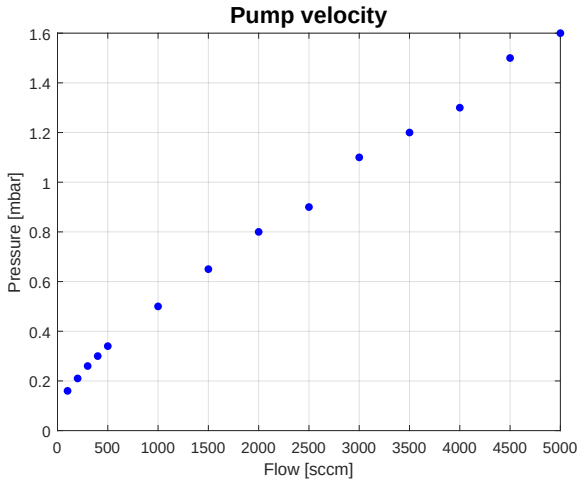

Figure A.2: Chamber pressure versus gas flow, used to assess the effective pumping speed for N_2.

Optical tables and alignment

Two optical tables are installed on the left and right sides of the chamber to host the collection optics and timing hardware; two additional small breadboards at the front and back provide access along the remaining axes. A He–Ne laser was split into two beams and re-crossed through the chamber; their intersection defined the reference point for mounting the bottom tungsten electrode in the pin-to-plate geometry.

Fiber matching

Light emitted by the plasma exits through side windows and is collected into an optical fibre, since the spectrograph and ICCD are located away from the chamber. A two-lens system collects the light from the right-side window and focuses it into the fibre, accounting for the fibre numerical aperture (NA = 0.22; maximum acceptance angle $\approx 12.7^\circ$). With an optimal lens pair, the coupled light is transported from the chamber to the spectrograph with typical transmission losses of $\sim$40%. Before coupling to the spectrograph, the circular fibre output is rearranged with a round-to-linear bundle to illuminate a single entrance row.

Spectrograph and ICCD

The fibre bundle output is coupled to the spectrograph via an F#-matcher mounted at the entrance slit (custom for the Andor Shamrock SR-303i-B). The spectrograph is equipped with interchangeable gratings; in the measurements reported in this thesis, the central wavelength and grating are chosen to cover the relevant spectral windows (e.g. N_2 SPS/FNS, H_2 Fulcher, Balmer lines) with a resolution compatible with the expected line widths. The spectrally dispersed light is detected by an Andor iStar DH334T ICCD camera, operated in gated mode and synchronised to the HV pulse via a delay generator.

Wavelength and response calibration. Wavelength calibration is performed using a low-pressure calibration lamp with well-known emission lines. The line centroids are fitted and a polynomial dispersion relation is derived for each grating/central-wavelength setting; typical residuals are well below the instrumental resolution. This wavelength solution is then applied to all plasma spectra acquired with the same spectrograph configuration.

A relative irradiance (spectral-response) calibration of the entire detection chain (collection optics, fibre, F#-matcher, spectrograph, ICCD) is carried out using a calibrated broadband light source with a known spectral irradiance distribution. The calibration source is positioned to illuminate the collection optics in the same geometry as the plasma, and spectra are recorded with the same settings (grating, central wavelength, slit width, ICCD gain/gate) used in the plasma measurements. After dark subtraction,

the measured lamp spectrum is divided by the certified irradiance curve of the source, yielding the system response function $C(\lambda)$ for each configuration. A smooth fit (e.g. spline or low-order polynomial) is used to suppress noise in $C(\lambda)$, and all plasma spectra are subsequently corrected as

$$I_{\mathrm{corr}}(\lambda) \;=\; \frac{I_{\mathrm{raw}}(\lambda)}{C(\lambda)}.$$

This relative-response calibration is essential for quantitative use of band intensities (e.g. vibrational population analysis and comparison of different spectral windows), and the same procedure is applied consistently throughout the thesis (see also Chapter 3).

High Voltage generator and Faraday cage

The discharge is driven by a burst-mode nanosecond HV pulse generator (NPG-18/100k), capable of delivering single ns pulses at 40–50 kV. For safe and reproducible operation, the HV unit is externally triggered via a delay generator.

The generator is housed in a Faraday cage mechanically integrated with the chamber base to suppress parasitic discharges outside the plasma volume. The cage encloses the HV feedthrough and the generator while leaving the two vacuum lines outside.

The cage consists of an upper and a lower compartment: the HV generator and cooling fans are mounted in the lower section; the upper section hosts a Tektronix Beaverton HV probe and a Magnelab current transformer for voltage and current measurements. The vacuum electrical feedthrough is connected to the power supply via a HV cable routed through both cage panels. Voltage and current probes are wired to an external oscilloscope using coaxial cables that exit the cage through small feedthrough holes.

Discharge

Examples of discharges in nitrogen and hydrogen were obtained across a wide pressure range, from low-pressure conditions (0.05 mbar) to higher-pressure operation (up to 500 mbar), demonstrating the setup's flexibility across different plasma regimes. The bulk of the measurements presented in this thesis (1–500 mbar) were performed in the pin-to-plate configuration, whereas the very-low-pressure case at 0.05 mbar used the plate-to-plate geometry to obtain a more homogeneous discharge across the gap.

Representative images of nitrogen discharges at intermediate pressure in pin-to-plate operation are shown in Fig. A.3. The low-pressure plate-to-plate geometry is illustrated in Fig. A.4 for a pure hydrogen discharge at 0.05 mbar. For completeness, Fig. A.5 provides an external view of the reactor ("cube") with the surrounding optical tables used for collection optics and timing electronics, while Fig. A.6 shows the glow of a 0.05 mbar nitrogen discharge as seen through one of the side windows.

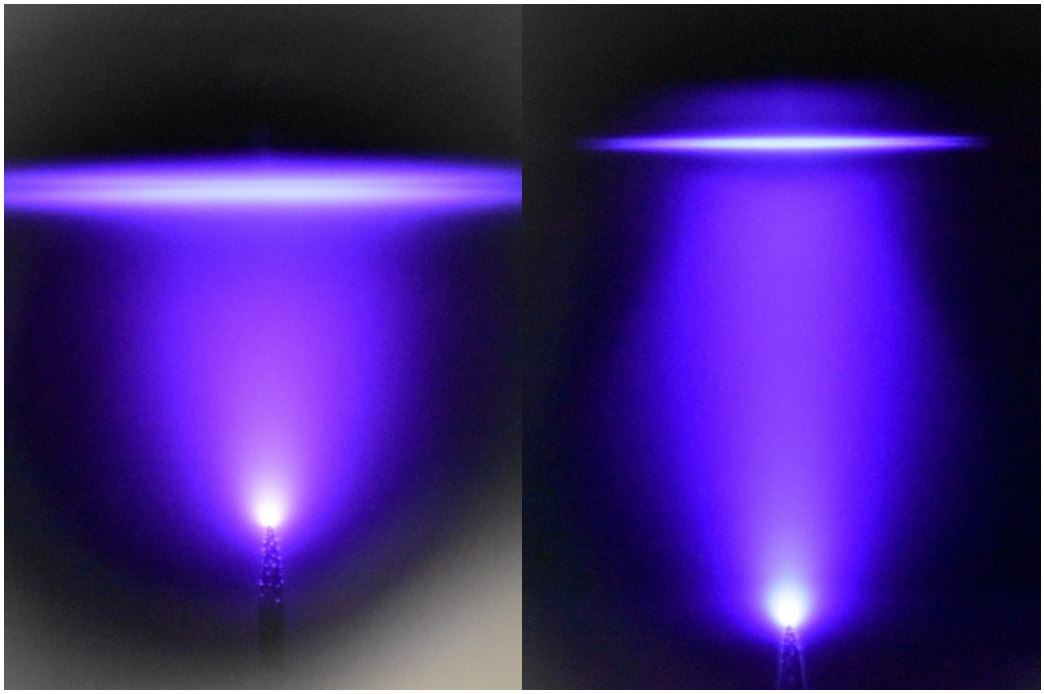

(a) **(b)**

Figure A.3: Discharge in pure nitrogen at (a) 1 mbar and (b) 11 mbar in pin-to-plate configuration.

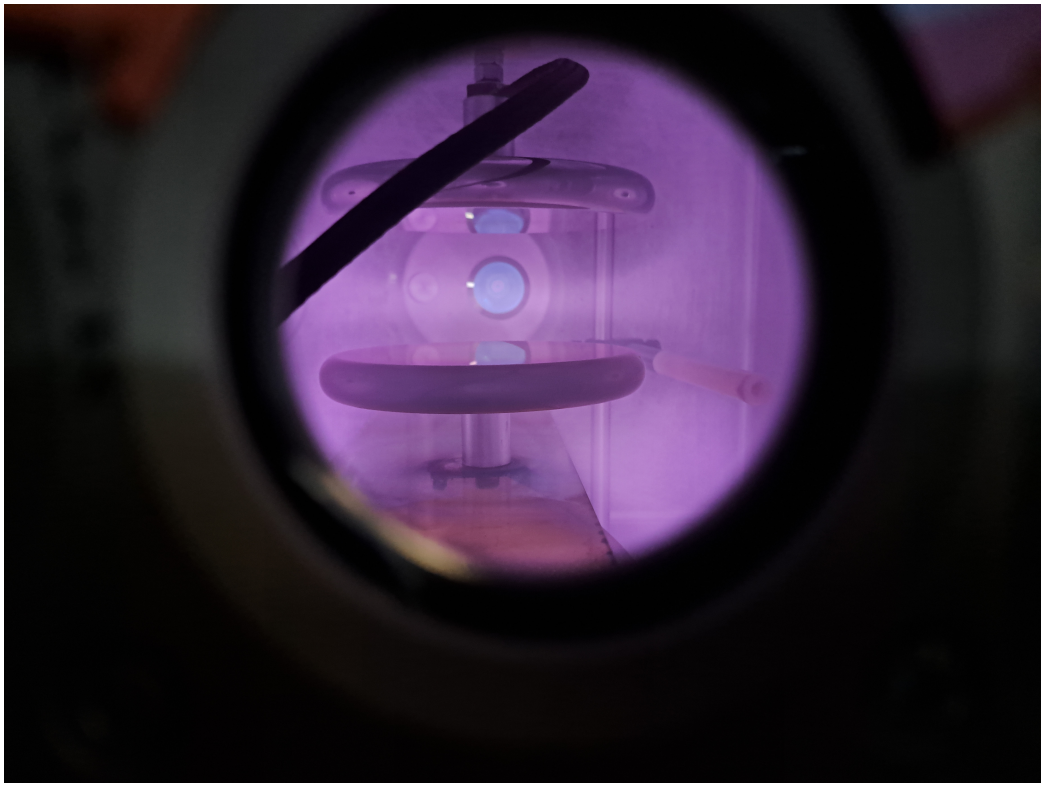

Figure A.4: Discharge in pure hydrogen at 0.05 mbar in plate-to-plate configuration, showing a diffuse glow across the electrode gap at very low pressure.

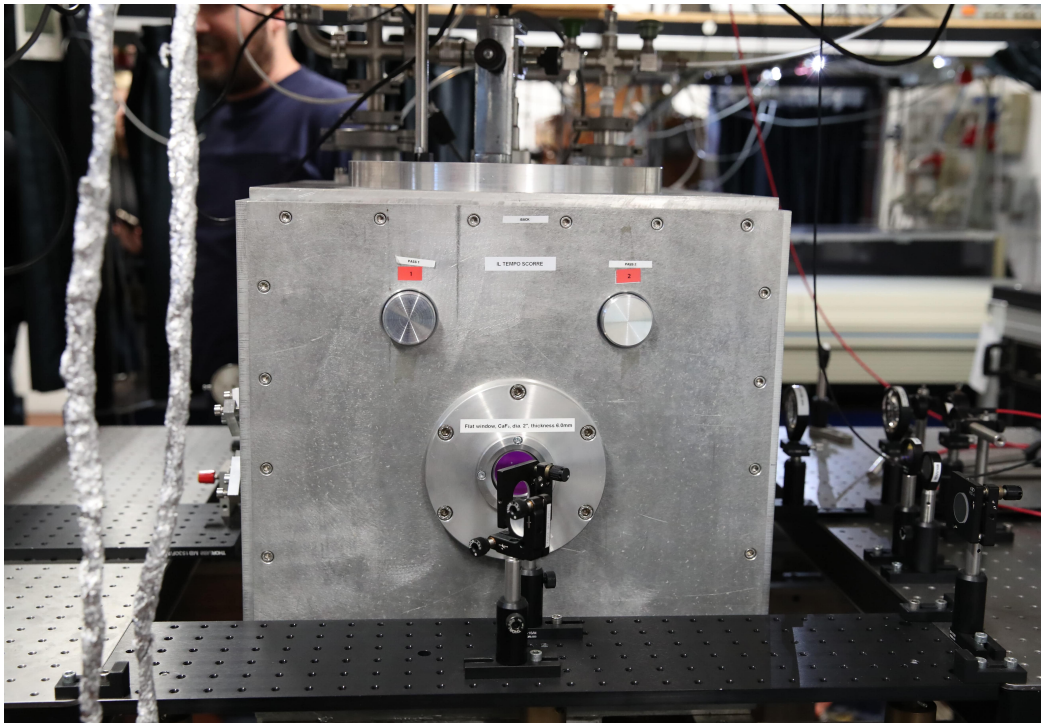

Figure A.5: External view of the NPD reactor (steel cube) with optical tables on both sides, hosting the collection optics, timing electronics, and ancillary hardware described in this appendix.

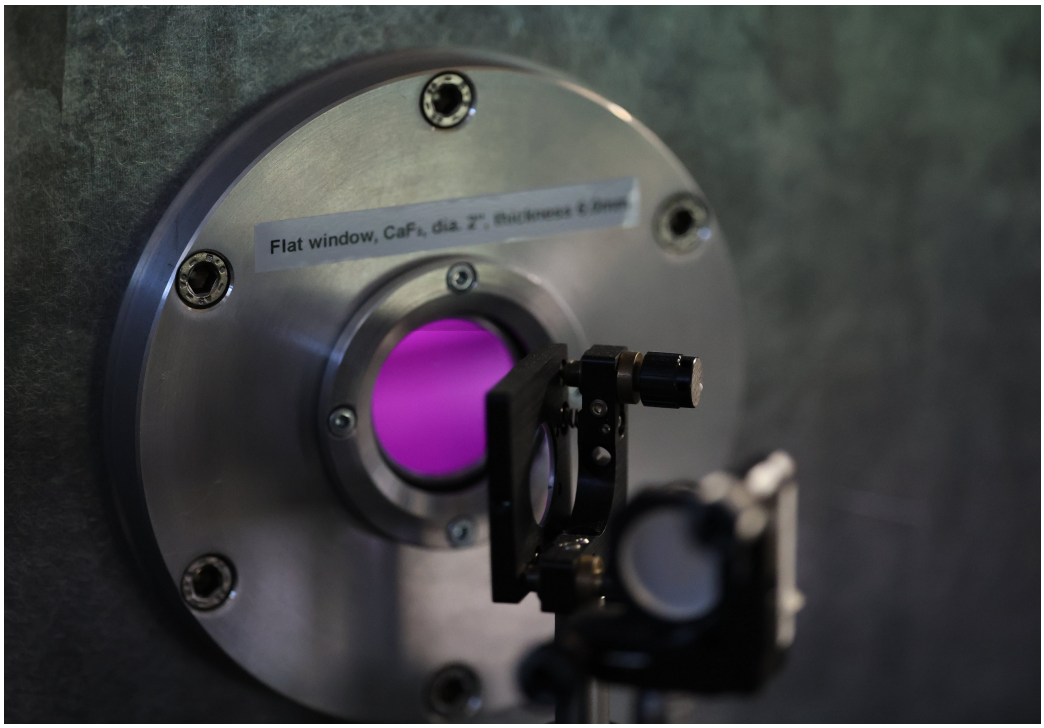

Figure A.6: View through a side window during a 0.05 mbar nitrogen discharge in plate-to-plate configuration, highlighting the homogeneous low-pressure glow in the chamber volume.

Appendix B: EBL2 setup

System overview

EBL2 comprises (i) a Sn-fueled LDP EUV source mounted on rails for maintenance access; (ii) a Collector Module with two Ru-coated grazing-incidence ellipsoids forming an intermediate focus (IF); (iii) an Exposure Chamber with high-stability chuck on a hexapod stage, imaging ellipsometer, and EUV diagnostics; (iv) a vacuum handler coupled to an atmospheric handler for SEMI dual-pod interfacing; and (v) an XPS system connected to the beamline via vacuum transfer [53,54,58]. A simplified top-view schematic of the beamline layout is shown in Fig. B.1, and a photograph of the full system is given in Fig. B.2.

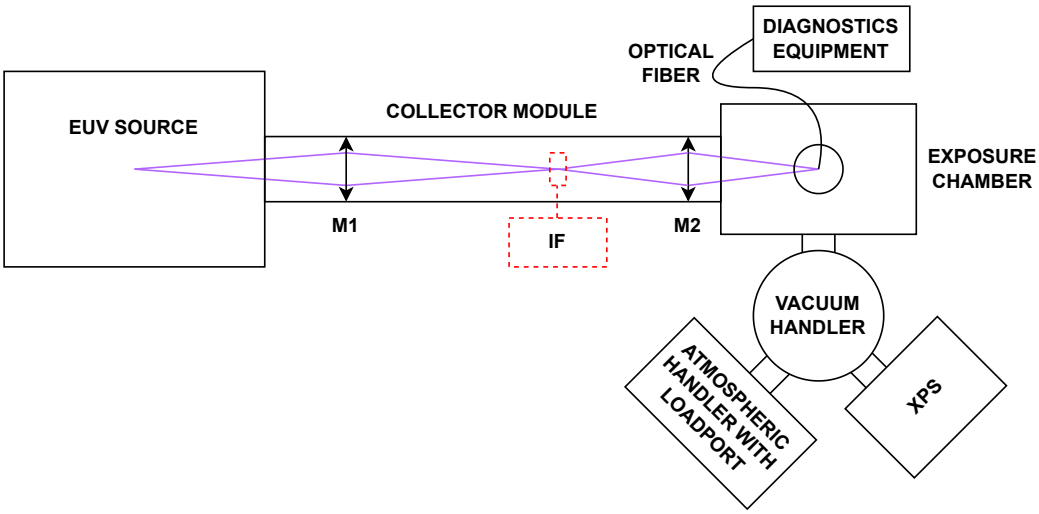

Figure B.1: Top-view schematic of the EBL2 beamline, showing the relative positions of the LDP EUV source, Collector Module (M1/M2), intermediate focus (IF), Exposure Chamber, vacuum handler, and XPS branch. The scheme also indicates the OES diagnostics used in this thesis: a lens stack on the top flange collects plasma-emitted light into an optical fiber, which feeds an external diagnostics setup comprising spectrograph, ICCD camera, delay generator, and control laptop. This highlights both the EUV optical path and the vacuum partitions between source, collector, and exposure environments.

Figure B.2: Photograph of the EBL2 system corresponding to the schematic in Fig. B.1, from left to right: EUV source, collector module, exposure chamber, vacuum handler with load lock, storage, and XPS. The atmospheric handler with pod opener is not yet present. Reproduced from [53].

In addition to the native EUV metrology, the top-view schematic also shows the optical emission spectroscopy (OES) chain used in this work: a fixed set of lenses mounted vertically on the top flange of the Exposure Chamber collects the plasma-emitted light, focuses it into an optical fiber, and guides it to an external diagnostics rack where a spectrograph and ICCD camera, controlled via a delay generator and laptop, perform time-resolved spectral measurements (analogous to the NPD setup in Appendix A).

The IF provides vacuum decoupling between the source and exposure environments and serves as an insertion plane for apertures and spectral purity filters (SPFs) [54, 58]. The source–collector assembly can translate along the rail to vary the beam focus at the sample plane, enabling spot-size and power-density control [53].

EUV source: LDP principle and performance

The Ushio LDP source generates EUV radiation at 13.5 nm in a 2% spectral bandwidth (BW) by triggering a discharge between rotating Sn-coated electrodes with a focused laser pulse. A short, focused laser pulse pre-ionizes a local tin vapour/plasma plume between the electrodes; a subsequent high-current electrical pulse then drives the main discharge, pinching the plasma and producing the in-band EUV emission. The source integrates a multi-stage debris shield to suppress Sn droplets, clusters, fast ions, and neutrals,

protecting downstream optics [55–57]. Brightness scales approximately linearly with repetition rate, and recent source generations report hundreds of W/mm^2/sr at ∼10 kHz at the plasma, with documented improvements in pulse-to-pulse stability and debris mitigation [55–57]. The production platform emphasizes reliability (multi-hundred-hour continuous runs) and availability for long-duration tests [56, 57].

Collector module and beam transport

The Collector Module uses two grazing-incidence ellipsoids:

- **M1** images the source into an intermediate focus (IF) at ∼2/3 of the distance from the source, which also functions as a differential pumping aperture to isolate the source and exposure chamber gas environments.
- **M2** images the IF onto the sample plane in the Exposure Chamber.

At the IF, apertures and SPFs can be inserted to tailor the beam pupil and suppress out-of-band (OoB) radiation [54, 58]. In-focus operation achieves W/mm^2-level in-band power densities on target; defocus is achieved by translating the source+collector along the rail, enabling spot sizes from ∼1 mm up to > 30 mm (donut-shaped at the largest defocus) [53, 58]. A more detailed view of the Collector Module optics, including the two ellipsoids and the IF plane, is shown in Fig. B.3. A dedicated metrology port on the source head can be used for low-power EUV diagnostics independent of exposure [54].

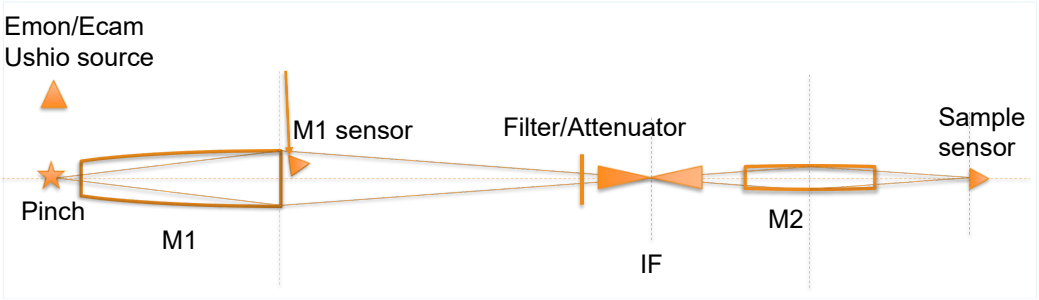

Figure B.3: Schematic of the EBL2 Collector Module. Two Ru-coated grazing-incidence ellipsoids (M1, M2) image the LDP plasma into an intermediate focus (IF) and subsequently onto the sample plane in the Exposure Chamber; the IF plane also hosts apertures and spectral purity filters (SPFs) for pupil and spectral tailoring. Reproduced from [74].

Exposure chamber: mechanics, metrology, and diagnostics

The Exposure Chamber is fully metal-sealed, electro-polished, and cleanliness-optimized. A high-stiffness chuck (mask-sized or custom holders) is mounted on an external hexapod via a large vacuum bellows so that

all motors/encoders remain in atmosphere for maintainability and cleanliness. Actuation for gripping/flipping is performed by pneumatically driven bellows (lubricant-free in vacuum). The chamber integrates:

- **Imaging ellipsometer** for in-situ tracking of surface condition, alignment marks, and optical contrast during exposure.
- **EUV diagnostics on stage:** calibrated photodiodes for power and dose metrology; a scintillator + camera system to visualize EUV spot position/shape (sub-mm crosshair alignment is correlated between the back-scintillator image and front-side ellipsometer view); crosshairs are embossed on the scintillator coating for absolute referencing to stage coordinates.
- **Thermal control:** the chuck is actively temperature-controlled via a resistive heater and closed-loop control; typical operation allows sub-ambient setpoints (e.g. down to $\approx$–20°C) during high-flux irradiation, with stable temperature during continuous exposure.

These mechanical and metrology features, and the alignment workflow correlating scintillator and ellipsometer views, are detailed in [53, 54].

Vacuum, gas environment, and cleanliness

The beamline implements vacuum decoupling at the IF. The exposure chamber achieves high vacuum base pressure ($< 10^{-6}$ mbar) and admits high-purity process gases with controlled partial pressures (typical up to a few mbar) to emulate scanner/source conditions. Allowed gases include H_2, He, Ar, N_2, O_2, and XCDA (Extreme Clean Dry Air, i.e. ultra-high-purity clean dry air), as well as selected contaminants for dedicated studies. A differentially pumped residual gas analyzer (RGA) monitors background and assures gas composition control [53, 54]. The atmospheric and vacuum handlers are designed for SEMI dual-pod compatibility and NXE backside cleanliness requirements (particle-addition specs verified over hundreds of load cycles) [53, 58].

Sample handling and load path

The automated handling chain accepts full-size reticles (with/without pellicles) and custom small-sample holders. The atmospheric handler unloads a dual pod, rotates/flips as needed, and loads the sample to the vacuum handler via a load lock. The vacuum handler transfers the sample to the Exposure Chamber chuck or to a Parking/Cleaning station. A Sample Rotation Unit (SRU) allows in-vacuum rotation. After exposure, the same chain can transfer the sample to XPS without breaking vacuum [53, 54].

Integrated XPS and vacuum transfer

A modified Kratos Nova XPS accepts full reticles and small-sample holders (including angle-resolved mounts). The vacuum handler provides contamination-safe transfer from the Exposure Chamber to XPS and back, enabling dose–response studies with immediate, in-vacuo surface analysis (e.g. carbon removal, oxidation, or adsorbate chemistry under EUV) [53, 54].

EUV metrology: power, dose, and spot

On-stage, calibrated photodiodes measure EUV power; intensity maps are obtained by scanning the beam over pinholes or by imaging on a scintillator with known conversion. The total in-band power at sample is calculated from the photodiode photocurrent, calibration factor, and pulse repetition frequency. Dose control is achieved by tuning repetition rate, focus/defocus (spot size), and exposure time. With SPFs installed (e.g. Zr/Si/Mo stacks), OoB light outside 12.5–18.5 nm can be reduced by an order of magnitude relative to in-band, yielding actinic conditions representative of scanner optics [53, 54, 58].

Performance envelope (typical)

Representative parameters (config-dependent):

- In-band EUV at 13.5 nm: $\gtrsim 1$ W in 2% BW at 3 kHz at sample; power density $> 1\,\mathrm{W/mm^2}$ in focus (scales with spot size).
- Repetition rate: 1 Hz–10 kHz (3 kHz nominal), linear scaling of brightness with pulse frequency.
- Spot size: $\sim 0.8 \times 1.2$ mm (focus) to > 30 mm (defocus donut).
- Exposure duration: >100 h uninterrupted exposures demonstrated; dose control $< 20\%$ in free-running mode.

These operating envelopes and scalings are consistent with reported performance and source-side improvements [54–58].

Safety, reliability, and maintenance

The source head employs proven debris shields to preserve collector reflectivity; incremental design and laser-trigger optimizations have reduced fast-ion flux and sputter rates at optics [56, 57]. The source/collector rail system permits rapid maintenance access. Reliability metrics (availability, continuous-run hours) have progressed to production-relevant levels, enabling extended campaigns with stable brightness and minimal downtime [53, 54].

Notes for experiment replication

When reproducing EBL2 conditions: (i) specify in-band EUV power and spot size (or focus setting), (ii) log repetition rate and duty cycle, (iii) record gas type/partial pressure and base pressure before admission, (iv) capture simultaneous scintillator and ellipsometer images for spatial registration, and (v) calibrate photodiodes and SPFs prior to dose-critical runs [53, 54].

Appendix C: OLT-TS setup

Scope and constraints

This appendix documents the optical–diagnostics implementation used on the OLT-TS 2.5 exposure platform for time-resolved optical emission spectroscopy (OES) of EUV-induced hydrogen plasmas. Only public information on EUV sources is included here; engineering details of the OLT-TS hardware and interfaces are proprietary and therefore omitted. The OES methodology (spectrograph, ICCD gating, calibration and analysis) follows the procedures already reported in the main text and earlier appendices, and is summarized below only as needed for completeness.

Public background on EUV sources and the intermediate focus

Industrial EUV lithography systems generate 13.5 nm radiation by creating a tin (Sn) plasma (laser-produced) and collecting the in-band EUV with a multilayer mirror collector. The beam is relayed to an *intermediate focus* (IF), which acts as a vacuum decoupling and insertion plane for apertures and spectral purity filters (SPFs). In operation, a low-pressure hydrogen ambient is present to mitigate mirror contamination and debris, and it also gives rise to a low-density EUV-induced hydrogen plasma in the illuminated volume.[1]

Notes for replication from public sources. Public literature consistently describes: (i) LPP Sn plasma at the source; (ii) a collector that images into the IF; (iii) optional SPFs at the IF to suppress out-of-band (OOB) light; and (iv) operation with hydrogen background gas for contamination control and debris mitigation (and the consequent formation of a weak EUV-induced H_2 plasma in the beam path).

[1]Representative public sources: ASML EUV overview; reviews and reports on EUV sources and spectral purity; and open literature on EUV-induced hydrogen plasma in scanners.

OLT-TS measurement concept (OES at the IF)

On OLT-TS we implemented a passive, line-of-sight OES diagnostic to monitor EUV-induced hydrogen plasma in the vicinity of the beam IF. Light from the plasma volume is collected through the chamber's sapphire window and transported to a Czerny–Turner spectrograph equipped with a gated ICCD. The collection optics (relay lenses and a vacuum feedthrough fiber) were arranged to image the IF region onto the fiber core while respecting the fiber numerical aperture. The same optical chain and data-reduction workflow used on the EBL2 beamline (Delft) were employed here, allowing a direct comparison between facilities. A schematic overview of the exposure chamber and the diagnostic line of sight is shown in Fig. C.1.

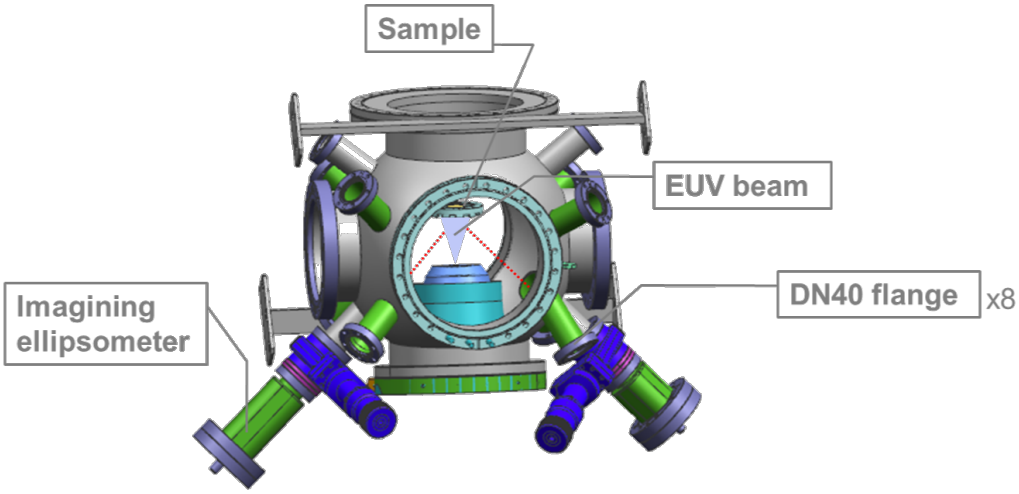

Figure C.1: Scheme of exposure chamber.

Field of view and focus. The relay was adjusted so that the collection depth of field spans the IF and a small axial region around it. Alignment was performed with visible surrogate beams and fiducials on the chamber, and verified by maximizing EUV-driven emission signals during test exposures, without revealing internal dimensions or optics placements.

Spectral ranges and targets. Spectra were recorded in two windows: (i) 385–395 nm for N_2^+(FNS) checks during mixture tests; and (ii) 600–635 nm for the H_2 Fulcher-α Q-branch analysis (Q1 lines of $v' = 0$–3), which is used to retrieve rotational temperatures and ground-state projections as detailed in Chapter 3 and Chapter 5.

Timing and gating. ICCD gate widths in the tens–hundreds of ns range were employed to resolve the prompt EUV-driven phase and the early afterglow. The trigger was synchronized to the EUV exposure timing provided

by the tool control, with fixed delays stepped across the exposure window to build time histories. (Exact trigger interfaces and electronic timing paths are excluded.)

Calibration and data processing (as used throughout the thesis)

Wavelength calibration was performed with a pen lamp in the identical optical configuration. Radiometric response was characterized with a calibrated broadband source where available; otherwise, relative-response corrections $C(\lambda)$ were used. The instrumental function (Gaussian width) was determined previously to the measurements in the cleanroom and used to constrain Gaussian (or Voigt) fits of Fulcher Q-branch lines. Rotational temperatures $T_{\mathrm{rot}}(d, v')$ were obtained from three-line Boltzmann plots ($\mathrm{Q1}(N' = 1, 2, 3)$) and projected to T_{gas} via rotational-constant ratios. Vibrational populations were formed from response-corrected band sums, using Franck–Condon factors for back-projection as in the main text.

C.5 Operating environment (public aspects)

In line with public reports for EUV exposure platforms, experiments were carried out in low-pressure hydrogen (and selected H_2/N_2 mixtures) representative of scanner-relevant ambients. The formation of a weak EUV-induced plasma in H_2 at the beam spot is well known in the literature and underpins hydrogen-based mitigation of carbon contamination on optics; the same phenomenon enables OES diagnostics of the transient plasma here.

Differences versus EBL2 (what matters for this work)

The two facilities use different EUV source types and operating regimes:

- **OLT-TS:** tin LPP source of the same class as ASML lithography machines, operating at ∼50 kHz repetition rate with scanner-level in-band power at the IF. The platform is an integrated exposure tool with a hydrogen ambient.
- **EBL2 (Delft):** tin LDP source, typically operated around ∼3 kHz (optimal). The in-band EUV power is of a similar order but somewhat lower than scanner tools.

For OES, these differences mainly affect the temporal structure and photon flux per pulse. Our diagnostics (collection optics, spectrograph, and

gated ICCD) and analysis workflow were kept identical across both facilities; gate widths and delays were chosen to resolve the prompt EUV-driven phase and early afterglow in each case. Where comparisons are shown, signals are normalized to exposure dose so that Fulcher-based temperature trends remain directly comparable between OLT-TS and EBL2.

C.7 Safety and non-disclosure

All alignments were performed with interlocks active and without exposing personnel or equipment to EUV radiation. No internal mechanical drawings, distances, mirror specifications, or timing schemas of OLT-TS are reported here. Only generally available information about EUV sources (LPP/LDP Sn plasma, collector, IF, SPFs, H_2 ambient) is referenced, and the spectroscopic workflow is identical to that already documented elsewhere in this thesis.

Summary. This appendix establishes how the OES diagnostic was coupled to the OLT-TS exposure chamber (via the sapphire window, focused at the IF) and clarifies that analysis follows the same, previously validated Fulcher-based workflow used on EBL2. The description is limited to publicly available information about EUV sources and to non-sensitive details of the optical chain.

Appendix D: EBR setup

Motivation and role of EBR

Electron Beam Research (EBR) provides a clean, configurable testbed to emulate key conditions of EUV-induced plasmas under scanner-relevant pressures while keeping all active source hardware outside the exposure chamber. Ion and radical fluxes, radical-to-ion ratios, and few-eV peak ion energies can be reproduced with continuous-wave (CW) or pulsed operation (pulse durations from hundreds of ns to 1 s, repetition rates from 1 to 100 kHz). The temporal evolution of EBR plasmas in pulse trains (build-up, plateau, decay) qualitatively mirrors that of pulsed EUV-induced plasmas, enabling mechanism-by-mechanism comparisons for plasma–surface interaction studies [72, 75].

EBR system overview

The EBR platform is a low-pressure, differentially pumped system in which a high-current, monoenergetic electron beam is injected into H_2 (and other gases) to produce plasma by electron-impact ionization. The architecture employs two vacuum chambers connected by a 10 mm orifice: the first houses the electron gun (e-gun), the second is the exposure/diagnostics chamber. This physical separation isolates all active source hardware from the exposure volume, reducing contamination risks relative to in-chamber sources [72]. A schematic cross-sectional view of the setup is shown in Fig. D.1.

Electron gun, extraction, and focusing

The e-gun (TES-63-ES, Polygon Physics) employs a micro ECR source that operates at 0.5–5 Pa within the ECR cavity. Ignition uses 5 W of microwave power; electrons are extracted with a 0–3000 V bias, which sets their kinetic energy, and focused by an Einzel lens (0–3000 V) to pass through the 10 mm orifice. Mechanical pre-alignment is performed with a port-aligner,

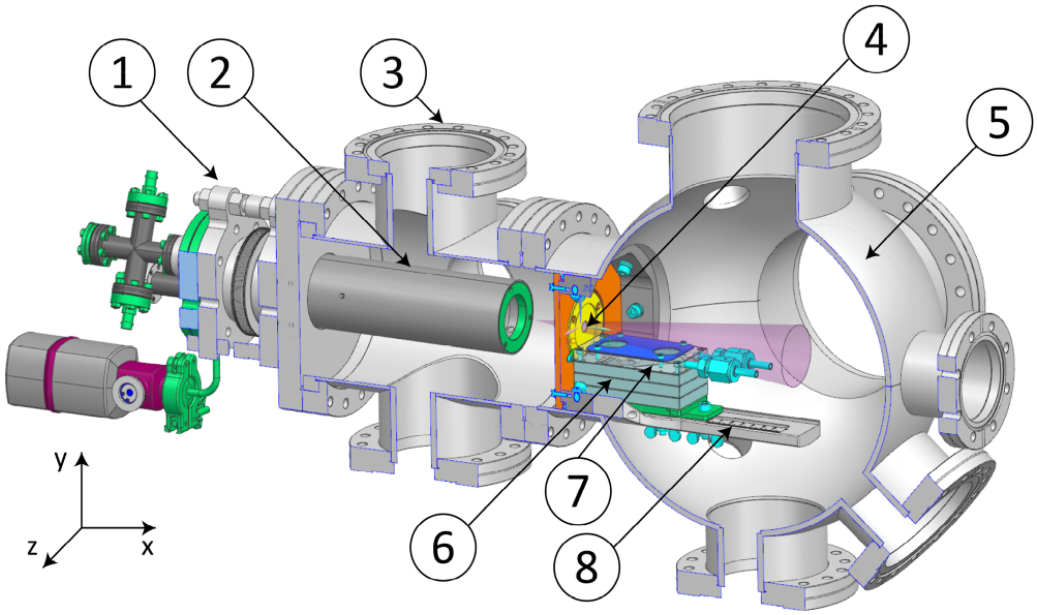

Figure D.1: Schematic cross-sectional view of the EBR setup containing a port aligner (1) used for mounting an e-gun (2) onto a smaller vacuum vessel (3), which is connected via a 10 mm orifice (4) with a main exposure chamber (5). A sample stage (6) consists of three 1 cm spacers and a top, water-cooled plate (7), which has openings for two 1 in. samples. The stage is positioned on a rail (8), which allows for stage movement along the x axis. Reproduced from [72].

and a Faraday cup behind the orifice is used to optimize transmission (measured $>$ 92% after optimization). The beam current is controlled via the ECR cavity pressure and microwave power; typical operating range is 0.1–30 mA (specification up to 50 mA). Reported electron energies span 500–2000 eV [72].

Exposure chamber, pumping, and sample handling

The exposure chamber is pumped by a 180 l/s turbomolecular pump (Pfeiffer TMU 2000M), achieving a typical base pressure of 2×10^{-6} Pa without bakeout. The sample platform consists of a copper/alloy mount with a water-cooled top plate. The y position relative to the beam can be adjusted using three removable 1 cm spacers; a linear guide enables translation along x with respect to the orifice. The stage accommodates two seats for 1 inch samples and cover plates, with threaded holes for mounting sensors [72].

Gas handling and operating conditions

High-purity gases (H_2 in the reported experiments, with N_2 and Ar also possible) are dosed into the exposure chamber using a mass-flow controller (Alicat MC500). Typical operating pressures are 1–10 Pa. Plasma ignition in H_2 occurs immediately when the beam enters the gas-filled chamber and is visible as a faint violet glow. The absence of antennas/electrodes in the exposure chamber minimizes hydrogen-induced outgassing compared with microwave/RF sources that place hardware in vacuum [72].

Ion-energy and radical diagnostics

Ion fluxes and ion energy distribution functions (IEDFs) are measured with a retarding field energy analyzer (RFEA, Semion, Impedans). In continuous-wave operation at 10 Pa H_2 and electron energy $E_e = 1000\,\mathrm{eV}$, the maximum ion flux reaches $6 \times 10^{18}\,\mathrm{m^{-2}\,s^{-1}}$ with a peak ion energy of about 2 eV; the IEDF peak shifts between 2.0 and 2.5 eV as the beam current is varied. In pulsed mode (500 ns pulses at 50 kHz), the plasma shows a clear build-up over successive pulses and a decay after the pulse train, qualitatively resembling pulsed EUV-induced plasmas in scanners [72, 75].

The recombinative H radical flux is measured with a differential thermopile H-Flux Sensor (HFS, dual surfaces with different recombination coefficients). Reported values reach up to $4\times10^{20}\,\mathrm{m^{-2}\,s^{-1}}$ at 10 Pa, $E_e = 1000\,\mathrm{eV}$, and 25 mA [72].

Cleanliness assessment

Cleanliness was benchmarked by exposing a Ru-on-sapphire sample for 8 h to H_2 plasma (integrated ion dose $1.7 \times 10^{23}\,\mathrm{m^{-2}}$) and performing post-exposure XPS. Trace contaminants (Zn, Si, S, P, Sn) totaling 3.4 at.% (<1 monolayer equivalent) were observed—superior to off-line microwave/RF plasma setups and comparable to ECR. Based on this analysis, Stodolna *et al.* recommend adding an ultra-clean metallic shroud around the stage to further reduce residual contamination [72].

Operating notes and comparison to EUV plasmas

For H_2, maximizing the ion flux typically occurs around $E_e \sim 1000\,\mathrm{eV}$: at higher energies the electron-impact ionization cross section decreases, whereas at lower energies competing excitation/dissociation channels become more prominent. In pulsed operation, EBR reproduces the qualitative temporal evolution of pulsed EUV-induced plasmas (build-up/plateau/decay),

despite the absence of EUV photons. Electron-induced secondary emission from surfaces can partially mimic EUV photoelectron secondaries in surface processes, supporting cross-comparisons of plasma–surface mechanisms [72, 75].

Bibliography

[1] Alexander Fridman. *Plasma Chemistry*. Cambridge University Press, Cambridge, 2008. doi:10.1017/CBO9780511546075.

[2] Yukikazu Itikawa. Cross sections for electron collisions with nitrogen molecules. *Journal of physical and chemical reference data*, 35(1):31–53, 2006. doi:10.1063/1.1937426.

[3] V. Guerra, P. A. Sa, and J. Loureiro. Kinetic modelling of low-pressure nitrogen discharges and the corresponding afterglows. *European Physical Journal Applied Physics*, 28(2):125–152, 2004. doi:10.1051/epjap:2004188.

[4] J. H. van Helden, P. J. van den Oever, W. M. M. Kessels, M. C. M. van de Sanden, D. C. Schram, and R. Engeln. Production mechanisms of NH and NH_2 radicals in N_2–H_2 plasmas. *Journal of Physical Chemistry A*, 111(45):11460–11472, 2007. PMID: 17929903. doi:10.1021/jp0727650.

[5] Yuri P. Raizer. *Gas Discharge Physics*. Springer, Berlin, Heidelberg, 1991. 1st ed., XI + 449 pp. URL: https://link.springer.com/book/9783642647604.

[6] Mario Capitelli, Gianpiero Colonna, and Antonio D'Angola. *Fundamental Aspects of Plasma Chemical Physics*, volume 66 of *Springer Series on Atomic, Optical, and Plasma Physics*. Springer, New York, NY, 2012. 1st ed., XVIII + 310 pp. doi:10.1007/978-1-4419-8182-0.

[7] Vasco Guerra, Antonio Tejero-del Caz, Carlos D. Pintassilgo, and Luís L. Alves. Modelling N_2–O_2 plasmas: volume and surface kinetics. *Plasma Sources Science and Technology*, 28(7):073001, jul 2019. doi:10.1088/1361-6595/ab252c.

[8] S. M. Starikovskaia. Plasma assisted ignition and combustion. *Journal of Physics D: Applied Physics*, 39(16):R265–R299, aug 2006. doi:10.1088/0022-3727/39/16/R01.

[9] Peter Bruggeman and Ronny Brandenburg. Atmospheric pressure discharge filaments and microplasmas: physics, chemistry and diagnos-

tics. *Journal of Physics D: Applied Physics*, 46(46):464001, oct 2013. doi:10.1088/0022-3727/46/46/464001.

[10] Cesare Montesano, Toine P. W. Salden, Luca Matteo Martini, Giorgio Dilecce, and Paolo Tosi. Co_2 reduction by nanosecond plasma discharges: revealing the dissociation time scale and the importance of pulse sequence. *The Journal of Physical Chemistry C*, 127(21):10045–10050, 2023. doi:10.1021/acs.jpcc.3c02547.

[11] Matteo Ceppelli, T. P. W. Salden, Luca Matteo Martini, Giorgio Dilecce, and Paolo Tosi. Time-resolved optical emission spectroscopy in co_2 nanosecond pulsed discharges. *Plasma Sources Science and Technology*, 30(11):115010, 2021. doi:10.1088/1361-6595/ac2411.

[12] L. M. Martini, S. Lovascio, G. Dilecce, et al. Time-resolved co_2 dissociation in a nanosecond pulsed discharge. *Plasma Chemistry and Plasma Processing*, 38:707–718, 2018. doi:10.1007/s11090-018-9893-3.

[13] A. Tejero-del Caz, V. Guerra, D. Gonçalves, M. Lino da Silva, L. Marques, N. Pinhão, C. D. Pintassilgo, and L. L. Alves. The LisbOn KInetics Boltzmann solver. *Plasma Sources Science and Technology*, 28(4):043001, 2019. doi:10.1088/1361-6595/ab0537.

[14] V. Y. Banine, K. N. Koshelev, and G. H. P. M. Swinkels. Physical processes in EUV sources for microlithography. *Journal of Physics D: Applied Physics*, 44(25):253001, 2011. doi:10.1088/0022-3727/44/25/253001.

[15] R. M. van der Horst, J. Beckers, E. A. Osorio, D. I. Astakhov, W. J. Goedheer, C. J. Lee, V. V. Ivanov, V. M. Krivtsun, K. N. Koshelev, D. V. Lopaev, F. Bijkerk, and V. Y. Banine. Exploring the electron density in plasma induced by EUV radiation: I. experimental study in hydrogen. *Journal of Physics D: Applied Physics*, 49(14):145203, 2016. doi:10.1088/0022-3727/49/14/145203.

[16] D. I. Astakhov, W. J. Goedheer, C. J. Lee, V. V. Ivanov, V. M. Krivtsun, K. N. Koshelev, D. V. Lopaev, R. M. van der Horst, J. Beckers, E. A. Osorio, and F. Bijkerk. Exploring the electron density in plasma induced by EUV radiation: II. numerical studies in argon and hydrogen, 2016. doi:10.1088/0022-3727/49/29/295204.

[17] J. Beckers, T. van de Ven, R. M. van der Horst, D. I. Astakhov, and V. Y. Banine. EUV-induced plasma: a peculiar phenomenon of a modern lithographic technology. *Applied Sciences*, 9(14):2827, 2019. URL: https://www.mdpi.com/2076-3417/9/14/2827, doi:10.3390/app9142827.

[18] J. Beckers, T. H. M. van de Ven, C. A. de Meijere, R. M. van der Horst, M. van Kampen, and V. Y. Banine. Energy distribution functions for ions from pulsed EUV-induced plasmas in low-pressure N_2-diluted H_2 gas. *Applied Physics Letters*, 114(13):133502, 2019. doi:10.1063/1.5091825.

[19] M. van de Kerkhof, A. Yakunin, V. Kvon, S. Cats, L. Heijmans, M. Chaudhuri, and D. Astakhov. Plasma-assisted discharges and charging in EUV-induced plasma. *Journal of Micro/Nanopatterning, Materials, and Metrology*, 20(1):013801, 2021. doi:10.1117/1.JMM.20.1.013801.

[20] R. M. van der Horst, E. A. Osorio, V. Y. Banine, and J. Beckers. The influence of the EUV spectrum on plasma induced by EUV radiation in argon and hydrogen gas. *Plasma Sources Science and Technology*, 25(1):015012, 2016. doi:10.1088/0963-0252/25/1/015012.

[21] Hans R. Griem. *Principles of Plasma Spectroscopy*. Cambridge Monographs on Plasma Physics. Cambridge University Press, Cambridge, 1997. doi:10.1017/CBO9780511524578.

[22] U. Fantz. Basics of plasma spectroscopy. *Plasma Sources Science and Technology*, 15(4):S137–S147, 2006. doi:10.1088/0963-0252/15/4/S01.

[23] S. V. Pancheshnyi, S. M. Starikovskaia, and A. Yu. Starikovskii. Collisional deactivation of $N_2(C^3\Pi_u, v = 0, 1, 2, 3)$ states by N_2, O_2, H_2 and H_2O molecules. *Chemical Physics*, 262(2–3):349–357, 2000. URL: https://www.sciencedirect.com/science/article/pii/S0301010400003384, doi:10.1016/S0301-0104(00)00338-4.

[24] J. H. van Helden, W. Wagemans, G. Yagci, R. A. B. Zijlmans, D. C. Schram, R. Engeln, G. Lombardi, G. D. Stancu, and J. Röpcke. Detailed study of the plasma-activated catalytic generation of ammonia in n_2–h_2 plasmas. *Journal of Applied Physics*, 101(4):043305, 2007. doi:10.1063/1.2645828.

[25] M. van de Kerkhof, A. M. Yakunin, V. Kvon, A. Nikipelov, D. Astakhov, P. Krainov, and V. Banine. Euv-induced hydrogen plasma and particle release. *Radiation Effects and Defects in Solids*, 177(5-6):486–512, 2022. doi:10.1080/10420150.2022.2048657.

[26] G. Denbeaux, R. Garg, C. Mbanaso, J. Waterman, L. Yankulin, Y.-J. Fan, W. Montgomery, K. Dean, K. Orvek, A. Wüest, and Y. Wei. Extreme ultraviolet resist outgassing and its effect on nearby optics. In *Proc. SPIE 6921, Advances in Resist Materials and Processing Technology XXV*, volume 6921, page 69211G, 2008. doi:10.1117/12.772670.

[27] Matteo Ceppelli. *Time-resolved optical diagnostics for plasma dissociation of CO_2*. PhD thesis, University of Trento, Trento, Italy, 2022. URL: https://dx.doi.org/10.15168/11572_336722, doi:10.15168/11572_336722.

[28] Cesare Montesano. *Experimental investigation of nanosecond pulsed discharges for CO_2 recycling*. PhD thesis, University of Trento, Trento, Italy, 2023. URL: https://dx.doi.org/10.15168/11572_372611, doi:10.15168/11572_372611.

[29] Ibrahim Sadiek, Alexander Puth, Grzegorz Kowzan, Akiko Nishiyama, Sarah-Johanna Klose, Jürgen Röpcke, Norbert Lang, Piotr Masłowski, and Jean-Pierre H. van Helden. Precision spectroscopy of non-thermal molecular plasmas using mid-infrared optical frequency comb fourier transform spectroscopy. *Plasma Sources Science and Technology*, 33(7):075011, 2024. doi:10.1088/1361-6595/ad5df4.

[30] Ibrahim Sadiek, Adam J. Fleisher, Jakob Hayden, Xinyi Huang, Andreas Hugi, Richard Engeln, Norbert Lang, and Jean-Pierre H. van Helden. Dual-comb spectroscopy of ammonia formation in non-thermal plasmas. *Communications Chemistry*, 7(1):110, 2024. doi:10.1038/s42004-024-01190-7.

[31] Richard Engeln, Bart Klarenaar, and Olivier Guaitella. Foundations of optical diagnostics in low-temperature plasmas. *Plasma Sources Science and Technology*, 29(6):063001, jun 2020. doi:10.1088/1361-6595/ab6880.

[32] D Burnette, A Montello, I V Adamovich, and W R Lempert. Nitric oxide kinetics in the afterglow of a diffuse plasma filament. *Plasma Sources Science and Technology*, 23(4):045007, jun 2014. URL: https://dx.doi.org/10.1088/0963-0252/23/4/045007, doi:10.1088/0963-0252/23/4/045007.

[33] N D Lepikhin, A V Klochko, N A Popov, and S M Starikovskaia. Long-lived plasma and fast quenching of N2($C^3\Pi_u$) by electrons in the afterglow of a nanosecond capillary discharge in nitrogen. *Plasma Sources Science and Technology*, 25(4):045003, may 2016. URL: https://dx.doi.org/10.1088/0963-0252/25/4/045003, doi:10.1088/0963-0252/25/4/045003.

[34] Ivan Shkurenkov, David Burnette, Walter R Lempert, and Igor V Adamovich. Kinetics of excited states and radicals in a nanosecond pulse discharge and afterglow in nitrogen and air*. *Plasma Sources Science and Technology*, 23(6):065003, aug 2014. URL: https://dx.doi.org/10.1088/0963-0252/23/6/065003, doi:10.1088/0963-0252/23/6/065003.

[35] Helen L. Davies, Vasco Guerra, Marjan van der Woude, Timo Gans, Deborah O'Connell, and Andrew R. Gibson. Vibrational kinetics in repetitively pulsed atmospheric pressure nitrogen discharges: average-power-dependent switching behaviour. *Plasma Sources Science and Technology*, 32(1):014003, 2023. doi:10.1088/1361-6595/aca9f4.

[36] Colin M. Western. Pgopher: A program for simulating rotational, vibrational and electronic spectra. *Journal of Quantitative Spectroscopy and Radiative Transfer*, 186:221–242, 2017. Satellite Remote Sensing and Spectroscopy: Joint ACE-Odin Meeting, October 2015. URL: https://www.sciencedirect.com/science/article/pii/S0022407316300437, doi:10.1016/j.jqsrt.2016.04.010.

[37] Laiz R. Ventura and C. E. Fellows. The N_2 second positive ($C^3\Pi_u \rightarrow B^3\Pi_g$) system reviewed: Improved data and analysis. *Journal of Quantitative Spectroscopy and Radiative Transfer*, 239:106645, 2019. URL: https://www.sciencedirect.com/science/article/pii/S0022407319304972, doi:10.1016/j.jqsrt.2019.106645.

[38] Jonggu Han, Woojin Park, Jongsik Kim, Keon-Hee Lim, Gwang-Ho Lee, Seongjin In, Jitae Park, Se-Jin Oh, Sang Ki Nam, Doug-Yong Sung, and Se Youn Moon. Synthetic molecular spectra modeling for determining rotational, vibrational, and excitation temperatures of low-pressure nitrogen plasma. *Spectrochimica Acta Part A: Molecular and Biomolecular Spectroscopy*, 304:123389, 2024. URL: https://www.sciencedirect.com/science/article/pii/S1386142523010740, doi:10.1016/j.saa.2023.123389.

[39] Augustin C Tibère-Inglesse, Sean D McGuire, and Christophe O Laux. Inferring gas temperature from N_2 emission via rotational distribution of the N2 $B^3\Pi_g$ and $C^3\Pi_u$ states. *Plasma Sources Science and Technology*, 32(7):075018, aug 2023. URL: https://dx.doi.org/10.1088/1361-6595/ace5d1, doi:10.1088/1361-6595/ace5d1.

[40] Hira Fatima, M. Usman Ullah, S. Ahmad, Mubashair Imran, S. Sajjad, S. Hussain, and A. Qayyum. Spectroscopic evaluation of vibrational temperature and electron density in reduced pressure radio frequency nitrogen plasma. *SN Applied Sciences*, 3(6):646, 2021. doi:10.1007/s42452-021-04651-z.

[41] https://webbook.nist.gov/cgi/cbook.cgi?ID=C7727379&Units=SI&Mask=1000.

[42] S. Briefi, D. Rauner, and U. Fantz. Determination of the rotational population of H_2 and D_2 including high-n states in low temperature plasmas via the fulcher-α transition. *Journal of Quantitative Spectroscopy and Radiative Transfer*, 187:135–144,

2017. URL: https://www.sciencedirect.com/science/article/pii/S0022407316303983, doi:10.1016/j.jqsrt.2016.09.015.

[43] S Briefi and U Fantz. A revised comprehensive approach for determining the h2 and d2 rovibrational population from the fulcher-α emission in low temperature plasmas. *Plasma Sources Science and Technology*, 29(12):125019, dec 2020. doi:10.1088/1361-6595/abc085.

[44] Z. Qing, D. K. Otorbaev, G. J. H. Brussaard, M. C. M. van de Sanden, and D. C. Schram. Diagnostics of the magnetized low-pressure hydrogen plasma jet: Molecular regime. *Journal of Applied Physics*, 80(3):1312–1324, 1996. doi:10.1063/1.362930.

[45] https://webbook.nist.gov/cgi/cbook.cgi?ID=C1333740&Mask=1000.

[46] U. Fantz and D. Wünderlich. Franck–condon factors, transition probabilities, and radiative lifetimes for hydrogen molecules and their isotopomeres. *Atomic Data and Nuclear Data Tables*, 92(6):853–973, 2006. URL: https://www.sciencedirect.com/science/article/pii/S0092640X06000386, doi:10.1016/j.adt.2006.05.001.

[47] U Fantz and B Heger. Spectroscopic diagnostics of the vibrational population in the ground state of and molecules. *Plasma Physics and Controlled Fusion*, 40(12):2023, dec 1998. doi:10.1088/0741-3335/40/12/003.

[48] K. Fujii, K. Sawada, A. Kuzmin, M. Goto, M. Kobayashi, L. H. Scarlett, D. V. Fursa, I. Bray, M. C. Zammit, and T. M. Biewer. Experimental validation of a collision–radiation dataset for molecular hydrogen in plasmas. *Physics of Plasmas*, 31(9), 2024. doi:10.1063/5.0220933.

[49] D L Rusterholtz, D A Lacoste, G D Stancu, D Z Pai, and C O Laux. Ultrafast heating and oxygen dissociation in atmospheric pressure air by nanosecond repetitively pulsed discharges. *Journal of Physics D: Applied Physics*, 46(46):464010, oct 2013. URL: https://dx.doi.org/10.1088/0022-3727/46/46/464010, doi:10.1088/0022-3727/46/46/464010.

[50] Xiao-Jiang Huang, Yu Xin, Lei Yang, Quan-Hua Yuan, and Zhao-Yuan Ning. Spectroscopic study on rotational and vibrational temperature of N_2 and N_2^+ in dual-frequency capacitively coupled plasma. *Physics of Plasmas*, 15(11):113504, 11 2008. arXiv:https://pubs.aip.org/aip/pop/article-pdf/doi/10.1063/1.3025826/14946701/113504_1_online.pdf, doi:10.1063/1.3025826.

[51] N Minesi, S Stepanyan, P Mariotto, G D Stancu, and C O Laux. Fully ionized nanosecond discharges in air: the thermal spark. *Plasma Sources Science and Technology*, 29(8):085003, aug 2020. URL: https://dx.doi.org/10.1088/1361-6595/ab94d3, doi:10.1088/1361-6595/ab94d3.

[52] Xin Yang, Elijah Jans, Caleb Richards, Sai Raskar, Dirk van den Bekerom, Kai Wu, and Igor V Adamovich. Measurements of atoms and metastable species in N_2 and H_2–N_2 nanosecond pulse plasmas. *Plasma Sources Science and Technology*, 31(1):015017, jan 2022. URL: https://dx.doi.org/10.1088/1361-6595/ac3053, doi:10.1088/1361-6595/ac3053.

[53] Norbert Koster, Edwin te Sligte, Freek Molkenboer, Alex Deutz, Peter van der Walle, Pim Muilwijk, Wouter Mulckhuyse, Bastiaan Oostdijck, Christiaan Hollemans, Björn Nijland, Peter Kerkhof, Michel van Putten, and Jeroen Westerhout. First light at EBL2. In Eric M. Panning, editor, *Extreme Ultraviolet (EUV) Lithography VIII*, volume 10143, page 101431N. International Society for Optics and Photonics, SPIE, 2017. doi:10.1117/12.2257997.

[54] Edwin te Sligte, Michel van Putten, Freek T. Molkenboer, Peter van der Walle, Pim M. Muilwijk, Norbert B. Koster, Jeroen Westerhout, Peter J. Kerkhof, Bastiaan W. Oostdijck, Wouter Mulckhuyse, and Alex F. Deutz. Characterization of EBL2 EUV exposure facility. In Paolo A. Gargini, Patrick P. Naulleau, Kurt G. Ronse, and Toshiro Itani, editors, *International Conference on Extreme Ultraviolet Lithography 2017*, volume 10450, page 1045027. International Society for Optics and Photonics, SPIE, 2017. doi:10.1117/12.2280356.

[55] Y. Teramoto, B. Santos, G. Mertens, R. Kops, M. Kops, F. Küpper, G. Niimi, H. Yabuta, A. Nagano, T. Yokoyama, M. Yoshioka, T. Shirai, N. Ashizawa, H. Sato, K. Nakamura, and K. Kasama. High-radiance LDP source for mask inspection application. In O. R. Wood and E. M. Panning, editors, *Extreme Ultraviolet (EUV) Lithography V*, volume 9048, page 904813. International Society for Optics and Photonics, SPIE, 2014. doi:10.1117/12.2046423.

[56] Yusuke Teramoto, Bárbara Santos, Guido Mertens, Ralf Kops, Margarete Kops, Wilko van Nunspeet, Marcel Schneider, Klaus Bergmann, and Yoshihiko Sato. High-brightness LDP source: variation of EUV-emitting plasma. Presentation, EUV Source Workshop 2021, Session S65, 2021. URL: https://www.euvlitho.com/2021/S65.pdf.

[57] Kazuya Aoki, Yoshihiko Sato, Yusuke Teramoto, Takahiro Shirai, Shunichi Morimoto, Hidenori Watanabe, Akihisa Nagano, Daisuke Yajima,

and Noritaka Ashizawa. High-brightness LDP source. In Yosuke Kojima, editor, *Photomask Japan 2023: XXIX Symposium on Photomask and Next-Generation Lithography Mask Technology*, volume 12915, page 1291509. International Society for Optics and Photonics, SPIE, 2023. doi:10.1117/12.2688117.

[58] Norbert Koster, Edwin te Sligte, Freek Molkenboer, Alex Deutz, Peter van der Walle, Pim Muilwijk, Wouter Mulckhuyse, Bastiaan Oostdijck, Christiaan Hollemans, Björn Nijland, Peter Kerkhof, Michel van Putten, and Jeroen Westerhout. Poster: First light on EBL2. Poster presented at the International EUVL Symposium, 2016. EUVL Symposium 2016. URL: https://www.tno.nl/media/9213/poster-first-light-on-ebl2.pdf.

[59] H. L. Davies, V. Guerra, M. van der Woude, T. Gans, D. O'Connell, and A. R. Gibson. Vibrational kinetics in repetitively pulsed atmospheric pressure nitrogen discharges: average-power-dependent switching behaviour. *Plasma Sources Science and Technology*, 32(1):014003, 2023. doi:10.1088/1361-6595/aca9f4.

[60] R. F. Wuerker, L. Schmitz, T. Fukuchi, and P. Straus. Lifetime measurements of the excited states of N_2 and N_2^+ by laser-induced fluorescence. *Chemical Physics Letters*, 150(6):443–446, 1988. URL: https://www.sciencedirect.com/science/article/pii/0009261488804342, doi:10.1016/0009-2614(88)80434-2.

[61] https://physics.nist.gov/PhysRefData/Handbook/Tables/nitrogentable2.htm.

[62] G. J. Bengtsson, J. Larsson, S. Svanberg, and D. D. Wang. Natural lifetimes of excited states of neutral nitrogen determined by time-resolved laser spectroscopy. *Phys. Rev. A*, 45:2712–2715, Mar 1992. URL: https://link.aps.org/doi/10.1103/PhysRevA.45.2712, doi:10.1103/PhysRevA.45.2712.

[63] A. F. M. Y. Haider, Mehera Kamal Ira, Z. H. Khan, and K. M. Abedin. Radiative lifetime measurement of excited neutral nitrogen atoms by time resolved laser-induced breakdown spectroscopy. *J. Anal. At. Spectrom.*, 29:1385–1392, 2014. URL: http://dx.doi.org/10.1039/C3JA50199J, doi:10.1039/C3JA50199J.

[64] E. H. Lock, R. F. Fernsler, S. Slinker, and S. G. Walton. Experimental and theoretical estimation of excited species generation in pulsed electron beam–generated plasmas produced in pure argon, nitrogen, oxygen, and their mixtures. Technical Report NRL/MR/6750–11-9333, Naval Research Laboratory, Washington, DC, May 2011. URL: https://www.researchgate.net/publication/235115837_

Experimental_and_Theoretical_Estimation_of_Excited_Species_Generation_in_Pulsed_Electron_Beam-Generated_Plasmas_Produced_in_Pure_Argon_Nitrogen_Oxygen_and_Their_Mixtures.

[65] F Sigeneger, J Ellis, J Harhausen, N Lang, and J H van Helden. Verified modeling of a low pressure hydrogen plasma generated by electron cyclotron resonance. *Plasma Sources Science and Technology*, 31(10):105011, nov 2022. doi:10.1088/1361-6595/ac963e.

[66] J. H. van Helden, W. Wagemans, G. Yagci, R. A. B. Zijlmans, D. C. Schram, R. Engeln, G. Lombardi, G. D. Stancu, and J. Röpcke. Detailed study of the plasma-activated catalytic generation of ammonia in n_2–h_2 plasmas. *Journal of Applied Physics*, 101(4), 2007. doi:10.1063/1.2645828.

[67] Annemie Bogaerts and Erik C. Neyts. Plasma technology: An emerging technology for energy storage. *ACS Energy Letters*, 3(4):1013–1027, 2018. doi:10.1021/acsenergylett.8b00184.

[68] Kevin H. R. Rouwenhorst, Yannick Engelmann, Kevin van 't Veer, Rolf S. Postma, Annemie Bogaerts, and Leon Lefferts. Plasma-driven catalysis: green ammonia synthesis with intermittent electricity. *Green Chem.*, 22(19):6258–6287, 2020. URL: http://dx.doi.org/10.1039/D0GC02058C, doi:10.1039/D0GC02058C.

[69] J. A. Andersen, J. M. Christensen, M. Østberg, A. Bogaerts, and A. D. Jensen. Plasma-catalytic dry reforming of methane: Screening of catalytic materials in a coaxial packed-bed dbd reactor. *Chemical Engineering Journal*, 397:125519, 2020. URL: https://www.sciencedirect.com/science/article/pii/S1385894720316478, doi:10.1016/j.cej.2020.125519.

[70] Francesco Spadoni, Sofia Perina, Gaia Castellani, Paolo Tosi, Paolo Fornasiero, Vincenzo M. Sglavo, and Luca Matteo Martini. The support can disguise the catalytic effect: The case of silver on alumina in plasma ammonia synthesis. *ChemSusChem*, 18(13):e202402778, 2025. URL: https://chemistry-europe.onlinelibrary.wiley.com/doi/10.1002/cssc.202402778, doi:10.1002/cssc.202402778.

[71] Sam Labeur. Electron beam and euv induced hydrogen plasma characterization with optical emission spectroscopy. Unpublished bachelor's thesis, Fontys University of Applied Sciences, 2025.

[72] A. S. Stodolna, T. W. Mechielsen, P. van der Walle, C. Meekes, and H. Lensen. Novel low-temperature and high-flux hydrogen plasma source for extreme-ultraviolet lithography applications. *Journal of Vacuum Science & Technology B*, 42(5):052601, 2024. doi:10.1116/6.0003701.

[73] U. Fantz. Basics of plasma spectroscopy. *Plasma Sources Sci. Technol.*, 15(4):S137–S147, 2006. doi:10.1088/0963-0252/15/4/S01.

[74] Norbert Koster, Herman Bekman, Michel van Putten, Rory de Zanger, Rob Ebeling, Arnold Storm, Chien-Ching Wu, Jetske Stortelder, Peter van der Walle, and Jochem Janssen. Status of EBL2: an EUV irradiation facility at TNO and upcoming upgrades. Presentation, EUV Source Workshop 2019, Session S31, 2019. URL: https://www.euvlitho.com/2019/S31.pdf.

[75] M. A. van de Kerkhof, A. M. Yakunin, D. Astakhov, M. van Kampen, R. van der Horst, and V. Banine. EUV-induced hydrogen plasma: pulsed-mode operation and confinement in scanner. *Journal of Micro/Nanopatterning, Materials, and Metrology*, 20(3):033801, 2021. doi:10.1117/1.JMM.20.3.033801.